A Measurement of Neutral-Current Neutrino Interactions at the Sudbury Neutrino Observatory with an Array of ^{3}He Proportional Counters

Noah S. Oblath

A dissertation submitted in partial fulfillment
of the requirements for the degree of

Doctor of Philosophy

University of Washington

2009

Program Authorized to Offer Degree: Physics

University of Washington
Graduate School

This is to certify that I have examined this copy of a doctoral dissertation by

Noah S. Oblath

and have found that it is complete and satisfactory in all respects,
and that any and all revisions required by the final
examining committee have been made.

Chair of the Supervisory Committee:

_____

R. G. Hamish Robertson

Reading Committee:

_____

R. G. Hamish Robertson

_____

Wick C. Haxton

_____

Nikolai Tolich

_____

John F. Wilkerson

Date: _____

In presenting this dissertation in partial fulfillment of the requirements for the doctoral degree at the University of Washington, I agree that the Library shall make its copies freely available for inspection. I further agree that extensive copying of this dissertation is allowable only for scholarly purposes, consistent with "fair use" as prescribed in the U.S. Copyright Law. Requests for copying or reproduction of this dissertation may be referred to Proquest Information and Learning, 300 North Zeeb Road, Ann Arbor, MI 48106-1346, 1-800-521-0600, to whom the author has granted "the right to reproduce and sell (a) copies of the manuscript in microform and/or (b) printed copies of the manuscript made from microform."

Signature_____

Date_____

University of Washington

Abstract

A Measurement of Neutral-Current Neutrino Interactions at the Sudbury Neutrino Observatory with an Array of ^{3}He Proportional Counters

Noah S. Oblath

Chair of the Supervisory Committee:
Professor R. G. Hamish Robertson
Physics

The Sudbury Neutrino Observatory is a heavy-water Cherenkov detector designed to detect ^{8}B neutrinos from the sun. It is sensitive to neutrino elastic-scattering interactions with electrons, and neutral-current (NC) and charged-current (CC) interactions with deuterium. SNO uses its extensive array of photomultiplier tubes (PMTs) to measure both the electron neutrino flux and the total neutrino flux. In doing so SNO conclusively demonstrated the existence of solar neutrino flavor change.

For its third phase of operation the detector was enhanced with an array of ^{3}He proportional counters called the Neutral Current Detection (NCD) Array. The counters detect neutrons from the NC interactions and measure the total solar neutrino flux independent of the PMT measurements. A unique and highly detailed Monte Carlo (MC) simulation of the NCD array was developed to assist in the understanding of the detector. It has been and continues to be an essential part of the analysis of NCD Array data.

The NCD MC is used to classify pulses from the NCD Array as either signal or background events. The data pulses are fit with libraries of simulated pulses composed of signal neutron-captures and background alphas. The fit results identify a subset of neutron pulses that are unique from the alphas. This subset is used to determine the total number of neutrons detected with a simple cut-based analysis. The result of this pulse-shape-based analysis is a measurement of the NC solar neutrino flux based on one third of the NCD

data: $\phi_{\rm NC}^{\rm NCD} = 5.93 \pm 0.43$ (stat.) $^{+0.27}_{-0.26}$ (syst.) ν cm^{-2} s^{-1}. This is in excellent agreement with the BPS08(GS) Standard Solar Model (SSM) prediction.

This NC neutrino flux measurement is placed in the context of the global set of solar-neutrino experiments. The experimental results combined with the solar luminosity constrain the values of the neutrino mixing angles and the solar neutrino fluxes. The experiments can also neutrino-based measurement of the solar luminosity. The effects of this NCD-based NC measurement are examined with this global solar-neutrino analysis. The results show excellent agreement with the SSM expectations, and the new measurement of $\phi_{\rm NC}^{\rm NCD}$ reduces the uncertainties on the ^{8}B solar-neutrino spectrum and the neutrino mixing angles θ_{12} and θ_{13}.

TABLE OF CONTENTS

LIST OF FIGURES

LIST OF TABLES

GLOSSARY

ADC: Analog-to-Digital Converter

AV: The Acrylic Vessel, which contains the D_2O in SNO

CC: Charged Current interaction of a neutrino with deuterium

CNO CYCLE: The Carbon-Nitrogen-Oxygen cycle; the sub-dominant hydrogen burning mechanism in the sun.

CVD: Chemical Vapor Deposition, the process used to form the ultra-pure nickel walls of the NCD counters

DAQ: Data-acquisition hardware and software

ENDCAP: The volumes at each end of the NCD counters with reduced sensitivity to charged particles

ES: Elastic Scattering interaction of a neutrino with an electron

EVENT: A collection of PMT and/or NCD signals that cross one or more of several trigger conditions and are recorded by the SNO DAQ system

LOGAMP: A logarithmic amplifier in the MUX system. Logarithmic amplification was used to increase the range of pulse sizes that could be recorded by an 8-bit digitizer

MC: Monte Carlo; a technique for simulating stochastic processes, usually performed with a software package

MINUIT: A function minimization and error analysis software package

MSW EFFECT: The Mikheyev-Smirnov-Wolfenstein effect, explaining matter-enhanced neutrino oscillations

MUX: The Multiplexer branch of the SNO NCD DAQ system, which combines signals from up to twelve NCD channels prior to digitization; also refers to the NCD data consisting of full digitized pulses

MUX BOX: One of the primary components of the Multiplexer branch of the NCD DAQ system, including the trigger threshold for each of up to twelve NCD strings, and the logarithmic amplifiers. There were four MUX boxes, numbered 0-3

NC: Neutral Current interaction of a neutrino with deuterium

NCD: Neutral-Current Detector; a ^{3}He proportional counter used to detect neutrons in the SNO detector

NCD MC: NCD Monte Carlo; the physics-based pulse simulation developed within SNOMAN for the NCD phase

NCD STRING: A set of three or four NCD counters welded end-to-end

PCA: PMT Calibration to determine the timing and gain characteristics of the PMT array

PMT: Photomultiplier Tube; a light detector with the capability to detect single-photons

PP CHAIN: The proton-proton fusion chain; the dominant hydrogen-burning mechanism in the sun

PSUP: The PMT Support Structure

PULSE: A 15,000-bin digitization of an NCD signal

RCD: Resistive Coupler Disconnect; several strings suffered from a failure of one of the components of the string, making them unusable in the analysis

ROOT: An object-oriented data-analysis software package

SCOPE: The digital oscilloscopes in the MUX system that digitizes pulses

SHAPER: The Shaper/ADC branch of the SNO NCD DAQ system, which integrates pulses to measure the energy; also refers to the NCD data consisting of the pulse energy

SNO: The Sudbury Neutrino Observatory experiment

SNOMAN: The SNO Monte Carlo and ANalysis software package; the custom software package developed by the SNO Collaboration to perform data analysis and Monte Carlo simulations

SNU: Solar-neutrino unit: 10^{-36} interactions s^{-1} per target nucleon

SRIM: The Stopping and Ranges in Matter software package; used to obtain the energy-deposition characteristics of protons, tritons and alpha particles

SSM: The Standard Solar Model, which provides theoretical predictions for the solar-neutrino fluxes

PREFACE

> If knowledge can create problems, it is not through ignorance that we can solve them.
>
> *Isaac Asimov*

To most people the field of neutrino physics seems rather obscure. One of the most frequent questions I'm asked by non-physicists is: "Why do we care?" The answer is surprisingly complicated, but all of the reasons to study them can be summed up in one over-simplified statement: "Because they're there."

Simply put, neutrinos are fascinating. They are all around us, all the time, but these elusive "ghost particles" are so hard to detect that they were not even observed until 1956. About 10^{11} neutrinos pass through a square centimeter every second just from the sun. The highest density of neutrinos comes from the cosmic neutrino background, left over from the Big Bang. They fill up space with roughly 100 neutrinos cm^{-3} of each flavor at very low energies. Though we've learned much about them, a variety of fascinating questions about the neutrinos remain yet unanswered, such as why their masses are so small, and whether or not they are their own antiparticles. Neutrinos are some of the fundamental building blocks of the universe, and when there are open questions about something so foundational those questions need to be answered.

After fifty-two years of neutrino experiments and almost eighty years of theoretical work we have actually learned a great deal about neutrinos themselves. Now we are able to use neutrinos as tools in astrophysical research, such as peering into the core of the sun, modeling large-scale structure formation in the universe, and understanding how supernovae take place. Part of my research focuses on using neutrinos to measure the luminosity of the sun. It has been measured to high accuracy using photons, but the use of solar neutrinos

allows us to probe into the stellar core and compare the results between the two methods.

Some of the motivation for doing this research is also the challenge of performing the experiments. Detecting neutrinos is a notoriously difficult task. It requires creative ideas to overcome the challenges, and the Sudbury Neutrino Observatory (SNO) is no exception. SNO is an ultra-low-background solar neutrino detector that has been incredibly successful in achieving its goals. Its large volume and the radioactive purity of its components allow it to be exceptionally sensitive. SNO is unique among water Cherenkov detectors in that it uses heavy water (D_2O) as the neutrino target instead of light water (H_2O). This feature allows it to independently measure the electron-neutrino flux and the total neutrino flux. SNO operated from 1999 to 2006. With its first publications the SNO Collaboration definitively showed that neutrinos change flavor, solving the 30-year-old mystery of why previous experiments detected too few solar neutrinos. With all of the measurements made over its lifetime SNO helped move the field of neutrino physics to an era of precision measurements.

The third and final phase of SNO in particular presented many unique challenges. Ultra-clean proportional counters were added to the detector. The array of counters is known as the Neutral Current Detection (NCD) Array. A large portion of my research involves understanding and modeling the NCD counters. I, along with a number of other members of the SNO Collaboration, have developed a Monte Carlo simulation of the NCD proportional counters that accurately simulates current pulses, something that had never previously been done. Furthermore, I have made use of that simulation to discriminate between signal and background pulses. This method of pulse-shape analysis can accurately determine the number of signal pulses from a data set that is dominated by backgrounds.

This dissertation is organized to start and end with solar neutrinos, and discuss the details of SNO and the NCD Monte Carlo in the middle. The backgrounds for my research are developed in Chapters 1, 2, and 3, describing the history and physics of solar neutrinos, the Sudbury Neutrino Observatory, and the third phase of SNO, respectively. In Chapter 4 I describe the Monte Carlo developed for the SNO proportional counters. Chapter 5 details three analyses performed in the course of refining and verifying the Monte Carlo model.

The heart of my analysis work starts in Chapter 6 where libraries of simulated pulses are fit to the data, and continues in Chapter 7 where the NCD MC is a key element in a unique pulse-shape analysis and calculation of the NC ^{8}B solar neutrino flux with the NCD Array. Finally, I have performed a global solar-neutrino analysis that is described in Chapter 8.

Noah Oblath

September 2, 2008

Seattle, WA

ACKNOWLEDGMENTS

I would first like to thank my advisor, Hamish Robertson, for his guidance over the past six years. I have learned an incredible amount from him and I have always appreciated his advice and seemingly-endless supply of ideas.

The faculty, staff, and students at CENPA have made working there a pleasure. John Wilkerson's admirable dedication to his students and to the EWI group as a whole gave everyone a chance to work and play together. Nikolai Tolich has been an immense help with many aspects of my SNO analyses, and I've appreciated his many insights. I want to thank Kate Higgins, Barb Fulton, Deb Nastaj, and Victoria Clarkson for making all of the practical matters at the lab so easy that I know I'll miss their efforts in the future. John Amsbaugh, Tom Burritt, Mark Howe, Allan Myers, Dick Seymour, Tim Van Wechel, and Doug Will, were incredibly knowledgeable and always helpful.

I want to thank and congratulate the entire SNO Collaboration for the amazing work they have done on the NCD phase of SNO. In particular I want to thank the NCD Monte Carlo group for their extensive efforts in developing and verifying the NCD simulation: Wan Tseung, Jocelyn Monroe, Berta Beltran, Hamish Robertson, Keith Rielage, Sean McGee, Gersende Prior, and all of the others who have made various contributions. While working on the ^{3}He detection system at SNO I would never have gotten anything accomplished without the help of Richard Ford and the other SNOLAB staff. And, of course, I'm grateful to the people at LBL who originally sparked my interest in neutrino physics and SNO in particular as an undergraduate student: Kevin Lesko, Alan Poon, Colin Okada, and everyone else I worked with in the LBL neutrino group.

My office mates, Laura Stonehill, Michelle Leber, Sky Sjue, and Laura Bodine, kept day-to-day life interesting and were always there for good conversation and help solving problems. For help with so many things, thanks to Kathryn Miknaitis, John Orrell, Adam

Cox, Joe Formaggio, Keith Rielage, Sean McGee, Jason Detwiler, Brent VanDevender, and Kazumi Tolich.

I'm also very grateful to my friends outside of CENPA. In particular, Beth Lindsey, Erin Lay, and Andy O'Bannon; we worked together through many problem sets during our first year of grad school, and I've appreciated their friendship and our weekly lunches in the years after that. I want to thank all of the members of the various Milk Carton Derby teams for helping to build some amazing boats, and Beth especially, who was into it from the very beginning and through four years of boat building. I also want to thank Kai Martin, Carol Walker, all of the other volunteers, and the staff, at the Pacific Science Center, for providing a friendly and fun place to spend time away from campus.

Even though she wasn't often there in person, I can't express enough how much I've appreciated Naomi's love and support. Thank you for being such a wonderful friend and putting up with me, even in the most stressful times, over the past seven years.

And finally, to my parents who have supported me through twenty-five years of school, thank you for all that you've given me. They always encouraged me to do the best I could and be the best person I can be, and I've not forgotten what I learned from them.

DEDICATION

To my parents.

Chapter 1

SOLAR NEUTRINOS

Any discussion of solar neutrinos necessarily involves two components: the sun, and neutrinos. The properties of neutrinos that make them so difficult to detect are the same properties that make them the ideal tools for studying otherwise inaccessible things, such as the interiors of stars. Unlike photons, which have a mean free path of centimeters in the solar interior, neutrinos freely stream through and out of the core of the sun, reaching the earth thousands of years before photons created at the same time and place.

The realistic possibility of detecting solar neutrinos has been discussed since the late 1950s [1]. Ray Davis and John Bahcall first collaborated on a realistic proposal to use neutrinos to verify the hypothesis of solar fusion in the early 1960s [2, 3]. It was eventually apparent that neutrinos were not as well understood as previously thought, and solar neutrinos became an invaluable instrument for discovering the nature of neutrinos themselves. Now that their properties are better known and continually being studied, the opportunity exists to use the neutrinos to help understand how the sun, and stars in general, work.

1.1 The Sun

1.1.1 Solar Fusion

People have probably speculated on how the sun produces energy ever since they were capable of asking the question. However, it was not until the late 1930s that the fusion-reaction chains taking place in the sun were detailed by Carl F. von Weizsäcker [4, 5], Hans A. Bethe and C. L. Critchfield [6] and Bethe [7]. At a basic level, energy is produced by the sun through the fusing of four protons into a helium nucleus:

$$4p \rightarrow {}^4\mathrm{He} + 2e^+ + 2\nu_e. \tag{1.1}$$

There are two primary processes by which this occurs. The "pp-chain" is a set of fusion reactions and nuclear decays that produces 99% of the sun's energy. The reactions that make up the pp-chain are shown in Figure 1.1. The average total energy released for every transformation is 26.7 MeV. Electron neutrinos are produced in five of the reactions, either by beta decay or electron capture. The size of the nuclear mass differences in the interactions that produce solar neutrinos are not high enough to allow for the production of anti-muons and muon neutrinos instead of positrons and electron neutrinos.

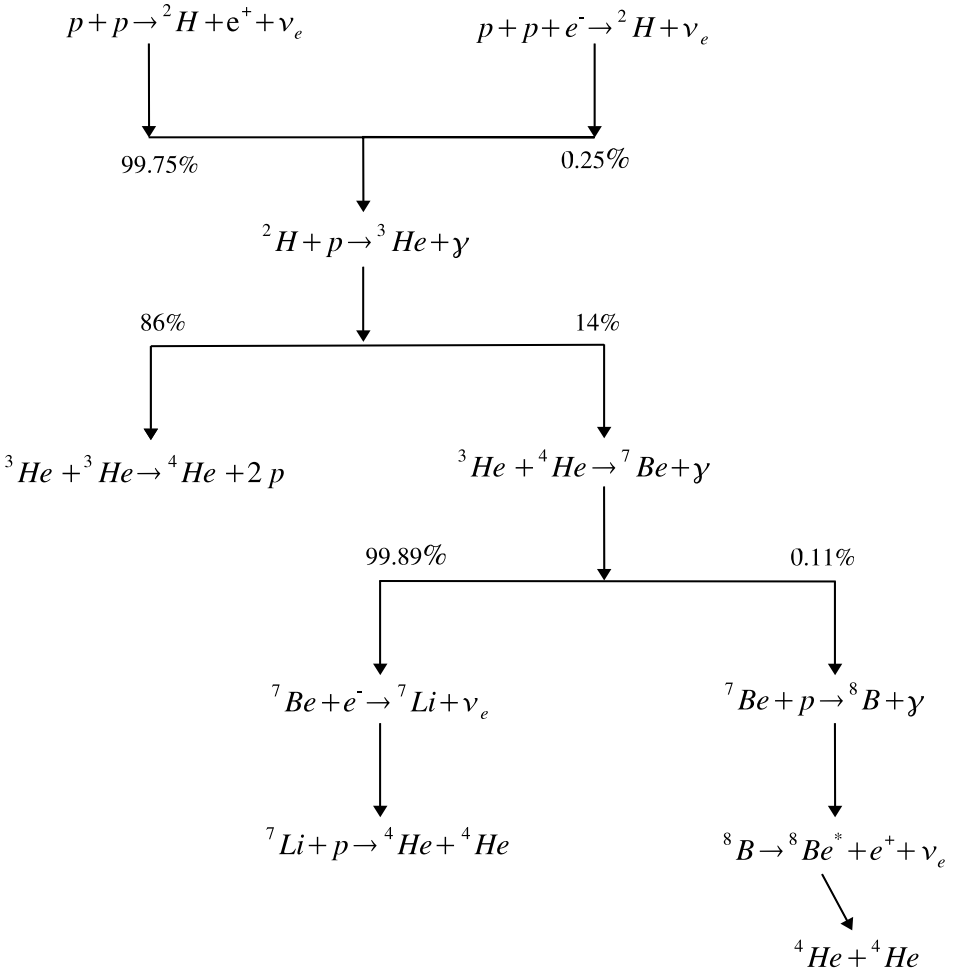

Figure 1.1: The reactions and branching ratios of the solar pp-chain. The hep branch is not shown in this diagram. This figure is from [8].

The energy spectra for the neutrinos produced by the pp-chain are shown in Figure 1.2. The dominant reaction is pp fusion, which occurs the most frequently, resulting in the highest solar neutrino flux with the lowest energy range, known as "pp neutrinos." The "pep neutrinos" are produced when an electron is captured during pp fusion. This produces neutrinos at a single energy. "^{7}Be neutrinos" are produced at two different energies, as the decay product ^{7}Li starts out in either of two energy states. The high-energy "^{8}B neutrinos" are produced during the decay of ^{8}B to ^{8}Be (the ^{8}B electron-capture flux is too small to appear on this plot). The highest energy neutrinos, known as the "hep neutrinos," also have the lowest flux. They are produced by the reaction of a ^{3}He nucleus and a proton: $^{3}\mathrm{He} + p \rightarrow {}^{4}\mathrm{He} + e^{+} + \nu_e$ (not shown in Figure 1.1).

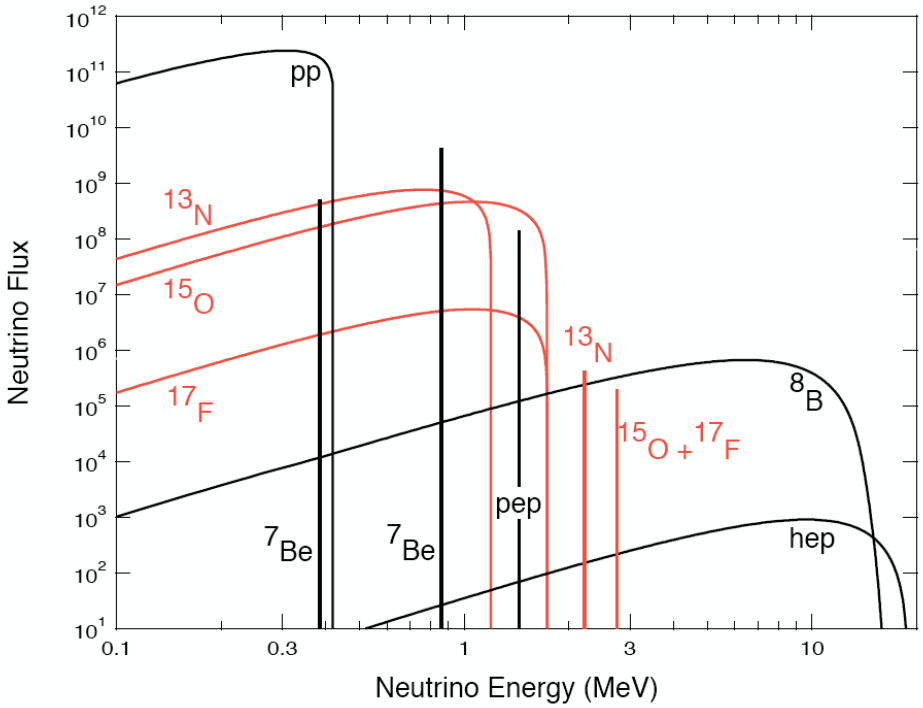

Figure 1.2: The electron neutrino energy spectrum from the pp-chain (black) and CNO cycle (red). This figure is from [9]. The units for the spectra are cm^{-2} s^{-1} MeV^{-1}, and the units for the line fluxes are cm^{-2} s^{-1}.

The other 1% of the solar energy is produced by the "CNO cycle," which uses carbon,

nitrogen, and oxygen nuclei as catalysts to fuse fuse protons into helium nuclei. At the current solar temperatures the CNO cycle is the subdominant process; at higher temperatures it would dominate over the pp-chain. The CNO cycle produces neutrinos in seven different reactions. The energy spectra (shown in Figure 1.2) differ from those of the pp-chain because they are produced by different reactions.

1.1.2 The Standard Solar Model[1]

The task of modeling the sun is based on a few fundamental assumptions. The first is that the sun is in hydrostatic equilibrium. That is, that the outwards radiative and mechanical pressure from inside the sun is exactly balanced by the inward force of gravity. The material that makes up the sun neither collapses inwards nor is expelled outwards. The second assumption is that energy is released through nuclear reactions, and that energy propagates outwards through radiative and convective processes. Furthermore, the sun is assumed to have been homogeneous before hydrogen burning began. The model is also constrained by the requirement that it reproduce the sun's present-day characteristics. The result is a detailed model known as the Standard Solar Model (SSM).

The SSM requires a few physical inputs to make an accurate model of the sun and its evolution. An equation of state relates the pressure and density within the sun. The current abundance of various elements on the surface of the sun is taken to represent the homogeneous initial conditions of the solar interior. Nuclear reaction rates and energies determine how the composition of the sun changes and how much energy is released at any given time in its evolution. Finally, the energy transport must be described. Radiative processes dominate the energy transport in the solar interior, so the opacity of the solar plasma to photons must be understood.

With the SSM one can make testable predictions to verify that the theory is accurate. One of those predictions is the speed of sound in the convective envelope near the surface of the sun. These can be compared with helioseismology data, which describe the propagation of pressure waves in the sun. In the past the agreement between helioseismology data and

[1] See [10, 11] as general references.

the SSM has been good. However, more recent revisions of the SSM have lower heavy-metal abundances, which affect the opacity of the solar plasma [12, 13]. These revised models no longer agree with the helioseismology data. Extensive work is being conducted on both the experimental and theoretical aspects of this conflict to try to find a resolution. The so-called BPS08 version of the SSM is the most recent update [13]. This reference includes both versions of the metallicity inputs and clearly illustrates the conflicting results. The high-metallicity SSM is known as BPS08(GS), and the low-metallicity SSM is BPS08(AGS).

A second important prediction is the set of solar neutrino fluxes described above. Figure 1.2 shows the energy spectra of the different solar neutrino fluxes predicted by the SSM. Accurate measurements of these fluxes are an extremely important test of the SSM in addition to exploring the properties of the neutrinos themselves. As an example, the two predictions for the ^{8}B neutrino flux (in units of 10^6 cm^{-2} s^{-1}) are 5.94 ± 0.65 (BPS08(GS)), and 4.72 ± 0.52 (BPS08(AGS)) They are incompatible, since the uncertainty on each prediction is 11%, while the difference between them is 23%. The other fluxes can be found in [13].

1.2 The Neutrino

The history of the neutrino starts with the picture of the nucleus that was emerging in the 1910s and 1920s, and two vexing problems associated with that picture and the understanding of nuclear beta decay. At the time the nucleus was thought to consist of protons and electrons; the neutron had not yet been discovered. For example, a ^{6}Li nucleus consisted of six protons (to account for the mass of 6) and three electrons (to cancel out the positive charges of three of the protons. The problem with this understanding is that for nuclei with even mass numbers and odd charges, such as ^{6}Li, the spin statistics could not be calculated correctly. The protons and electrons were known to be fermions, each with a spin of 1/2. With nine total fermions in the nucleus should therefore have had a half-integer spin. However, measurements of the spin of the ^{6}Li nucleus showed that it has a spin of 1. Similar problems were seen with the ^{14}N nucleus as well. While this issue, at the time, was thought to be suggestive of the existence of an unseen fermion, the problem was actually a result of the incorrect underlying model of the nucleus.

A more applicable problem arose when nuclear beta decays were carefully measured. Under the prevailing nuclear models of the time it was thought that the beta decay simply consisted of the electron being ejected from the nucleus. In such a two-body decay the electron should always have the same energy (or, in the case of nuclear excitations, one of several well-defined energies). In careful measurements of beta decays the electron energy spectrum was observed to be a continuous distribution up to some endpoint, rather than a discrete distribution at that endpoint.

Instead of giving up on the principles of spin and energy conservation, Wolfgang Pauli suggested a novel solution that would solve both problems [14, 15]: in an unpublished letter in 1930 he proposed that a third, neutral, and very light particle must also exist in the nucleus accompanying each electron, and be ejected with the electron during beta decay. The even number of particles in the nucleus would account for the spin of the nucleus, and the three-body decay would account for the continuous electron energy distribution. Furthermore, since it was neutrally charged and as light as the electron, it would be difficult to detect.

In 1932 James Chadwick discovered the neutron [16], and it was realized that the previous model of the nucleus was incorrect. As a result the spin-statistics problem vanished, but the issue of the electron-energy distribution was still solved by Pauli's hypothetical particles. Two years later, in 1934, Enrico Fermi formulated a basic model of beta decay that would later become the foundation for the entire theory of weak interactions [17]. His model included the new particles that he named *neutrinos*, or "little neutral ones." In this framework beta decays would occur when a neutron converts to a proton with the emission of an electron and an antineutrino, all acting at a point:

$$n \rightarrow p + e^{-} + \overline{\nu}. \tag{1.2}$$

Instead of being components of the nucleus, the electron and neutrino were spontaneously generated by the decay of the neutron. Fermi's theory also suggested a method for detecting

neutrinos, via the inverse beta decay:

$$\overline{\nu} + p \rightarrow n + e^{+}. \tag{1.3}$$

The cross section for this interaction was first calculated by theorists Hans Bethe and Rudolf Peierls in 1936 to be on the order of 10^{-44}cm^2 [18]. With such a small cross section Bethe and Peierls concluded that the neutrino would never be detected. A typical neutrino would be capable of passing through a light year of lead before interacting, making detection of neutrinos from radioactive sources virtually impossible.

The eventual detection of neutrinos would come twenty years later with the invention of neutrino sources that produced extremely large numbers of neutrinos: nuclear bombs and nuclear reactors. Frederick Reines and Clyde Cowan decided to use the reaction in Equation 1.3 to detect antineutrinos. After briefly considering using a nuclear bomb as the neutrino source they and their collaborators built their first neutrino detector outside the Hanford nuclear reactor in 1953. They later moved the experiment to the Savannah River reactor where they were able to make the first detection of antineutrinos in 1956 [19]. Reines was awarded the Nobel Prize for the discovery in 1995.

In 1937 theorist Ettore Majorana suggested that neutrinos could be their own antiparticles [20], since they lack an electric charge. However, in 1955 [21] Raymond Davis, Jr., showed that the antineutrinos released from nuclear reactors were not capable of initiating the reaction

$$\nu + {}^{37}\text{Cl} \rightarrow {}^{37}\text{Ar} + e^{-}. \tag{1.4}$$

This conclusion confirmed that neutrinos and antineutrinos were therefore distinct particles.[2] Two years later, when parity was shown to be violated in the weak interaction, the failure of antineutrinos to induce the reaction in Equation 1.4 could be ascribed to the different handedness of neutrinos and antineutrinos, rather than to an intrinsic quantum number. Neutrinos were left-handed particles that initiated interactions with neutrons, and

[2]The distinction between neutrinos and antineutrinos was deduced prior to 1955, when several double beta-decay experiments showed that double beta-decay lifetimes exceeded what would be expected if neutrinos were the same as their antiparticles [22].

antineutrinos were right-handed particles that initiated interactions with protons. The distinction between the neutrinos and antineutrinos is based on their handedness, rather than any other indication of particle-antiparticle nature such as electric charge. As a result the question of whether neutrinos and antineutrinos are truly distinct particles remains one of the actively pursued open questions in neutrino physics.

Further experimental discoveries regarding the nature of neutrinos would slowly be made as theories were developed and more sensitive experiments were built. In 1961 an experiment at Brookhaven National Laboratory determined that neutrinos associated with the decays of pions into muons were distinct from neutrinos that initiated interactions with electrons [23]. This was the first experiment to use neutrinos produced by a particle accelerator. It was later assumed that a third flavor of neutrino would be associated with the tau lepton that was discovered in 1975 [24]. This assumption was experimentally confirmed by the DONUT collaboration at Fermilab in 2000 [25]. In addition to the artificial neutrino sources, neutrinos from the sun were first detected by Davis and collaborators in the 1970s with the famous Homestake experiment [26]. Neutrinos produced as a result of cosmic rays hitting the atmosphere, so-called atmospheric neutrinos, were first seen by the Kolar Gold Fields neutrino experiment in 1965 [27]. In 1987 both the Kamiokande and IMB experiments detected neutrinos from supernova SN1987a [28, 29]. Davis and Masatoshi Koshiba were awarded the 2002 Nobel Prize for the detection of cosmic (solar , atmospheric, and supernova) neutrinos.

1.3 Neutrinos in the Standard Model[3]

Up to the 1950s physicists had always assumed that parity was not violated in fundamental interactions. That is, that the mirror image of an interaction would have the same results as the interaction itself. In the early 1950s it was observed that the decays of two strange mesons, then known as the τ and θ, that were otherwise identical resulted in final states with opposite parities. This led Tsung-Dao Lee and Chen Ning Yang, in 1956, to question the assumption of parity invariance [31]. They realized that, while parity had been shown

[3]See [30] as a general reference.

through experiments to be invariant for electromagnetic and strong nuclear interactions, it had not been tested for weak interactions. If parity were violated for weak interactions then a single particle could have decay channels whose final states have different parity. One year later Chien-Shiung Wu and collaborators showed that parity was indeed violated in the beta decays of ^{60}Co nuclei [32], and R. L. Garwin and collaborators showed that parity violation occurs in meson decays [33]. Further experiments with beta decays demonstrated that the weak interaction violates parity maximally. In the case of the τ and θ mesons it was realized that they were actually the same particle, the K^+.

The properties of helicity and chirality were fundamental in the understanding of parity violation. The helicity of a particle is the particle's spin projected on its direction of motion. A left-handed neutrino has a spin that is anti-parallel to its momentum. Helicity is not Lorentz invariant, since an observer could boost to a reference frame in which any particle traveling slower than the speed of light reversed its direction of motion. If neutrinos were to always be in a left-handed helicity state they must travel at the speed of light, and therefore be massless. For massless particles, helicity states are the eigenstates of the γ^5 Dirac matrix.

Massive particles, on the other hand, do not have a definite helicity because of the dependence on the frame of reference. For massive particles helicity must be generalized to a Lorentz-invariant property known as chirality. The left- and right-handed chiral particle states, ψ_L and ψ_R, are the eigenstates of γ^5: the eigenvalue of ψ_R is $+1$, and the eigenvalue of ψ_L is -1. Based on these relationships the chirality projection operators are defined as

$$\begin{aligned} P_L &= \tfrac{1-\gamma^5}{2}, \quad P_L\psi_L = \psi_L, \quad P_L\psi_R = 0; \\ P_R &= \tfrac{1+\gamma^5}{2}, \quad P_R\psi_L = 0, \quad\;\; P_R\psi_R = \psi_R. \end{aligned} \tag{1.5}$$

For massless particles the states ψ_L and ψ_R are states of definite helicity. For massive particles they are states of definite helicity only when viewed from a reference frame in which the particles are relativistic.

The statement that the weak interaction violates parity implies that such interactions act differently on left- and right-handed chirality states. The statement that weak interactions violate parity maximally means that weak interactions act only on either left- or right-

handed neutrinos (but not both). In 1957 Lee and Yang suggested [31] that the maximal violation of parity implied that all neutrinos were found in a definite helicity state (they did not know whether it was left-handed or right-handed at the time). The only way for this to be true in a Lorentz-invariant theory was if neutrinos were massless and therefore able to travel at the speed of light. Indeed, one year later, Maurice Goldhaber, Lee Grodzins, and Andrew Sunyar conducted an experiment to measure the helicity of the neutrino [34]. They found that neutrinos were in left-handed helicity states. The developing Standard Model therefore included only left-handed, massless neutrinos (and right-handed antineutrinos).

To satisfy the maximal violation of parity and to match experimental data on neutrino helicity the Standard Model Lagrangian describing weak interactions must have a "vector minus axial vector," or "V-A" form:

$$\mathcal{L}_{\text{weak}} = \overline{\psi}\gamma^{\mu}(1-\gamma^{5})\psi. \tag{1.6}$$

Since a particle is the sum of its right- and left-chirality components, $\psi = \psi_R + \psi_L$, the Lagrangian term reduces to $\overline{\psi}_L\gamma^{\mu}\psi_L$. In other words, the weak interaction acts only on left-handed particles (and right-handed antiparticles). Of course, the fact that it is the weak interactions selecting the handedness of any neutrinos detected leaves open the possibility of massive neutrinos when interpreting the neutrino-helicity measurements.

In Fermi's original beta-decay theory the weak interaction was modeled as a current-current interaction, similar to the theory of electromagnetic interactions. However, whereas electromagnetic interactions took place over long distances by photon exchange, the weak interaction was modeled as a point-like contact interaction.

The boson actually responsible for the weak exchange is the W. The range of the weak interaction is short because of the high mass of the W, but it is not point-like as in Fermi's theory. The W exists in two charge states, W^+ and W^-, which explains the existence of charged-current weak interactions. Charged-current vertices connect a charged lepton to the uncharged neutrino of the same flavor, as in Figure 1.3a.

In the 1960s the Glashow-Weinberg-Salam (GWS) theory of electroweak interactions included the idea of neutral-current weak interactions [35]. The theory suggested the exis-

tence of a heavy neutral boson, called the Z^0, which mediated neutral-current interactions in which the interaction vertex leaves the particle unchanged. After 1971, when the GWS theory was shown by Gerard 't Hooft to be renormalizable [36], the idea gained traction in the physics community. Such weak neutral currents were finally observed in the Gargamelle bubble-chamber experiment at CERN in 1973 [37]. The $W^{\pm}$ and Z^0 were created at CERN in 1983, and their masses matched the predictions of the GWS theory [38, 39]. The observation of neutral-current weak interaction and the creation and measurement of the vector bosons in accelerator experiments was an outstanding confirmation of the GWS electroweak theory. For neutrinos, neutral-current vertices connect two neutrinos of the same flavor, as in Figure 1.3b. Sheldon Glashow, Abdus Salam, and Steven Weinberg were awarded the 1979 Nobel prize for their formulation of the GWS theory. 't Hooft shared the 1999 Nobel prize with Martinus Veltman for demonstrating that the GWS theory is renormalizable.

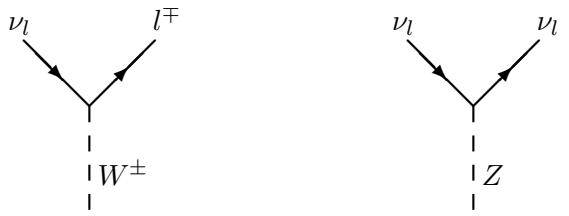

(a) Charged current (b) Neutral current

Figure 1.3: Examples of neutrino (a) charged-current and (b) neutral-current weak interaction vertices. The charged-current interaction couples a neutrino, ν_l, with a charged lepton of the same flavor, $l^{\mp}$. The neutral-current vertex couples two neutrinos of the same flavor.

1.4 Neutrinos Beyond the Standard Model[4]

1.4.1 Adding Neutrino Mass

While the Standard Model Lagrangian does not include a mass term for neutrinos there is no fundamental argument against the existence of neutrino mass. Left-handed and right-handed fermion states are treated differently in the Standard Model. The left-handed states are SU(2) doublets, while the right-handed states are singlets. If, for the sake of argument, we include right-handed neutrinos that have never actually been observed, then the leptons are arranged as follows:

$$\begin{pmatrix} \nu_e \\ e \end{pmatrix}_L, \quad \begin{pmatrix} \nu_\mu \\ \mu \end{pmatrix}_L, \quad \begin{pmatrix} \nu_\tau \\ \tau \end{pmatrix}_L, \quad e_R,\ \mu_R,\ \tau_R,\ \nu_{eR},\ \nu_{\mu R},\ \nu_{\tau R}. \tag{1.7}$$

The left-handed particles are arranged in "isodoublets," and the right-handed particles are in singlet states. The $W^\pm$ and Z^0 bosons act only on the isodoublet states, with the $W^\pm$ interactions connecting the upper and lower components.

The massive Standard Model particles obtain their masses through terms in the Lagrangian that couples the right- and left-handed states:

$$\mathcal{L}_{\text{mass}} = -m\overline{\psi}\psi. \tag{1.8}$$

One could add such a term for neutrinos as well. ψ is the sum of the left- and right-handed components of the fermion field, $\psi = (P_L + P_R)\psi = \psi_L + \psi_R$, so the mass term becomes

$$\begin{aligned} -\mathcal{L}_{\text{mass}} &= m\overline{\psi}(P_L + P_R)(P_L + P_R)\psi \\ &= m(\overline{\psi}_R\psi_L + \overline{\psi}_L\psi_R). \end{aligned} \tag{1.9}$$

If there is no right-handed neutrino state then the mass term disappears. If there is a right-handed neutrino, even if it cannot be detected, then neutrinos can have mass. This type of mass term in the Lagrangian is known as a Dirac mass, and particles with this type

[4]See [30, 40, 41] as general references.

of mass, including all of the charged fermions, are known as Dirac particles.

Due to the unique nature of neutrinos, being fermions with no electrical charge, they have the potential to be "Majorana" particles, with some very special properties. Both ν and $\overline{\nu}$ satisfy the same Dirac equation, $(i\gamma^{\mu}\partial_{\mu} - m)\psi_{\nu} = 0$, where ψ_{ν} is either the neutrino or antineutrino field. There is nothing in the Standard Model preventing one from describing the neutrino field as [30]

$$\psi_M = \frac{1}{\sqrt{2}}(\psi + \psi^c), \tag{1.10}$$

where ψ is the neutrino field and ψ^c is the the conjugate of the neutrino field under the particle-antiparticle conjugation operator, C. C also has the effect of reversing the chirality of the particle. Equation 1.10 allows one to write a Lagrangian that, in addition to the Dirac mass, also includes terms that couple neutrinos and antineutrinos:

$$-\mathcal{L}_{\mathrm{M-mass}} = \frac{m_L}{2}(\overline{\psi}_L\psi_L^c + \overline{\psi_L^c}\psi_L) + \frac{m_R}{2}(\overline{\psi}_R\psi_R^c + \overline{\psi_R^c}\psi_R). \tag{1.11}$$

The Majorana mass term changes U(1) charges by two units. The conservation of electric charge precludes the existence of such a term for any fermion other than the neutrino. For neutrinos, however, it requires that the conservation of lepton number is broken. Lepton number conservation is not based on any fundamental symmetry in the Standard Model,[5] so the existence of a Majorana mass term for neutrinos is considered a possibility.

1.4.2 Neutrino Flavor Oscillations

In the Standard Model the three quark states that participate in weak interactions are linear combinations of the states that participate in strong interactions. One could imagine applying a similar "mixing" to massive neutrinos. If the neutrino eigenstates of the weak interaction are not exactly the same as the mass eigenstates, then it is possible for the neutrinos to effectively change flavor, or "oscillate." Neutrino oscillations were first suggested in 1958 by Bruno Pontecorvo, who was considering neutrino-antineutrino oscillations [42]. Four years later Ziro Maki, Masami Nakagawa, and Shoichi Sakata presented the idea of

[5]While this is true, Majorana masses were not included in the Standard Model because such terms are non-renormalizable.

oscillations between neutrino flavors [43]. A matrix relating the mass eigenstates to the flavor eigenstates was developed based on the work of the Maki, Nakagawa, Sakata, and Pontecorvo, known as the MNSP matrix. It is the lepton analogue of the CKM quark-mixing matrix:

$$U_{\text{MNSP}} = \begin{pmatrix} U_{e1} & U_{e2} & U_{e3} \\ U_{\mu 1} & U_{\mu 2} & U_{\mu 3} \\ U_{\tau 1} & U_{\tau 2} & U_{\tau 3} \end{pmatrix}. \tag{1.12}$$

Each flavor eigenstate is made up of a linear combination of the mass eigenstates. For instance, the relative contributions of the mass 1, 2, and 3 eigenstates in an electron neutrino are given by the parameters, U_{e1}, U_{e2}, and U_{e3}, respectively.

If neutrinos are oscillating between the flavor eigenstates the results should be observable by sensitive neutrino-detection experiments. Given a known source of neutrinos, where both the total flux and the relative contribution of each flavor are understood to some precision, neutrino oscillations can be observed either by seeing an increase or decrease in the contribution of one or more flavors. If a neutrino source produces only ν_e, for example, then the detection of ν_μ or ν_τ would be evidence of neutrino oscillations. If a different source produced equal numbers of ν_e and ν_μ, but a ν_e:ν_μ ratio of 4:1 was detected, that too would be evidence of neutrino oscillations.

One can simplify the picture of oscillations by considering the situation given two flavor states and two mass states. We can characterize the relationship between the mass states and the flavor states by a rotation angle, θ_{12}:

$$\begin{pmatrix} \nu_e \\ \nu_\mu \end{pmatrix} = \begin{pmatrix} \cos\theta_{12} & \sin\theta_{12} \\ -\sin\theta_{12} & \cos\theta_{12} \end{pmatrix} \begin{pmatrix} \nu_1 \\ \nu_2 \end{pmatrix}. \tag{1.13}$$

Neutrinos are created in definite flavor eigenstates since the process occurs via a weak interaction. We can write the flavor states as

$$\begin{aligned} |\nu_e\rangle &= \cos\theta_{12}|\nu_1\rangle + \sin\theta_{12}|\nu_2\rangle \\ |\nu_\mu\rangle &= -\sin\theta_{12}|\nu_1\rangle + \cos\theta_{12}|\nu_2\rangle. \end{aligned} \tag{1.14}$$

As is true for any other massive particle, neutrinos propagate in definite mass eigenstates. Equation 1.14 can be inverted to determine the flavor contribution to each mass state. For a generic neutrino, $|\nu\rangle = a_e|\nu_e\rangle + a_\mu|\nu_\mu\rangle$, the propagation equation in a vacuum is [41]

$$i\frac{\mathrm{d}}{\mathrm{d}t}\begin{pmatrix} a_e \\ a_\mu \end{pmatrix} = \frac{1}{4E}\begin{pmatrix} -\Delta m^2_{21}\cos 2\theta_{12} & \Delta m^2_{21}\sin 2\theta_{12} \\ \Delta m^2_{21}\sin 2\theta_{12} & \Delta m^2_{21}\cos 2\theta_{12} \end{pmatrix}\begin{pmatrix} a_e \\ a_\mu \end{pmatrix}. \tag{1.15}$$

The neutrino is also detected via a weak interaction, and therefore the act of detecting it will collapse the wavefunction into a definite flavor state. Under the assumption that the neutrino is relativistic, one can write the oscillation probability, the probability that the neutrino will be detected as a ν_μ, as

$$P_{e\mu} \equiv P(\nu_e \to \nu_\mu) = |\langle\nu_\mu|\nu_e(L)\rangle|^2 = \sin^2(2\theta_{12})\sin^2\left(1.27\Delta m^2_{21}\frac{L}{E}\right), \tag{1.16}$$

where $\Delta m^2_{21} = m^2_2 - m^2_1$ in eV^2, E is the energy of the neutrino in MeV, and L is the distance traveled in meters. The factor of 1.27 accounts for the units and the factors of 4π, $\hbar$, and c. Δm^2_{21} and θ_{12} are properties of the neutrinos, while L and E are properties of the experiment. $P_{ee} \equiv 1 - P_{e\mu}$ is called the "survival probability." The flavor of the neutrino oscillates as the probability of detecting it in the original flavor varies up and down. For a neutrino source with a given energy, the amplitude of the oscillation is determined by the mixing angle, θ_{12}, and the oscillation length is determined by Δm^2_{21}. The oscillation probability approaches a limit for very large L, $P_{e\mu} \to \frac{1}{2}\sin^2(2\theta_{12})$, after the oscillations are averaged out to 1/2 due to separation of the wavepackets into distinct mass eigenstates.

Generalizing to the three-flavor oscillation model, a special case applies:

$$|\Delta m^2_{21}| \ll |\Delta m^2_{31}| \approx |\Delta m^2_{32}|. \tag{1.17}$$

With this condition, and the condition that, for solar neutrinos $\Delta m^2_{32}\frac{L}{2E} \gg 1$, the electron-neutrino survival probability is

$$P_{ee} \approx \cos^4\theta_{13}P_{2\nu} + \sin^4\theta_{13}, \tag{1.18}$$

where $P_{2\nu}$ is P_{ee} for two neutrinos. For small values of θ_{13}, depending on the precision of the calculation, the two-neutrino approximation is often sufficient.

1.4.3 Neutrinos in Matter

In 1985 Mikheyev and Smirnov [44], building on ideas by Wolfenstein from 1978 [45], suggested that neutrino oscillations might be enhanced as neutrinos passed through matter. This outcome and the theory predicting it became known as the "MSW" effect.

Since normal matter is composed in part of electrons, but contains no muons or taus, the electron neutrino states feel an additional interaction potential. ν_e can interact via the charged and neutral weak bosons, while ν_μ and ν_τ can interact only via the Z^0. The interaction potential experienced by the ν_e is density dependent:

$$V_e = \sqrt{2} G_F N_e, \tag{1.19}$$

where N_e is the electron density, and G_F is the Fermi coupling constant. The propagation equation is modified in the presence of the matter potential:

$$i\frac{\mathrm{d}}{\mathrm{d}t}\begin{pmatrix} a_e \\ a_\mu \end{pmatrix} = \frac{1}{4E}\begin{pmatrix} -\Delta m^2_{21}\cos 2\theta + \sqrt{2}G_F N_e & \Delta m^2_{21}\sin 2\theta \\ \Delta m^2_{21}\sin 2\theta & \Delta m^2_{21}\cos 2\theta \end{pmatrix}\begin{pmatrix} a_e \\ a_\mu \end{pmatrix}. \tag{1.20}$$

The states that diagonalize this Hamiltonian are the neutrino eigenstates in matter:

$$\begin{aligned} |\nu_{1m}\rangle &= \cos\theta_m|\nu_e\rangle + \sin\theta_m|\nu_\mu\rangle \\ |\nu_{2m}\rangle &= -\sin\theta_m|\nu_e\rangle + \cos\theta_m|\nu_\mu\rangle, \end{aligned} \tag{1.21}$$

where θ_m, the effective mixing angle, is defined by

$$\tan 2\theta_m = \frac{\frac{\Delta m^2}{2E}\sin 2\theta_{12}}{\frac{\Delta m^2}{2E}\cos 2\theta_{12} - \sqrt{2}G_F N_e}. \tag{1.22}$$

The effective mixing angle is a function of the density of the matter through which the neutrino is propagating. Recalling Equation 1.16, with the vacuum mixing angle replaced by θ_m, it is the mixing angle that sets the amplitude of the oscillations between the flavor

states. Therefore the oscillation amplitude is a function of the matter density:

$$\sin^2 2\theta_m = \frac{\left(\frac{\Delta m^2_{21}}{2E}\right)^2 \sin^2 2\theta_{12}}{\left(\frac{\Delta m^2_{21}}{2E}\cos 2\theta_{12} - \sqrt{2}G_F N_e\right)^2 + \left(\frac{\Delta m^2_{21}}{2E}\right)^2 \sin^2 2\theta_{12}}. \tag{1.23}$$

There is a critical density where the first term in the denominator goes to zero: $\sqrt{2}G_F N_e = \frac{\Delta m^2}{2E}\cos 2\theta_{12}$. At this density the mixing between the states is maximal, with $\theta_m = 45°$, independent of the vacuum mixing angle. The mass eigenstates are equal combinations of the flavor eigenstates. For a wide range of Δm^2 and neutrino energies the critical density exists in the sun. Therefore, when determining the survival probability for solar neutrinos the density gradient of the sun must be taken into account.

Since the mass eigenstates are density dependent, as a neutrino travels through matter with a changing density, the mass eigenstates themselves change. If the density changes slowly enough the neutrino will remain in the same mass eigenstate. If it changes more rapidly, then there is a non-zero probability, P_c, of jumping one mass-eigenstate trajectory to the other. The survival probability can be written in terms of P_c [46]:

$$P_{ee} = \frac{1}{2} + \frac{1}{2}(1 - P_c)\cos 2\theta^0_m \cos 2\theta_{12}, \tag{1.24}$$

where θ^0_m is the local mixing angle where the neutrino was created, and θ_{12} is the vacuum mixing angle. In the adiabatic limit [47], P_c goes to zero, and the neutrino stays in the same mass eigenstate.

At high densities, θ^0_m approaches the limit of $\pi/2$, and $|\nu_e\rangle \approx |\nu_{2m}\rangle$. The ν_e survival probability simplifies to

$$P_{ee} = \sin^2 \theta_{12}. \tag{1.25}$$

Electron neutrinos are created in the core of the sun where they are almost entirely in the ν_{2m} state. The change in density as the neutrino travels towards the surface of the sun is close to adiabatic, so P_c is small and most of the neutrinos remain in the ν_{2m} state. By the time the neutrinos reach the surface of the sun, $\theta_m \approx \theta$, and $|\nu_{2m}\rangle \sim 0.6|\nu_e\rangle + 0.6|\nu_\mu\rangle + 0.6|\nu_\tau\rangle$. The MSW effect changes the relative contributions of the different flavors to the neutrinos

as they exit the sun, which affects the measurements of the neutrino flux made at the earth.

The MSW effect differentiates between the hierarchy options for ν_1 and ν_2: $m_1 < m_2$ or $m_1 > m_2$. The scenario in which the MSW effect enhances ν_e oscillations assumes the former. In Equation 1.23 the parameter Δm^2_{21} appears in the denominator such that flipping its sign will change $\sin^2\theta_m$. In the case where $\Delta m^2_{21} \equiv m^2_2 - m^2_1 > 0$ (assuming $\theta_{12} < 45°$, as has been measured), at high densities the electron neutrino has a large overlap with $|\nu_2\rangle$, the heavier of the two mass eigenstates. This is different than the situation in vacuum, where the electron neutrino is primarily composed of ν_1. In the opposite case, where $\Delta m^2_{21} < 0$, the oscillations are suppressed by the matter effects. The former case is found to be true. Solar neutrino experiments have been able to determine that $\Delta m^2_{21} > 0$ by observing the enhancement of the oscillation probability.

To generalize to the three-neutrino case $P_{2\nu}$ in Equation 1.18 is replaced by the appropriate MSW survival probability, such as Equation 1.24. The effective potential, V_e, is replaced by $\cos^2\theta_{13}V_e$ [48].

1.5 The Discovery of Neutrino Mass

While the possibilities of neutrino mass and flavor oscillations were theoretically established starting in the 1950s, their discovery would take several decades and a wide variety of experiments. In the neutrino-oscillation model the sensitivity of an experiment in θ-Δm^2 space depends on the energy of the neutrinos and the distance between the source and the detector. The limited variety of strong neutrino sources and the various ways in which one can build a detector determine how one searches that parameter space.

Typical neutrino sources that have been used in experiments include nuclear reactors, accelerators, cosmic-ray showers in the atmosphere, and the sun. Reactor-neutrino experiment baselines range from a few meters from the reactor core to hundreds of kilometers. The baseline for atmospheric neutrino experiments is the distance from the upper atmosphere to the experiment on or in the surface of the earth (possibly traveling through part or all of the earth as well). The baseline for an accelerator experiment is somewhat flexible since the neutrinos are steered in a beam, though there can be geographical and geological limitations, and the flux still decreases proportional to $1/L^2$. The baseline for solar neutrino

experiments is set by the orbit of the earth around the sun.

Each source also has a typical energy or energy range. The combination of the baseline and the neutrino energy determine the sensitivity of the experiment in Δm^2_{21}. The approximate baselines, energies, and Δm^2 sensitivities for the four typical types of neutrino experiments are shown in Table 1.1.

Table 1.1: Typical baselines, energies, and Δm^2 sensitivities for accelerator, reactor, atmospheric, and solar neutrino experiments.

Source	L (m)	E (MeV)	Δm^2 sensitivity (eV^2)
Accelerator	$10^2 - 10^5$	10^3	$10^{-2} - 10$
Reactor	$10^1 - 10^5$	1	$10^{-5} - 10^{-1}$
Atmospheric	10^7	10^4	10^{-3}
Solar	10^{11}	1	10^{-11}

Raymond Davis, Jr., and John Bahcall detailed an experiment to detect solar neutrinos via capture on ^{37}Cl (Equation 1.4) in 1964 [2, 3], an idea that had been proposed by Bruno Pontecorvo [49] and studied by Luis W. Alvarez [50]. Their purpose was to test the hypothesis of fusion burning in the sun and, specifically, the calculations of the solar-neutrino fluxes performed by Bahcall, Fowler, Iben, and Sears [51] a year earlier. Neutrinos were ideal for this goal since, assuming they were being produced in the pp-chain and CNO cycle, they would travel unimpeded out of the sun, retaining their original energies. The photons emitted from the sun, on the other hand, have a short scattering length in the stellar material and therefore lose information about their production. They could also potentially be produced by other (non-fusion) energy-generating mechanisms. Davis and collaborators built the experiment in the following years in the Homestake gold mine in South Dakota. It was primarily sensitive to ^{8}B solar neutrinos, which are produced in the core of the sun with a flux that is extremely sensitive to the core temperature ($\phi_{^8B} \sim T^{18}$ [10]). That dependence on the temperature makes it an excellent probe of the conditions in the solar core.

In 1968 Davis, Harmer, and Hoffman reported the first results from the Homestake

experiment [26], though no neutrinos were detected and a limit was placed on the flux. With an improvement to the electronics in 1970, Davis and his collaborators were able to make the first measurements of the solar neutrino flux [1]. They found the first hint that either something was wrong with the solar model, or something was wrong with the Standard Model description of neutrinos. They measured only one third of the expected flux. The mysterious discrepancy between theory and experiment became known as the "Solar Neutrino Problem." The Homestake experiment continued to record the solar-neutrino flux for thirty years, with a final cumulative measurement of 2.56 ± 0.23 SNU[6] [52], whereas the expected value from the SSM is $8.46^{+0.87}_{-0.88}$ SNU [13]. Without verification by other experiments a third possibility remained, that the experimental results were wrong. That possibility was essentially eliminated with evidence from the Kamiokande experiment in 1987 [53]. The results of the Homestake experiment, along with the other solar-neutrino experiments mentioned below, are compared to the theoretical expectations in Figure 1.4. The question of whether the SSM was wrong or the understanding of neutrinos from the Standard Model was wrong remained unanswered for some time.

The solar-neutrino mystery was confirmed by two other radiochemical experiments that used neutrino capture on ^{71}Ga:

$$\nu_e + {}^{71}\mathrm{Ga} \rightarrow {}^{71}\mathrm{Ge} + e^- \tag{1.26}$$

The gallium reaction has an energy threshold of 233 keV, so it is able to detect the pp neutrinos. The two experiments, SAGE (1990-present)and GALLEX (1991-2003; later renamed GNO), resulted in a combined measurement of 68.1 ± 3.75 SNU [55]. The expectation from the SSM was $127.9^{+8.1}_{-8.2}$ SNU [13].

The Kamiokande experiment was a water-Cherenkov detector built in Japan for the original purpose of looking for proton decay. It was eventually realized that, with improved electronics, the detector could be a sensitive method for observing neutrinos in real time. Unlike the radiochemical experiments, which periodically removed the products of the neu-

[6] A Solar Neutrino Unit, or "SNU", is defined as 10^{-36} neutrino capture reactions per second per absorber nucleus.

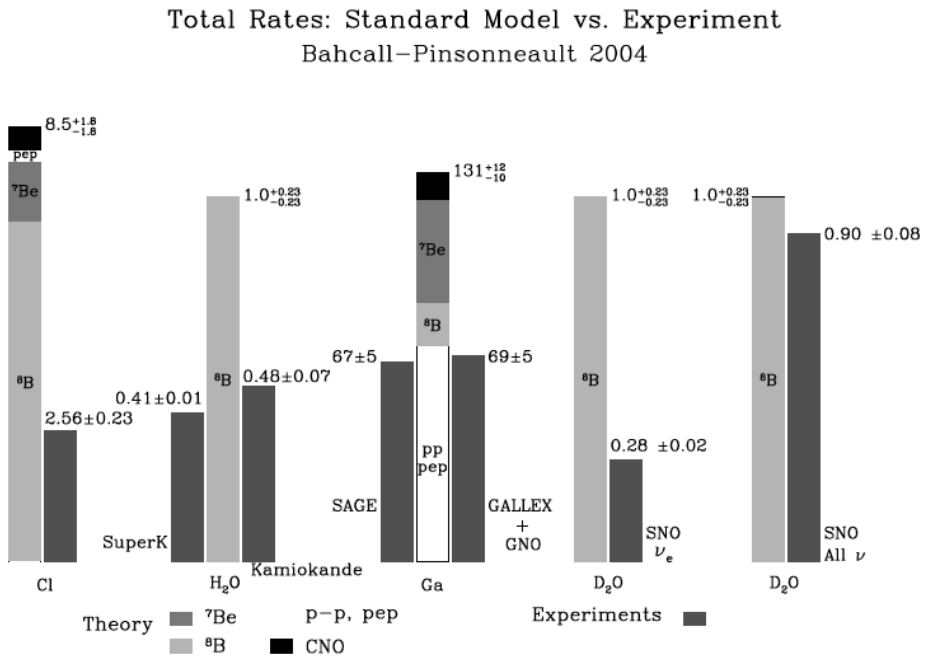

Figure 1.4: A comparison of six solar-neutrino experimental results with the corresponding theoretical predictions from the SSM. The different types of experiments, Cl, Ga, H_2O and D_2O, have different energy thresholds. As a result they are sensitive to different fluxes of solar neutrinos. The fluxes for the radiochemical experiments are given in units of SNU, where 1 SNU = 10^{-36} neutrino captures per target nucleus per second. The fluxes for the H_2O and D_2O experiments are given relative to the SSM predictions. This figure is from [54], so the SSM flux predictions differ slightly from [13].

trino interactions (^{37}Ar and ^{71}Ge) to count the number of interactions that had occurred, Cherenkov detectors would see each interaction. The tradeoff is a higher energy threshold; water-Cherenkov detectors are only able to see the ^{8}B and hep solar neutrinos. Kamiokande, operating from 1987 to 1996 as a neutrino detector, detected neutrinos via elastic scattering in a 3-kton volume of water. The struck electron, traveling faster than the speed of light in the water, created a cone of Cherenkov radiation that was detected with photomultiplier tubes (PMTs). The total detected flux of neutrinos[7] was $(2.80 \pm 0.38) \times 10^6$ cm^{-2} s^{-1} [56]. The expected flux from the SSM was 5.28×10^6 cm^{-2} s^{-1} [54]. The successor to Kamiokande, Super-Kamiokande, began operation in 1996 with a 50-kton volume of water. It measured a ^{8}B solar-neutrino flux of $(2.35 \pm 0.08) \times 10^6$ cm^{-2} s^{-1}; the results were consistent with the Kamiokande measurement and approximately half of the expected flux.

In addition to detecting solar neutrinos, Kamiokande [57] and another experiment, IMB [58], measured atmospheric neutrinos coming from cosmic-ray showers. The characteristic decays of the secondary and tertiary particles in the showers result in a ν_μ:ν_e ratio of 2:1. Both experiments, however, detected too few muon neutrinos; this discrepancy became known as the "atmospheric neutrino anomaly."

In 1998 the Super-Kamiokande collaboration reported the first unambiguous evidence for neutrino-flavor disappearance, using the flux of atmospheric neutrinos [59]. This high-statistics experiment was able to determine the zenith-angle dependence of the observed neutrino flux ratio, and map out its behavior as a function of L/E. They found that the ratio of atmospheric ν_μ to ν_e depended on the distance the neutrinos traveled; neutrinos created on the far side of the earth had a significantly longer distance to travel to reach the detector than neutrinos created directly above it. The data could be explained by the neutrino oscillation model with ν_μ oscillating into ν_τ that were not observed. The data suggested a "maximal" mixing angle of $\theta_{23} = 45°$, and $\Delta m^2_{32} \sim 3 \times 10^{-3}$ eV^2. This result has been supported more recently by further atmospheric neutrino measurements, as well as the accelerator neutrino experiments K2K [60] and MINOS [61].

The resolution of the Solar Neutrino Problem finally came in 2001 and 2002 with mea-

[7] A light-water (H_2O) detector is primarily sensitive to ν_e, with limited sensitivity to ν_μ and ν_τ. However, it is unable to distinguish between neutrino flavors.

surements by the Sudbury Neutrino Observatory (SNO) [62, 63, 64]. SNO was also a water Cherenkov detector, but it used heavy water, D_2O, instead of light water as the neutrino target. As a result SNO was able to measure both the ν_e-only and the total solar-neutrino fluxes. The SNO results showed that ν_e created in the sun were being detected as ν_μ and ν_τ, the first detection of neutrino flavor appearance. Results from the third phase of SNO measured the appearance of ν_μ and ν_τ in the solar neutrino flux at the 8.2-σ level[8] [65]. When these data are combined with previous solar-neutrino results, as well as the reactor-neutrino experiment KamLAND [66], and interpreted within the neutrino-oscillation framework, the best-fit mixing angle is $\theta_{\text{solar}} \approx 34^\circ$, and the mass splitting is $\Delta m^2_{\text{solar}} \approx 7.9 \times 10^{-3}$ eV^2. By decisively solving the Solar Neutrino Problem SNO started the transition to an era of precision neutrino measurements.

[8] $\phi_{NC} - \phi_{CC} = \phi_{\mu\tau} = 3.87^{+0.50}_{-0.47}$(total), which is 8.2 σ from zero.

Chapter 2

THE SUDBURY NEUTRINO OBSERVATORY

2.1 Overview of the SNO Detector

The SNO detector is a neutrino detector located 2092 m underground in the Vale-INCO Creighton nickel mine near Sudbury, Ontario, Canada. A diagram of the detector is shown in Figure 2.1. The primary neutrino target consists of 1000 tonnes of heavy water (D_2O). That target differentiates SNO from previous water Cherenkov detectors which used H_2O as the neutrino target. Like the Kamiokande [56] and Super-Kamiokande [67] experiments SNO can detect neutrinos via the elastic scattering interaction of a neutrino with an electron. In addition, however, SNO takes advantage of the neutral- and charged-current interactions of a neutrino with a deuteron. These are discussed below. The experiment was conducted in three phases, each of which corresponds to a different method for detecting the neutral-current interaction.

The D_2O target is contained within a 12-m diameter acrylic sphere. Surrounding the acrylic, at a radius of 8.9 m, is an array of approximately 9500 inward-looking photomultiplier tubes (PMTs). The PMT array is used to detect Cherenkov light from the neutrino interactions. Ultra-pure H_2O fills the space between the acrylic sphere and the PMT array as well as the space outside the PMT array. This light water provides physical support for the detector and shielding from background radiation. A detailed description of the entire detector can be found in [68].

For the third phase of the experiment an array of ^{3}He proportional counters was installed within the acrylic sphere. Forty "strings" of proportional counters were anchored to the bottom of the sphere. Thirty-six of them contained ^{3}He and were used to detect the neutral-current interaction, while four contained ^{4}He and were used to measure the background.

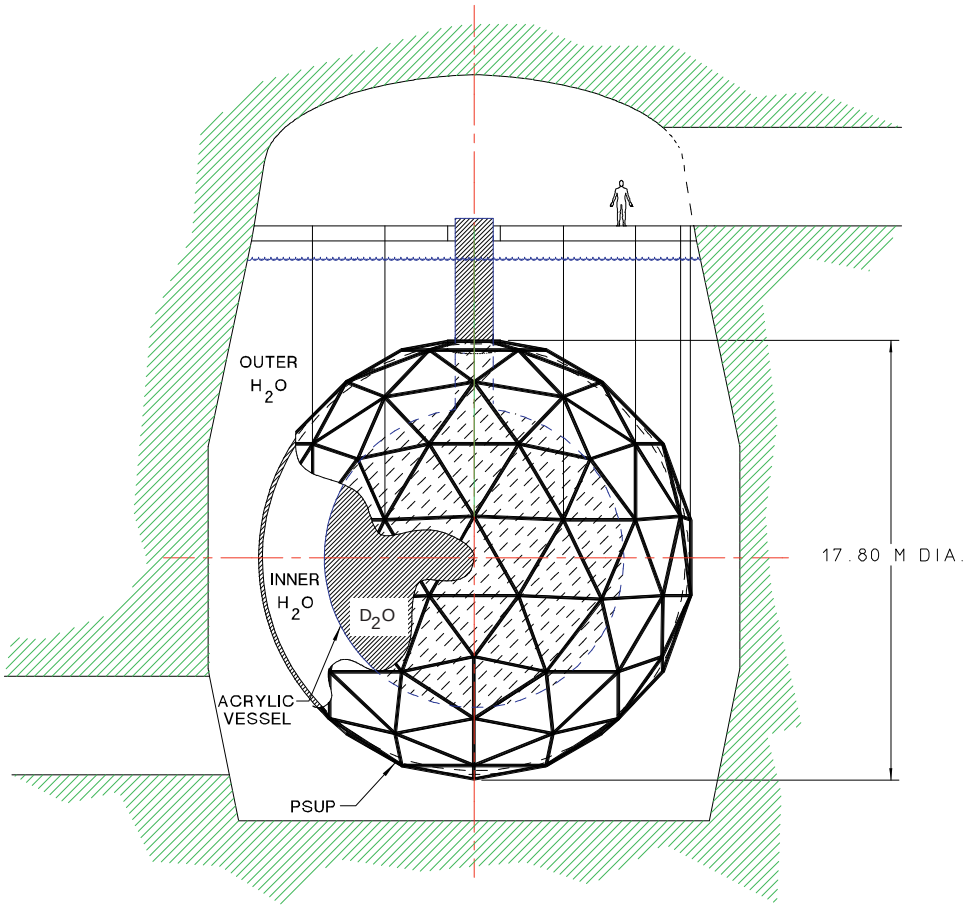

Figure 2.1: The SNO Detector. This figure is from [68].

2.2 Using D_2O to Detect Neutrinos

SNO primarily detects solar neutrinos coming from the beta decay of ^{8}B in the pp chain. The experiment was designed to determine definitively whether or not there is a non-electron-neutrino component to the ^{8}B solar neutrino flux. To accomplish this goal SNO takes advantage of the different flavor sensitivities of the three neutrino interactions: elastic scattering (ES), charged current (CC), and neutral current(NC).

2.2.1 Elastic Scattering

Like previous water Cherenkov detectors SNO is sensitive to the elastic scattering of a neutrino from an electron:

$$\nu_x + e^- \rightarrow \nu_x + e^-. \tag{2.1}$$

This interaction can take place by the exchange of either a W or a Z boson, as is shown in Figures 2.2 and 2.3, respectively. Any flavor of neutrino, $x = e, \mu, \tau$, can scatter by Z exchange, but only electron neutrinos can scatter through W exchange. As a result of the large cross section for ν_e elastic scattering via W exchange the ES interaction is primarily sensitive to electron neutrinos, but has a limited sensitivity to μ and τ neutrinos as well. The two types of ES interactions are completely indistinguishable to SNO, s-channel and t-channel. Both are detected by observing the cone of Cherenkov light emitted by the scattered electron.

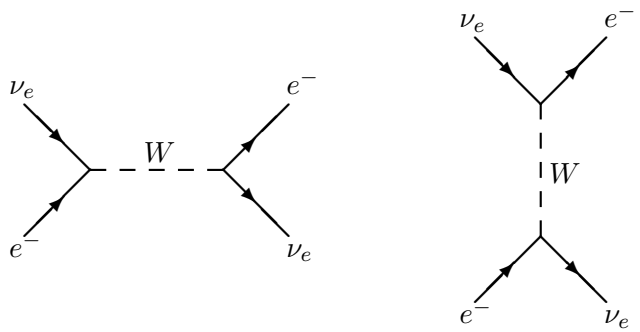

(a) (b)

Figure 2.2: Feynman diagrams of the (a) s-channel and (b) t-channel elastic scattering interactions via the W bosons. Only electron neutrinos can participate in these interactions.

One of the most important features of the ES interaction is its directional sensitivity. The scattered electrons are highly forward peaked in the direction of the incoming neutrino. This can be used to show that the neutrinos detected by SNO are actually coming from the sun. Additionally, this feature can be used to differentiate ES events from other neutrino

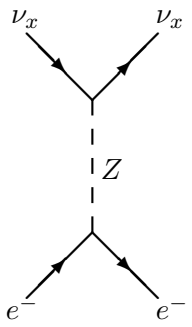

Figure 2.3: Feynman diagram of the elastic scattering interaction via the Z boson. Any flavor of neutrino can participate in this interaction.

interactions detected with the PMTs.

2.2.2 Charged Current

Neutrinos also interact with the deuterons in the heavy water. The CC interaction is mediated by a W boson. The neutrino is absorbed and the neutron is converted to a proton and an electron:

$$\nu_e + {}^2H \rightarrow p + p + e^-. \tag{2.2}$$

The Feynman diagram is shown in Figure 2.4. For ^{8}B neutrinos this reaction is only energetically allowed for electron neutrinos. As a result the CC interaction provides a measurement of the electron neutrino flux.

The electron carries away most of the energy of the interaction, minus the 1.44 MeV threshold and the recoil energies of the protons. Therefore the energy spectrum of the CC interaction is a reliable measure of the neutrino energy spectrum. Since that energy spectrum is altered by neutrino oscillations (or any other exotic effect present) it provides a valuable tool for learning about neutrino oscillations.

The CC interaction has some directional sensitivity which can help differentiate it from the ES and NC interactions. The electrons are emitted preferentially in the backwards

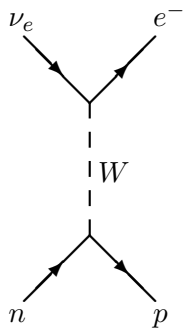

Figure 2.4: Feynman diagram of the charged-current interaction with a neutron. Only electron neutrinos can participate in this interaction.

direction. The directional distribution is approximately described by $1 - 1/3 \cos\theta_\odot$, where $\theta_\odot$ is the angle between the direction of the incoming neutrino and that of the recoil electron.

2.2.3 Neutral Current

If a neutrino interacts with a deuteron via a Z boson then the deuteron can be dissociated into a proton and a neutron:

$$\nu_x + d \rightarrow p + n + \nu_x. \tag{2.3}$$

The Feynman diagram is shown in Figure 2.5. The NC interaction is equally sensitive to all flavors of neutrinos, $x = e, \mu, \tau$, as long as the energy of the neutrino exceeds the binding energy of the deuteron, 2.2 MeV. It provides a measurement of the total neutrino flux above the threshold, weighted by the cross section. If the fluxes measured by the CC and NC interaction are different, then the solar neutrinos definitely have a non-electron-flavor component.

Of the reaction products only the neutron can be detected. SNO has utilized three different methods for detecting the NC neutron, all of which are described in the next section. The neutron thermalizes in the surrounding medium and, in the process, it loses all directional and energy information.

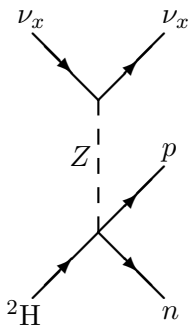

Figure 2.5: Feynman diagram of the neutral-current interaction with deuterium. Any flavor of neutrino can participate in this interaction.

2.3 Detection of the Neutral Current Signal

The three phases of SNO correspond to three independent methods for detecting the NC neutron: capture on a deuteron, capture on ^{35}Cl, and capture on ^{3}He. The different phases involved different backgrounds, systematic uncertainties, and analysis techniques. To a certain extent they can be considered separate, though related, experiments that provide three different measurements of the ^{8}B neutrino flux.

2.3.1 Phase 1: Pure D_2O

The first phase of SNO lasted from November 1999 to May 2001. Neutral-Current neutrons thermalized in the D_2O and were detected by their capture on a deuteron. That capture releases a 6.25 MeV gamma ray which then would Compton scatter an electron in the water. The electron then produces a detectable cone of Cherenkov radiation. In the process of thermalizing in the D_2O the neutron undergoes a random walk, and in some cases it would reach the acrylic sphere. Neutrons that captured in the acrylic or in the surrounding H_2O would be undetectable. The probability of this occurring increases for NC neutrons produced at higher radii, so the detected NC events had a radial dependence that was used to separate the NC signal from the CC and ES signals.

2.3.2 Phase 2: Salt

The second phase of SNO lasted from July 2001 to September 2003. Two tonnes of NaCl were dissolved in the D_2O to enhance the NC signal. Since the neutron-capture cross-section of ^{35}Cl is much higher than that of deuterium (44 barns versus 0.0005 barns) neutrons are more likely to capture close to their point of origin, so fewer were lost to the acrylic or H_2O. The increase in capture efficiency increased the statistical accuracy of the measurement, though it made the radial distribution of neutron captures less useful for separating the neutrino signals. However, instead of a single gamma ray, the capture of a neutron on ^{35}Cl releases a shower of gammas totaling 8.6 MeV as the nucleus de-excites. These result in multiple Cherenkov cones, so the isotropy of the light from such an interaction was significantly different than that seen in the ES or CC interactions.

2.3.3 Phase 3: Neutral Current Detection Array

The third phase of SNO lasted from November 2004 to November 2006. The work presented in this dissertation primarily concerns this phase of the experiment. An array of thirty-six strings of ^3He proportional counters was used to detect the NC neutrons after the salt from the previous phase was removed. Because the cross section for neutron capture on ^3He is higher than that of deuterium by a factor of 10^7, a sparse array of counters still achieved a $\sim$30% neutron capture efficiency. The Neutral-Current Detection (NCD) Array provided a measurement of the NC neutrons that was almost completely independent of the measurement by the PMT array. Whereas, in previous phases, the ES, CC, and NC fluxes were separated statistically and therefore highly correlated, the NCD Array measurement breaks the correlations between the NC flux and the other two fluxes. The details of the operation of the NCD Array will be discussed in Chapter 3.

2.4 Results from Phases 1 and 2

The SNO Collaboration published the first results from the D_2O phase in 2001, including measurements of the CC and ES fluxes [62]. By combining the CC and NC flux measurements from SNO and the ES flux measurement with higher statistics from Super-

Kamiokande the $\nu_{\mu\tau}$ flux was determined to be $\phi_{\mu\tau} = 3.69 \pm 1.13$, in the units that will be used for fluxes throughout this section, 10^6 cm^{-2} s^{-1}. This measurement demonstrated that there is a non-ν_e flux at a 3.3-σ level.

In 2002 the SNO Collaboration published results from the full D_2O phase, with measurements of all three fluxes, and definitely showed that neutrinos change flavor [63]. The non-ν_e component of the ^{8}B solar-neutrino flux was measured by SNO alone at a 5.3-σ level ($\phi_{\mu\tau} = 3.41^{+0.66}_{-0.64}$), and at a 5.5-$\sigma$ level when combined with the Super-Kamiokande ES measurement ($\phi_{\mu\tau} = 3.45^{+0.65}_{-0.62}$). Figure 2.6 shows the measurements of the CC, ES, and NC fluxes by SNO, along with the SSM prediction. The intersection of the three fluxes indicates that some of the solar neutrinos are detected as ν_μ or ν_τ neutrinos. The existence of a non-ν_e component of the ^{8}B solar-neutrino flux proves that neutrino flavor change occurs.

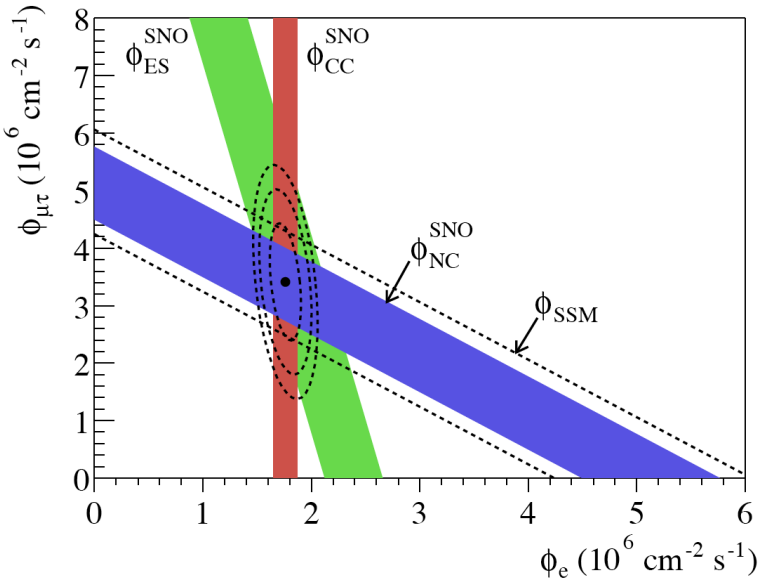

Figure 2.6: The flux of ν_μ+ν_τ versus the flux of ν_e as measured by the CC, NC, and ES fluxes during the D_2O phase. The bands represent the 1-σ errors on each flux, and the dashed lines are the SSM prediction. The intersection between the fluxes shows that approximately 2/3 of the ^{8}B solar-neutrino flux measured by SNO consisted of μ or τ neutrinos.

The total neutrino flux, as measured by the NC reaction, was $5.09^{+0.44}_{-0.43}$(stat.)$^{+0.46}_{-0.43}$(syst.), in good agreement with the 2001 SSM prediction of $5.05^{+1.01}_{-0.81}$. These are represented by

the blue band and the dashed lines in Figure 2.6, respectively. Despite having a limited sensitivity to ν_μ and ν_τ, the ES measurement was a critical factor in determining the total flux because of its sensitivity to the neutrino energy spectrum. The energy spectrum is constrained to the SSM prediction of the ^{8}B spectrum. The fit can also be performed without including the energy spectrum constraint, though the NC flux is only determined at the 24% level ($6.42 \pm 1.57(\text{stat.})^{+0.55}_{-0.58}(\text{syst.})$) in this case.

The salt phase improved upon the results from the D_2O phase [69]. By using neutron capture on chlorine instead of deuterium to detect the NC events, a precision measurement of the fluxes could be made without relying on the event energy, and therefore independent of the predicted ^{8}B spectrum. The isotropy of the light ("β_{14}") resulting from neutron capture on chlorine is different from that of the CC and ES signals; it replaces the energy spectrum in the fit to separate the fluxes. The total flux was determined by the energy-unconstrained fit to be $4.81 \pm 0.21(\text{stat.})^{+0.38}_{-0.34}(\text{syst.})$, while the energy-constrained fit was only slightly more precise, $4.81 \pm 0.19(\text{stat.})^{+0.28}_{-0.27}(\text{syst.})$. $\phi_{\mu\tau}$ was determined to be non-zero at a 7.2-σ level by the unconstrained, model-independent, fit ($3.26 \pm 0.25(\text{stat.})^{+0.40}_{-0.35}(\text{syst.})$).

The raw fluxes measured by SNO are interpreted within the two-flavor neutrino-oscillation framework to determine the values of Δm^2_{21} and θ_{12}. The two-flavor model is an approximation of the three-flavor model that is valid within the precision of the existing measurements under certain circumstances. The mixing-matrix element U_{e2} can be written as $\cos\theta_{13}\sin\theta_{12}$ [70], which is approximately $\sin\theta_{12}$ when θ_{13} is small. The measurement of ϕ_{CC}/ϕ_{NC} is a direct measure of P_{ee}, and therefore, using approximations discussed in Section 1.4.3, $P_{ee} \approx \sin^2\theta_{12} \approx |U_{e2}|^2$.

Within the two-flavor oscillation model the SNO salt results can be combined with other solar-neutrino measurements, including the Homestake, SAGE, Gallex/GNO and Super-Kamiokande experiments, and the KamLAND reactor-neutrino experiment. Figure 2.7a shows the fit with only the solar-neutrino measurements in the $\Delta m^2_{21}/\tan^2\theta_{12}$ parameter space, and Figure 2.7b includes the KamLAND results in the fit. With a high degree of precision the best-fit point is determined to be $\theta_{12} = 33.9^{+2.4}_{-2.2}$ degrees, $\Delta m^2_{21} = 8.0^{+0.6}_{-0.4} \times 10^{-5}$ eV^2. SNO provides a strong constraint on the mixing angle, while KamLAND constrains the mass splitting.

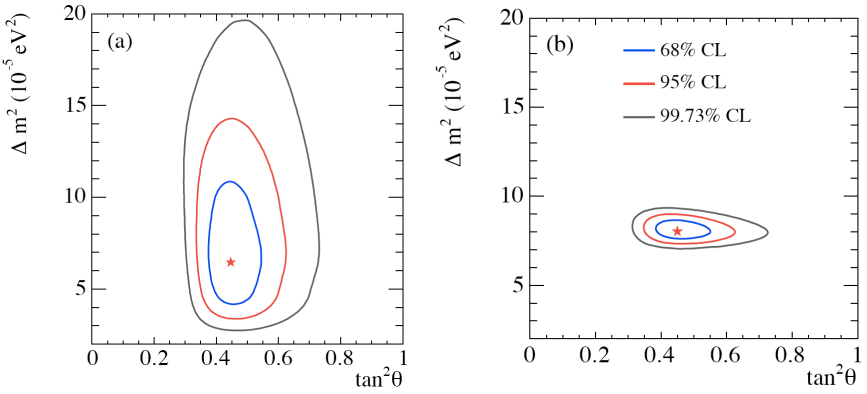

Figure 2.7: The SNO results from the salt phase are combined with the Cl, Ga, and Super-Kamiokande solar-neutrino measurements in (a) to determine the best-fit two-neutrino flavor oscillation parameters, Δm^2_{21} and θ_{12}. (b) includes the reactor-neutrino measurements by KamLAND as well, significantly constraining the best-fit region in Δm^2_{21}. This figure is from [69].

2.5 Monte Carlo Simulation

Having an accurate understanding of an experimental apparatus is an absolute necessity for a successful experiment. For the SNO experiment this goal is achieved in the form of a detailed model of the detector and the physics events involved, and the use of the Monte Carlo method of simulation. These tools, along with the primary data processing functions, are provided by the SNO Monte Carlo and ANalysis (SNOMAN) package, which has been developed by the SNO Collaboration over the lifetime of the experiment.

SNOMAN is written in FORTRAN77 and uses the ZEBRA database manager for both the event data structure and the database of software and detector parameters. SNOMAN is responsible for processing the raw data and applying calibration constants for every channel of the PMT and NCD arrays. It also includes processors to perform data cleaning, as well as the fitting of PMT events to estimate the event vertex location, direction, and energy. A set of C++ classes, known as QSNO, is used in conjunction with SNOMAN to produce ROOT [71] files from the raw data that are used in further analyses. Some components of SNOMAN, including many of the NCD-related elements, are classes in QSNO that are

used by SNOMAN. The data are typically output in a QSNO-based data structure known as a QTree. For Monte Carlo production the information about the particle and interaction simulations is contained in a separate structure known as an MCTree.

The SNO Monte Carlo is a highly detailed simulation of the SNO detector and the physical processes that are involved. Some of the physics simulations are performed by existing packages, such as EGS4 [72], MCNP [73], FLUKA [74], and, more recently, NUANCE [75]. The rest, however, is custom-built, including the detector geometry and data acquisition. The NCD simulation, in particular, will be discussed in greater detail in Chapter 4. Monte Carlo simulations are used to build Probability Distribution Functions (PDFs) of the various observables associated with SNO for the different classes of signal and background events. Furthermore, by comparison with calibration data we can better understand and quantify the systematic effects in the data.

2.6 Calibrations

Along with Monte Carlo the other method of understanding the SNO detector is through calibrations. One can look at the detector response from known sources placed inside the detector to determine, for instance, the neutron detection efficiency, or the PMT angular response. The results from these calibrations are used as inputs to the Monte Carlo to guarantee an accurate model of the detector.

Calibrations have been a major focus of the SNO experiment throughout its lifetime. In each phase approximately one-third of the detector livetime was devoted to calibrations. The accuracy of SNO's results is limited by the systematic errors, so it was reasonable to use a considerable amount of time calibrating the detector and thereby reducing systematic errors, instead of detecting more solar neutrinos.

The various calibrations fall into three categories depending on how they are deployed in the detector. The first category includes encapsulated sources that are deployed using a manipulator system, as shown in Figure 2.8. The source is passed through the neck of the acrylic vessel and into the main volume of D_2O. The position of the source can be controlled in two ways. In the one-dimensional mode it can be dropped vertically along the z axis with a single rope. For three-dimensional control of the source position two ropes control

the source position in the $x - z$ and $y - z$ planes. Typically the source is moved in one plane or the other, using only one rope at a time. The second category of calibrations is dissolved sources. For these calibrations the source is dissolved in the D_2O (usually through the use of the manipulator system) with the goal of forming a uniformly-distributed source. Eventually the introduced activity decays away. The third category of calibrations includes the various electronics calibrations. In this case no sources are deployed. The electronics parameters are measured by injecting signals into either the NCD or PMT systems.

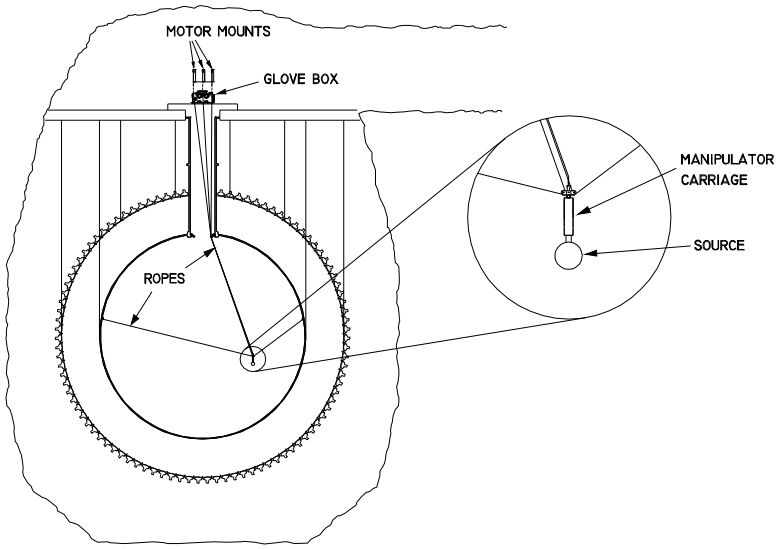

Figure 2.8: The SNO encapsulated-source deployment and manipulator system. This figure is from [68].

In each phase the set of calibrations used depended on the characteristics of the particular phase. For the NCD phase the suite of calibrations included the following:

- **^{24}Na Spike:** At two times during the NCD phase the D_2O was spiked with ^{24}Na. The beta decay of ^{24}Na releases a 2.74 MeV gamma ray that photodisintegrates ^{2}H, releasing neutrons into the water. The goal is to produce a uniformly-distributed neutron source, mimicking the distribution of the neutral-current events. This can be used to determine the neutron capture efficiency for a uniform source. The data are

also used to produce a data set consisting almost entirely of neutron-capture pulses in the NCD array (see Chapter 3 for more details on this process). The ^{24}Na data sets are used to study data-cleaning sacrifices, to train pulse-shape analysis algorithms, and to validate the NCD Monte Carlo.

- **AmBe:** Extensive point-source neutron calibrations were conducted with two ^{241}Am-^{9}Be neutron sources. ^{241}Am decays via the release of an alpha particle. Alphas that hit the ^{9}Be target produce neutrons via the ^{9}Be(α,n)^{12}C reaction. The two-component source is enclosed in acrylic. The neutron-production rate of the "medium rate" source is 23.6 Hz, while the rate of the "high rate" source is 68.7 Hz (the "low rate" source, at approximately 7 Hz, was not used). Neutron detection efficiency and dead times were studied with the AmBe sources. An AmBe source was also used during the deployment and undeployment of the NCD strings to measure each counter's gain and to verify that they were working correctly.

- **^{252}Cf:** During the D_2O and salt phases the ^{252}Cf source was the primary means of determining the neutron-capture efficiency. During the NCD phase it was also used for that purpose. A small amount of ^{252}Cf is encapsulated in an acrylic source that is lowered into the D_2O volume. Neutrons are produced by fission decays. The average multiplicity for a single decay is 3.77 neutrons [69]. This multi-neutron characteristic allows the neutron-capture efficiency measured by the other two neutron sources to be verified with an alternate analysis, the Time Series Analysis, which is independent of the source strength. Furthermore, with a source producing bursts of neutrons, one can also study the deadtimes of the NCD system.

- **^{16}N:** A D-T generator was used to create ^{16}N, which was then carried into a cylindrical stainless-steel decay chamber that was suspended inside the detector. The beta decay of ^{16}N releases a 6.13 MeV gamma 66% of the time and a 7.12 MeV gamma 4.8% of the time. The gamma passes through the stainless steel wall and showers in the water to produce Cherenkov light. The beta is stopped by the stainless steel. A sleeve of scintillator and a 5-cm PMT inside the decay chamber were used to trigger the SNO

detector. In this way gammas from external sources and from beta decays of ^{16}N that had not yet reached the chamber could be vetoed. This source was used as the primary method for determining the energy scale of the detector and for examining the energy systematics. The vertex reconstruction accuracy, detector stability, and data-cleaning sacrifice could also be studied.

- **Rn Spike:** Low-energy backgrounds were examined by dissolving ^{222}Rn in the D_2O. Its decay provided a uniform source of background events and could be used to understand the radial profile of the real background events.

- **Th:** This source consisted of Th encased in multiple layers of acrylic. It was used to study the low-energy backgrounds from radioactive contaminants in the detector components. It was also deployed in the light-water region of the detector to study the detector response to background events originating outside of the D_2O.

- **^{8}Li:** The energy response at the high end of the neutrino energy spectrum is studied with a ^{8}Li beta-decay source. The endpoint for the decay is 13.5 MeV. This source is also used to study the data-cleaning sacrifice at high energies.

- **Laserball:** A gaseous nitrogen laser was used to determine the optical properties of the detector. The laser light, at one of a number of different frequencies, was passed into the detector via a fiber optic cable that terminated in an acrylic diffuser ball. Light pulses 8-ns wide were used to make a number of measurements of the PMT system. High-occupancy runs were used to determine timing and gain constants (see Appendix C for details on performing this calibration during the NCD phase). Lower-occupancy runs were used to make other measurements, such as of the angular and frequency responses of the PMTs, and to measure the NCD positions and tilts.

- **Electronics:** Electronics calibrations for both the PMT and NCD systems were performed by injecting pulses into the electronics systems and measuring various properties of the output signals. For the NCD system the properties measured included

the thresholds for both the shaper and multiplexer systems, the linearity and gains of the shapers, and the parameters that defined the logarithmic amplification in the multiplexer system.[1] For the PMT system the electronics calibrations included the number of ADC counts corresponding to zero charge, and the timing of the signals.

[1]Chapter 3 includes a brief description of the NCD data acquisition, and a more detailed description is found in [76]

Chapter 3

THE NCD PHASE

The goal of the third and final phase of the SNO experiment was to complement the previous two phases and improve the measurement of the CC and NC fluxes. Unlike the previous two phases, in the NCD phase the NC flux was measured by two independent sets of detectors. Previously the ES, CC, and NC fluxes were all measured by the PMTs and the events had to be separated statistically through an extended Maximum Likelihood fit. This type of analysis led to measured fluxes that were naturally correlated to various extents. The use of the NCD array to detect only the NC flux breaks the statistical correlations between the ES and CC fluxes and the NC flux. Most of the systematic effects that apply to the NCDs were also different from those that applied to the PMTs.

3.1 Motivation for the NCD Phase

The ability to make an independent measurement of the NC flux was crucial to improving the accuracy of SNO's solar-neutrino measurement. The correlations from the salt and NCD phases are compared in Table 3.1. By reducing two of the correlations significantly the expected uncertainties on the NC and CC fluxes, as well as the expected uncertainty on the day-night asymmetry, are also reduced. The measured and expected uncertainties are shown in Table 3.2. As of the initial publication of the NCD-phase data [65], the uncertainties are comparable to the salt-phase results. With future analysis developments, including the analysis described in Chapters 6 and 7, leading to further reductions of the uncertainties SNO has the opportunity to make the best possible measurement of the CC/NC flux ratio and the total ^{8}B solar neutrino flux.

The uncertainties on the measurement of the CC/NC flux ratio determine how well we can measure the oscillation parameters. That ratio is most sensitive to the value of θ_{12}, and no other experiment currently planned will have the same sensitivity. Therefore the best

Table 3.1: Correlations between the measured fluxes for the salt phase and the NCD phase. The salt-phase numbers are from [69]. The NCD-phase numbers are from [77].

Correlation	Salt Phase	NCD Phase
NC:CC	-0.521	-0.192
CC:ES	-0.156	0.238
ES:NC	-0.064	0.017

Table 3.2: Uncertainties on the NC and CC fluxes, and the day-night asymmetry. The actual NCD-phase numbers are from [65], and the others are from [78]. SNO is undertaking further analysis of the NCD-phase data to lower the uncertainties from that data.

Uncertainty	D_2O	Salt	NCD (expected)	NCD
NC (σ_{NC}/NC)	12%	8%	$\sim 6\%$	8.7
CC (σ_{CC}/CC)	6%	6%	$\sim 4\%$	5.5
Day-Night (σ_A)	5%	7%	$\sim 5\%$	N/A

measurement that SNO can make of CC/NC ratio will produce the best value for θ_{12} in the foreseeable future. Figure 3.1 shows the allowed region of Δm^2_{21}-θ_{12} space including the first NCD-phase results from SNO and the best-available results from other solar-neutrino experiments and KamLAND. The solar-neutrino experiments are more sensitive to θ_{12} than Δm^2_{21}, while KamLAND narrows the allowed region along the Δm^2_{21} axis significantly.

3.2 The NCD Array

The NCD Array, which was deployed between December 2003 and April 2004, consists of thirty-six strings of ^{3}He proportional counters and four strings of ^{4}He proportional counters. The ^{4}He strings are not sensitive to neutrons and are used to characterize the non-neutron backgrounds in the array.

The strings are arranged on a grid with 1-meter spacing, as shown in Figure 3.2. Each string is labeled with an alphanumeric name. The letter corresponds to the ring, with the N strings being the innermost four, and the I strings being the outermost eight. The number roughly corresponds to the location around each ring. They are also numbered, 0-39, though

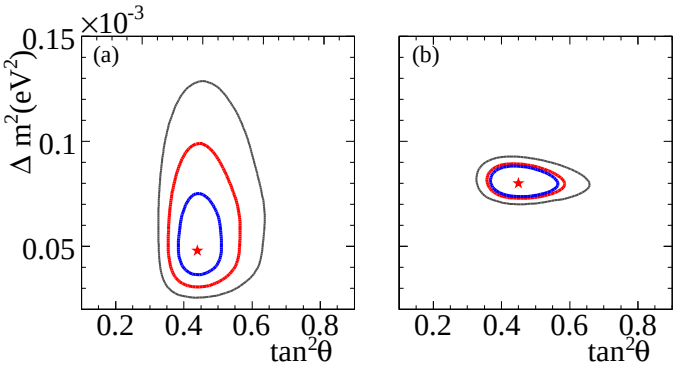

Figure 3.1: The global fit of (a) solar-neutrino experiments and (b) solar-neutrino experiments plus KamLAND from SNO's first NCD-phase results [65]. KamLAND is extremely sensitive to Δm^2_{21} relative to the combined solar-neutrino experiments, while the latter are more sensitive to θ_{12}.

the numbers are not shown in the figure.

The sparse array is sufficient because the thermal neutron-capture cross-section of ^{3}He is 5330 barns, seven orders of magnitude larger than that of deuterium. For neutrons created uniformly throughout the D_2O volume the NCD Array capture efficiency is approximately 21%, and the D_2O capture efficiency is approximately 17%. Reducing light loss due to shadowing was the main motivation for implementing a sparse grid of counters. The loss is approximately 9% [79].

Each string is 9-11 meters in length and is made up of three or four cylindrical counters made of nickel, 5 cm in diameter. The total length of the array is 398 meters. A diagram of an NCD string is shown in Figure 3.3. The gas in the counters is a mixture, by volume, of 85% ^{3}He or ^{4}He and 15% CF_4. The total pressure is 1920 Torr (2.5 atmospheres). The individual counters in a string have independent gas volumes and the walls are welded together at the points where they join.

Cleanliness was an important concern when constructing the NCD counters. Commercially-available counters would not have had sufficiently low levels of radioactive contaminants, particularly ^{238}U and ^{232}Th. Instead the counter bodies were custom-built at the University of Washington and Los Alamos National Laboratory. They were made with

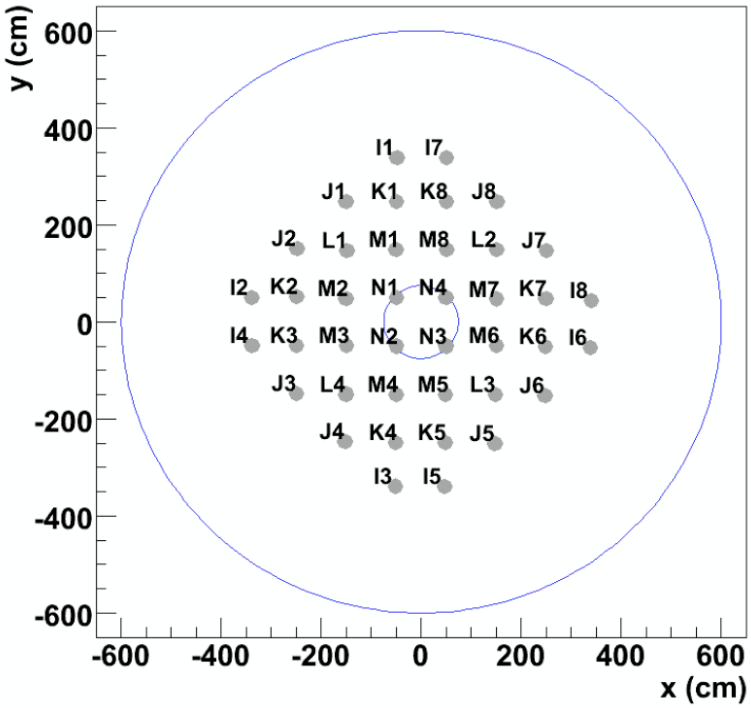

Figure 3.2: The layout of the NCD array showing all forty strings in the $x-y$ plane of the detector. The outer circle is the radius of the acrylic vessel at the equator. Strings I2, I3, I6, and I7 are filled with ^{4}He. The direction defined as "north" is along the $+y$ axis. This figure is from [80]

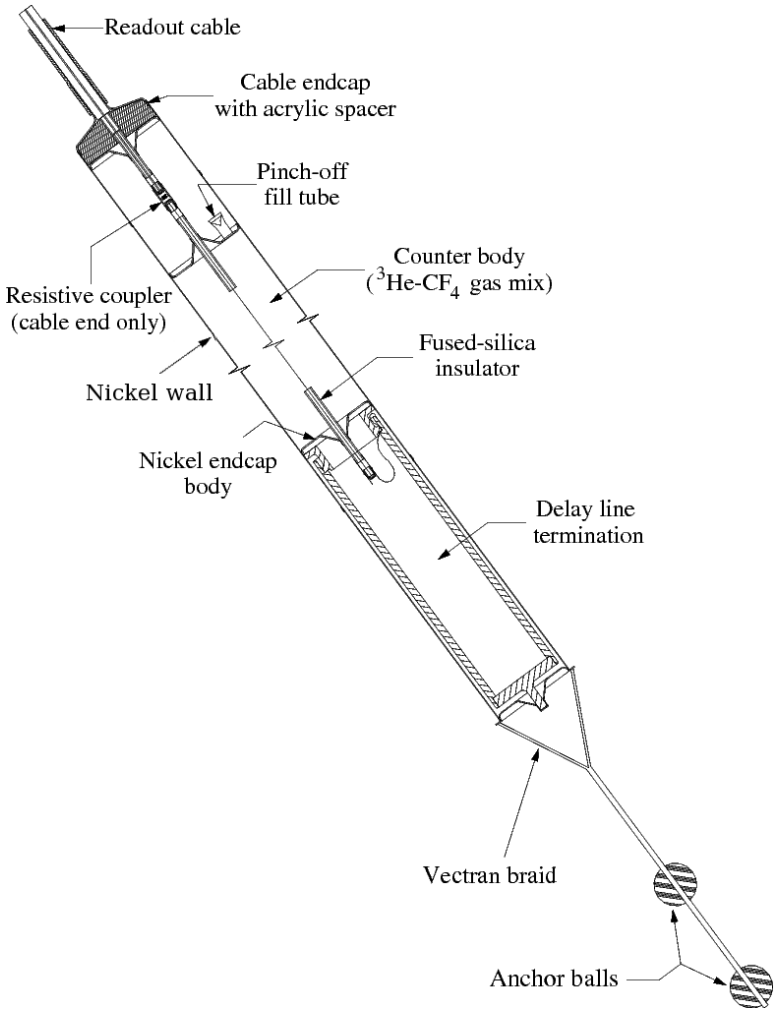

Figure 3.3: Diagram of an NCD string, including the readout cable and upper end-cap, the counter bodies (not to scale), and the delay-line at the bottom of the string. There are also counter end-caps between the individual counts that are not shown in the diagram. This figure is from [68].

a chemical-vapor-deposition (CVD) process that separates the nickel from all but trace amounts of the impurities [78]. The anode wire was made of low-background copper to further reduce radioactive contamination in the counters.

The proportional counters that make up the NCD Array operate by measuring the current pulse created on the anode wire by ionization of the counter gas. A charged particle passing though the gas with sufficient energy will ionize the gas. The anode wire is kept at high voltage (1950 V) relative to the cathode wall, and the primary ionization electrons drift toward the wire. Except near the counter end-caps the electric field within the counters is cylindrical, with a magnitude that is proportional to $1/r$, where r is the radius from the center of the counter.

The NCDs detect neutrons via capture on ^{3}He: ^{3}He(n,p)^{3}H. This interaction has a Q-value of 764 keV. The proton and triton are released back to back with kinetic energies of 573 keV and 191 keV, respectively, every time due to momentum and energy conservation. Each particle has a characteristic energy deposition profile that gives the basic shape of a neutron-capture NCD pulse. Figure 3.4 shows the characteristic energy deposition profile as a function of distance traveled by the proton and triton, and for alphas starting with different initial energies. The triton energy is low enough that the Bragg peak is not present, while the lower-energy alpha starts near the top of its Bragg peak. The double-peaked shape of the energy deposition for neutron-capture pulses will help discriminate them from alpha pulses.

The exact shape of the current pulse that forms on the anode wire depends on the radius at which each primary ionization occurred. Therefore the shape of the pulse also depends strongly on where in the counter the ionization track occurred and in what direction the proton and triton or alpha were traveling. This leads to a wide variety of possible pulse shapes. Some examples of simulated neutron-capture pulses are shown in Figure 3.5. A track that is oriented radially and perpendicular to the anode will create a pulse that preserves the shape of the energy deposition. A track that is parallel to the anode, however, will create a pulse that loses all of that information because the primary ionization electrons arrive at the wire at the same time.

The pulse shapes can be further affected by either or both of the proton and triton

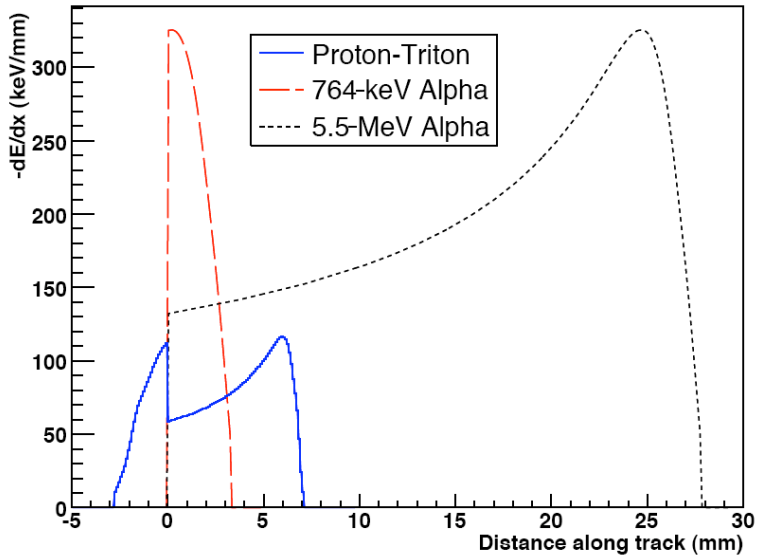

Figure 3.4: Energy deposition as a function of distance traveled for a back-to-back proton-triton pair (blue), a 764-keV alpha (red, long dashed), and a 5.5-MeV alpha (black, short dashed). This figure is from [81].

running into the wall of the NCD. In the case where a particle hits the wall the total energy deposited in the gas will be less than 764 keV, and these situations result in the characteristic shape of the NCD energy spectrum. The energy of a pulse is proportional to the pulse integral. Figure 3.6 is the measured-energy spectrum from a neutron calibration of the NCD Array. One can see the neutron peak at the full energy of 764 keV. There is also a low shoulder that slopes off to 573 keV due to the proton losing all of its energy in the gas and the triton hitting the wall. The sloping shelf that extends to 191 keV is a result of the proton hitting the wall while the triton deposits all of its energy in the gas.

The primary ionization electrons drift towards the anode in the cylindrical electric field. Within a few wire-radii of the anode the field is high enough that the drifting electrons produce secondary ionizations. This leads to an avalanche of ionization that multiplies the original signal by a factor that depends strongly on the anode voltage, called the gas gain. For the NCD Array at 1950 V the gas gain is approximately 220 [82]. Without this multiplicative factor the signal-to-noise ratio would be small.

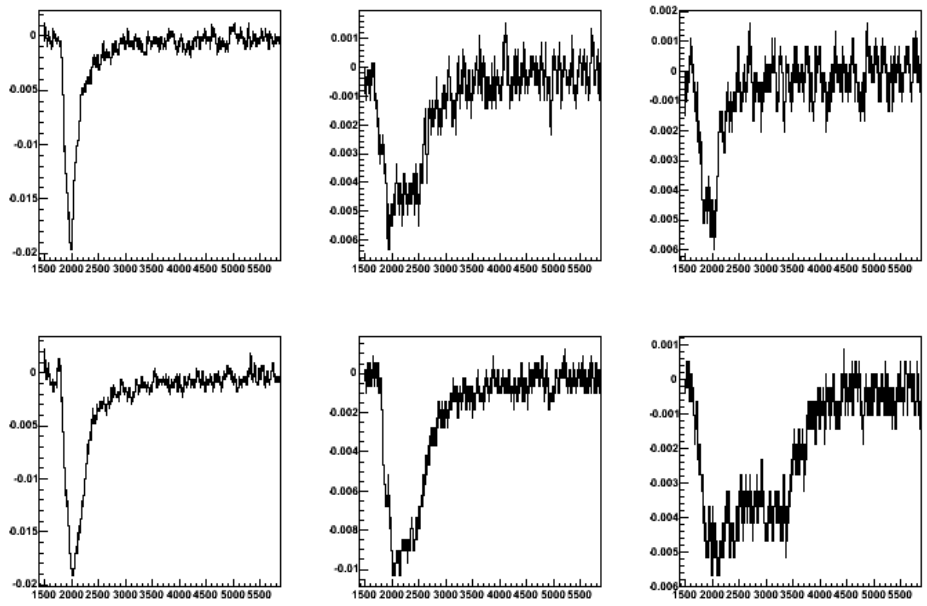

Figure 3.5: A small sample of neutron-capture pulses created with the NCD Monte Carlo discussed in this dissertation. The narrow pulses on the left have ionization tracks approximately parallel to the anode wire. The widest pulse, in the bottom row, right side, has a track that is perpendicular to the anode and approximately radial. The proton traveled towards the anode, producing the left peak, and the triton traveled away from the anode, producing the smaller peak on the right.

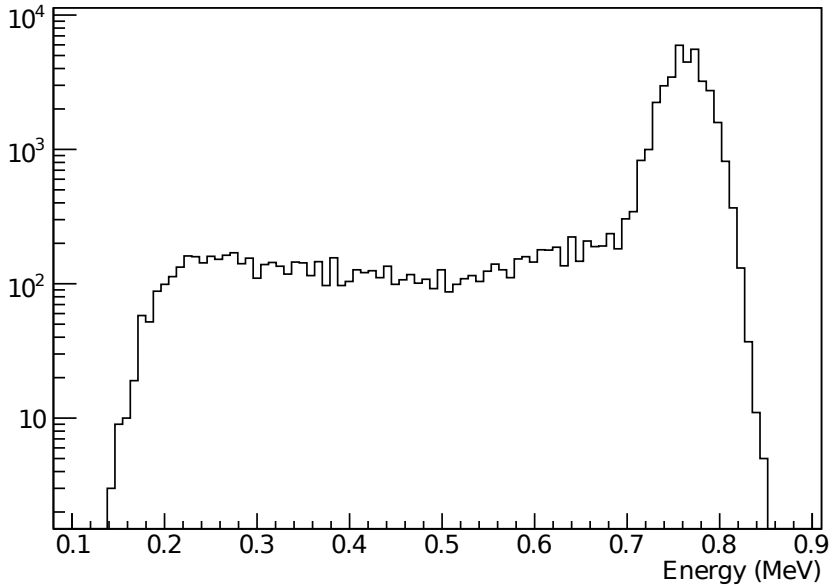

Figure 3.6: Simulated energy spectrum of NCD events not including the space-charge effects that mask the effects of the geometry.

One can think of the process of creating a current pulse on the anode in terms of the image charges that are created as a result of the ions and electrons in the gas. As the ionization avalanche builds, each electron-ion pair forms a positive and a negative image charge in the anode. The magnitude of the charge depends on the cylindrical radius of corresponding real charge. The electrons drift to the wire and cancel out their image charges very quickly ($\sim$10 ps). The ions, however, drift outwards more slowly. The current pulse that is measured and recorded is mainly a result of the image charges from the ions drifting slowly toward the cathode. The time at which each avalanche (from the individual primary ionization electrons) is formed determines the shape of the current pulse, while the slow ion drift gives every pulse a long tail that is characteristic of pulses formed in this manner.

The ions from one avalanche can affect the size of later ionization avalanches near the same location on the anode wire. The ions still near the anode affect the local electric field, and can therefore lessen the size of the latter avalanches. This charge-saturation effect, known as the "space-charge" effect, can modify the pulse shapes. This is also an effect that is dependent on the geometry. It is most significant when the ionization track is perpendicular to the anode wire, so that the ionization avalanches overlap more frequently, and least significant when the track is parallel to the anode and there is little overlap of the avalanches.

Current pulses on the anode wire travel in both directions, up and down the NCD string. The delay-line at the bottom of each string adds approximately 90 ns to the travel time of the portion of the pulse that travels down the string. The termination at the end of the delay line is an open circuit, so the pulse is reflected back upwards. The direct and reflected portions of the pulse are separated by approximately 90-350 ns, depending on the location of the origin of the pulse along the length of the NCD string.

At the top of each NCD string is a coaxial cable that leads to a current preamplifier. The preamplifier linearly transforms the current pulse into a voltage pulse with a gain of 27.5 mV/μA.

The voltage pulse is recorded with the NCD data acquisition (DAQ) system. The DAQ is divided into two paths, Shaper and Multiplexer (MUX). The Shaper system uses a shaping/peak-detection network to integrate the pulse and measure the energy. It is trig-

gered by the pulse integral crossing a threshold and can handle event rates on the order of kHz (such as one might expect for a galactic supernova). The MUX system digitizes and records the entire 15 μs pulse. It consists of four independent sets of electronics, or MUX boxes (numbered 0-3), each of which can accept signals from up to twelve NCD strings. Each channel is triggered by the pulse amplitude crossing a threshold. The pulse is logarithmically amplified (by the "logamp") to increase the range of pulse sizes that can be recorded. It is then digitized with a 1-GHz sampling rate (1-ns bin widths) by a digital oscilloscope with an 8-bit digitizer. The maximum event rate for MUX events is approximately 1.8 Hz. If the oscilloscope is busy but the MUX system triggers, a "partial MUX" event is recorded without the digitized pulse. Though slow, the MUX system is sufficient to handle typical solar-neutrino signal and background event rates. More detail on the entire NCD DAQ system can be found in [76].

3.3 NCD Backgrounds

In addition to the neutron-capture signal there are various backgrounds that must be understood. These can be separated into two classes: non-physics backgrounds, including any pulses not created by ions traveling in the gas, and physics backgrounds, primarily consisting of alphas from radioactive decays traveling through the counter gas.

The non-physics backgrounds are generally easily distinguished from neutron-capture pulses. Two sets of data-cleaning cuts were developed to identify and flag them in the data [83]. For instance, electrical discharges appear as extremely sharp spikes lacking the long tail that is characteristic of ionization pulses. Also, oscillatory noise pickup creates pulses that are radically different in shape. The cuts removing these pulses were required to sacrifice no more than 1% of the neutron-capture pulses.

The primary physics background is alpha pulses from the decays of radioactive contaminants in and on the nickel walls and copper anode wire. Extreme care was taken during construction of the counters, but some contamination was inevitable [78]. Because of the efforts to use clean materials and construction methods the alpha background is low enough that we can make a measurement of the neutron-capture signal.

The majority of the radioactive contaminants are from the ^{238}U and ^{232}Th decay chains,

as well as surface ^{210}Po (discussed below). The ^{238}U and ^{232}Th contamination is in the bulk of the nickel walls. There is also contamination in the wire, but the total volume of copper is insignificant relative to that of the nickel, so almost no ^{238}U and ^{232}Th-chain alphas are seen [84].

Due to an unfortunate exposure to high-radon air while the counter bodies were in storage during NCD construction, progeny of ^{222}Rn, including ^{210}Pb and ^{210}Po, plated onto the surfaces of the counters. Electropolishing was used to remove as much as possible of the surface contamination, but some still remained. There is a clear peak of alpha events at 5.3 MeV from the decay of ^{210}Po which has a tail that extends down into the neutron energy region.

Figure 3.7 shows the the energy spectrum of NCD events. The black data points are blind data, and the line histograms are Monte Carlo alphas and calibration neutrons. Both plots are fits of the neutron and alpha energy distributions to the data from [85]. In Figure 3.7a the energies range from 1.2 MeV to 5.8 MeV, above the neutron-energy region. The red histogram is from ^{210}Po alphas on the nickel surface. The large peak is from alphas starting out with an energy of 5.3 MeV. The small bump at 2.5 MeV is due to ^{210}Po alphas that deposit all of their energy in the gas but are have ionization tracks that are nearly perpendicular to the anode wire. The measured energy is therefore significantly reduced by the space-charge effect. The blue dotted histogram is from a combination of uranium and thorium alphas in the nickel bulk. Figure 3.7b shows the neutron energy region, from 0.4 MeV to 1.2 MeV. The cyan histogram is the combined bulk and ^{210}Po alpha spectrum, and the magenta dashed histogram is the neutron energy spectrum taken from ^{24}Na calibrations. Clearly the alpha background underneath the neutron events is significant, and it is desirable to use the additional information in the neutron and alpha pulse shapes to help separate signal from background.

The energy-deposition profile of an alpha is easily distinguished from that of a back-to-back proton and triton. However, due to the various geometric effects discussed in the previous section, some current pulses from alphas and from neutron captures can be similar or even indistinguishable. These factors are taken into account by the analysis techniques that attempt to determine the number of neutrons detected. Because of their similarity to

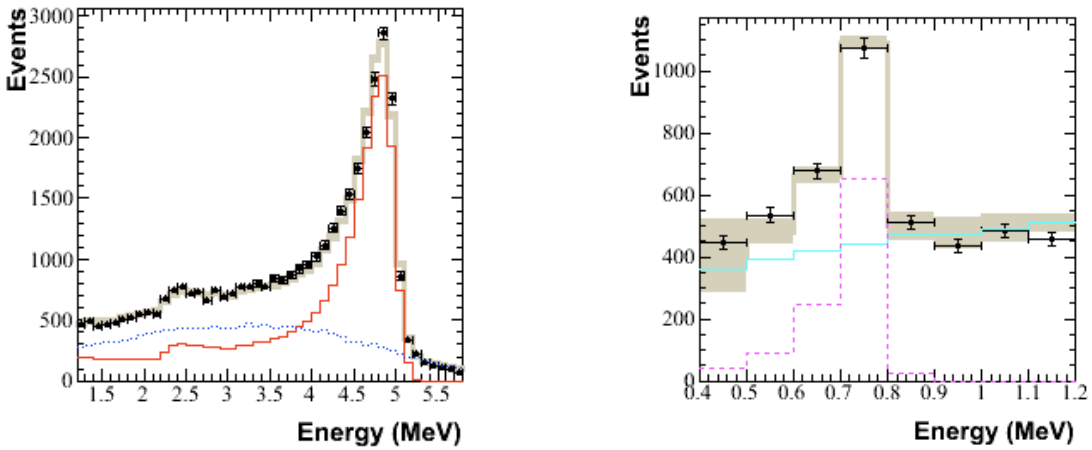

(a) (b)

Figure 3.7: (a) High-energy and (b) low-energy fit from [85], with data (black points, statistical errors), ^{24}Na data neutron template (magenta), Monte Carlo total alpha background template (cyan), and the total alpha + neutron template (grey curve, includes statistical and systematic errors). The χ^2/ndf for (b) is $3.9/7 = 0.56$.

neutron-capture pulses the challenge of separating neutron-capture and alpha pulses was assigned to these higher-level analyses.

In addition to alpha backgrounds there are a number of sources of neutron backgrounds. For instance, radioactive decays that release a gamma ray with more than the 2.2-MeV binding energy of deuterium can photodisintegrate a deuteron releasing a neutron into the heavy water. ^{208}Tl in the ^{232}Th chain and ^{214}Bi in the ^{238}U chain can emit gammas above 2.2 MeV. The neutron backgrounds for the NCD phase include:

- The radioactive hot-spots on NCD strings K2 and K5,
- "external" neutrons produced by photodisintegration by radioactivity originating in the H_2O, and by (α, n) reactions in the AV,
- Bulk radioactivity in the NCD bodies and NCD cables,
- Radioactive nuclei in the D_2O,

- and photodisintegration produced by the products of cosmic-ray interactions in the atmosphere (known as the "atmospheric" background).

Neutrons produced as a consequence of these decays are almost indistinguishable from NC signal neutrons, and therefore SNO relies on careful independent measurements to understand the radioactive backgrounds. The measurements include regular assays of the water, as well as *in situ* measurements using the PMT system [86].

3.4 Analysis Techniques

The addition of the NCD array to SNO provides two simultaneous measurements of the NC signal and certain backgrounds, but it also requires a more complicated analysis strategy than was used in the previous two phases. In an ideal world the NCD array would measure the NC flux and neutron backgrounds completely independent of the PMT array. The method of neutron detection used with the NCDs is different from that used by the PMTs, so the observables and the systematic errors of the measurement are different. The additional information would break the correlations between the NC flux and the CC and ES fluxes.

Unfortunately, since the world is not ideal, the NCD and PMT measurements are not entirely independent. The PMT array is much more sensitive to the radial dependence of events than the NCD array. Therefore the external neutron background is constrained by the PMT measurement. Furthermore some of the systematic effects associated with the calibration of the detector are shared between the NCD and PMT arrays because the neutron calibration sources are observed by both systems.

The separation of the different fluxes, for the combination of the NCD and PMT data sets, is performed with an extended Maximum Likelihood fit. Such fits were used in the previous two phases, as well, with observables specific to the particular requirements of the phase. For the first flux paper of the NCD phase, the PMT observables include vertex radius, reconstructed energy, and angle relative to the sun. The NCD contribution is the energy spectrum. A variety of systematic uncertainties that are floated in the fit. The results of the fit are the number of background neutrons, and alphas from the NCD system, the background-neutron PMT events, and the NC, CC, and ES neutrino fluxes.

The NCD and PMT systems detect neutrons in completely different ways. As a result the data from the two systems are also very different. Whereas all of the PMTs are available to view every event inside the D_2O (with the exception of the shadowing discussed earlier), NCD events are limited to the counter in which the neutron captures. The NCD data are comprised of several types of observables that can be used in an analysis to determine the number of neutrons detected. The data include two types of events: Shaper events, which record the energy of each pulse, and MUX/Scope events, which contain the actual digitized pulse. The goal of any NCD analysis is to determine how many of the pulses were from neutron captures.

The most basic analysis strategy uses the pulse energy recorded by the Shaper events. As was discussed above, the neutron events have a characteristic energy spectrum that can be easily distinguished from the alpha spectrum if PDFs of both are available either from Monte Carlo or calibrations. This is the analysis method that was chosen for the first flux measurement of the NCD phase [65]. The neutron PDF was created from a ^{24}Na calibration, and the alpha PDF was created with a Monte Carlo simulation. The energy spectrum from the NCDs then becomes another input into a joint extended Maximum Likelihood fit with the PMT data.

As an alternative to the energy-only NCD analysis, one can use the digitized pulses to help separate neutron-capture and background events. The pulse shapes contain far more information about the ionization event than the energy alone. In principle this should allow for a better separation of neutron-capture and alpha events. Several so-called Pulse-Shape Analysis (PSA) methods have been developed, though as of this writing they have not been used in a published analysis of the NCD data. Each PSA method has a parameter space in which, hopefully, neutron and alpha events are easily separable. A cut can be used to increase the signal-to-background ratio before the energy spectrum is used in a fit, or the PSA parameter space itself can be used in the extended Maximum Likelihood fit. Alternatively, if the PSA method is able to completely remove the alpha background without removing too many signal events, then the remaining events and the cut efficiency would easily provide the total number of neutrons detected.

The choice of which type of analysis to perform on the NCD data has to be based on how

well the data is understood. If the energy spectrum is well understood for both neutrons and alphas, but the pulse shapes are not, then the energy-only analysis should be chosen. This particular strategy was chosen for the first NCD flux analysis [65]. The NCD Monte Carlo, which is one of the primary focuses of this dissertation, was responsible for producing the alpha energy spectrum and associated systematic variations. The goal of the primary analysis presented here, detailed in Chapter 6, is to use the pulse shapes themselves to improve the separation between neutron-capture and alpha events, and thereby improve the NC flux measurement.

Chapter 4

THE NCD MONTE CARLO

The NCD Monte Carlo is now an integral part of the overall SNO Monte Carlo in SNOMAN.[1] A cartoon flowchart of the SNO Monte Carlo is shown in Figure 4.1. If the SNO Monte Carlo determines that a proton, triton, or alpha[2] is going to propagate in one of the gas volumes of an NCD (both live and dead volumes), then the NCD Monte Carlo takes over and simulates an ionization track. The specific portions of the simulation involved at this point are described in Sections 4.1.1, 4.1.2, and 4.1.3.

After the SNO Monte Carlo finishes propagating all particles and simulating interactions, the data-acquisition (DAQ) simulation begins. For the NCD system, this starts with the calculation of the gas gain and the formation of the current pulse on the anode (Sections 4.1.4 and 4.1.5), and continues with the electronics and NCD DAQ systems (Section 4.2).

4.1 Physics

The 'physics' portion of the NCD Monte Carlo consists of simulating the ionization track inside the counter, the propagation of the primary ionization electrons to the anode, the avalanche of secondary ionization near the anode, and the slow drift of the ions from the secondary ionizations to the cathode. When the standard particle propagation simulation in SNOMAN determines that a proton, triton, or alpha enters or is created in the NCD gas, the separate NCD MC code takes over and creates an ionization track that consists of many ($\sim 10^4$) segments. The primary ionization electrons formed in each segment drift towards the anode. In the high-electric-field region within a few wire radii of the anode they create avalanches of secondary ionization. The electrons are quickly captured on the anode, while the ions slowly drift outwards. The ions actually determine the current pulse on the anode.

[1] Along with the work done by the author of this thesis, much of the development of the NCD Monte Carlo was done by H. S. Wan Chan Tseung and is described in detail in [87].

[2] See Section 4.3.2 for information on the NCD e^- simulation

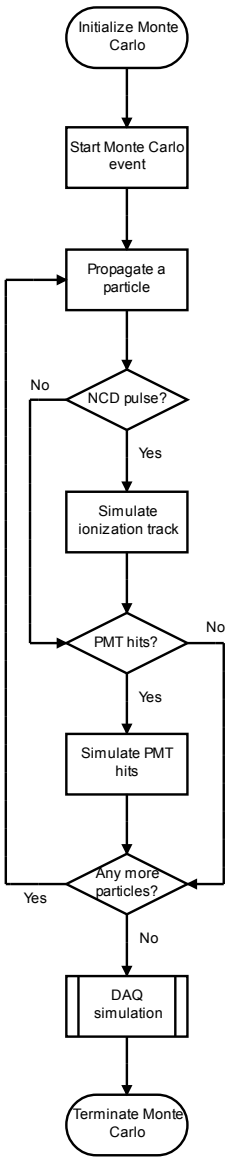

Figure 4.1: Flowchart representing the basic operation of the SNO Monte Carlo. The NCD Monte Carlo will be discussed in detail in this chapter. In particular, the ionization track simulation is described in Section 4.1, and the SNO DAQ simulation includes later parts of Section 4.1 and all of Section 4.2.

As they drift slowly away they result in a long tail at the end of the pulse. Figure 4.2 shows the progression in the pulse shape as each stage is simulated. The energy deposition occurs as a function of distance along the ionization track. It is plotted as a function of time by linearly converting that distance to time such that it has the same width as the 'electron drift' pulse.

While the ions are relatively close to the anode they can produce an observable reduction in the local electric field that reduces the size of later ionization avalanches. This process is known as the "space-charge" effect.

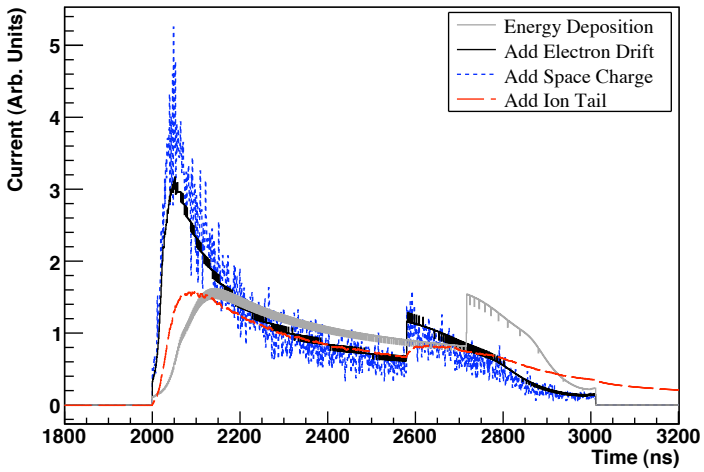

Figure 4.2: A simulated neutron pulse ($r = 1$ cm, $\theta = 90°$, $\phi = 0°$) at different stages of the physics simulation. The peak on the left is due to the proton, and the peak on the right due to the triton. The energy deposition occurs as a function of distance along the ionization track; the units on the abscissa are converted to time linearly to include the pulse in this figure. The "noise" on the energy-deposition and electron-drift pulses is a result of track elements being binned in time. Simulated gain fluctuations are added at the same time as the space-charge effect, though the ion tail smoothes out most of the high-frequency variation. The pulse after the ion tail is added is identical to the pulse before NCD propagation in Figure 4.5.

4.1.1 Ionization Track

Before reaching the gas, some alphas travel in the nickel of the counter wall or the copper of the anode. Such alphas will lose energy and scatter before exiting the material. The energy loss in the metals comes from SRIM 2003 [88]. The alpha track simulation in nickel and copper includes multiple scattering, according to the algorithms described in [89], and the energy straggling was studied in collaboration with H. Bichsel [84].

Each ion in the gas has an initial energy, position, and direction. The initial energy of an alpha depends on the energy with which it started and how much energy, if any, was lost in the nickel or copper. For neutron-capture tracks, the proton starts with 573 keV, and the triton starts with 191 keV. Because of the cylindrical geometry of the proportional counters the initial position of a track includes the z position along the length of the counter, and the cylindrical radius, r. For alpha particles the radius is always the inner radius of the nickel wall or the radius of the anode wire (2.5421 cm and 25 μm, respectively). Two angles are necessary to describe the orientation of the track. θ is the polar angle, running from 0 (upwards) to π (downwards). ϕ is the azimuthal angle. It is between $-\pi$ and $+\pi$ for neutrons, and between $-\frac{\pi}{2}$ and $+\frac{\pi}{2}$ for alphas, with zero being radial towards the anode. Since the proton and triton are always released back-to-back, the angle ascribed to a neutron track is defined as the direction of the proton, with $\theta_{\text{triton}} = \pi - \theta_{\text{proton}}$, and $\phi_{\text{triton}} = \pi - \phi_{\text{proton}}$. θ, ϕ, and r are defined graphically in Figure 4.3.

Ionization tracks in the gas are simulated by breaking the track into small segments. The segment size was selected to be 1 μm. Smaller track segments would slow down the simulation unnecessarily, and larger segments would be too large for the time and amplitude resolution of the pulses produced. The ion loses energy as it travels, and it travels through the gas until its energy drops too low, or it runs into the anode or the wall.

The ionization tracks in the counter gas can be simulated in two ways: straight or bendy tracks. The straight-track simulation propagates the ion along a straight line. There is an option to add a small amount of smearing to the location of each track segment to account for lateral straggling in an average way.

The bendy-track simulation takes into account the multiple scattering as the ion travels

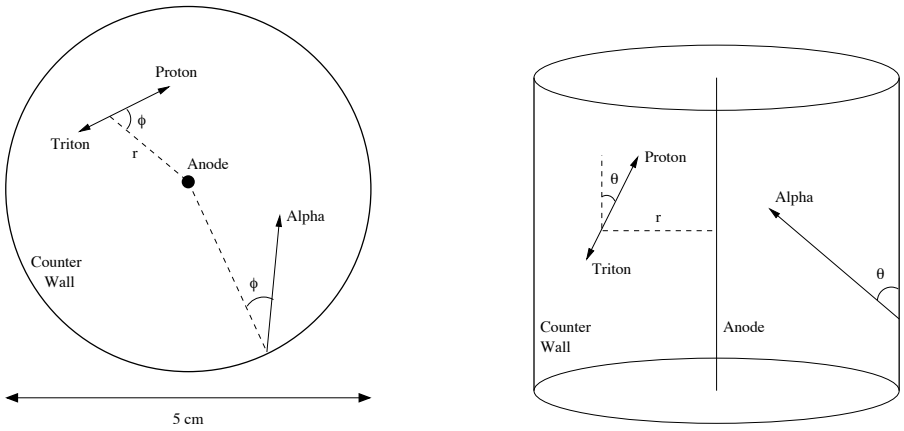

Figure 4.3: (a) Horizontal and (b) vertical sections of an NCD counter showing the geometric parameters, θ, ϕ, and r. (a) shows the $x-y$ plane, and (b) shows the $z-r$ plane. A neutron-capture proton and triton, a wall alpha, and a wire alpha are shown. For the neutron-capture tracks the proton is used to define the track direction.

through the gas. It is based on the algorithms used in the TRIM simulation package [89]. The average of many bendy tracks is the straight track, but any given bendy track can differ significantly from the straight-track approximation. Overall we have seen that this has a relatively small impact on the pulse shapes.

4.1.2 Energy Deposition

The energy deposition for protons, alphas and tritons in the counter gas comes from SRIM 2003 [88]. It is specific to the ^{3}He-CF_4 gas mixture in the 36 ^{3}He strings, though it is also used for the 4 ^{4}He strings. The differences between the energy loss in the ^{3}He mixture and the energy loss in the ^{4}He mixture were insignificant.

The gas densities (for the ^{3}He and ^{4}He mixtures) are an important input to the SRIM calculation. The calculations of the gas densities are given in Appendix D. The ^{3}He mixture density is found to be $(1.62 \pm 0.01) \times 10^{-3}$ g/cm^3, and the ^{4}He mixture is $(1.70 \pm 0.01) \times 10^{-3}$ g/cm^3.

The energy loss is implemented as a function of ion energy. We studied energy straggling

in the gas but it was determined to have an insignificant effect on the pulse shapes.

The average energy deposited per ion pair produced, W, was measured for the NCD gas mixture (see Section 5.1). The actual measurement is a function of the gas gain, so the value of W (34 eV [82]) was determined using A. Hime's measurement of the gas gain [90].

4.1.3 Electron Drift

Electrons drift towards the anode in the cylindrical electric field within the counter. The drift time for electrons to reach the anode is a function of the radius at which they start. We used an in-house "first-principles" simulation of electrons drifting in a cylindrical electric field in the ^{3}He-CF_4 gas mixture [91]. In addition to determining the drift times the simulation also determined the drift-time resolution due to the random nature of the primary-ionization electron drift toward the anode. This simulation was verified with Garfield [92] calculations. The NCD MC uses the drift-time as a function of initial radius from this simulation, as well as the drift-time resolution. The resolution smears the pulse in a small but noticeable way, with Gaussian widths typically ranging from 20-40 ns.

Based on later work with wire alphas (see Section 4.3.1), the drift curve was scaled up (i.e. longer pulses) by about 10%, giving a maximum drift time of 3360 ns. We also studied the effects of electron attachment and found that they would not affect the pulse shapes.

4.1.4 Gas Gain and Space Charge

The strength of the electric field through which the primary ionization electrons pass increases as they drift towards the anode. Within a few wire radii of the anode the field is high enough that an avalanche of secondary ionization occurs. The average charge multiplication factor is the gas gain of the counter. For the NCDs, the gas gain is approximately 220, as determined by A. Hime [90]. Pulse amplitudes are scaled to match the overall gain of the NCD array in the simulation to that of the ^{24}Na calibrations.

String-by-string and counter-by-counter gain differences are also implemented in the Monte Carlo. The string-by-string differences are calculated relative to a reference string and are determined by the energy-calibration constants for the actual array. Since energy

calibrations were performed throughout the NCD phase the calibration constants allow changes in the actual string gains to be propagated into the Monte Carlo.

Counter-by-counter gain differences, relative to the string-average gain, were measured during deployment and undeployment by placing an AmBe neutron source next to each counter. We use the undeployment measurements, as recommended by S. McGee, since the DAQ system was not in a stable configuration during early stages of NCD deployment [93].

Depending on the orientation of the ionization track in the counter, charge saturation, or "space charge," effects can become important. For example, if primary ionization electrons from track segment A arrive before those from track segment B, and the avalanche regions from the two segments overlap spatially, then the ion cloud created by segment A's avalanche will lower the gas gain for segment B. This is illustrated in the cartoon in Figure 4.4. In the model currently used in SNOMAN, each avalanche has a fixed extent along the anode wire, characterized by the avalanche width, w, and the effect of each avalanche on the local gas gain is calculated based on the Diethorn model [84, 94]. There are seven parameters in the model. Four are independently constrained, including the mean gas gain, M, the ion mobility, the electric field, and the mean ionization energy. Of the remaining three, the avalanche width and the constant of proportionality between the gas gain and the change in gas gain as a function of the change in charge density on the anode are highly inversely correlated. Therefore two parameters are tuned to match features in the neutron and alpha energy spectra: the low-energy side of the neutron peak, the Polonium "bump," and the relative positions of the neutron and ^{210}Po alpha peaks with data. The two tuned parameters are the avalanche width and the mean avalanche radius, r_{av}. A detailed description of the space-charge model and the optimization of the parameters is found in[84, 94]

4.1.5 Ion Drift

The time structure of the current pulse on the anode is actually dominated by the ions drifting out from the anode, as discussed in [95]. The arrival times of the primary-ionization electrons at the anode are determined by the track geometry and electron drift, as described above. In the MC this distribution is calculated numerically with 1-ns bin widths. The

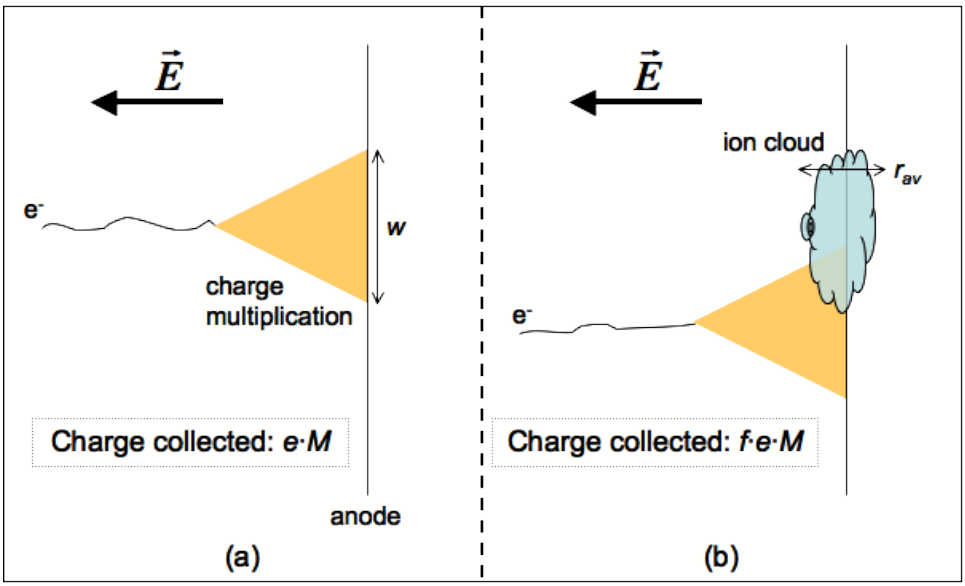

Figure 4.4: A cartoon depicting the basic principles of the space-charge model. In (a) the first primary-ionization electron drifts to the anode and starts an avalanche of secondary ionizations. The charge collected on the anode is eM. The avalanche results in a cloud of secondary-ionization ions slowly drifting away from the anode, as shown in (b). They start out with mean radius r_{av}. The image charges from the ion cloud reduce the charge density on the anode, temporarily reducing the electric field in the vicinity of the cloud. When a second primary-ionization electron arrives near the first avalanche region a short time later its secondary-ionization avalanche is reduced in magnitude by some fraction, f, as a result of the smaller electric field.

pulse is then convolved by Fast Fourier Transform (FFT) with the ion-drift function given by Wilkinson [96]:

$$I_{\text{ion}}(t - t_0) = \frac{1}{2\ln(b/a)} \int_0^t \frac{I_{e^-}}{t - (t_0 + \tau)} \mathrm{d}t_0, \tag{4.1}$$

where I_{e^-} and I_{ion} are the currents before and after accounting for the ion drift, respectively. τ is the ion time constant that was measured with an NCD counter (see Section 5.2). b and a are the NCD wall and wire radii, respectively. In the end, I_{ion} is the current pulse that is formed on the anode wire, which is then propagated through the NCD electronics and data acquisition simulation.

4.2 Electronics and Data Acquisition

After a current pulse forms on an anode wire it propagates along the counter, through the NCD cable to the preamplifier. The amplified pulse is then transferred to the multiplexer system, at which point it is split between the two data-acquisition paths. One path integrates the pulse with a Shaper-ADC to determine the energy deposited in the counter. Its trigger is based on the pulse integral. The second path is triggered by the pulse amplitude. The pulse is logarithmically amplified and digitized with a sampling rate of 1 GHz. Each recorded pulse is 15 μs long, so a pulse in the data is composed of 15,000 bins. The electronics and data-acquisition components, and the *in situ* and *ex situ* measurements made to determine the various simulation parameters are described in more detail in [80] and [97]. In the Monte Carlo the simulated current pulses are stored in 17,000-element arrays with 1-ns bin-widths. A 15,000-element subset of that array is eventually stored in the standard SNO data structure for each pulse that causes a trigger. Great efforts were made throughout the electronics and data-acquisition code to optimize the time required to simulate a pulse. Figure 4.5 shows a simulated neutron pulse at various stages of the electronics simulation.

4.2.1 Pulse Propagation and Reflection

Propagation of the pulse along the NCD is simulated with a lossy-transmission-line model. Half of the pulse is propagated down the NCD string, through the delay line (delay time = 89 ns), and back to the point-of-origin of the pulse. The delay-line attenuation is also simulated as a lossy transmission line. Both halves of the pulse (reflected and direct) are then transmitted up to the top of the NCD. The attenuation of the pulse due to transmission along the NCD is dependent on the distance traveled, so pulses starting at different z positions will look slightly different when they exit the NCD.

The inductance, capacitance, and conductance parameters used in the NCD counter and delay-line transmission lines come from fits of the lossy-transmission-line model to data from injected pulses with the SPICE simulation package [98, 99]. They are all given in Table 4.1.

Due to skin effects in the anode wire, the resistances for the counters and the delay lines are frequency dependent. The frequency dependence for the 50-μm-diameter copper

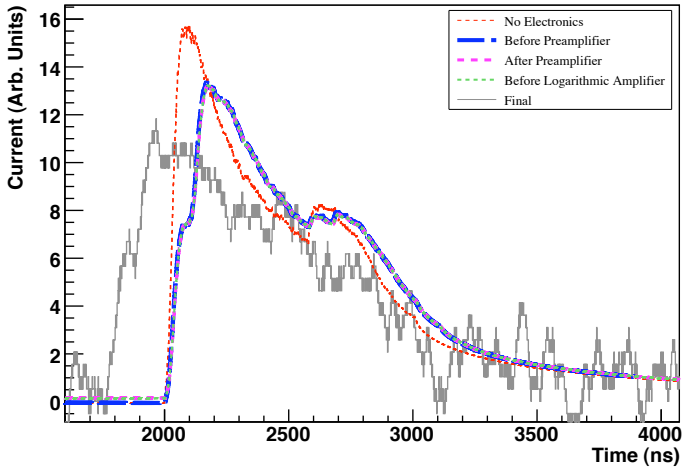

Figure 4.5: A simulated neutron pulse ($r = 1$ cm, $\theta = 90°$, $\phi = 0°$) at different stages of the electronics simulation to show the effects of the different components. The 89-ns delay between the reflected and direct components of the pulse can be seen in the rising edge of the "before preamplifier" pulse. The final pulse is logarithmically amplified and shifted in time according to the trigger threshold.

wire used in the NCDs was measured while the NCD counters were being designed [100]. The resistance as a function of frequency is shown in Figure 4.6. The resistance data were extracted from the plot and fit with an empirical formula that accounts for the region of frequency space in which there is a $\sqrt{f}$ dependence and the region where the resistance is constant:

$$R(f) = \frac{A}{\exp((f-B)/C)+1)} + \frac{D\sqrt{f}+E}{\exp((B-f)/C)+1)}, \tag{4.2}$$

where the fit parameters, A, B, C, D, and E are given in Table 4.2, and the frequency is given in MHz.

Propagation in the NCD cable is simulated with a low-pass filter (RC $\approx$ 3 ns). There is a small reflection (reflection coefficient = 15%) at the preamplifier input due to the slight impedance mismatch between the preamplifier input and the cable. The fraction of the pulse that reflects off the preamplifier input travels to the bottom of the cable, reflects off the combination of the resistive coupler and the top of the NCD, and then travels back up

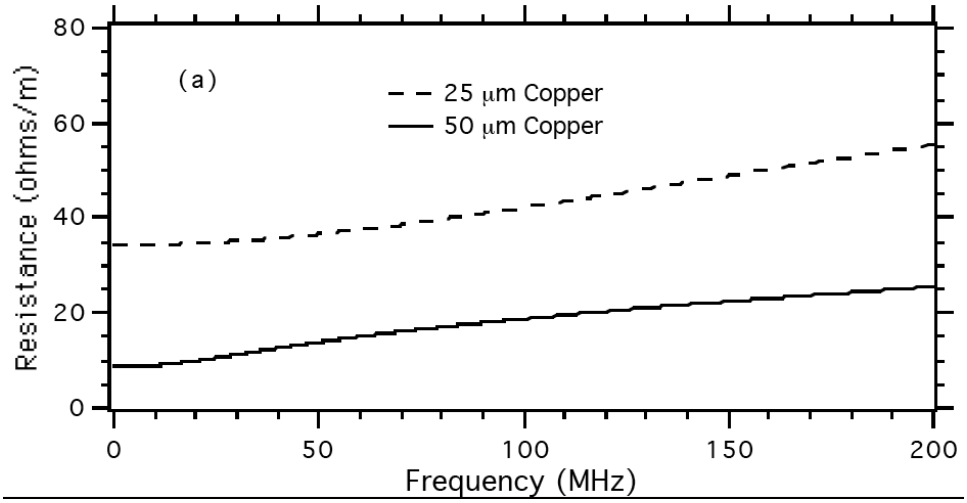

Figure 4.6: Anode wire resistance as a function of frequency for both a 25-μm-diameter wire and a 50-μm-diameter wire. 50 μm wires were used in the NCD counters. This Figure is from [100].

Table 4.1: The inductance, capacitance, and conductance parameters used in the lossy-transmission-line model of the NCD counters and delay line. These were produced using the SPICE simulation package [98, 99].

Parameter	Value
Counter	
Inductance	1.33×10^{-8} H/cm
Capacitance	7.68×10^{-14} F/cm
Conductance	0 S/cm/MHz
Delay Line	
Inductance	9.91×10^{-7} H/cm
Capacitance	5.5266×10^{-12} F/cm
Conductance	3×10^{-12} S/cm/MHz

Table 4.2: The resistance parameters used in the lossy-transmission-line model of the NCD counters and delay line. These were produced by fitting data in [100].

Parameter	Value
Counter and Delay Line	
Resistance - A	0.1024 Ω/cm
Resistance - B	13.4 MHz
Resistance - C	8.4 MHz
Resistance - D	0.01643 $\Omega/\mathrm{cm}/\sqrt{\mathrm{MHz}}$
Resistance - E	0.0232 Ω/cm

the cable to the preamplifier input.

4.2.2 Preamplifier

The preamplifier converts the current pulse to a voltage pulse. The gain is 27,500 V/A. The circuit elements of the preamplifier also affect the shape of the pulse. We simulate this with a low-pass filter (RC $\approx$ 22 ns) and a high-pass filter (RC = 58000 ns). The RC constants were measured by fitting the model to *ex situ* injected pulses.

The implementation of the low- and high-pass filters performs the calculation in a single loop over the pulse array ($\sim N$, $N = 17,000$ elements). Furthermore, in the case where the RC constant approaches the size of the bin width, the bins are subdivided to maintain the accuracy of the simulation. The low-pass filter is implemented as follows:

$$\begin{aligned} \overline{V}_0 &= \frac{\Delta t}{2\tau_{RC}} V_0 \\ \overline{V}_i &= \left(\overline{V}_{i-1} + \frac{\Delta t}{2\tau_{RC}} V_{i-1} \right) e^{\Delta t/\tau_{RC}} + \frac{\Delta t}{2\tau_{RC}} V_i, \quad i \in [1, N) \end{aligned} \tag{4.3}$$

where V and $\overline{V}$ are the pulse before and after passing through the filter, respectively. Δt is the bin width and τ_{RC} is the RC time constant. The high-pass filter implementation is

similar:

$$\begin{aligned} \overline{V}_0 &= \left(1 - \frac{\Delta t}{2\tau_{RC}}\right) V_0 \\ \overline{V}_i &= \left[\overline{V}_{i-1} - \left(1 + \frac{\Delta t}{2\tau_{RC}}\right) V_{i-1}\right] e^{\Delta t/\tau_{RC}} + \left(1 - \frac{\Delta t}{2\tau_{RC}}\right) V_i, \quad i \in [1, N) \end{aligned} \tag{4.4}$$

4.2.3 Multiplexer

The multiplexer branch of the electronics chain consists primarily of a $\approx$ 300-ns delay cable, the logarithmic amplifier, and the digital oscilloscope. The delay cable and some of the circuit elements prior to the logarithmic amplification are simulated with a low-pass filter (RC $\approx$ 13.5 ns). The analytic form of the logarithmic amplification is

$$V_{\log}(t) = a \log_{10}\left(1 + \frac{V_{\text{lin}}(t - \Delta t)}{b}\right) + c_{\text{chan}} + V_{\text{PreTrig}}, \tag{4.5}$$

where $V_{\log}$ and V_{lin} are the logarithmic and linear voltages, respectively, and a, b, c_{chan}, and V_{PreTrig} are constants determined by regular *in situ* calibrations during the NCD phase.

The circuit elements after the logarithmic amplification are simulated with the final low-pass filter (RC $\approx$ 16.7 ns). The RC constants for the two low-pass filters in the multiplexer simulation were determined by fitting the model to pulses injected into the components *ex situ*.

Before simulating digitization electronics noise is added to the pulse. The final element of the multiplexer branch of the simulation is the digital oscilloscope. The pulse-array values are rounded off to the nearest integer to replicate the digitization.

4.2.4 Noise

There are a variety of electronic noise sources within the NCD system. Due to the difficulty of identifying and measuring all of the individual contributions, noise is added to the pulses after the rest of the simulation, with the exception of the digitization, is complete. The frequency spectrum of the noise was measured for each channel using the baseline portions of injected calibration pulses. This provides the mean value, μ_i, of the noise power spectrum

at each frequency bin, i. Assuming that the real and imaginary Fourier components of the noise are independent Gaussian-distributed random variables, then their standard deviations are related to the mean value by [101]:

$$\mu_i = 2\sigma_i^2. \tag{4.6}$$

The noise is added to each pulse by convolution in the frequency domain. Unfortunately the order of the electronics elements with respect to the logarithmic amplification (all of the other elements are linear) makes the adding of the noise more complicated. The pulses that were used to measure the noise spectrum had been logarithmically amplified, passed through the final low-pass filter, and then "de-logged" (by inverting Equation 4.5). The addition of the noise to the simulated pulses needs to be done when the pulses are in the linear domain. It cannot, however, be done before the logarithmic amplification, because it would again pass through the final low-pass filter, ruining the accuracy of the noise spectrum. Instead, the final simulated pulses without noise are de-logged, convolved with the noise, and then "re-logged." Finally, the fully-simulated pulse, with noise, is passed to the digital oscilloscope simulation. It is impossible to avoid the double-simulation of the digitization noise, but the effect is negligible.

4.2.5 Shaper-ADC

The Shaper-ADC branch of the electronics is simulated by a sliding-window integral of the preamplified pulse. This number is then converted to units of ADC counts by doing an inverse linearity calibration. The calibration constants used in the uncalibration are the same constants that are used to calibrate the data. Since the shaper simulation acts on electronic-noise-free pulses, noise is added with a Gaussian-distributed random number. The mean and standard deviation of the noise for each channel were determined by *in situ* neutron calibrations and studies of the energy resolution.

4.2.6 Triggers & Deadtimes

The multiplexer and shaper systems include independent triggers. Thresholds were determined by *in situ* calibrations throughout the NCD phase. Once all elements of each system are simulated flags indicate whether or not the multiplexer or shaper thresholds were exceeded. The deadtimes of the two systems are then taken into account within each Monte Carlo event. After a multiplexer trigger the system is open to further triggers for 15 μs, after which it is dead for 1 ms. Each oscilloscope is dead for about 0.9 s after recording a pulse. After a shaper trigger the system is open to further triggers for 180 ns, after which it is dead for 350 μs. These times were only simulated within each Monte Carlo event, and not between events. For instance, a single Monte Carlo event could involve the decay of a ^{252}Cf nucleus during a calibration. Such a decay releases multiple neutrons and could result in multiple multiplexer and shaper events. The deadtimes would be simulated in that case, but they would not apply between multiple ^{252}Cf decays.

All NCD-system triggers are then integrated with the photomultiplier (PMT) signals in the SNO-detector-wide data-acquisition simulation, which was upgraded to fully implement the NCD system. Unlike the NCD system, PMT triggers are determined by PMT signals falling within ≈500 ns of each other. Therefore the PMT trigger simulation functions by time-ordering an array of all PMT signals in a Monte Carlo event and scanning through it to look for any trigger conditions that are satisfied. If that occurs, then a global trigger is created and the simulated data is recorded. The NCD signals are integrated into the PMT trigger simulation by inserting each signal into the time-ordered array of PMT signals. As the simulation scans over the combined PMT+NCD signals, any individual NCD signal is sufficient to cause a global detector trigger. For any global trigger all relevant NCD and PMT information is recorded in the data structure.

4.2.7 Shaper-Only Simulation

Certain parts of the overall NCD simulation are relatively slow due to the number of calculations that must be made. For instance, the space-charge simulation requires a nested loop over the segments of an ionization track, performing calculations of the effects on the

gas gain $\sim N^2$ times, where $N = 17,000$. The electronics and data-acquisition simulation also include several $\sim N$ and $\sim N\sqrt{N}$ loops over the pulse arrays. NCD-event simulations can take anywhere from five seconds to one or two minutes, depending on the length of the ionization track.

To allow faster simulations for users not interested in the NCD pulse information we have implemented a fast alternative to the full simulation. The ionization track is simulated to determine the timing of the event and the energy deposited in the gas. That energy is converted directly to an approximate shaper-ADC measurement by smearing it with a Gaussian to roughly account for the missing physics and electronics. This option allows simulations that do not require pulse shapes to be performed in a reasonable amount of time. The analysis to determine the neutron-detection efficiency successfully took advantage of the shaper-only simulation. On the other hand, the production of the alpha energy spectrum required the full-pulse simulation.

4.3 Other Features

4.3.1 Wire Alphas

A small fraction of the alpha events are expected to come from the anode wire due to radioactive contaminants in and on the copper. Wire alpha pulses would differ from standard wall-alpha pulse shapes in that their Bragg peak is late in the pulse, instead of early, since the end of the track is farther from the anode. This track orientation results in wider pulses (at a given fraction of the amplitude) than standard alphas due to the sharp rise and fall times because of the large amount of charge being collected at the end of the pulse.

Figure 4.7a shows the pulse-width-vs.-energy distributions for four different classes of Monte Carlo alpha pulses: bulk uranium- and thorium-chain alphas from the wall and wire, and ^{210}Po alphas from the wall and wire. There is a great deal of overlap between the wall-alpha and wire-alpha distributions except at high pulse width. Both the bulk and ^{210}Po distributions include a set of exceptionally-wide pulses. Due to the different initial-energy distributions of the bulk and ^{210}Po alphas the wide wire alphas also differ between bulk and ^{210}Po.

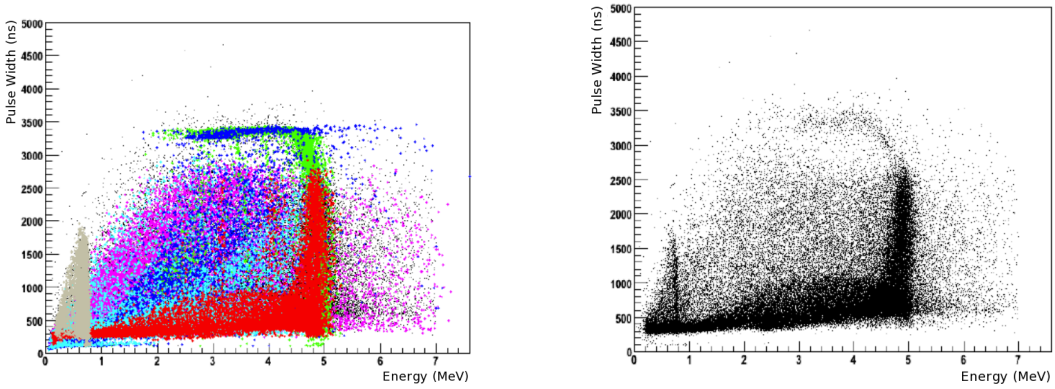

(a) Monte Carlo (b) Data

Figure 4.7: The pulse-width-vs.-energy distribution for (a) Monte Carlo alphas and (b) the blind NCD-phase data. Included in the Monte Carlo plot are: Green = Wire ^{210}Po; Blue = Wire U; Cyan = Endcap Nickel ^{210}Po; Red = Nickel ^{210}Po; Magenta = Bulk U; Grey = Neutrons. A unique subset of the wire alphas appears at high pulse width in both the (a) and (b) showing that the wire alphas in the data are due to ^{210}Po contamination on the wire surfaces. These plots are from [84].

If wire alphas exist in the data the NCD Monte Carlo predicts that they should be observable in the high-pulse-width region. Figure 4.7b shows the pulse-width-vs.-energy distribution for the blind NCD-phase data set. There is indeed a clump of events at high pulse width, appearing to extend from the top of the ^{210}Po peak. By comparing the details of the distributions in Figures 4.7a and 4.7b, in particular the lack of wide pulses above 5 MeV, it is clear that the wire alphas are entirely, or almost-entirely a result of surface ^{210}Po contamination. This highly-accurate NCD pulse Monte Carlo was able to specify where one should look to establish the existence of wire alpha events, and to show that they are present and due to ^{210}Po on the surface of the anode wires.

4.3.2 Betas

Betas from radioactive decays are another potential background. They are expected to be concentrated at low energies ($\lesssim$ 0.4 MeV). SNOMAN is capable of simulating betas using the EGS4 package. The integration of the EGS4 simulation with the NCD pulse simulation

was recently upgraded to include Poisson fluctuation of the distances between ion pairs and electron diffusion in the gas. These improvements, along with other code upgrades to match improvements made in the proton/triton/alpha simulation, allow for the fairly-accurate simulation of beta pulses [102]. Most beta pulses are wide, with low amplitude, and such pulses are not seen in the NCD-phase data.

Chapter 5

NCD MC DEVELOPMENT ANALYSES

Many analyses went into the development and verification of the NCD Monte Carlo. They were performed by various members of the NCD MC working group, in addition to studies performed by other groups, such as the Electronics Calibration working group [97], to characterize the behavior of the NCD system as accurately as possible. Several of these analyses were performed by the author, three of which will be described here: a study of the average energy deposited in the NCD gas per ion pair created, an analysis of sharp pulses to determine the ion mobility, and a study of the sacrifice of physics events from the data-cleaning cuts.

5.1 Average Energy per Ion Pair

5.1.1 Background

Two parameters are primarily responsible for determining the current measured with a proportional counter in response to a given amount of energy, E, deposited in the gas: the average energy deposited per ion pair created, W, and the gas gain, M. For some E the size of the current pulse is inversely proportional to W, and proportional to M. Integrating over many current pulses, the relationship is [95]

$$\frac{W}{M} = \frac{ne\overline{E}}{I}. \tag{5.1}$$

For the NCDs, $\overline{E}$ is the average energy deposited in a neutron-capture event. According to a SNOMAN simulation [103] E is (701 ± 7) keV. n is the rate of neutron captures and e is the electron charge. M/W is the constant of proportionality between $\overline{E}$ and the current, I.

As an ion travels through the NCD gas it loses energy primarily though electromagnetic interactions. Some, but not all, of those interactions will result in exciting an atomic electron

enough that it is no longer bound to the atom. The average amount of energy deposited per ionization, W, is a characteristic of the ion and the medium in which it is traveling. This value had not been measured previously for the NCD gas mixture, but the values for protons and alphas in a variety of other gases are all fairly similar [104]. Without an accurate way of measuring this value for different particles we will assume, with reasonable accuracy, it is the same for the proton, triton, and alpha.

W is actually the average value over some energy range of the energy-dependent w. However, the deviation from the average value is quite small until the ion energy drops very low [104]. As a result, it is reasonable to use the energy-independent W.

The gas gain, and therefore the current, is voltage dependent. Figure 5.1 shows how the total current in a general cylindrical ionization counter varies with voltage. This behavior is described in detail in [95]. The voltage in the general counter creates an electric field that separates the ionization pairs, pulling the electrons towards the anode, and the positive ions towards the cathode. At low voltages, the initial rise is due to the increasing electric field reducing the fraction of primary ionization pairs that recombine. Above a certain voltage there is a plateau in the current, at which point the field is strong enough that none of the primary ionization pairs recombine. This is the "ionization saturation" region.

Going further up in voltage, at some point the field near the anode is high enough that the drifting electrons produce an avalanche of secondary ionizations. The characteristic size of each avalanche is proportional to the voltage by the factor M, the gas gain. This is the "proportional" region on the voltage axis. At still-higher voltages charge-saturation, or space-charge, effects start to appear for pulses with larger amplitude. In the "limited proportionality" region the net gas gain depends on the amount of energy deposited. It is at the lower end of this region that the NCDs are typically operated. For the NCDs, $\overline{M} = 220$ [90], and space-charge effects are definitely present. Finally, in the "Geiger-Mueller" region the charge-saturation effects are completely dominant, so all pulses are the same size, regardless of the amount of energy deposited in the gas.

Two voltage regions are particularly important for this analysis: The ion saturation region will provide a direct measurement of W, and at the operating voltage of the NCDs we can measure M/W.

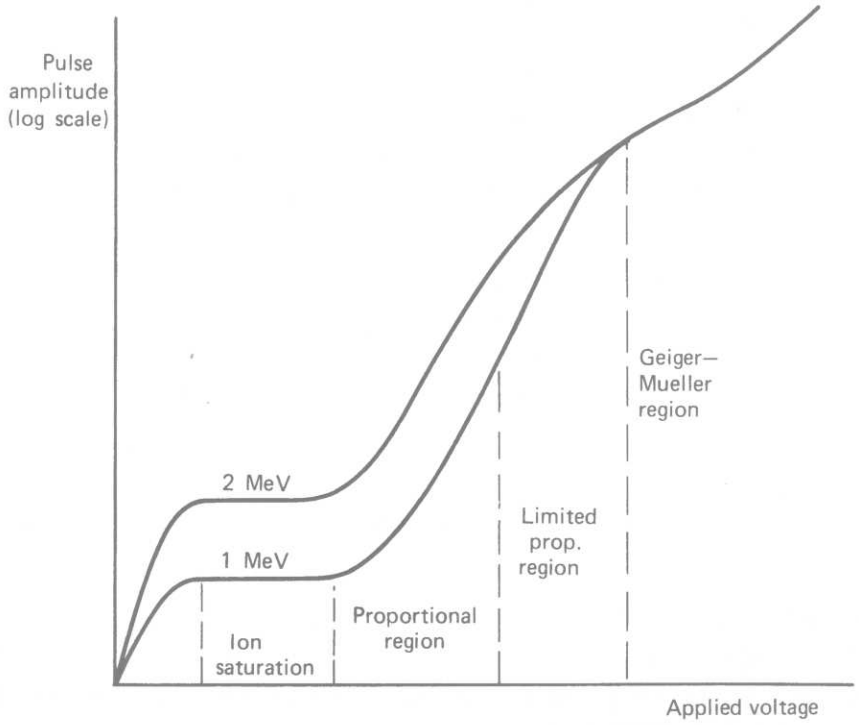

Figure 5.1: The pulse amplitude, or current, as a function of applied voltage for a cylindrical ionization counter. The different regions are a result of different effects becoming dominant at different voltages. In the ion saturation and proportional regions the gas gain does not depend on the energy deposited in the gas. In the limited proportionality region the gas gain decreases as energy increases. In the Geiger-Mueller region the pulse size does not depend on energy. This figure is from [95].

5.1.2 Setup

We conducted a test with the "87-cm" NCD, a counter built early in the NCD production for the purpose of performing tests such as this one. Three radioactive sources were used simultaneously to provide a large neutron flux: ^{241}AmBe, ^{252}Cf, and Pu-^{13}C. They were set within approximately 30 cm of the NCD counter with blocks of polyethylene in between to act as a neutron moderator. A layer of aluminum foil was wrapped around the counter to act as a Faraday cage to avoid currents induced on the NCD by external electromagnetic fields. The foil was separated from the NCD body by a layer of plastic bubble wrap.

The counter was first set up with standard data acquisition hardware to determine the event rate. This included the high-voltage supply set at 1950 V, preamplifier, Shaper-ADC, and ORCA hardware control/data acquisition software (see [105] for more information about the data acquisition hardware and software). In this case the foil shield was present but not electrically connected to anything. The rate, corrected for deadtimes [106], was (429.9 ± 1.1)Hz.

The second setup replaced the data acquisition system with a Keithley 485 picoammeter to read the DC current from the NCD. Instead of reading the current from the digital display on the picoammeter, which fluctuated rapidly due to statistical uncertainties at the low current levels we were measuring, the analog output was fed into a digital oscilloscope that averaged the reading over periods of a few seconds. It was found that the average value would stabilize reliably within that amount of time. The high-voltage supply was connected to the anode wire, and ORCA was used to control the voltage setting. The picoammeter read the current from the cathode (i.e. the nickel wall of the NCD). The foil shielding layer was electrically connected to ground. The picoammeter had multiple ranges current ranges. The lowest range was able to measure the current from settings up to 1500 V (hereafter referred to as the "low-voltage" measurement). By switching to the next-higher current range measurements were made up to 2000 V (the "high-voltage" measurement). Due to differences in how the high-voltage supply was calibrated relative to the supplies used in the actual NCD system, the setting which corresponded to the voltage used for the NCD array was 1943.9 V. The set voltage in ORCA was calibrated to find the actual applied voltage

with a high-voltage probe. The calibration data are shown in Figure 5.2.

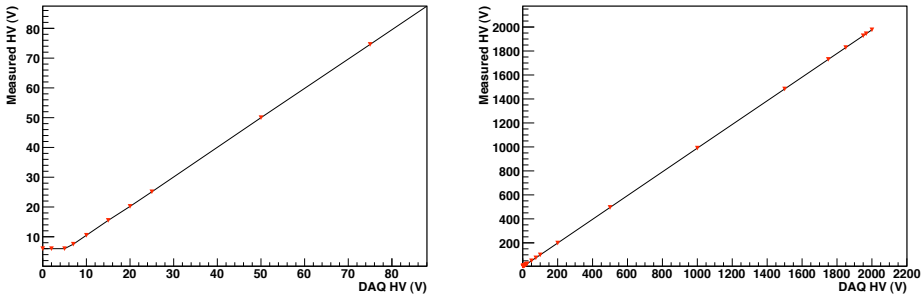

(a) (b)

Figure 5.2: Data points used to calibrate the voltages set by ORCA to the actual applied voltages. (a) shows the non-linearity at low voltages, while (b) shows the full range used in this analysis.

5.1.3 Low-Voltage Measurement

The low-voltage measurement focused on measuring W by operating the NCD in the ion-saturation region. Currents were measured at eighteen voltages between 0 V and 1500 V, both with and without the neutron sources present. The current without sources was subtracted from that with sources at each voltage to remove background contributions. The current difference was then converted to a measurement of M/W as a function of voltage, as shown in Figure 5.3. The error bars on each data point are statistical uncertainties only. The systematic uncertainty is due to the limited accuracy of the picoammeter. 200-800 V was chosen to represent the ion saturation region based on the flat trend of the data at those voltages. Figure 5.3 also includes a fit with a zeroth order polynomial between 200 and 800 V. The result of the fit is $M/W = (2.93 \pm 0.65\ (\text{stat.}) \pm 0.84\ (\text{syst.})) \times 10^{-2}\ \text{eV}^{-1}$ ($\chi^2/\text{dof} = 1.572/6$; $p = 0.955$). Since $M = 1$ in the ion saturation region, we find $W = 34.13 \pm 12.4$ eV.

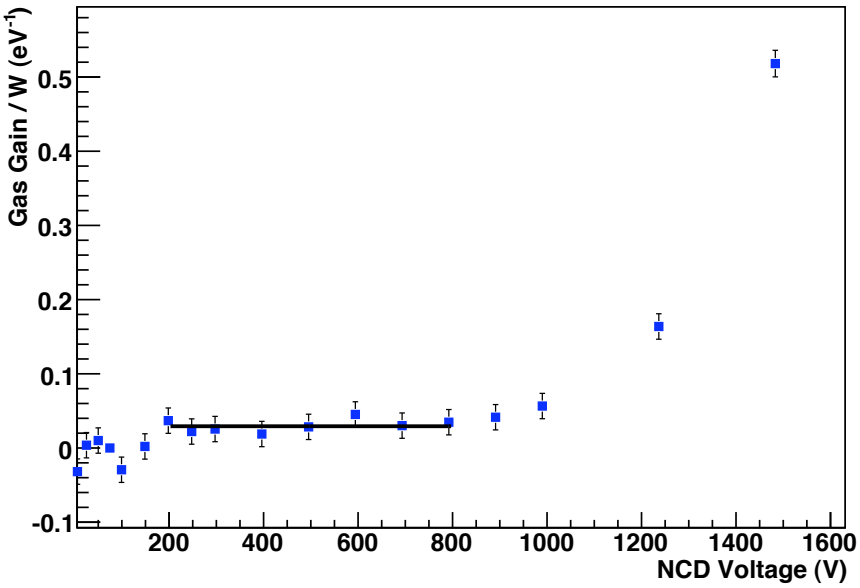

Figure 5.3: The low-voltage measurement of M/W, including a fit in the ion saturation region to determine W. The error bars represent statistical uncertainties only.

5.1.4 High-Voltage Measurement

The high-voltage measurement determined M/W for a wider voltage range, from 0 V to 2000 V. The primary point of interest for understanding the NCD system is at 1943.9 V, which corresponds to the ideal 1950-V set-point for the NCD array. Figure 5.4 shows the values of M/W for both the low- and high-voltage measurements. The error bars for most of the points are hidden by the markers. The data point at 1943.9 V is $M/W = 6.36 \pm 0.33(\text{stat}) \pm 0.03(\text{syst})$ eV^{-1}. A measurement accurate to 5% is sufficient for the purposes of the NCD MC, particularly since the gains of each string are individually tuned using the neutron energy peak to match the ^{24}Na calibrations. Any inaccuracy in M/W in the context of the space-charge simulation is also compensated for with the two tuned parameters in that model.

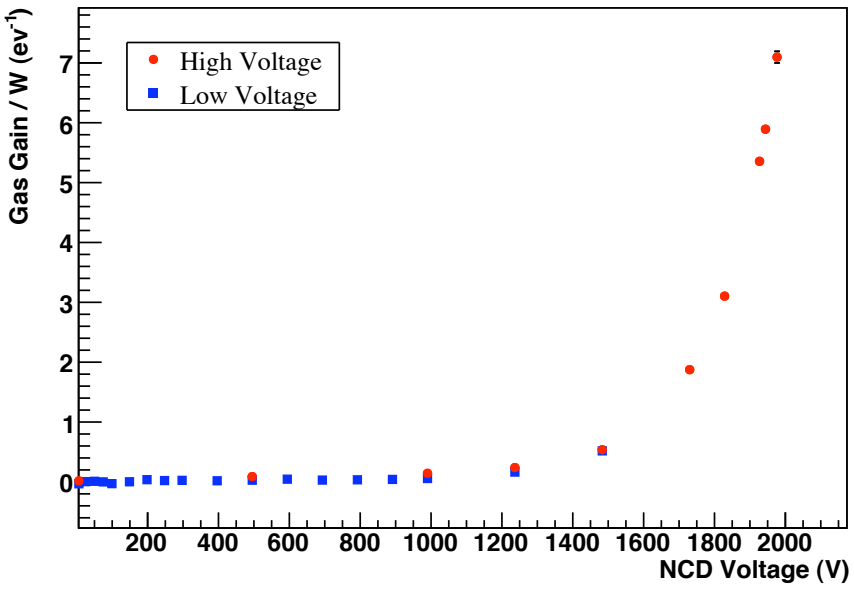

Figure 5.4: The low- and high-voltage measurement of M/W. The error bars represent statistical uncertainties only, and are smaller than the data-point markers for almost every point. The low-voltage and high-voltage measurements agree well, though there may be a small systematic shift between the two of them that is accounted for by the systematic uncertainty due to the picoammeter accuracy.

An independent measurement of the gas gain at the NCD operating voltage was performed by A. Hime [90] by measuring the location of the neutron peak as a function of voltage. The gas gain was found to be $M \approx 220$ (no uncertainty given). W can be determined by combining that measurement of G with the measurement of M/W above. W was found to be $220/6.36 = 34 \pm 5$ eV [82]. This is in excellent agreement with the W measured with the low-voltage measurement above, and it was implemented in the NCD MC used to in the NCD phase analysis [65].

5.2 Ion Mobility

The small ion mobility, relative to that of the electrons, results in the long tail that is characteristic of pulses from ionization in the NCD counters. Therefore it is important to know the ion mobility so that the tail of each pulse can be simulated correctly.

The ion mobility depends on the particular ion being studied and the gas in which it is traveling. For the NCDs, the ions present consist primarily of CF_3^+, F^-, and CF_3^-, and insignificant fractions of other species [107]. The measured value of the ion mobility in an NCD will therefore be a combination of the ion mobilities of the positive ions in the gas (almost entirely CF_3^+).

According to [108] the evolution of a charge pulse in a cylindrical proportional counter can be characterized as

$$Q(t) = \int_0^t \frac{\mathrm{d}q(t_0)}{\mathrm{d}t} \frac{1}{2 \ln b/a} \ln\left(1 + \frac{t - t_0}{\tau}\right) \mathrm{d}t_0, \tag{5.2}$$

where $\mathrm{d}q(t_0)/\mathrm{d}t$ is the electron current arriving at the anode, a and b are the anode wire radius and the inner radius of the counter, and τ is the ion time constant. τ is inversely proportional to the ion mobility, μ:

$$\tau = \frac{r_0^2 p \ln(b/a)}{2\mu V_0}, \tag{5.3}$$

V_0 is the applied voltage, p is the gas pressure, and r_0 is the radius at which the ions are created.

If the underlying shape of a pulse, not including the tail, were understood, it would be simple to extract the shape of that tail. There is one class of pulses that has a relatively simple underlying structure: ionization tracks that are parallel to the anode wire. The primary ionization electrons all reach the anode at approximately the same time, with some spread due to straggling. Therefore the basic shape of the underlying pulse is Gaussian. Reflections and the effects of propagation along the counter and through the electronics also affect the shape of the pulse. Those secondary effects have all been modeled independent of the ion mobility.

The procedure for extracting the ion mobility is to select the narrowest neutron pulses from a calibration data set and fit each pulse with a Gaussian convolved with a reflection and the electronics model. The free parameters in each fit are τ, the three Gaussian parameters (amplitude, mean and width), and the reflection time. An example fit is shown in Figure 5.5. The generic pulse model fits the peaks well enough to allow for a characterization of the ion tail, even though the second reflection (due to the pulse partially-reflecting off the preamplifier input, traveling down the NCD cable, and reflecting back upwards from the cable-bell connection to the NCD) is not present in the simulation.

Twenty-six AmBe neutron calibration runs were analyzed. The narrow pulses of interest are from proton-triton tracks that are parallel to the anode wire and deposit all of their energy in the gas. The neutron peak typically falls between 120 and 130 ADC counts, so an initial selection of pulses was made by restricting the ADC charge to be between 100 and 150. The second selection cut was based on the width and height of each pulse. The sharpness of a pulse can be approximately characterized by the ratio of the amplitude to the width. A cut of $0.5 \times 10^{-4} <$ amplitude/width $< 1 \times 10^{-4}$ A/ns removed approximately 99.36% of the pulses.

Figure 5.6 shows the results from all of the fits in the AmBe-run data set. The histogram has a broad peak of successful fits, and a smaller peak at low τ of non-physics background pulses (spikes from electrical discharges would not have an ion tail). Of the 393 pulses that were fit, 337 ($\approx$86%) fits include ion tails longer than $\tau = 2$ ns. The main peak was fit to a Gaussian using a log-likelihood minimization because of the small number of entries in many of the bins. The mean of the Gaussian fit is $\tau = 5.50 \pm 0.14$ ns ($\sigma = 2.15 \pm 0.12$ ns). The time

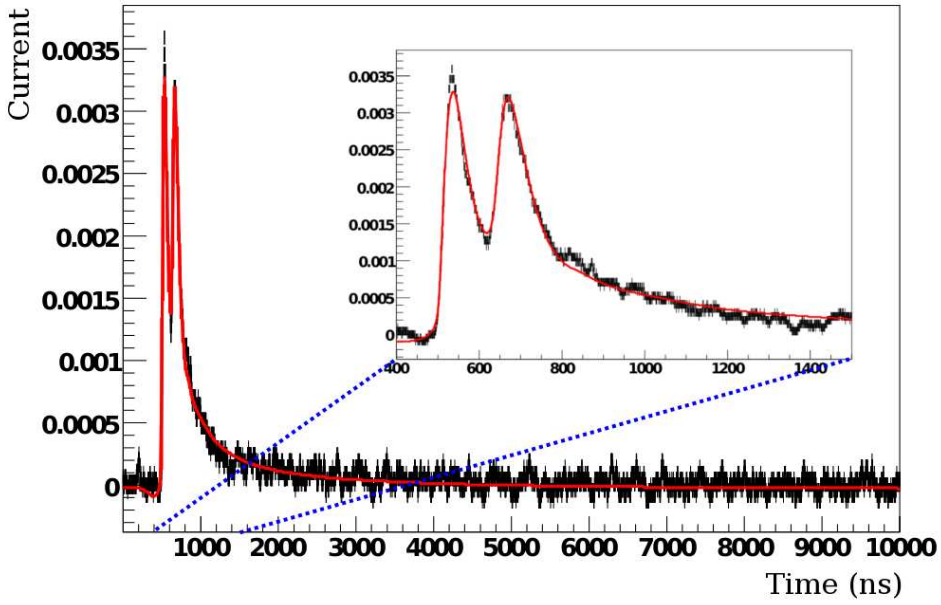

Figure 5.5: An example of a fit to extract the value of the ion-tail time constant.

constant corresponds to an ion mobility of $\mu = (1.082 \pm 0.027) \times 10^{-8}$ cm^2 ns^{-1} V^{-1}. This value of the ion mobility was implemented in the NCD MC, and the uncertainty was used to calculate its systematic effects in the Monte Carlo. For comparison, in the approximate range of electric field strengths found in the NCDs [109], for CO_3^- in He gas the ion mobility is $\mu \approx 10 - 12 \times 10^{-8}$ cm^2 ns^{-1} V^{-1}; for CO_2^+ in He it is $\mu \approx 10 - 15 \times 10^{-8}$ cm^2 ns^{-1} V^{-1}; and for O^- in He it is $\mu \approx 13 - 20 \times 10^{-8}$ cm^2 ns^{-1} V^{-1} [110].

5.3 Data Cleaning

The data cleaning cuts have been shown to have an energy-dependent neutron sacrifice [83]. They were designed to remove instrumental backgrounds, and not necessarily alphas, and the alpha sacrifice of the cuts is not known because there is no alpha calibration source (the ^{4}He strings provide some information, but it is somewhat limited).

For NCD events there are two sets of data cleaning cuts that are applied to the pulse shapes: path A cuts are performed in the time domain, while path B cuts are performed

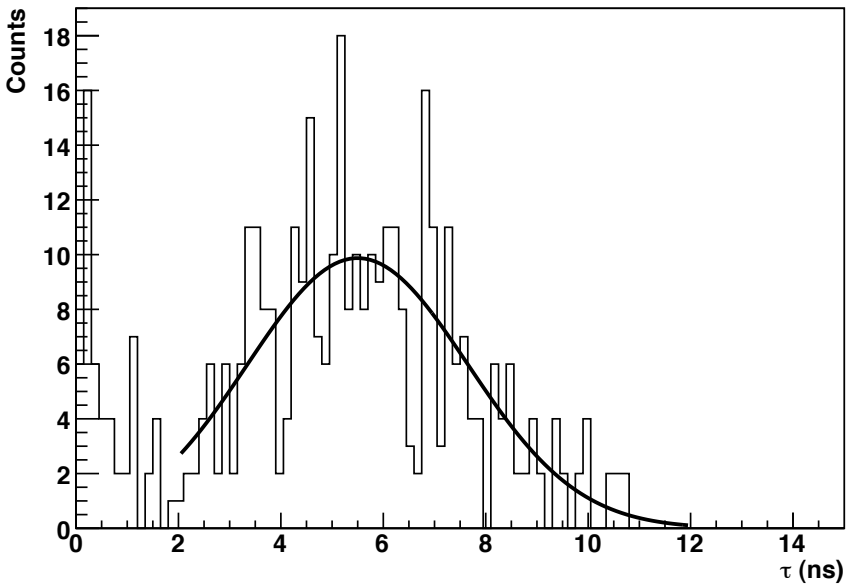

Figure 5.6: Fit results from the ion tail pulse fit. The data set includes 393 pulses from twenty-six AmBe calibration runs. The low-τ peak is from non-physics background pulses. By fitting a Gaussian to the main peak with a log-likelihood minimization the ion time constant is determined to be 5.50 ± 0.14 ns.

in the frequency domain. Both consist of five cuts. Path A's cuts are labeled Fork1, Fork2, Oscillatory Noise, Flat Trace, and Narrow Pulse. Path B's cuts are labeled Flatness, Fork, Symmetry, Spike, and Oscillation. The similarity between some of the names in the two paths does not necessarily imply similar behavior of the cuts.

We want to know whether the MC sacrifice as a function of energy matches that of the data. The best way to make this comparison is to use the ^{24}Na calibration. We can make comparisons for both data-cleaning paths. Additionally, we will use only the "superclean" ^{3}He strings, the set of strings on which no or almost no events are cut in the neutrino data. The strings used in this study are 2, 4-6, 9, 11, 12, 14, 21-24, 33, 36, and 39 whenever the superclean strings are specified.

The comparison of the path A cuts applied to ^{24}Na data and MC looks very good. The cut fraction comparison as a function of Shaper ADC[1] is shown in Figure 5.7. The total cut fractions are given in the legend in parentheses. It should be noted that it is necessary to consider the shape of the neutron energy spectrum when comparing the total cut fraction to the cut fraction as a function of energy; a simple comparison of the absolute numbers will be deceptive. While the MC cut fraction is slightly above the data cut fraction at low Shaper ADC, the difference is not really significant considering the small number of events in that energy window. There are a significant number of MC events cut at the neutron peak, around ADC = 125. These are primarily cut by the Fork1 cut, and are probably due to problems simulating the noise on the top of pulses with the double-peaked structure of a neutron [111]. The disagreement will not be a problem for alphas because they do not have a double-peaked structure. Overall the agreement for the path A cuts is considered satisfactory.

The comparison of path B cuts applied to ^{24}Na data and MC did not go as smoothly as for path A, as can be seen by comparing Figures 5.8a and 5.8b. Two cuts, in particular, were problematic: the spike and the symmetry cuts. The data show a rise in the cut fraction at low energy. In the MC that rise started too high in energy, resulting in too many pulses being cut. We investigated both cuts and identified the pulse parameters responsible for

[1]Calibrated energy was not available when the cuts were being developed; 764 keV approximately corresponds to a Shaper ADC value of 127, and 191 keV is approximately a Shaper ADC value of 30.

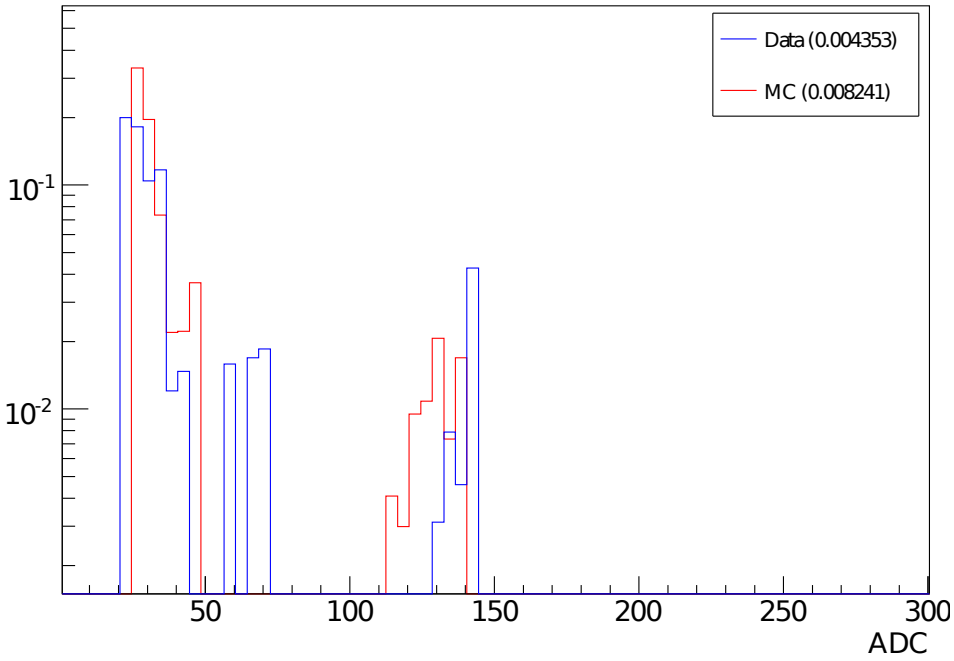

Figure 5.7: A comparison of data and MC cut fractions from the path A data-cleaning cuts. The data and MC are ^{24}Na runs from only the superclean strings.

the disagreements.

The spike cut uses several pulse parameters, one of which is the area of the logged pulse. For delogged pulses the area of the pulse is proportional to the energy, and we know that we have to scale the MC energies on a string-by-string basis by a few percent. A scaling of the pulse area in the linear domain corresponds to a shifting of the area in the log domain (in some complicated way that depends on the shape of the pulse). While the linear-pulse area distribution needs to be scaled so that the MC will match the data, the logged-pulse area distribution needs to be shifted horizontally, as is shown in Figure 5.9. The values of each string's area shift are given in Table 5.1. After shifting the logged-pulse area the MC and data distributions agree fairly well. Some features of the distribution move or are altered more than others because the shifting is on a string-by-string basis, and the shift for some strings is negligible while for others it is much more significant. The spike cut itself depends

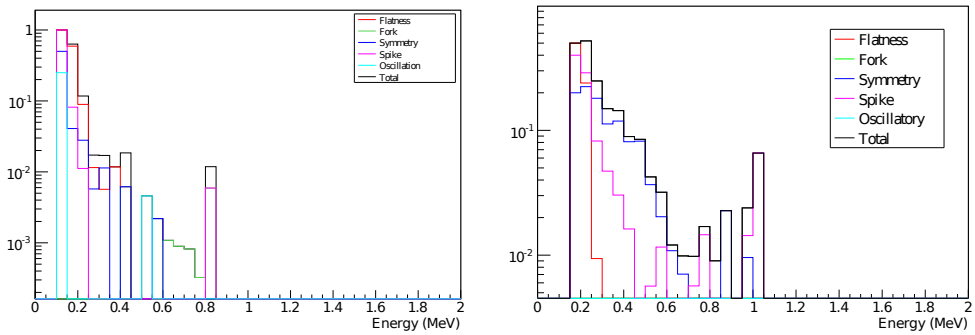

(a) Data (b) MC

Figure 5.8: A comparison of (a) data and (b) MC cut fractions from the path B data-cleaning cuts. The data and MC are ^{24}Na runs. The individual cuts are shown, in addition to the total cut fraction. The main disagreements between data and MC are due to the spike and symmetry cuts.

on two other parameters in addition to the area that both agree fairly well between data and MC.

The symmetry cut uses a parameter called the offset. N. Tolich explains the cut in the path-B data-cleaning document [112]: "...the offset (the intercept of the phase at zero frequency) is an indicator of the waveform symmetry. The offset is calculated from a fit to the first three non-zero frequency bins." The offset distribution for the MC and data are shown in Figure 5.10a. The main difference between the distributions is a shift along the offset axis.

The offset cut has some MUX-box dependency. The cut threshold is different for MUX box 0 and for MUX boxes 1, 2, and 3. Similarly, the disagreement in this parameter between data and MC is different for MUX box 0 and for MUX boxes 1, 2, and 3. The shift on MUX box 0 was 0.02228, and the shift on MUX boxes 1, 2, and 3 was 0.0759. By shifting the offset parameter on a MUX box-by-MUX box basis the parameter distributions agree well.

The fact that something is wrong with the offset distribution means that the asymmetry of the MC pulses differs from that of the data pulses. This is probably a problem with the tail of the pulses; this issue is also seen in the disagreement of the integrated rise-time

Table 5.1: Values by which each string's area distribution was shifted to match up the data and MC neutron peaks.

String	Shift	String	Shift
0	2988	20	N/A
1	3521	21	1029
2	7588	22	3485
3	N/A	23	-664
4	-378	24	2520
5	1402	25	2
6	1830	26	3744
7	-266	27	2804
8	1936	28	1883
9	1360	29	-797
10	N/A	30	N/A
11	1904	31	2139
12	3147	32	3811
13	2742	33	-554
14	2526	34	3520
15	306	35	2804
16	2877	36	2776
17	2811	37	-337
18	3973	38	1700
19	2635	39	2061

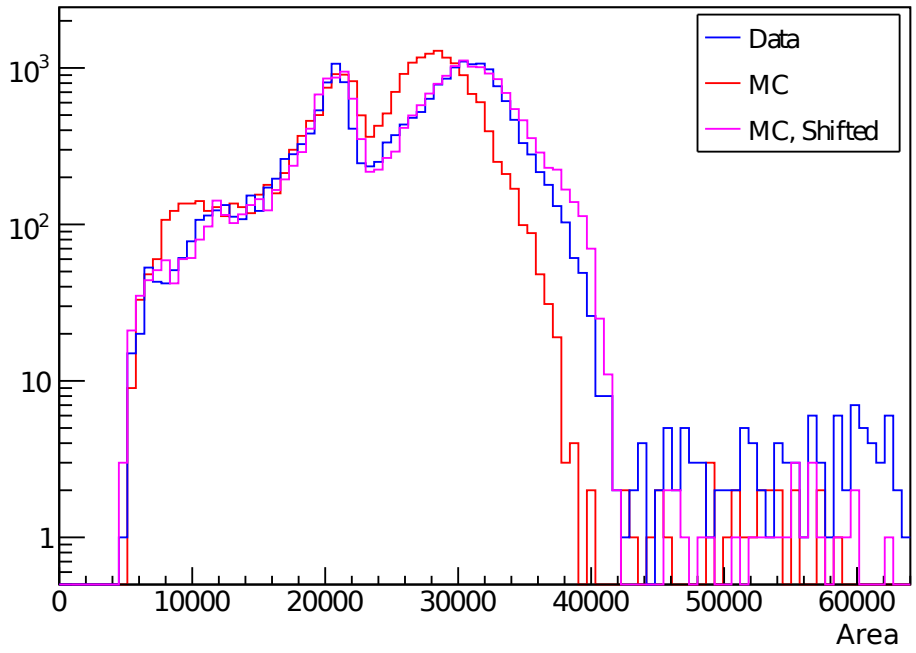

Figure 5.9: Data and MC logged-pulse area distributions. The MC area is shown before and after performing string-by-string shifts.

distributions (see [85] Section 3).

The shifted MC is compared to data in Figure 5.10b, respectively. The cut threshold for MUX box 0 is at -3, and the cut threshold for MUX boxes 1, 2, and 3 is at -2.95; offsets greater than those thresholds are considered good. Clearly the data contains some high-offset pulses which are not simulated by the MC. This may be the low-level alpha background, as MC alphas extend up into that region of offset space.

After applying the shifts for the spike and symmetry cuts the agreement between the data cut fraction and the MC cut fraction is excellent. The histograms are shown in Figure 5.11. The MC stops cutting events at approximately 0.5 MeV, with a small peak just below 0.8 MeV. A small fraction of data pulses are cut between those two energies. The overall cut fractions, indicated by the values in parentheses in the plot legend, also agree well.

The shifts of the offset and area parameters were performed after those parameters were

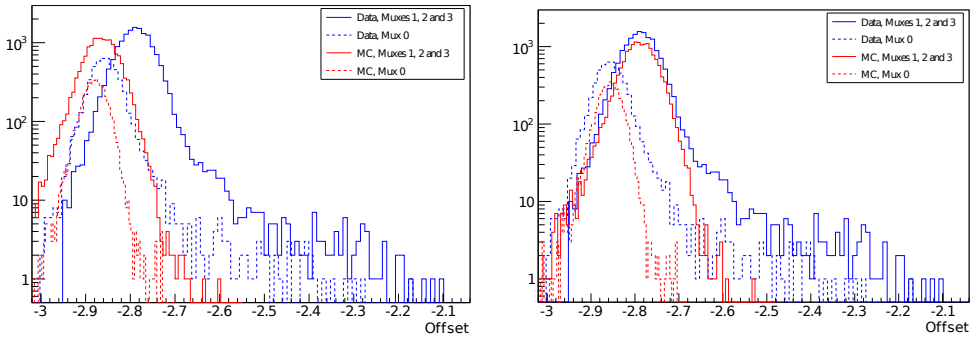

(a) Before Shift (b) After Shift

Figure 5.10: Data and MC offset distributions from ^{24}Na data/simulations before (a) and after (b) shifting the offset parameter for the MC. The data distribution is from the ^{24}Na skim file, so the data distributions cut off at offset $= -3$ and -2.95. The excess in the data at high offset is probably due to low-level alpha contamination.

calculated from the pulses. In other words, the pulses themselves were not changed. Since we make changes to parameters that affect how the pulses are cut but we are not changing the pulses themselves, the difference between the post-data-cleaning energy spectra with and without the shifts will have to be included as a systematic effect. As long as that systematic is included then the data-cleaning verification test has been passed.

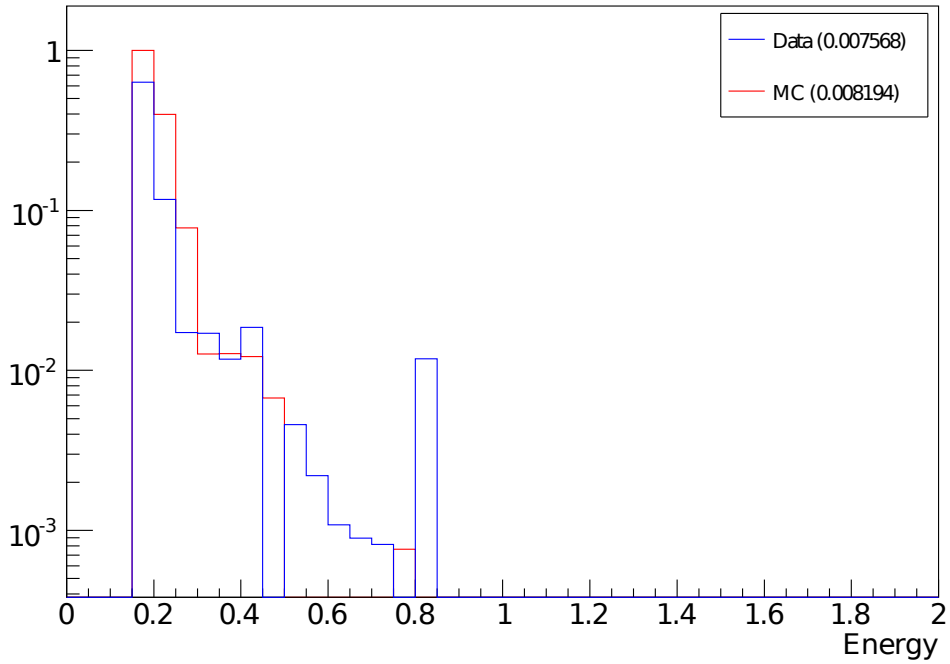

Figure 5.11: A comparison of data and MC cut fractions from the path B data-cleaning cuts. The data and MC are ^{24}Na runs from only the superclean strings.

Chapter 6

MC-BASED PULSE FITTING

After developing such a detailed model of the NCD system the natural question to ask is, "How can I use this model to help separate neutron-capture pulses from alpha pulses?" A great deal of information about the potential shapes of neutron-capture and alpha pulses is available through the simulation of NCD signal and background pulses, though it is difficult to parameterize it in some useful way.

The most direct strategy to take advantage of a set of simulated pulses is to fit them to the data. With a library of simulated neutron-capture pulses and a library of simulated alpha pulses, one could fit the data with both libraries and use the results to determine if each data pulse looks more like it came from an alpha track or from a neutron-capture track. Though seemingly a simple solution, the details quickly complicate the analysis.

6.1 MC Pulse Libraries

The simplest and most convenient method for fitting MC-generated pulses against a data set is to produce the pulses ahead of time and save them in one or more pulse libraries. It would be inefficient to generate the pulses as a fit is performed because of the time needed to generate each pulse. Furthermore, most minimizing routines perform best when the fit function (i.e. the simulated pulse shape) changes smoothly as a function of its parameters (r, E, θ, ϕ, and z). This is not the case in the NCD simulation when a change of any of those coordinates can cause a track to hit the wall or wire and therefore change shape discontinuously.

For neutrons the relevant coordinates of the parameter space are r, θ, ϕ, and z. The initial energy is fixed at 574 keV and 191 keV for the proton and triton, respectively. For alphas the relevant coordinates are E, θ, ϕ, and z, with the radius fixed at either the inner

radius of the wall or the outer radius of the wire.[1]

The three types of events, neutrons, wall alphas, and wire alphas, are produced in separate libraries. The three libraries are generated by varying the parameters on the four-dimensional grids in the respective parameter spaces. The grid spacings and numbers of pulses in each library are given in Table 6.1. Certain modifications were made to the otherwise-uniform grids, as is discussed below, so the number of pulses in each library is not necessarily the same as the product of the number of grid points in each dimension of the parameter space.

Table 6.1: Spacings for the grid points along each dimension in the relevant simulation parameter space for the three libraries produced. The numbers of pulses in each simulation grid space are also given. The radius points are spaced uniformly in r. * This energy is the initial energy of the alpha particle. ** The number of ϕ points depends on θ to uniformly cover the spherical space. The maximum number of ϕ points is given in this table. † Each library has a different range for ϕ; See the text for details. †† Two extra grid points are added in energy to account for high-energy ions that reenter the NCD wall, depositing only some of their energy in the gas.

	r	α E*	θ	ϕ**	z	Pulses
Range	[0.1, 2.5] cm	[0.2, 1.2] MeV	[0, 90]°	†	[−535, 535] cm	
Neutron	5	N/A	10	10	10	3350
Wall Alpha	N/A	10+2††	10	5	10	4200
Wire Alpha	N/A	10	10	5	10	3500

The overall size of each library is determined by the need to cover all possible pulse shapes and the fact that the average fit time grows linearly with library size. The first version of the libraries was generated with roughly half as many pulses are in the final libraries. Monte Carlo neutron and alpha data sets were fit with the neutron and alpha pulse libraries. By hand scanning the fit results refinements were made in the grid-point spacings to produce the libraries used in this analysis. As an example, the initial libraries had too few grid points in z. The result was that sharp pulses, where the reflection peaks

[1]From the perspective of what causes different pulse shapes, the exact origin of an alpha particle in the nickel or copper does not matter; the relevant details are the energy and radius where the particle enters the gas.

are distinct, did not fit well. This problem was solved by doubling the number of z grid points. The various details of selecting the grid points shown in Table 6.1 are discussed below.

There are two "types" of energies relevant to the alpha grid. Each alpha particle starts with a particular initial energy. Some of that energy can be lost without contributing to the pulse (e.g. if the alpha reenters the wall or if the gas gain is reduced by space charge effects). The measured energy of the pulse is the shaper energy. The grid points are defined by the initial alpha energy, but the selection of events for the library is based on shaper energy.

Selecting alpha pulses within a specified shaper-energy range is somewhat complicated. The energy cutoff for this analysis is 1.0 MeV. All of the neutrons fall below that energy, but the highest-energy alphas in the uranium and thorium decay chains extend above 8 MeV. It is possible that, due to inaccuracies in the MC, there are pulse shapes that, in reality, have shaper energies just below 1.0 MeV, but are simulated with shaper energies just above that cutoff. To be sure that all alpha shapes are included in the library the maximum shaper energy for the alpha library pulses being simulated is 1.2 MeV. Pulses above that cutoff are discarded. This measure is particularly important since the 1.0-MeV cutoff falls close to the alpha Bragg peak where small changes in initial alpha energy can result in significantly different pulse shapes.

The space-charge effect can reduce the measured energy of a pulse below the actual initial energy of the alpha particle. This affects pulses up to 2.0 MeV. A 2.0 MeV alpha traveling radially towards the anode will result in a pulse with an energy around 1.2 MeV, so 2.0 MeV was selected as the maximum initial energy for the alpha library grids.

High initial-energy alphas can also result in lower shaper-energy pulses by reentering the wall soon after being emitted and therefore only depositing some of their energy in the gas. The majority of the high-energy alphas are from the decay of ^{210}Po and have an energy of 5.3 MeV. Therefore 5.3 MeV and 3.65 MeV alphas were added to the wall alpha library to sample these pulse shapes, but only in cases where they resulted in a pulse with a shaper energy below 1.2 MeV. This energy-reduction mechanism does not apply to wire alphas since the wall is too far away. The highest-energy alphas, starting at 8.8 MeV, traveling

radially away from the anode (and therefore subject to the maximum space-charge effect) will hit the wall and result in a pulse with a measured energy around 1.4 MeV.

To accommodate the spherical phase space represented by θ and ϕ the number of grid points in the ϕ dimension was varied as a function of θ:

$$N_\phi = \text{integer}[(N_{\phi-\max} - 1)\sin\theta + 1]. \tag{6.1}$$

The spacing of the grid points as a function of θ was kept constant. For $\theta = 0°$ there is only one point along ϕ, but for $\theta = 90°$, along the equator of the spherical phase space, $N_\phi = N_{\phi-\max}$.

Different ranges for ϕ apply to the different libraries.[2] For all libraries the negative ϕ range produces pulse shapes that are redundant with the positive ϕ range. For neutrons, ϕ varies from 1° to 179°. For wall alphas ϕ ranges from 0° to 85°, since the alpha tracks need to point into the gas and alphas that travel only very short distances in the gas will not deposit enough energy. For wire alphas the ϕ range is from 91° to 180° to avoid directing the alpha into the anode.[3]

z coordinates were only changed from the even grid spacing on the few occasions when the ion track would be created in an endcap or dead volume. Instead of modifying the geometry the track was moved a few centimeters to put it in the live volume. Since the speed of propagation in the counters is approximately 25 cm/ns, the separation of the direct and reflected pulses changes by less than a single 1-ns bin.

The number of pulses that end up in each MC library can be different than the number of pulses simulated because either too little energy was deposited to create a pulse, or the maximum energy of 1.2 MeV was exceeded. Table 6.2 gives the number of pulses in each library after all cuts are applied.

Two modified versions of SNOMAN were used to produce the library pulses, one for neutrons and one for alphas. All of the code modifications are listed in Appendix E, though

[2]Figure 4.3 might be helpful for interpreting ϕ for the different types of tracks.

[3]An alpha that passes through a slice of the anode wire enters the gas with less than its initial energy, and produce a pulse that looks just like an alpha starting on the surface with a lower initial energy.

Table 6.2: The final number of pulses in each MC-generated library.

Neutrons	Alphas	Wire Alphas
3329	2974	2599

the primary modifications are discussed here. One of the modifications was common between the two versions. During normal operation of the NCD Monte Carlo pulses are rounded off as integers and packed into arrays that are smaller than would be required to store a 16- or 32-bit floating-point number for each of the 15,000 bins. The real data is passed through an ADC, so this data-packing solution is an efficient way of storing the pulses. For pulse fitting, however, library pulses should be "ideal" pulses, without noise or digitization. A pulse whose bin values have been rounded off and stored as integers is therefore unacceptable for the purpose of creating a pulse library. Fortunately SNOMAN includes an optional "Ntuple Histogram Producer" (NHP) processor that could output pulse histograms at multiple stages of the simulation.[4] The output of the NHP is a pulse stored as a histogram with floating-point, non-"digitized" bin contents. With a few code modifications the NCD MC and NHP were modified to output delogged pulses without digitization, with histogram names that would facilitate the matching of the pulse histograms with the corresponding event in the standard Monte Carlo data structure.

The SNOMAN modifications that were specific to the neutron and alpha versions were responsible for reading in the simulation phase-space coordinates for each pulse from an external text file. The neutron version read in a file that gave values for r, θ, ϕ, and z, while the alpha version read in a file that gave values for E, θ, ϕ, and z. These files were read in prior to simulating the events and the grid points were stored in arrays that were accessed for every Monte Carlo event.

Pulse libraries consist of a ROOT TTree object whose branch structure is described by the QCPulse2 QSNO class. A QCPulse2 object is filled with information about each library

[4]The original purpose of the NHP was to be able to look at simulated pulses easily before more standard tools had been developed for use during the NCD phase.

pulse. Most of the information is extracted from the QTree and MCEvent data structures. The information taken from the QTree includes the event number, trigger ID number, time and date, string number, and shaper energy. The MCEvent tree provides the string position, shaper energy, track position and orientation, energy deposited, and particle identification. The pulse itself is extracted from the NHP file.

6.2 Pulse Fitting

The philosophy behind the Monte Carlo pulse fitter is to determine whether each data pulse fits better within the class of pulse shapes that can be assumed by neutron captures or the class of pulse shapes that can be assumed by alphas. A fit is performed by fitting a single data file with a single library. Each NCD pulse is extracted from the data and compared to every pulse in the library.

The quality of each fit is determined by a Pearson's χ^2 test. The library pulse that has the smallest χ^2 per degree of freedom (dof) when compared to the data pulse is the best fit to the data.

The fit region on a pulse extends from the rising edge to midway down the falling tail. Specifically, the fit region calculated for every pulse being fit is determined by finding where the pulse amplitude drops to some fraction of the peak amplitude on the rising and falling edges. The tail of every neutron-capture and alpha pulse quickly becomes dominated by the characteristic ion-drift shape. On the other hand, the rising edge of each pulse contains important information about the pulse structure. As a result, the left (rising) and right (falling) edges of the pulse are treated differently. The left edge of the fit region is the point at which the pulse crosses 10% of its peak value. 10% of the peak amplitude is typically above the baseline noise, even for low pulses, and almost the entire rise of the pulse is included in the fit region. The right edge of the fit region is the point at which the pulse crosses 30% of its peak value. A larger percentage is chosen for the falling edge than the rising edge to avoid most of the ion-drift tail, which is almost the same for every pulse and would therefore make the χ^2 parameter less effective in separating pulse shapes. Neutron-capture pulses with a clear two-peak structure can sometimes drop below 40% of the pulse amplitude between the two peaks due to noise fluctuations, which could place the right edge

of the fit region in the middle of the pulse. Based on tests with the ^{24}Na calibration data, when using a 30% threshold all neutrons are fully contained within the analysis window. Noise is, of course, a factor when finding pulse edges by this amplitude method. The effect of the noise is reduced by using a 5-bin-wide window average to calculate the pulse amplitude (Note: when the pulses are actually fit no averaging or rebinning is used).

The variance used in the χ^2 calculation is also determined for each pulse. There are four sources of variance that can contribute to the difference between a MC library pulse and a data pulse:

- Electronic noise: Various parts of the electronics contribute to the background noise on a pulse. The exact frequency spectrum of that noise depends on the bandwidths of downstream electronics components, but it can be approximated by taking the RMS of the tail of a pulse about the mean value. In particular, bins 11000 to 14999 are used. This contribution to the variance is the largest of the four.

- Digitization: When the pulse is digitized some uncertainty is added to every bin because each digitized value could represent a range of actual values. The non-voltage-dependent portion of the digitization variance is already accounted for by taking the RMS of the tail of the pulse. The voltage-dependent portion is calculated separately.

- Library sparseness: Since the MC libraries are created on grids in the pulse parameter spaces before any fitting is performed, they represent a selection of the available pulse shapes. Differences between the MC library pulse and the actual track parameters of the pulse being fit will add to the variance.

- MC imperfections: Since the MC is not perfect, even if an MC pulse is created with the exact same track parameters as a real pulse there will still be differences between the two pulses because the MC is not an exact model.

The contribution to the variance depends on the size of a single step in the digitizer, Δ:

$$\sigma_D^2 = \frac{\Delta^2}{12}. \tag{6.2}$$

This factor, known as "Sheppard's Correction," [113] is the correction that would need to be applied to determine the true width of a Gaussian peak in a spectrum that has been binned. According to [114] it is an approximation that is accurate to better than 2.5% if $\Delta \leq 2\sigma$. For an NCD pulse, $\sigma \sim 6 \times 10^{-4}$ V, while Δ ranges from around 1×10^{-4} V in the tail of a pulse to 3×10^{-4} V at the peak of a large pulse. The condition to use Sheppard's Correction is therefore satisfied.

The logarithmic amplification of the NCD pulses makes Δ voltage dependent. It is also dependent on the characteristics of the logarithmic amplifiers that go into the analytic description of the amplification, Equation 4.5. Taking the log-amplified pulse minus the baselines, $V_0(t) \equiv V_{\log}(t) - c_{\text{chan}} - V_{\text{PreTrig}}$,

$$V_0(t) = a \log_{10}\left(1 + \frac{V_{\text{lin}}(t - \Delta t)}{b}\right). \tag{6.3}$$

A change of input voltage by Δ results in a change of V_0 by 1 digitization unit:

$$\begin{aligned} V_0(t) + 1 &= a \log_{10}\left(1 + \frac{V_{\text{lin}}(t - \Delta t) + \Delta}{b}\right) && (6.4) \\ 1 &= a\left[\log_{10}\left(1 + \frac{V_{\text{lin}}(t - \Delta t) + \Delta}{b}\right) - \log_{10}\left(1 + \frac{V_{\text{lin}}(t - \Delta t)}{b}\right)\right] \\ &= a \log_{10}\left(\frac{V_{\text{lin}}(t - \Delta t) + \Delta + b}{V_{\text{lin}}(t - \Delta t) + b}\right). && (6.5) \end{aligned}$$

Equation 6.5 can be solved for Δ in terms of the linear voltage and the parameters describing the logarithmic amplifier:

$$\begin{aligned} \frac{\Delta}{V_{\text{lin}}(t - \Delta t) + b} &= \exp\left(\frac{1}{a \log_{10} e}\right) - 1 && (6.6) \\ &\approx \frac{1}{a \log_{10} e} \\ \Delta &\approx \frac{V_{\text{lin}}(t - \Delta t) + b}{a \log_{10} e}. && (6.7) \end{aligned}$$

The contribution to the variance due to digitization is therefore:

$$\sigma_D^2 = \frac{1}{12}\left(\frac{V_{\text{lin}}(t - \Delta t) + b}{a \log_{10} e}\right)^2. \tag{6.8}$$

Equation 6.8 can be expanded and separated into two voltage-dependent terms, and a voltage-independent term. The latter is a part of the variance that is calculated by taking the RMS of the noise in the tail of each pulse. The voltage-dependent component of the digitization variance turns out to be a relatively small contribution to the total variance. It is an order of magnitude smaller than the voltage-independent variance (including the electronics and part of the digitization), for pulses with large amplitudes (and therefore the largest digitization variance).

Unfortunately there is no well-defined method for quantifying the contributions to the variance from the sparseness of the libraries or the imperfections in the MC. However, the mean reduced χ^2 from fitting MC and calibration neutrons should reveal how much variance is being added by each. If the libraries perfectly described the data one would expect $\chi^2/dof = 1$. When fitting a data set of neutron MC with the mean neutron library χ^2/dof is 1.16. The sparseness of the neutron library therefore contributes a 16% increase in the reduced χ^2. When fitting a data set ^{24}Na calibration neutrons with the neutron library the mean χ^2/dof is 1.26. The MC imperfections therefore contribute a 9% increase on top of the sparseness contribution. These contributions were not pursued because it was not apparent that it would result in any significant improvement to the analysis.

An energy term of the form $(E-E_{\text{fit}})^2/V[E]$ is also added to the χ^2 statistic to take into account the difference in energy between the MC pulse and the pulse being fit. The variance for the energy term is set by the alpha-library energy spacing, ΔE_α: $V[E] \equiv (\Delta E_\alpha/2)^2$. This has a small effect on the total χ^2 when the difference between the energies is small, particularly since the number of bins in each pulse's fit region is large.

During the fitting of a single library pulse to a single data pulse the horizontal shift between the pulses is also determined by χ^2 minimization. The MINUIT minimization package [115] is used (via the TMinuit class in ROOT [71]) to find the best shift. The MINUIT minimization process involves testing different shifts between the library pulse and the pulse being fit. The fit boundaries are calculated at each shift. The left boundary of the fit is determined by whichever is furthest right, the first bin of the library pulse or the left edge of the data pulse. The right boundary of the fit is determined by whichever is furthest left, the last bin of the library pulse or the right edge of the data pulse. In almost

all cases the fit takes place between the left and right edges of the data pulse. The library pulse is allowed to extend beyond the fit region to account for data pulses that were cut off (e.g. if the track starts or ends in the endcap region).

Library pulses are scaled such that the integral of the library pulse that overlaps with the fit region of the data pulse is the same as the integral of the data pulse in the fit region. This procedure helps account for the sparseness of the libraries and fixes any systematic normalization difference between the MC and the real data.

Figure 6.1 shows an example of Monte Carlo neutron pulse fit with both the neutron library and the alpha library, accompanied by the respective fit residual. Figure 6.2 shows a fit of an alpha Monte Carlo pulse with the neutron and alpha libraries. The neutron pulse selected is fit well with the neutron library ($\chi^2/dof = 0.58$, with approximately 1070 degrees of freedom) and fairly well with the alpha library ($\chi^2/dof = 0.97$). Qualitatively, it is clear that the fit with the neutron library better represents the overall structure of the pulse.

The neutron and alpha pulse libraries were shown to cover the pulse-shape parameter space sufficiently by using them to fit Monte Carlo neutron and alpha data sets. Figures 6.3a and 6.3d show the χ^2 distributions for the Monte Carlo neutron data set fit with the neutron library and for the Monte Carlo alpha data set fit with the alpha library, respectively. The alpha histogram has a sharper peak than the neutron histogram because the neutron pulse-shape phase space is larger than that of the alphas (i.e. there is a larger variety of neutron pulse shapes). However, the fact that neither distribution has a large tail extending to high χ^2 qualitatively suggests that both libraries adequately cover their respective pulse-shape phase spaces. Fits with previous incarnations of the libraries had larger tails extending to higher values of χ^2. By hand-scanning the fits in those tails certain deficiencies in the libraries were identified and corrected (e.g. one earlier set of libraries had grid points spaced too widely on the z axis, resulting in bad fits for narrow pulses). The highest-χ^2 fits when using these libraries do not point to any particular library deficiencies.

It is also important to use the libraries to fit actual data and compare the results to the fits of the Monte Carlo data set. The ^{24}Na data set can be used to test the neutron fit, and the ^{4}He-string data set can be used to test the alpha fit. The neutron-fit comparison is

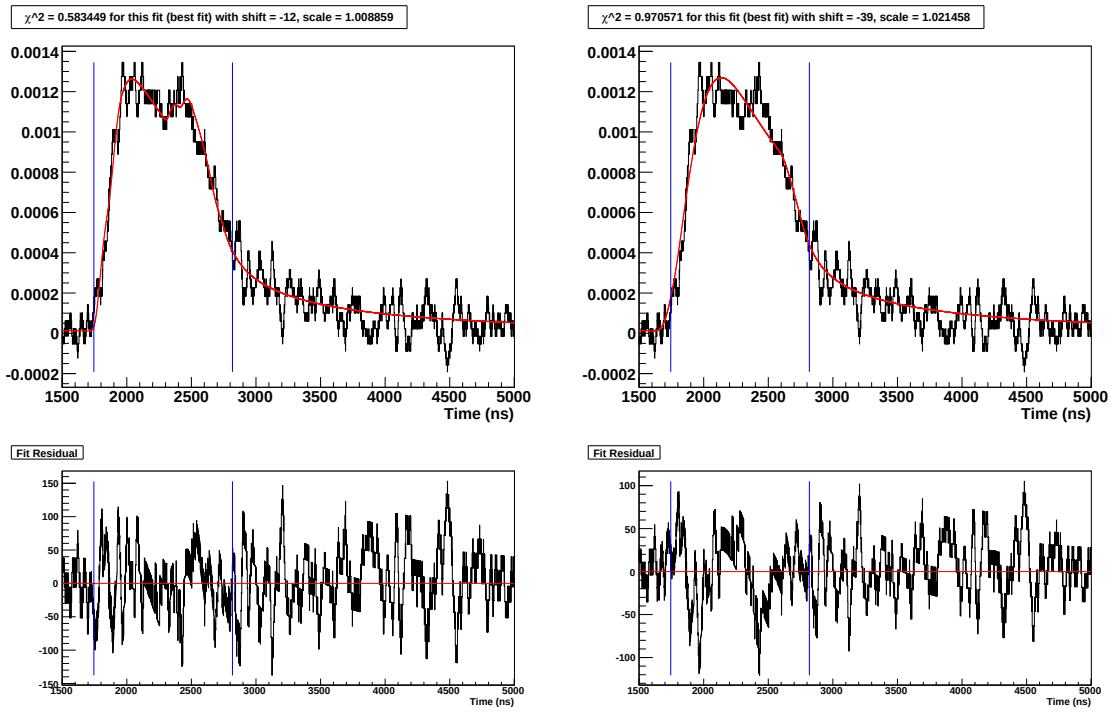

(a) (b)

Figure 6.1: An example of a Monte Carlo neutron pulse fit with the neutron library (a), and the same pulse fit with the alpha library (b). The vertical blue lines indicate the fit region, in which the χ^2 was calculated. The χ^2 in (b) is larger than in (a), though this example serves to show how a neutron pulse (even one that is not extremely narrow) can still be fit fairly well with the alpha library. The numbers given in the plot title for shift and scale are how the library pulse was shifted horizontally and scaled vertically to fit the Monte Carlo pulse.

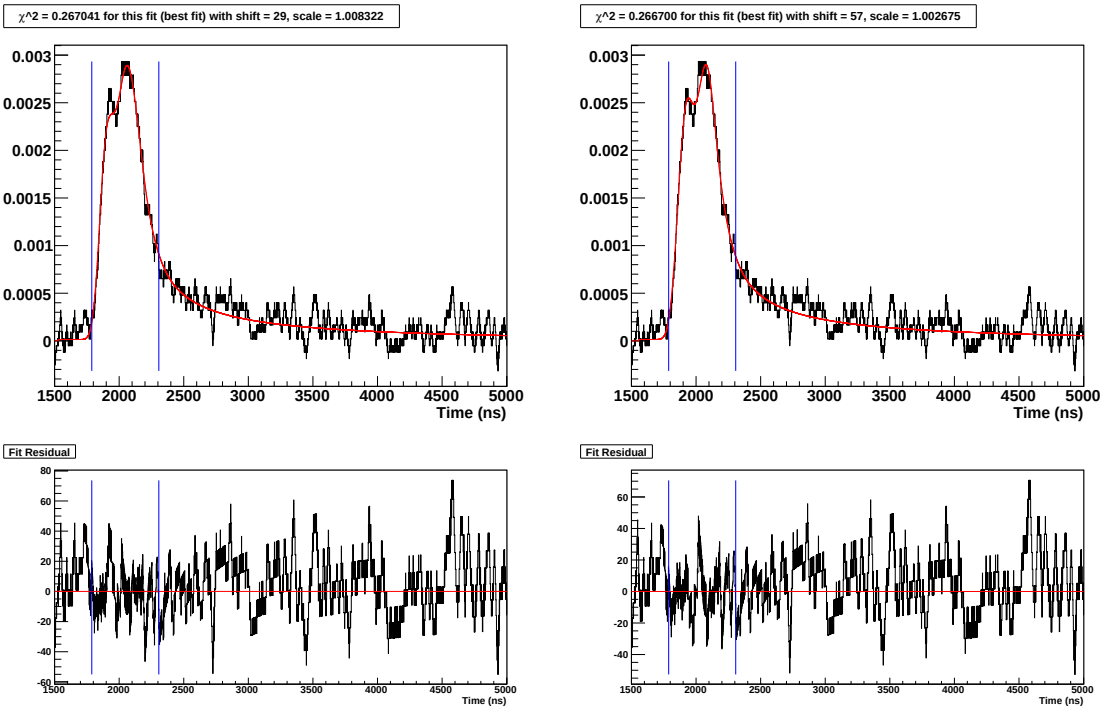

(a) (b)

Figure 6.2: An example of a Monte Carlo alpha pulse fit with the neutron library (a), and the same pulse fit with the alpha library (b). The vertical blue lines indicate the fit region, in which the χ^2 was calculated. Alphas tend to be fit well with both the neutron and alpha libraries, as is the case with this example. The numbers given in the plot title for shift and scale are how the library pulse was shifted horizontally and scaled vertically to fit the Monte Carlo pulse.

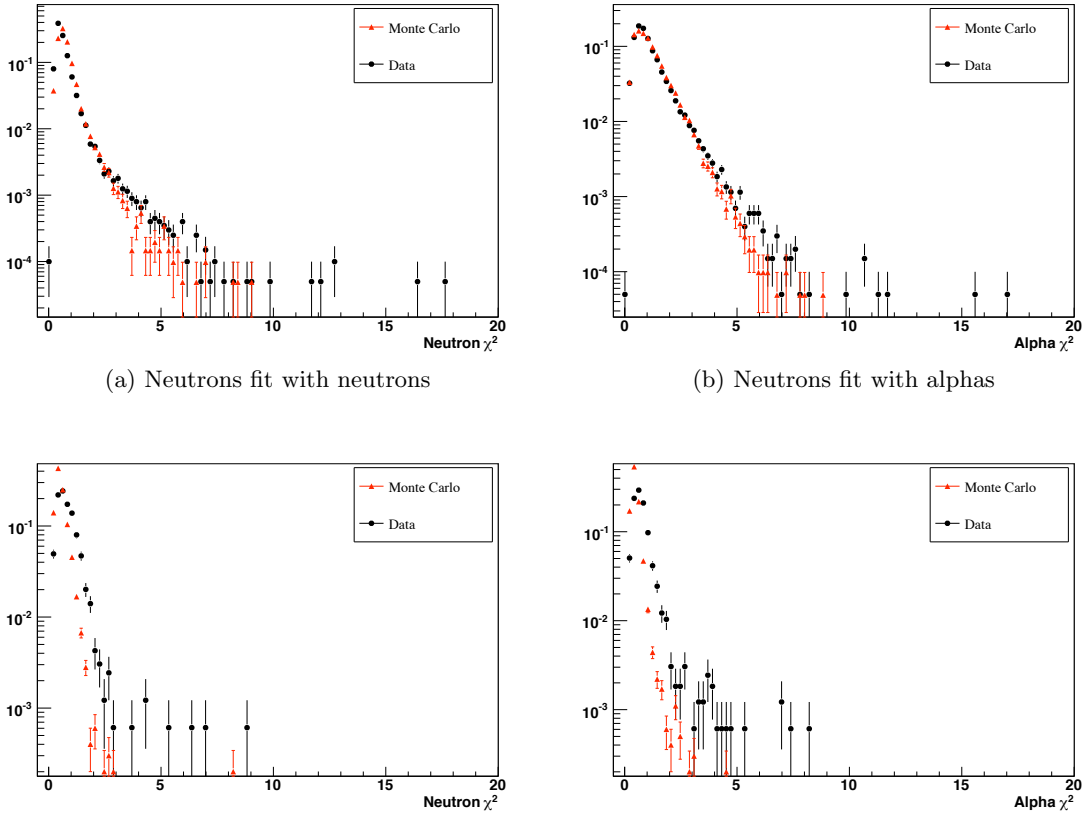

(a) Neutrons fit with neutrons

(b) Neutrons fit with alphas

(c) Alphas fit with neutrons

(d) Alphas fit with alphas

Figure 6.3: The χ^2/dof distributions for fitting both simulated and real neutron and alpha data sets. The top row of plots are the neutron data sets, and the bottom row are the alpha data sets. The left column of plots are data sets fit with the neutron library, and the right column are the data sets fit with the alpha library. The low χ^2 values in (a) and (d) show that the libraries adequately cover the pulse-shape phase space. The neutron data sets show excellent agreement between data and Monte Carlo, though there are still systematic differences. The extended tail in (a) is most likely due to the sparseness of the neutron library. The alpha data sets show larger systematic differences between the Monte Carlo and data fits. Some of these differences are likely due to the presence of wire alphas in the ^{4}He data and different mixtures of ^{210}Po and bulk alphas.

more powerful than the alpha-fit comparison for understanding data-MC differences in the fit results because the neutron Monte Carlo is a direct simulation of the ^{24}Na data, while the various flavors of Monte Carlo alphas need to be combined in the proper ratios to make an accurate simulation of the ^{4}He alpha data set. It is, nonetheless, important to look at both fits. Figure 6.4 shows a pulse from the ^{24}Na data set and a pulse from the ^{4}He strings fit with the neutron and alpha libraries, respectively.

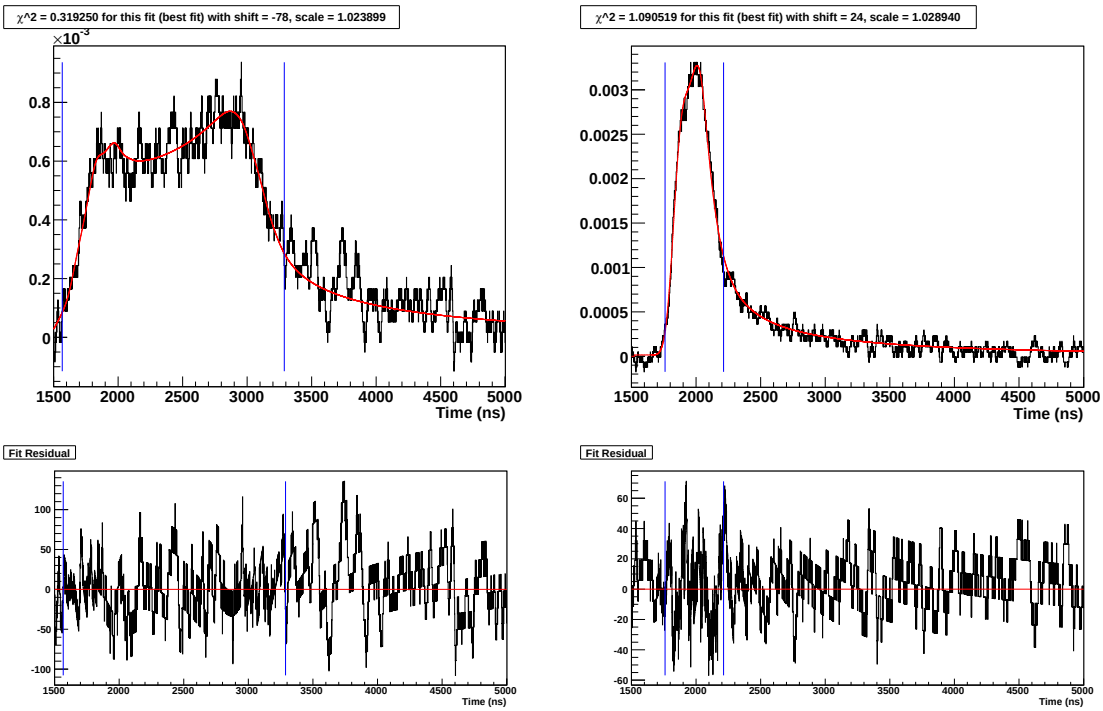

(a) (b)

Figure 6.4: (a) A pulse from the ^{24}Na data set fit with the neutron library and (b) a pulse from the ^{4}He strings fit with the alpha library. The blue lines indicate the fit region, in which the χ^2 was calculated. The numbers given in the plot title for shift and scale are how the library pulse was shifted horizontally and scaled vertically to fit the Monte Carlo pulse.

The χ^2 distributions comparing data to Monte Carlo are shown in Figure 6.3. The agreement is quite good for the neutrons, but not as good for the alphas. In both cases there are definitely systematic differences where the differences between Monte Carlo and

data exceed the expectations from the statistical errors. The data/Monte Carlo differences could contribute a systematic error to the neutron/alpha separation analysis and will be discussed in the next chapter.

Chapter 7

NCD-ONLY NEUTRAL CURRENT FLUX

Previous pulse-shape-analysis (PSA) methods developed for the NCD data (including the energy-spectrum fit) [65, 116, 117, 118] have all suffered from a common problem: it is difficult to accurately characterize the alphas. Characterizing the neutrons is easier, since there is only one category of neutron events and extensive neutron calibrations were conducted throughout the NCD phase. One can use that calibration or a Monte Carlo data set to make a PDF to represent neutrons in whichever parameter space is being analyzed.

While there were no alpha calibrations, the ^{4}He strings do provide a source of alpha events. The problem with using those events to characterize all of the NCD alpha events is that, for three primary reasons, the ^{4}He strings and the alpha events they produce are not necessarily representative of the ^{3}He strings and their alpha events in every way:

- The statistics of the ^{4}He-string data are limited; the number of events in that data set is smaller than the number of alphas in the NCD neutrino data set.

- There are multiple categories of alpha events: ^{210}Po and bulk alphas from the wall, and ^{210}Po alphas from the wire. The contribution to the total background of each category of alpha events varies from string to string, and will be different between the ^{4}He strings and the ^{3}He strings.

- The gains on the ^{4}He strings are less well known than those of the ^{3}He strings.

To generate an alpha PDF in any particular parameter space one should have many more events than are in the actual data, and one must understand all of the various alpha contributions. For the energy-spectrum analysis the NCD Monte Carlo was used to generate large numbers of alpha events and the high-energy alphas were used to determine the contributions of bulk and ^{210}Po alphas [65]. However the uncertainty in our understanding of

the alpha energy spectrum was one of the largest contributions to the overall systematic uncertainty, and the very existence of a large alpha background added to the statistical uncertainty.

The alpha-related statistical and systematic uncertainties can be largely avoided by making a background-free cut in some parameter space. This strategy can potentially increase the statistical uncertainties, since it removes the neutron pulses that resemble alpha pulses, but it is offset by the removal of the uncertainties on the background events. It relies on an accurate understanding of the efficiency of the background-free cut, which is available through the use of the neutron calibrations. The alpha background remaining after the cut is a significant systematic uncertainty and must be made as small as possible without sacrificing too many neutrons.

To find the ideal cut one must balance the statistical and systematic uncertainties to find the smallest total uncertainty. A lower cut results in an improved statistical uncertainty because more events in the data are being kept,[1] but it also increases the contribution to the systematic uncertainty from the alpha background. A higher cut will increase the statistical uncertainty as more events are removed from the data, but decrease the systematic uncertainty because there are fewer background events remaining. The key is to find the ideal position where the total uncertainty is kept as small as possible.

One of the benefits of a background-free cut is its simplicity. At a basic level the total number of neutrons in the data, N_n, is determined by the number of events that pass the cut, P_{data}, the expected alpha contamination, P_α, and the neutron cut efficiency, ϵ_n:

$$N_n = \frac{(P_{data} - P_\alpha)}{\epsilon_n}. \tag{7.1}$$

The determination of these parameters and the various factors that complicate the analysis are discussed throughout the rest of this chapter.

---

[1] If the cut is low enough, the statistical uncertainty will worsen because the larger background makes the number of neutrons more uncertain.

7.1 Data Sets

The data set that is used for the final analysis is the full NCD-phase neutrino data set. It consists of data taken over 385.17 live days, from January 2005 to November 2006. An analysis of the full neutrino data set, however, will not appear in this thesis.

As with all SNO analyses, this analysis method has been developed with blindness measures implemented to avoid biasing the result. The blindness measures will be lifted once the entire SNO analysis is finalized for publication, which has not happened as of this writing. The final analysis in this thesis is therefore performed on the "one-third" data set, consisting of 1/3 of the full neutrino data set.[2] A fake data set with realistic statistics is also used to estimate the size of the uncertainties that will be achieved with the full neutrino data set.

Two ^{24}Na calibrations were performed during the NCD phase, one in 2005 and one in 2006. The latter has approximately three times the statistics of the former though both are used in the analysis. AmBe neutron calibrations are also essential; seven array-wide calibrations were performed during the NCD phase, and are used to look at time dependences. A central scan of ^{252}Cf runs is used to study the z-dependence of the background-free cut.

The ^{4}He strings provide a pure sample of alpha events over the course of the NCD phase. The statistics are somewhat limited, but they are the only source of real alpha events in the neutron energy region.

Monte Carlo data sets have also been created for both neutrons and alphas. These are full simulations intended to replicate the neutron and alpha data. Unlike the libraries discussed in the previous chapter, they include noise and the pulse shapes are properly distributed according to the random nature of the ion track formation. The neutron MC mimics the ^{24}Na calibration by simulating neutrons created isotropically throughout the D_2O volume. The MC alpha data sets include both surface ^{210}Po on the NCD walls and anode wires, and alphas produced in the bulk of the walls from the ^{232}Th and ^{238}U decay chains. All of these MC data sets were produced at approximately ten times the statistics

[2]The one-third data set was created by taking every third event on the ^{3}He strings.

expected in the neutrino data set.[3] The alpha MC was used to produce the energy-spectrum PDF that was used in [65]. As will be shown below, by fitting with MC pulse libraries this pulse-shape analysis is extremely sensitive to MC/data differences. It is sensitive enough that the MC is of limited use in determining either the alpha contamination or the neutron cut efficiency. Instead the MC data sets are used in several qualitative ways to develop and understand the analysis.

Eight of the NCD strings, including two ^{4}He strings, suffered from a variety of problems that prevented their use in the analysis [119]. These problems included loose connectors and gain changes from gas leaking into the dead volume between two counters. The problem strings were identified through a variety of analyses of the blind data during the NCD phase. Two of the ^{3}He strings detected significant numbers of instrumental backgrounds of unknown origin that were somewhat difficult to distinguish from neutron and alpha events. The strings were removed from the analysis. However, the background events found on these strings were characterized and used to search for similar contaminations on the other strings (see Section 7.10). For the neutron calibrations and the neutrino data set, only data from the thirty "good" ^{3}He strings are used. For the ^{4}He data set, only data from the two good ^{4}He strings are used. The same is true for MC data sets, since the "bad" strings were not calibrated consistently.

7.2 Neutron Capture Efficiency and Acceptance

Some fraction of the NC neutrons created in the D_2O are captured in the NCD counters and produce pulses, and not all of those pulses result in a usable event. All of these effects were measured carefully for the analysis in [65], and they are discussed in more detail in [120] and [121].

The capture efficiency of the NCD array was studied with a variety of neutron calibrations and the SNO Monte Carlo [121]. The total capture efficiency for NC neutrons is $\epsilon_{cap} = 0.211 \pm 0.007$.

The maximum event-acquisition rate of the shaper system is approximately 2 kHz, which

[3]The number of neutrons can be estimated based on the SSM prediction, and the number of alphas can be determined by looking at the alphas above the neutron energy region.

is far above the event rate in the neutrino data. However, the MUX and scope systems suffer dead-time limitations with data rates of a few Hz. Even at the typical sub-Hz rate of neutrino data there is a measurable effect on the array live time that can slightly affect the number of pulses that result in events. The "live fractions" for the MUX and scope systems are 0.9980 ± 0.0001 and 0.957 ± 0.004, respectively [120].

The first cut made on the data is a selection of the Shaper energy window. For the first NCD-phase analysis the minimum energy was chosen to be 0.4 MeV. This choice avoids complications in the low-energy tail of the energy spectra due to each string's MUX and shaper thresholds. The same low-energy threshold is used in this analysis. The maximum energy previously used was 1.4 MeV. The efficiency of the 0.4-MeV shaper-energy cut for neutrons was calculated with a maximum of 0.85 MeV [120]; the number of neutrons falling above 0.85 MeV is insignificant. That efficiency is 0.91170 ± 0.00014. For this analysis, a maximum energy of 0.82 MeV is used for reasons discussed in Section 7.4. A correction factor of 0.99662 ± 0.00041 is applied to the Shaper-energy cut efficiency.

The MUX system is triggered by pulse amplitude, rather than energy. This means that pulses can trigger the shaper system but not the MUX system, and vice versa. The number of pulses removed above 0.4 MeV is small, but non-negligible. Since analyses of the NCD data require paired MUX and shaper events, the MUX threshold efficiency is calculated after the shaper energy cut: 0.99491 ± 0.00031 [120].

Data cleaning cuts were applied to the real data, including both the NCD-phase neutrino data set and the calibrations. These cuts are described in [83]. They remove instrumental events such as electrical discharges and oscillatory noise, but a small fraction of the physics events will be incidentally cut. The efficiency of the data cleaning cuts for neutrons above 0.4 MeV is 0.99521 ± 0.00011 [120].

The various efficiencies are collected in Table 7.1. The shaper-energy cut and its correction, MUX threshold efficiency, and data-cleaning cuts are combined into the neutron acceptance: $\epsilon_{acc} = 0.859 \pm 0.004$ [120].

Table 7.1: The neutron capture efficiency and the total neutron acceptance. The latter includes the MUX and scope live fractions, the shaper energy cut efficiency, the MUX threshold efficiency, and the data-cleaning cut efficiency.

Efficiency	Value	Uncertainty	Reference
ϵ_{cap}	0.211	0.007	[121]
MUX Live Fraction	0.9980	0.0001	[120]
Scope Live Fraction	0.957	0.004	[120]
Shaper Energy Cut	0.91170	0.00014	[120]
Energy Cut Corr.	0.99662	0.00041	[120]
MUX Threshold	0.99491	0.00031	[120]
Data Cleaning	0.99521	0.00011	[120]
ϵ_{acc}	0.859	0.004	[120]

7.3 χ^2 Parameter Space

The neutron- and alpha-fit χ^2 distributions described in Chapter 6 form a two-dimensional parameter space where a subset of the neutron events are almost entirely free of contamination by alpha events. The neutron χ^2, or χ^2_n, is from the fit with the MC neutron library detailed in Section 6.1. The alpha χ^2, or χ^2_α, is from the fits with the MC wall alpha and MC wire alpha libraries also detailed in Section 6.1. The smallest χ^2 between the alpha libraries is χ^2_α.

The χ^2 parameter space is shown in Figure 7.1. The three MC data sets fit include ^{24}Na neutrons, thorium wall alphas, and polonium wire alphas.[4] The shapes of the alpha distributions indicate that most alpha events fit equally well as neutrons or alphas. The shape of the neutron distribution, on the other hand, indicates that there is a subset of neutrons that does not fit well as an alpha, and some neutrons that do fit well as alphas. As has been discussed previously, since the ionization track from a neutron capture consists of two particles it can result in a wide double-peaked pulse. There are no configurations of the alpha track that resemble this shape, so these neutron pulses will stand out from the alpha background.

[4]The actual fraction of alpha events that come from the wire is much smaller than is represented here.

Figure 7.2 shows the $\log(\chi^2_\alpha)$-versus-$\log(\chi^2_{\rm n})$ space for ^{24}Na calibrations, the ^{4}He-string data, and the total NCD-phase data set. The real neutron and alpha data confirm that there is a significant background-free region that can be used to determine the total number of neutrons.

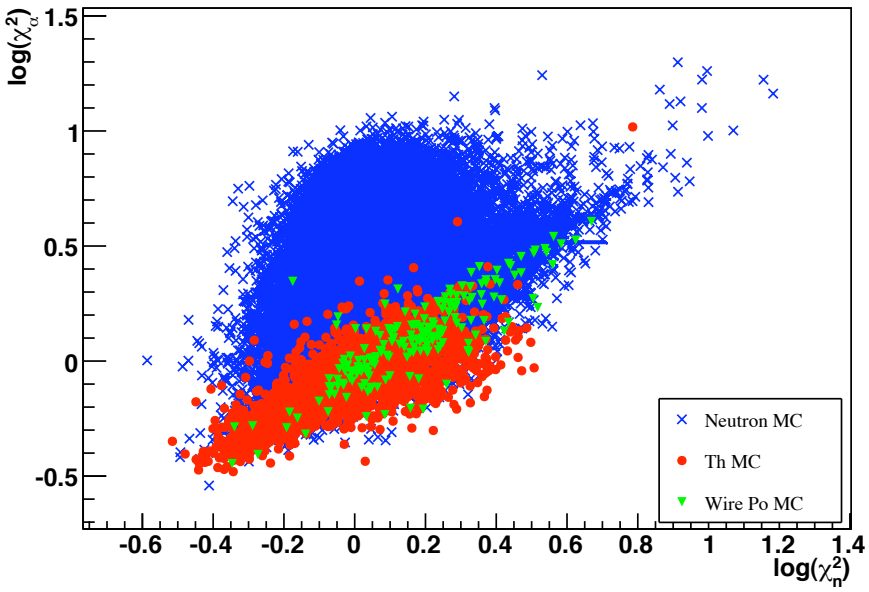

Figure 7.1: The $\log(\chi^2_\alpha)$-versus-$\log(\chi^2_{\rm n})$ distributions for neutron and alpha (thorium wall and ^{210}Po wire) MC data sets. There is a clear background-free region in the upper-left half of the plot that includes approximately 1/3 of the neutron events.

The $\log(\chi^2_\alpha)$-vs-$\log(\chi^2_{\rm n})$ distributions for alpha pulses are highly correlated, and the distributions for neutron pulses also includes a subset of events that are correlated. By rotating the $\log(\chi^2)$ space by 45° we create two linear combinations that are basically uncorrelated:

$$\Delta\log(\chi^2) \equiv \log(\chi^2_\alpha) - \log(\chi^2_{\rm n}), \tag{7.2a}$$

$$\Sigma\log(\chi^2) \equiv \log(\chi^2_\alpha) + \log(\chi^2_{\rm n}). \tag{7.2b}$$

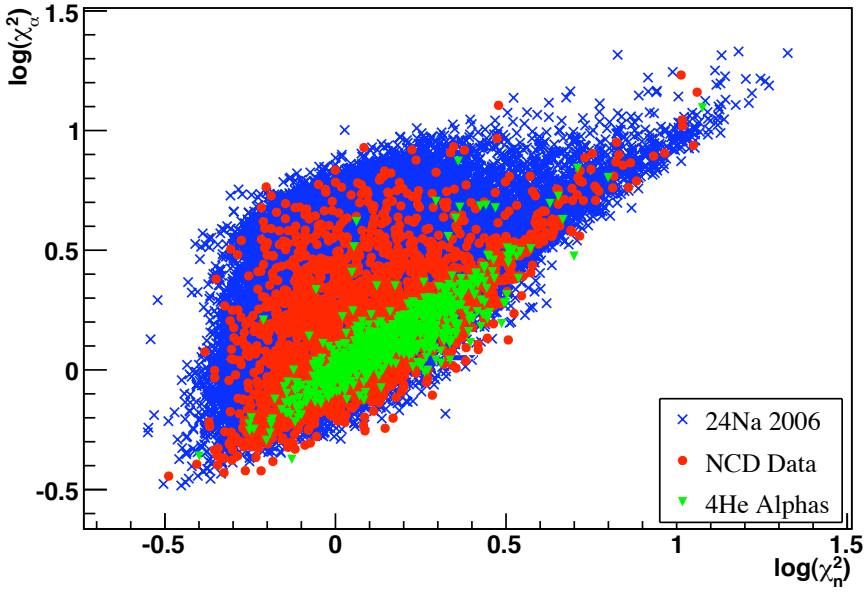

Figure 7.2: The $\log(\chi^2_\alpha)$-versus-$\log(\chi^2_n)$ distributions for the 2006 ^{24}Na calibration, the ^{4}He strings, and the full NCD-phase data set. The existence of the background-free region found with the simulated data is confirmed with real neutron and alpha pulses.

These two distributions for ^{24}Na neutrons and ^{4}He alphas are shown in Figure 7.3. $\Sigma\log(\chi^2)$, in Figure 7.3a, does not differentiate between the neutrons and alphas, while $\Delta\log(\chi^2)$, in Figure 7.3b, has a region where the alpha background is almost entirely removed, and a significant number of neutrons remain. A cut in $\Delta\log(\chi^2)$ is therefore used to separate neutrons and alphas without the complexity of a two-dimensional cut.[5] The exact position of the cut is determined by optimizing the total uncertainty. A cut value of $\Delta\log(\chi^2)>0.271$ is used throughout the development of the analysis prior to cut optimization. The neutron cut efficiency and alpha contamination of the $\Delta\log(\chi^2)$ cut are described in Sections 7.6 and 7.8, respectively.

[5] A two-dimensional cut was studied, but it was found that it did not add significantly to the statistics of the passing neutrons.

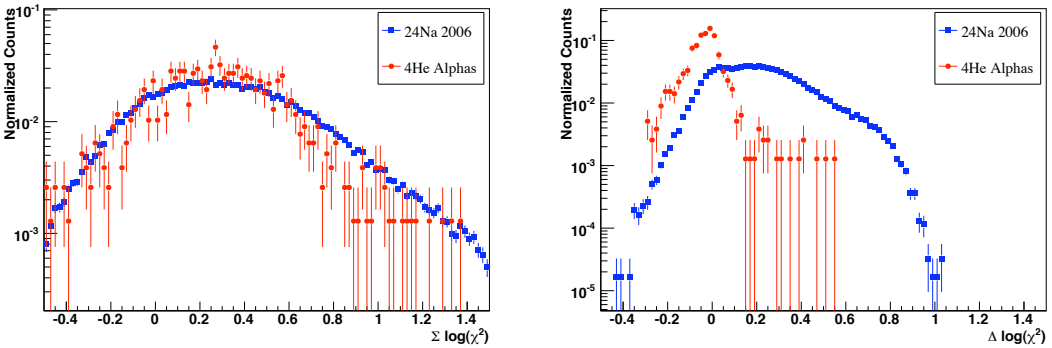

(a) $\Sigma \log(\chi^2)$ (b) $\Delta \log(\chi^2)$

Figure 7.3: (a) $\Sigma \log(\chi^2)$ and (b) $\Delta \log(\chi^2)$ distributions for ^{24}Na and ^{4}He alpha data sets. (a) has very little separation between neutrons and alphas, while (b) contains a region at high values of $\Delta \log(\chi^2)$ where there is little alpha background remaining under the signal.

7.4 Energy Dependence

Energy dependences of the neutron cut fraction and alpha contamination are expected because the pulse shapes of all classes of events change with energy. For the neutrons, events with the full 764 keV of energy detected have ionization tracks parallel to the anode wire, while events slightly lower in energy detected are due to perpendicular tracks that are more affected by space-charge effects. Events even lower in energy are a result of either the proton or triton hitting the wall of the NCD, and therefore not depositing their full kinetic energy in the gas. Events in which the proton and triton deposit their full kinetic energies in the gas and that have tracks that are not parallel to the anode wire have pulse shapes that are more easily distinguished from the alpha events. Figure 7.4 shows the energy dependence of the $\Delta \log(\chi^2)$ cut for ^{24}Na (2006) neutrons. As expected, events just below the neutron peak are concentrated at higher $\Delta \log(\chi^2)$, and therefore have a higher cut fraction compared to events right at the neutron peak or at lower energies.

The pulse shapes for alphas are fairly uniform across the energy range of the neutrons. However, the Bragg peak for alphas in the NCD gas lies just above 800 keV, and therefore the alpha pulse shapes above that energy have somewhat different pulse shapes than lower-

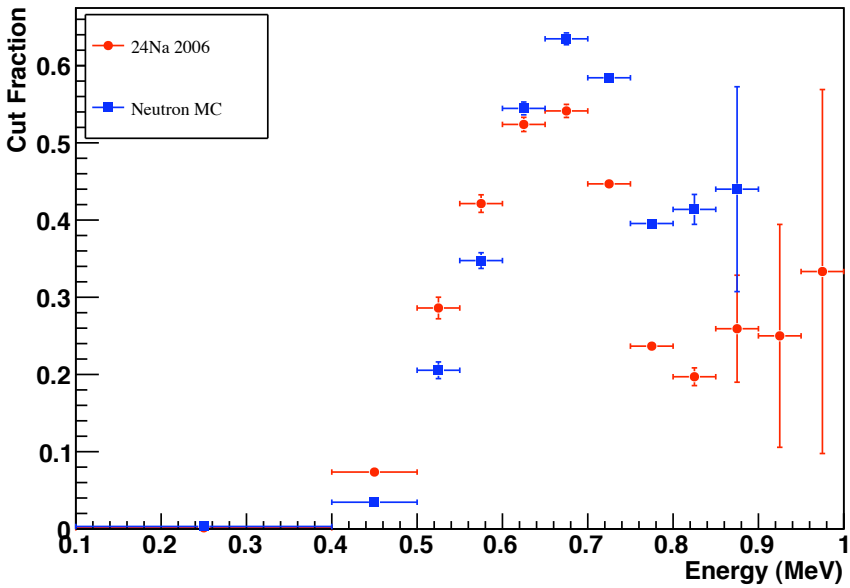

Figure 7.4: The energy dependence of a $\Delta \log(\chi^2) > 0.271$ cut for ^{24}Na and MC neutrons.

energy alpha pulses. The effect of the Bragg peak can be seen in Figure 7.5. The alpha contamination rises at higher energies, which indicates that alpha tracks that include the Bragg peak result in pulses that slightly-better resemble neutron pulses.

The energy dependences of the neutron cut fraction and alpha contamination are used to select an energy window for this analysis. The minimum energy is selected to be 0.4 MeV for three reasons: neutron pulses of lower energy are not easily distinguished from alpha pulses; the shaper thresholds for all strings are below 0.4 MeV and, for the most part, pulses with shaper energies above 0.4 MeV pass the MUX thresholds;[6] the previous analysis of the NCD data used a minimum energy of 0.4 MeV and included a full estimation of the various sources of background neutrons that can be used in this analysis to extract the number of NC neutrons from the total number of neutrons detected. The upper energy limit is selected to be 0.82 MeV because all of the neutrons fall below that energy, and the

[6]The MUX thresholds are cuts on pulse amplitude. However, 99.5% of pulses above 0.4 MeV are large enough that their amplitude passes the MUX threshold [120].

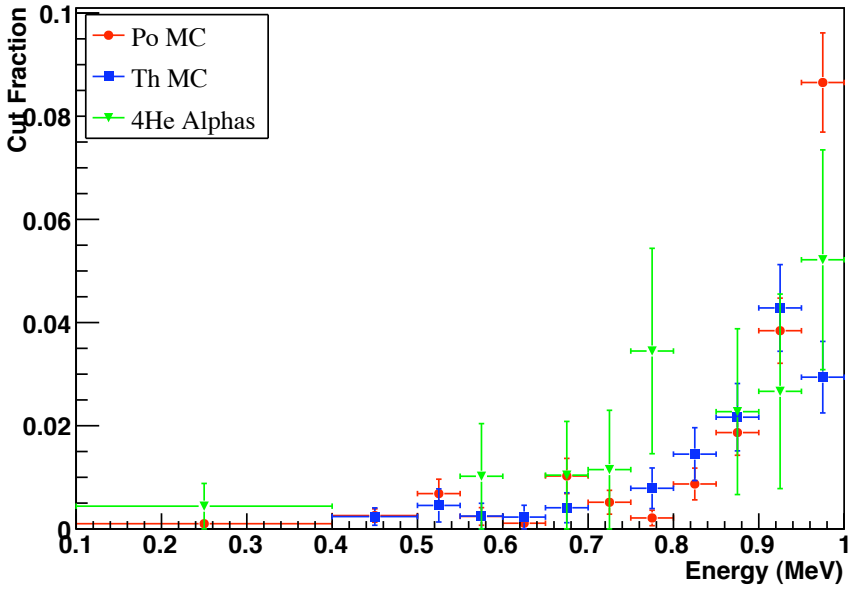

Figure 7.5: The energy dependence of a $\Delta \log(\chi^2) > 0.271$ cut for MC and ^{4}He alphas.

alpha contamination is still fairly small. The efficiency of a $0.4 < E < 0.85$ MeV cut is $\approx 0.91170 \pm 0.00014$ [120] (based on the ^{24}Na 2005 calibration). A correction of 0.99662 accounts for the difference between the 0.85 MeV and 0.82 MeV maximum energies. Any exceptions to the 0.4-0.82 MeV energy window will be noted.

7.5 MC/Data Comparisons

The extensive efforts that went into developing the NCD MC produced a simulation that replicated the alpha energy spectrum so well that it could be used in the energy fit of the first NCD analysis [65]. One could have also used the neutron energy spectrum in the fit as well, since the MC energy spectrum agreed well with that of the ^{24}Na calibrations. The primary advantage to using the MC to determine a PDF is that the statistics are only limited by the computation time available. Generally this means that the PDF can have a better statistical accuracy than a calibration. The disadvantage is that differences between data and MC can potentially be problematic.

The use of MC-generated pulse libraries to fit pulses will, by definition, highlight any differences between the MC and the data. A MC data set will be fit better by the library than a calibration data set because, besides the sparseness of the library and the random elements of the MC, there are essentially no differences between the pulses in the library and those in the MC data set. Because this analysis is so sensitive to MC/data differences (small as they may be), those differences are amplified such that the MC data sets cannot be used to determine the neutron cut efficiency or alpha contamination.

Figures 7.6a and 7.6b show the $\Sigma\log(\chi^2)$ and $\Delta\log(\chi^2)$ distributions for MC and ^{24}Na calibration neutrons. The agreement between MC and data is fair, qualitatively, as the distributions are showing the same general behavior. However, as a result of the sensitivity of this analysis to MC/data differences, the agreement is not good enough to use the MC $\Delta\log(\chi^2)$ distribution quantitatively in this analysis.

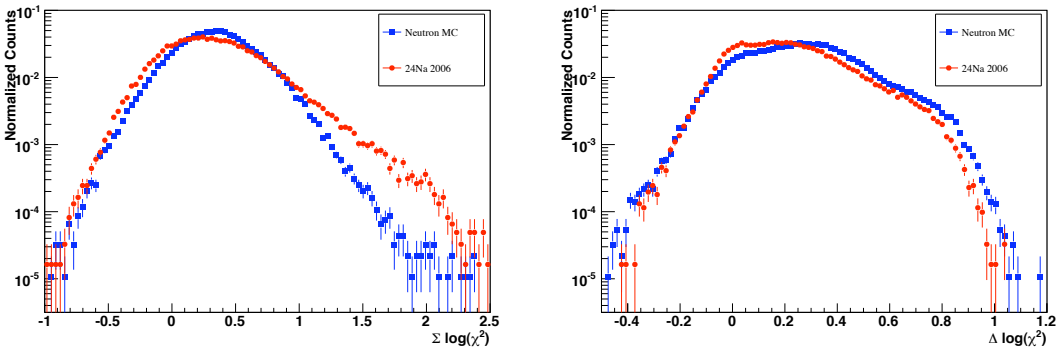

(a) $\Sigma\log(\chi^2)$ (b) $\Delta\log(\chi^2)$

Figure 7.6: The (a) $\Sigma\log(\chi^2)$ and (b) $\Delta\log(\chi^2)$ distributions for neutron events, including Monte Carlo and ^{24}Na calibration data.

The $\Sigma\log(\chi^2)$ and $\Delta\log(\chi^2)$ distributions for MC and ^{4}He alphas are shown in Figures 7.7a and 7.7b. The three distributions are all normalized in each plot. The most significant differences between the MC and ^{4}He data sets is in the $\Sigma\log(\chi^2)$ distributions. There is a systematic shift between data and MC. The $\Delta\log(\chi^2)$ agree reasonably well, qualitatively. Their falling edges at high $\Delta\log(\chi^2)$ coincide fairly well, while the behavior

of the ^{4}He alphas at low $\Delta\log(\chi^2)$ compared to that of the MC shows the presence of thorium alphas. The ^{4}He alphas have a larger tail extending to higher values of $\Delta\log(\chi^2)$ than the MC. This tail is thought to be due to wire alphas, as is discussed below. The MC alpha data sets will be used to a limited extent to understand the behavior of the alpha background in this analysis.

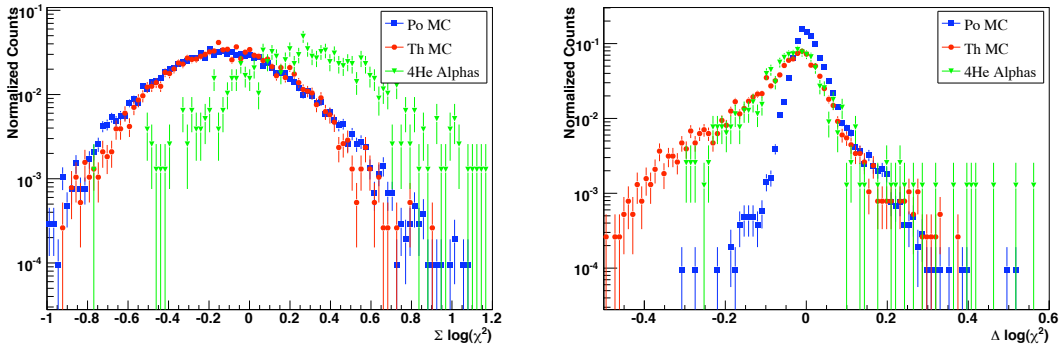

(a) $\Sigma\log(\chi^2)$ (b) $\Delta\log(\chi^2)$

Figure 7.7: The (a) $\Sigma\log(\chi^2)$ and (b) $\Delta\log(\chi^2)$ distributions for alpha events, including Monte Carlo (thorium and polonium) and data (^{4}He).

7.6 Basic Analysis

Calculating the number of NC neutrons, $N_{\rm NC}$, in a background-free analysis involves determining the number of total neutrons, and then subtracting off the background neutrons, $N_{\rm bkgnd}$:

$$N_{\rm NC} = \frac{P_{data} - P_\alpha}{\epsilon_n} - N_{\rm bkgnd}. \tag{7.3}$$

P_{data} is simply the number of events in the data set that pass the $\Delta\log(\chi^2)$ cut. The alpha contamination, P_α, is more complicated to determine. That portion of the analysis is addressed in Section 7.8.

The neutron cut efficiency, ϵ_n, is determined using the ^{24}Na calibrations. It is the number of events passing the cut, P_n, minus the small alpha contamination in the calibration,

$P_{\alpha,n}$, divided by the total number of neutrons minus the total alpha contamination in the calibration, $T_{\alpha,n}$:

$$\epsilon_n = \frac{P_n - P_{\alpha,n}}{T_n - T_{\alpha,n}}. \tag{7.4}$$

The 2005 ^{24}Na calibration collected approximately 20,000 neutron pulses, while the 2006 calibration collected approximately 74,000 events. Combined together there are approximately 10 times the number of events below 1 MeV than in the full NCD-phase data set. However, the calibrations are used independently to provide a method of verifying the cut efficiency results. The statistics of either calibration are sufficient to determine the neutron cut efficiency accurately.

The total alpha contamination in the ^{24}Na calibration data is miniscule, but easily estimated with the number of alpha events immediately above the neutron energy region and the alpha energy spectrum from MC. Between 0.4 and 0.82 MeV $T_{\alpha,n}$ is approximately 17.9 alphas in the 2005 calibration and 25.5 alphas in the 2006 calibration. With the typical cuts used in this analysis $P_{\alpha,n}$ is less than one event, which results in a negligible change in ϵ_n, and is therefore it can be ignored. The contribution of either contamination to the uncertainty on the neutron cut efficiency is small enough that it can be ignored.

The sources of neutron backgrounds are discussed in Chapter 3. N_{bkgnd} is the sum of the neutron background components, N_{K2} and N_{K5} (the neutrons produced by the K2 and K5 hot-spot radioactivity), N_{ext} (external neutrons), N_{NCD} and N_{cable} (the neutrons produced by radioactivity in the NCD bulk and cables), N_{D_2O} (neutrons produced by radioactivity in the D_2O), and N_{atmos} (atmospheric neutrons). The measured neutron backgrounds in the neutrino data, and their associated uncertainties, are given in Table 7.2. For the one-third data analysis, the backgrounds are divided by three, and their uncertainties by $\sqrt{3}$.

7.7 String Dependence

Naively one would expect the $\Delta\log(\chi^2)$ distributions from all strings to be the same. That is, a "good" string should produce the same pulse shapes as any other good string. If something is different about a string, such as its gain or electronics parameters, the pulse shapes can be subtly different. Therefore string-to-string differences in the $\Delta\log(\chi^2)$ distributions for

Table 7.2: Measured neutron backgrounds in the neutrino data. This table is adapted from [77].

Parameter	Value	Uncertainty
N_{ext}	40.9	20.6
N_{D_2O}	31.0	4.7
N_{NCD}	27.6	11.0
N_{K2}	32.8	5.3
N_{K5}	31.6	3.7
N_{cable}	8.0	5.2
N_{atmos}	13.6	2.7
Total	185.5	25.4

each string are a powerful indicator of systematic effects in the analysis. Figure 7.8 shows the $\Delta\log(\chi^2)$ distributions for every string, colored by MUX box. There is obviously a significant amount of variation between the strings. Strings on MUX box 0, in particular (black lines), produce pulses that are significantly different from the strings on the other MUX boxes. This latter observation is not entirely a surprise because MUX box 0 had a slightly different hardware configuration than the other three boxes (specifically, a resistor in MUX box 0 was different, which led to a shift in the voltage offset [76].

In general string variations would not be a problem, since they could be measured with the neutron calibrations and accounted for in calculating the average neutron cut efficiency. However, since the alpha contamination is estimated with the ^{4}He strings (see Section 7.8), if there are $\Delta\log(\chi^2)$ variations between the strings then the ^{4}He-string data will not correctly predict the contamination on the ^{3}He strings. Therefore having a uniformity of the $\Delta\log(\chi^2)$ distributions across the entire array is necessary for a successful analysis.

The string variations can be compared more quantitatively by looking at the means and standard deviations of the $\Delta\log(\chi^2)$ distributions as a function of string. These are shown in Figures 7.9 and 7.10. Two histograms are plotted in each figure: the 2006 ^{24}Na calibration and MC neutrons. The large variations in the MC neutron and ^{24}Na calibration data sets are unexpected. They indicate that there is something having a significant effect on the $\Delta\log(\chi^2)$ distributions. Furthermore, the string-to-string variations in the MC neutron

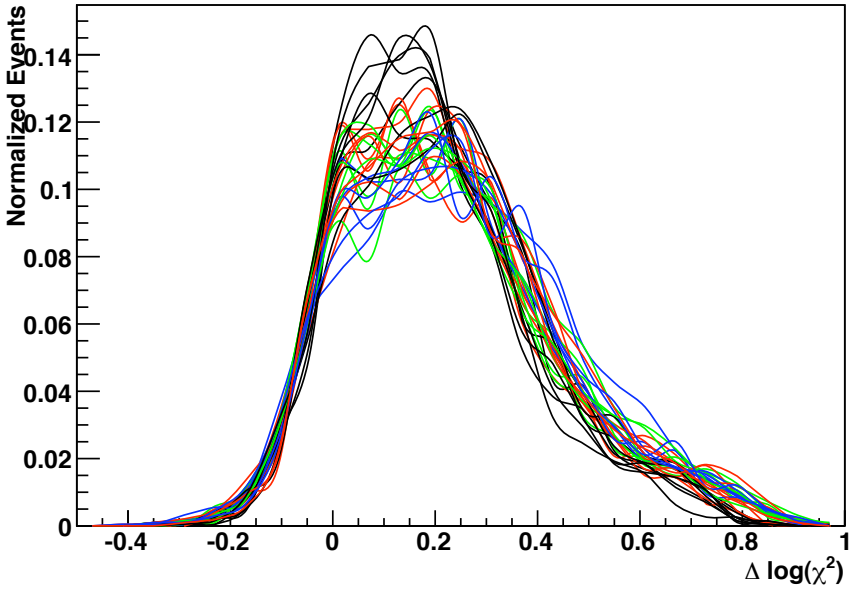

Figure 7.8: The $\Delta \log(\chi^2)$ distribution for each string. The coloring is by MUX box, with black = box 0, red = box 1, green = box 2, blue = box 3.

data set are different from those in the ^{24}Na data set. This is a further demonstration of the inability to use the MC to quantitatively understand the $\Delta \log(\chi^2)$ distributions in the data.

An extensive search for the cause of the string-to-string differences was conducted. The goal was to find the cause of the variations and devise a method to normalize the distributions across the array. All conceivable string-dependent parameters were compared to the $\Delta \log(\chi^2)$ means and standard deviations to search for correlations within the ^{24}Na data sets. No definitive causes were found. However, the search for string-to-string variations and other systematics in general did result in the discovery of the z dependence discussed in Section 7.9, and a generally-improved understanding of the array's pulse-shape characteristics.

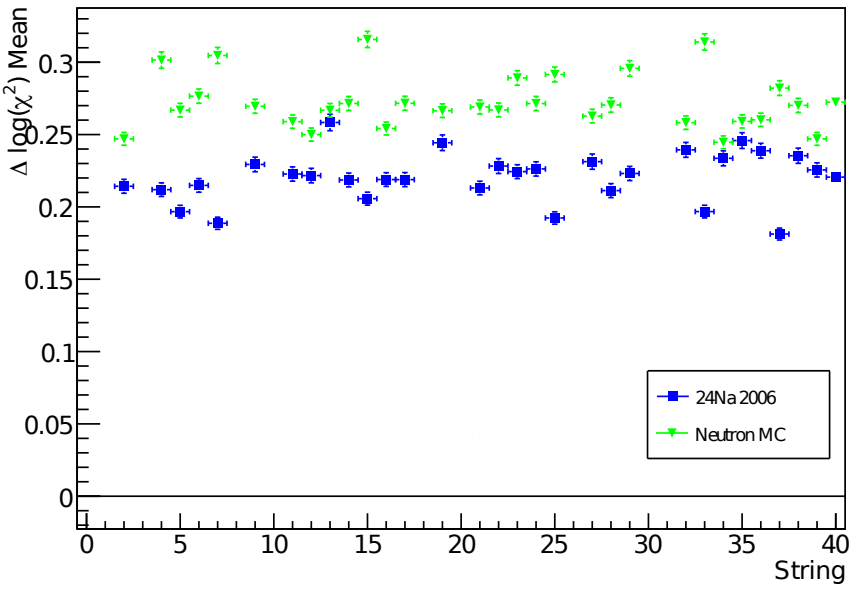

Figure 7.9: The means of the $\Delta\log(\chi^2)$ distributions for each string for the ^{24}Na 2006 data set and neutron MC.

7.7.1 $\Delta\log(\chi^2)$ *Corrections - Neutrons*

Identifying a method to correct each string's $\Delta\log(\chi^2)$ distribution is necessary because otherwise the ^{4}He strings would not correctly predict the alpha contamination on each string. Without understanding the cause of the string-to-string differences, the strategy is to correct each of the strings' distributions to match each other by quantifying the differences between the distributions extremely well.

Each string's distribution is well characterized with the available neutron calibrations, primarily the two ^{24}Na data sets. Basic zeroth- and first-order corrections would consist of shifting and scaling the $\Delta\log(\chi^2)$ distribution for each string to match some reference. The shift is applied first to move the mean of each string's distribution to 0. Then a scale is applied to match the standard deviations to the standard deviation of the entire array.

The shifts for each string, as determined by the two ^{24}Na calibrations, are shown in Figure 7.11 (the points for the non-good-^{3}He strings are addressed later). A search for

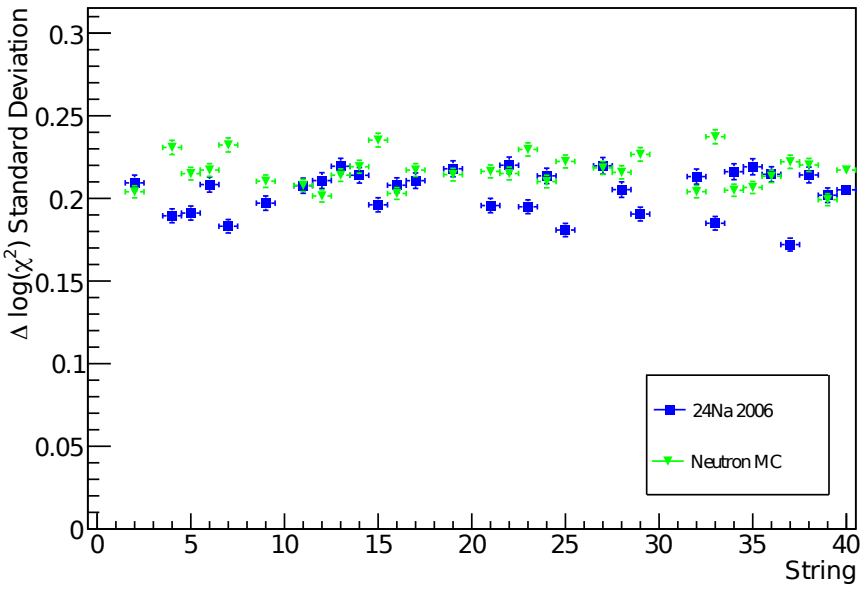

Figure 7.10: The standard deviations of the $\Delta \log(\chi^2)$ distributions for each string for the ^{24}Na 2006 data set and neutron MC.

correlations of the shifts with the various string-dependent parameters did not identify any underlying cause for this correction factor.

For many of the points there is a significant difference between the two ^{24}Na calibrations. This suggests that the shift may be time-dependent. A set of seven array-wide AmBe calibration scans was added to the analysis to obtain a finer time resolution than is available with only two data points. The shifts as a function of time are shown in Figure 7.12 for the N strings. Linear interpolation is used to determine the shifts between data points. The shifts for each string do not follow any obvious trend as a function of time, so the standard deviation of those points is added to the shift uncertainties when the systematic uncertainty on the number of NC neutrons is calculated.

Figure 7.13 shows the scalings for each string, as determined by the two ^{24}Na calibrations. Unlike with the shifts, the two ^{24}Na calibrations agree well, and the 2006 calibration was selected for use because of the superior statistics. Additionally, a distinct correlation with

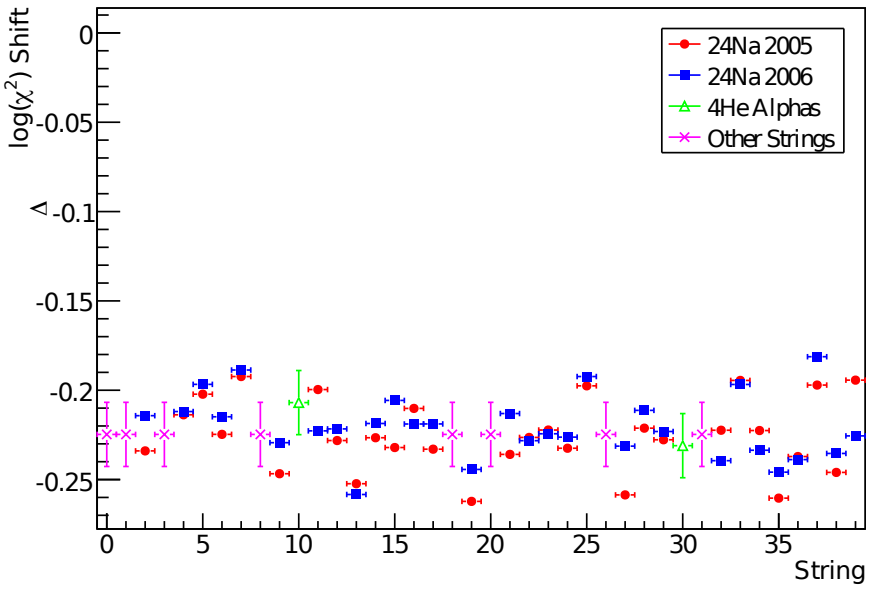

Figure 7.11: $\Delta \log(\chi^2)$ shifts to correct each string's distribution to have a mean of $\Delta \log(\chi^2) = 0$. The determination of the ^{4}He-string shifts is discussed in Section 7.7.2. The shifts for the other strings are set to the ^{3}He array-wide average. The vertical error bars on the ^{3}He-string points are smaller than the data points. The ^{4}He-string shifts are discussed in Section 7.7.2, and the "other"-string shifts are discussed in Section 7.7.3.

MUX box was found, implying that the primary cause of the scaling differences is a result of MUX-box electronics. Figure 7.14 shows the scaling parameter for each MUX box. There is scatter of the points within each box, but the most obvious effect is the difference between MUX box 0 and the other three MUX boxes.

The corrected $\Delta \log(\chi^2)$ will be referred to as $\Delta \log(\chi^2)_{corr}$:

$$\Delta \log(\chi^2)_{corr} = (\Delta \log(\chi^2) + \text{shift}) * \text{scaling}. \tag{7.5}$$

The most significant change is the shift, with the scaling being a smaller effect for the array as a whole. Therefore the cut of $\Delta \log(\chi^2) > 0.271$ produces almost the same cut fraction as a cut of $\Delta \log(\chi^2)_{corr} > 0.05$. The other cut that will be used is the cut determined by

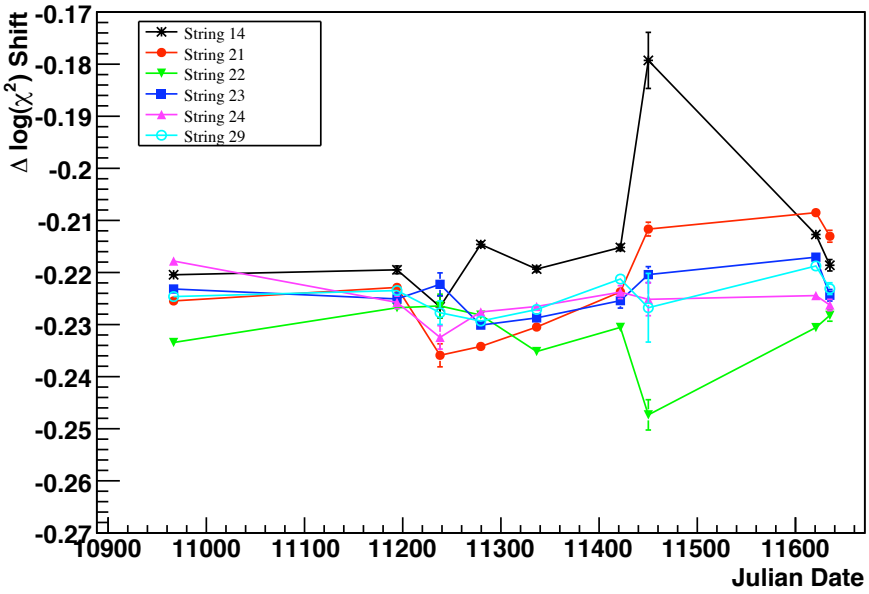

Figure 7.12: $\Delta \log(\chi^2)$ shifts as a function of time for six different strings. The data points include the two ^{24}Na calibrations and seven AmBe array-wide calibrations.

optimizing the total uncertainty (see Section 7.11.1): $\Delta \log(\chi^2)_{corr} > -0.062683$.

7.7.2 $\Delta \log(\chi^2)$ Corrections - Alphas

Since the $\Delta \log(\chi^2)$ distribution for alphas is not expected to be the same as the distribution for neutrons, and the ^{4}He strings do not detect neutrons, an alternative approach must be used to determine the shift and scaling corrections for the ^{4}He strings. There is, fortunately, one characteristic in the alpha distribution that is common between the ^{4}He and neutrino data: the peak of alpha and alpha-like neutron events. Since alphas dominate the neutrino data set there is an obvious peak on strings that have already been corrected based on the ^{24}Na calibrations.

While the strategy of using the alpha peak in the ^{4}He-string data and the neutrino data works well for determining the shift, it cannot be used to determine the scaling. The neutrons in the neutrino data can affect the width of the peak while not changing the peak

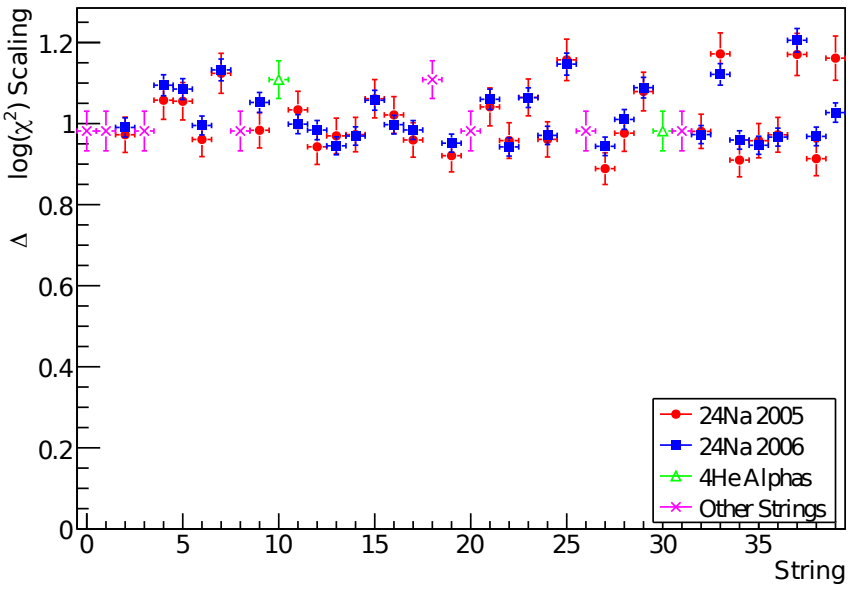

Figure 7.13: $\Delta\log(\chi^2)$ scalings to make the standard deviation of each string's $\Delta\log(\chi^2)$ distribution the same as that of the whole array. The MUX-box average values (boxes 1, 2, and 3 are averaged together; box 0 is averaged independently) are used for the non-standard ^{3}He-array strings. The ^{4}He-string scalings are discussed in Section 7.7.2, and the "other"-string scalings are discussed in Section 7.7.3.

location significantly. Instead the MUX-box-average scaling values are used for the ^{4}He strings, and the uncertainty assigned is the spread of the ^{3}He-string data points on each particular box. The ^{4}He-string scalings are shown in Figure 7.13.

To determine the shift corrections for the ^{4}He strings the $\Delta\log(\chi^2)_{corr}$ values for the neutrino data are "unscaled" with the scaling corrections for each ^{4}He strings.[7] The unscaled peaks are fit with a Gaussian to determine the peak locations. Similarly, the uncorrected $\Delta\log(\chi^2)$ distributions on the two ^{4}He strings are fit with a Gaussian, as shown in Figure 7.15, and the difference between the peak locations on each ^{4}He string and the neutrino data gives the shift values. The uncertainties on the means of the fit produce large uncertainties on the shift values for the ^{4}He strings: 0.19 and 0.15 for strings 10 and 30, respectively.

[7]The unscaled $\Delta\log(\chi^2)$ is $\Delta\log(\chi^2)_{\text{unsc.}} \equiv \left[\left(\Delta\log(\chi^2) + \text{shift}(^3\text{He})\right) \times \text{scale}(^3\text{He})\right]/\text{scale}(^4\text{He})$.

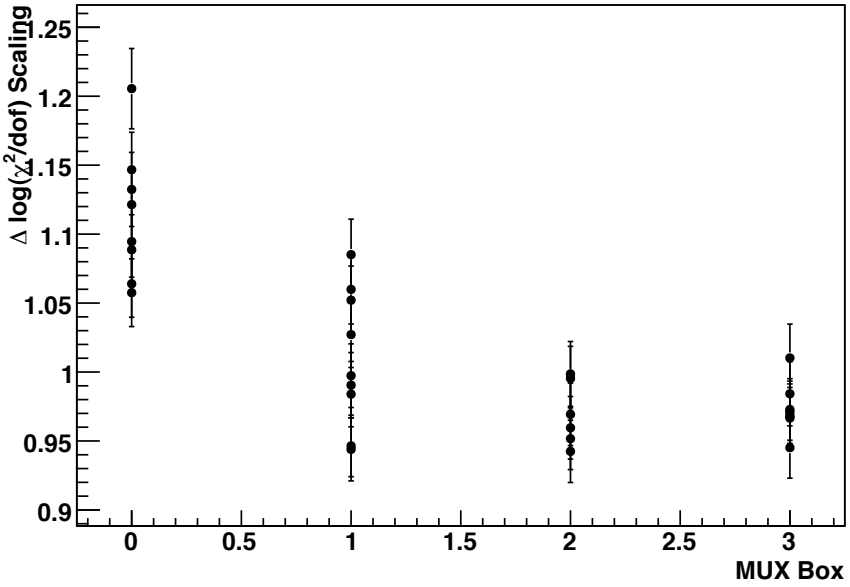

Figure 7.14: $\Delta \log(\chi^2)$ scalings for each good ^{3}He string from the ^{24}Na 2006 calibration, plotted by MUX box.

The spread of the ^{3}He-string shifts is 0.018, and the ^{4}He shifts fall within the well-grouped ^{3}He shifts. Since the differences in the $\Delta \log(\chi^2)$ distributions are suspected to be due to subtle differences in the electronics on each channel, the ^{4}He shift and scalings should not be significantly different than those of the ^{3}He strings. Therefore the uncertainties from the fits are considerably larger than necessary. The uncertainties assigned to each ^{4}He shifts are the spread in the ^{3}He shifts. The ^{4}He-string shifts are included in Figure 7.11.

There is not enough data to investigate the ^{4}He-string shifts as a function of time. Since it appears that the differences in the $\Delta \log(\chi^2)$ distributions are due to subtle effects in the electronics it is reasonable to assume that the time variations of the ^{4}He $\Delta \log(\chi^2)$ distributions would have similar characteristics to those of the ^{3}He $\Delta \log(\chi^2)$ distributions. The spread of the ^{3}He-string shifts calculated throughout the NCD phase is used as a contribution to the systematic uncertainty for the ^{4}He strings to account for the possible time variations.

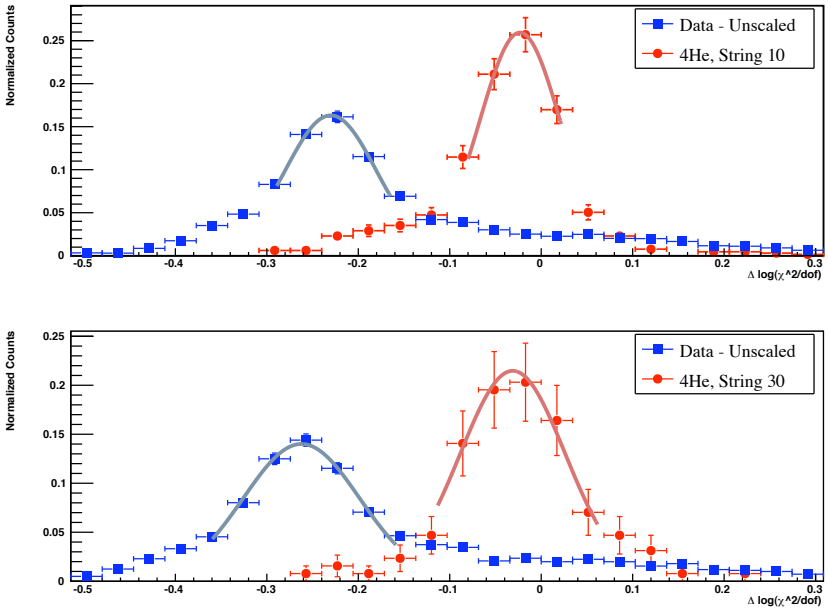

Figure 7.15: Fits of the alpha/alpha-like-neutron peaks in the ^{4}He and ^{3}He neutrino data to determine the shift corrections for the ^{4}He strings. The fit functions are Gaussians, and the fits are performed in three iterations to accurately locate the peak. The data peaks appear different in the two plots because they are "unscaled" with each ^{4}He-string's scaling factor.

7.7.3 $\Delta\log(\chi^2)$ Corrections - Other Strings

The ten "bad" strings are not used to determine the number of neutrons and alphas in the NCD data. However, two strings, strings N4 and J3, are used to characterize two types of potential instrumental backgrounds. These backgrounds are discussed in Section 7.10. The shifts for the bad strings are estimated from the ^{3}He-array-wide average, and the scalings are estimated from the MUX-box averages.

7.8 Alpha Contamination

Unlike the neutrons, there is no large calibration data set that mimics the alpha backgrounds on the ^{3}He strings. The only available source of alpha events is the ^{4}He data, which is limited in statistics and comes from independent strings. The latter point is important because the

ratio of ^{210}Po to bulk alpha events varies on each string, as does the contribution of wire alphas. The wire alphas become important even though they are a a relatively small fraction of the overall alpha background, as is discussed below. The wall alphas are separated from the wall alphas in determining the contamination.

Estimating of the alpha contamination is a two-step process:

1. Characterize the alphas on the ^{4}He strings.

2. Convert the alpha contamination on the ^{4}He strings to the contamination on the ^{3}He strings.

As an equation, the calculation of the alpha contamination is

$$P_\alpha = P^{wall}_{^4He} \frac{N^{HE,narrow}_{data}}{N^{HE,narrow}_{^4He}} + P^{wire}_{^4He} \frac{N^{HE,wide}_{data}}{N^{HE,wide}_{^4He}}. \tag{7.6}$$

$P^{wall}_{^4He}$ and $P^{wire}_{^4He}$ are the wall and wire alpha contaminations on the ^{4}He strings, as determined by a model of the $\Delta\log(\chi^2)_{corr}$ tail (Section 7.8.1). Events above the neutrons in shaper energy are used to convert the ^{4}He contamination to the contamination on the ^{3}He strings. The numbers of events in the two data sets satisfying two different cuts are $N^{HE,narrow}_{data}$, $N^{HE,narrow}_{^4He}$, $N^{HE,wide}_{data}$, and $N^{HE,wide}_{^4He}$ (Section 7.8.3).

7.8.1 Modeling the Alpha $\Delta\log(\chi^2)_{corr}$ Tail

Only the tail of the $\Delta\log(\chi^2)_{corr}$ distribution for alphas is important, since the vast majority of the alphas do not pass the $\Delta\log(\chi^2)_{corr}$ cut. An empirical model is used to characterize that tail based on the ^{4}He-string data. The choice of the function is qualitatively based on the MC data sets, which suggests that the tail falls as an exponential. The falling edge of the wall-alpha MC (both bulk and ^{210}Po is well-fit with an exponential, so a similar model is used to describe the ^{4}He tail as well. It turns out that the wire alphas in the ^{4}He-string data become important in the $\Delta\log(\chi^2)_{corr}$ tail, even though it is a small background overall. The wire-alpha tail in the ^{4}He distribution requires a second exponential be added to the

fit.[8] The fit function is therefore:

$$f = p_0^{\text{wall}} p_1^{\text{wall}} \exp\left[\Delta\log(\chi^2)_{corr} p_1^{\text{wall}}\right] + p_0^{\text{wire}} p_1^{\text{wire}} \exp\left[\Delta\log(\chi^2)_{corr} p_1^{\text{wire}}\right]. \quad (7.7)$$

This model only fits well to the falling edge of the alpha $\Delta\log(\chi^2)_{corr}$ distribution. Below that the alpha contamination cannot be calculated from the model. Therefore the choice of $\Delta\log(\chi^2)_{corr}$ threshold in this analysis is restricted to the range in which the fit is valid.

Figure 7.16 shows the fit of the ^{4}He $\Delta\log(\chi^2)_{corr}$ tail with the above model. The fit range is $-0.16 < \Delta\log(\chi^2)_{corr} < 0.40$, up to and slightly above the last ^{4}He events. Log-likelihood minimization is used because of the low statistics in most bins. The resulting fit parameters are given in Table 7.3. The model fits the data quite well, with $\chi^2/\text{dof} = 17.6/16$, $(p = 0.35)$. The covariance matrix for the fit parameters is given in Table 7.4. All parameter correlations are accounted for when determining the uncertainty on the alpha contamination.

Table 7.3: Fit parameters for the double-exponential model fit to the $\Delta\log(\chi^2)_{corr}$ tail of the ^{4}He-string data. The parameter uncertainties listed here do not take into account the correlations between the parameters.

Parameter	Value	Uncertainty
p_0^{wall}	-0.0028	0.0050
p_1^{wall}	-36	10
p_0^{wire}	-0.49	0.21
p_1^{wire}	-3.4	2.0

The integrals of the wall and wire exponentials give $P_{^4He}^{wall}$, and $P_{^4He}^{wire}$, respectively. For the fit parameters above, with the uncertainties propagated analytically, the number of passing wall and wire alphas are given in Table 7.5.

The systematic uncertainty from the choice of alpha model is determined by taking the excess reduced χ^2 (i.e. $\chi^2/\text{dof} - 1$), and multiplying it by the total statistical uncertainty of the ^{4}He events above $\Delta\log(\chi^2)_{corr}$ threshold.

[8] The reasoning behind identifying the second exponential tail as wire alphas is discussed in Section 7.8.2.

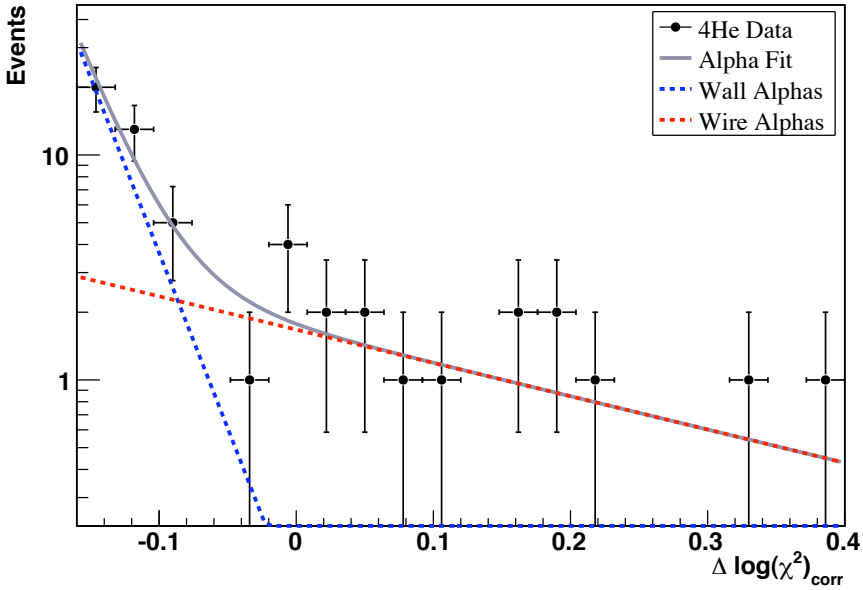

Figure 7.16: Fit of the ^{4}He $\Delta\log(\chi^2)_{corr}$ tail with a double exponential. One exponential represents the wall alphas, and the second the wire alphas. The χ^2 for the fit is $\chi^2/\text{dof} = 17.6/16$, $(p = 0.35)$.

7.8.2 Wire Alphas

Alpha events from decays on the anode wire are relatively infrequent[84]. However, the pulses they produce tend to be wider than typical alphas, and sometimes have a double-peaked structure, because they have both a fast rising edge and a peak at the end of the pulse. The former is a result of the shape of the electron drift curve near the anode [91]; the arrival times of the primary ionization electrons at the anode are closely grouped together, resulting in a fast risetime, and sometimes a small peak. The peak at the end of the pulse is due to the Bragg peak near the end of the ionization track. As a result, one would expect that they might resemble neutrons more than do wall alphas in the $\Delta\log(\chi^2)$ test.

Monte Carlo data sets composed of wire alphas can be used to determine, qualitatively, the $\Delta\log(\chi^2)$ distribution for wire alphas. The top plots of Figure 7.17 shows a comparison of the wall- and wire-alpha $\Delta\log(\chi^2)$ distributions when the alpha library consists of only

Table 7.4: Covariance matrix for the double-exponential model fit to the $\Delta\log(\chi^2)_{corr}$ tail of the ^{4}He-string data.

	p_0^{wall}	p_1^{wall}	p_0^{wire}	p_1^{wire}
p_0^{wall}	2.506×10^{-5}	-0.05181	0.0001731	-0.004156
p_1^{wall}		109.2	-0.2961	7.523
p_0^{wire}			0.04407	-0.3416
p_1^{wire}				4.008

Table 7.5: Integrals of the wall and wire alpha models above $\Delta\log(\chi^2)_{corr} = -0.062683$. The uncertainties listed here do not include the correlations between the wire- and wall-alpha fit parameters

Parameter	Value	Uncertainty
$P_{^4He}^{wall}$	0.958	0.042
$P_{^4He}^{wire}$	17.23	0.21

wall alphas (left) to the distributions when the alpha library consists of both wall and wire alphas (right). Since the wire alphas do not resemble wall alphas, if wire alphas are not present in the alpha library the $\Delta\log(\chi^2)$ test suggests that they look more like neutrons (higher value of $\Delta\log(\chi^2)$). When wire alphas are included in the alpha library, the wire alpha events are clumped with the wall alphas since they find a good fit in the alpha library.

The qualitative behavior of the MC wire alphas when going from a wall-alpha-only library to a wire-and-wall-alpha library can be applied to the data. The bottom row of Figure 7.17 shows a comparison similar to that of the top row, but for the ^{4}He data. The difference between the two plots is that the high-$\Delta\log(\chi^2)$ tail extends further up when the alpha library consists of only wall alphas. It is a particularly subtle effect since the number of wire alphas is so small. Once the full alpha library is used pulses that are presumably wire alphas are pushed to lower $\Delta\log(\chi^2)$. This leads to the conclusion that the high-$\Delta\log(\chi^2)$ tail in the ^{4}He data is probably composed of wire alpha events.

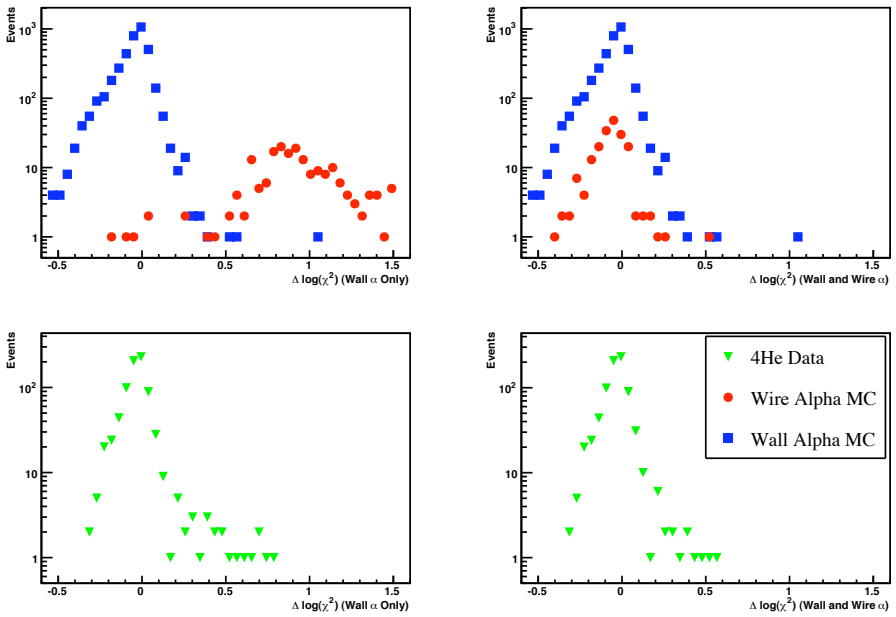

Figure 7.17: A comparison of the behavior of wire alphas under different alpha library fits: on the left the pulses were fit with an alpha library consisting of only wall alphas; on the right the pulses were fit with the full (wall + wire) alpha library. Wire (red circles) and wall (blue squares) are plotted in the top row; ^{4}He data (green triangles) are plotted in the bottom row.

7.8.3 High-Energy Alpha Events

The second task is to convert the ^{4}He alpha contamination into the contamination on the ^{3}He strings. The alphas above the neutron peak are ideal for this purpose. The number of wall alphas immediately above the neutrons, from 0.82 to 1.0 MeV, is assumed to be in proportion to the number of wall alphas in the analysis energy region (0.4-0.82 MeV). The number of wire alphas present can be determined by looking at the wide alphas (width$(10-40\%) >$ 3200 ns) just below the Po peak in energy. Table 7.6 gives the number of events in the two high-energy regions that are used to determine the alpha contamination on the ^{3}He strings.

Table 7.6: The number of events in the two high-energy regions in the ^{4}He and ^{3}He data sets. The ratio of events on the ^{4}He strings to the alpha events on the ^{3}He strings does not correspond to the ratio of the numbers of strings (i.e. 2/30) because string 10 has an unusually high alpha rate. This finding agrees with previous measurements of the alpha rates [85].

	^{4}He	^{3}He
"Narrow"	361	1,117
"Wide"	255	789

7.8.4 Bulk Versus ^{210}Po Alphas

As was noted in Chapter 3 the primary sources of alpha events are the decay chains of ^{238}U and ^{232}Th in the bulk of the NCD walls, and ^{210}Po on the surfaces of the walls and anode wires. The bulk alphas can have different pulse-shape characteristics than the ^{210}Po alphas because the energies of the alphas from the variety of decays in the ^{238}U and ^{232}Th decay chains range from 3.9 to 8.8 MeV, and the ^{210}Po alphas all start with 5.3 MeV. Furthermore the bulk alphas can travel through a significant portion of the nickel wall before reaching the NCD gas, while the surface alphas travel through, at most, a thin layer of nickel or copper. The energy loss in the nickel affects the energy each particle has when it enters the gas, and that can affect the shape of the pulse.

Since the pulse shape distributions for ^{210}Po and bulk alphas are expected to be different, we expect that the $\Delta\log(\chi^2)$ distributions for the different types of alphas will also differ to some extent. Figure 7.7b includes the $\Delta\log(\chi^2)$ histograms for ^{210}Po and bulk MC. They are similar, but there are significant differences, particularly on the low-$\Delta\log(\chi^2)$ edge. Fortunately, this analysis is concerned primarily with the high-$\Delta\log(\chi^2)$ edge. The MC will be useful in characterizing the difference between the ^{210}Po and bulk distributions even though it is not accurate enough to fully describe the distributions from the real data.

When some amount of ^{210}Po and a different amount of bulk alphas are combined together on a string or set of strings the resulting $\Delta\log(\chi^2)$ distribution will be a particular combination of the $\Delta\log(\chi^2)$ distributions for ^{210}Po and bulk alphas. The ^{4}He strings,

collectively, have a particular ratio of ^{210}Po to bulk alphas that is not necessarily the same as the ratio for the ^{3}He strings.[9] Since the ^{4}He strings are used as the model to characterize the tail of the alpha $\Delta\log(\chi^2)$ distribution the difference between the bulk and ^{210}Po distributions must be implemented as a systematic uncertainty on the number of wall alphas. The wire alphas have been determined to have no practical contribution from the ^{238}U and ^{232}Th decays [85], and therefore the difference between the ^{210}Po and bulk distributions does not need to be applied.

The systematic uncertainty from the bulk-vs.-^{210}Po difference is estimated with the alpha MC data sets. The tails of the $\Delta\log(\chi^2)_{corr}$ distributions for ^{210}Po alphas and bulk alphas are close, but not exactly the same according to the MC. The tails of both distributions are fit with the exponential model (a single exponential, since only wall alphas are simulated). The fractional uncertainties, given in Table 7.7, are the fractional difference between the ^{210}Po fit parameters and the bulk fit parameters. These are systematic uncertainties on the wall-alpha parameters in Table 7.3. The uncertainty contribution on the number of NC neutrons is found by calculating the alpha contamination after changing p_0^{wall} and p_1^{wall} by their 1-σ uncertainties.

Table 7.7: Fractional uncertainties on the wall-alpha fit function. These are determined by taking half of the difference between the respective parameters after fitting the MC ^{210}Po alphas and after fitting the MC bulk (^{232}Th) alphas.

Parameter	Fractional Uncertainty
p_0^{wall}	0.119
p_1^{wall}	0.066

7.9 z Dependence

An analysis of neutron calibration runs where the neutron source (^{252}Cf, in particular) was placed at different z positions in the detector reveals that the cut fraction changes as a function of z. This effect is understandable because the pulse shapes depend, in part, on

[9] See [85] for detailed measurements of the ^{210}Po and bulk contributions from each string

the origin of the pulse along the NCD string. The difference in propagation time between the portion of the pulse that reflects off the bottom of the string and the portion that travels up the string results in wider pulses, on average, from the tops of NCD strings and narrower pulses from the bottoms. Furthermore, the NCD acts as a lossy transmission line and the pulse shapes are affected by the transmission-line characteristics of the NCD as pulses propagate through it. The further a pulse propagates, the more its shape is affected. Pulses originating at different distances from the bottom of the string will be affected differently.

Since this effect depends on the distance of the pulse origin from the bottom of the string, the z dependence is actually a dependence on the distance from the bottom of the string. However, the NCD strings are installed such that the counters, not including the delay line, are well centered about the equator of the AV. Therefore z is a good variable to use in this context.

Figure 7.18 shows the neutron cut efficiency as a function of ^{252}Cf-source z position for a cut of $\Delta\log(\chi^2)_{corr} > -0.062683$. For all of these calibration runs the neutron source was in the center of the detector in the $x-y$ plane, so the N strings received the majority of the neutron captures. The points in Figure 7.18 are for each good string receiving at least 10% of the pulses in each calibration run. The dependence of the cut fraction on z appears to be linear. Therefore symmetric neutron sources can be analyzed by the average neutron cut efficiency determined by a symmetric (e.g. the ^{24}Na calibrations) neutron source. Fitting the data points with a straight line gives the slope of the z dependence: $(-1.457 \pm 0.072) \times 10^{-4}$ cm^{-1}.

The uncertainty on the slope results in a systematic uncertainty only if the neutron source is asymmetric in z. The NC neutrons are produced isotropically throughout the D_2O volume, and the ^{24}Na source was determined to be highly uniform [86].

Of the neutron background sources, however, there are two that are significantly asymmetric: the hot spot on string K2 ($z \approx -300$cm), and the NCD cables (above the NCD strings). The asymmetry is an issue because of the known z dependence in the $\Delta\log(\chi^2)_{corr}$ cut efficiency. The neutrons produced by cable radioactivity will capture near the tops of the strings. Therefore, since the cut efficiency is lower, fewer neutrons than expected will pass the $\Delta\log(\chi^2)_{corr}$ cut. At the elevation of the K2 hot spot the cut efficiency is higher

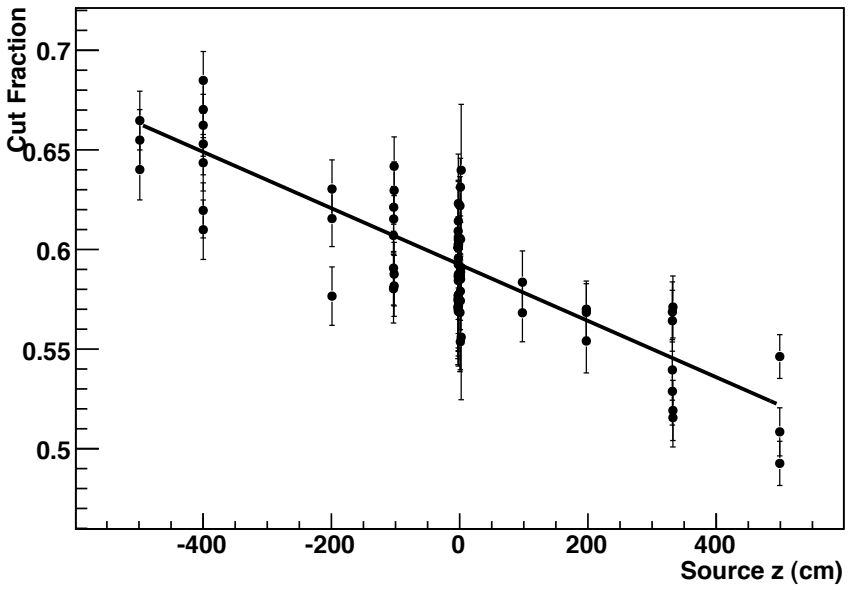

Figure 7.18: Dependence of the $\Delta\log(\chi^2)_{corr}$ cut fraction for each N string on z. The cut used was $\Delta\log(\chi^2)_{corr} > -0.062683$. The data come from a set of 24 central ^{252}Cf calibrations. Each string with greater than 10% of the calibration run's events is plotted separately. The slope of the fit line is $(-1.457 \pm 0.072) \times 10^{-4}$ cm^{-1}.

than the average value, so more neutrons than expected will pass the cut. Since these two sources have known z, and h, distributions, the expected number of neutrons passing the $\Delta\log(\chi^2)$ cut can be calculated:

$$P_{cable} = N_{cable}\epsilon_n^{cable} \quad (7.8)$$

$$P_{K2} = N_{K2}\epsilon_n^{K2} \quad (7.9)$$

The cable and K2-hotspot backgrounds result in a systematic uncertainty that is due to the uncertainty on the slope of the neutron-cut-fraction z dependence.

The azimuthal asymmetry of the external neutrons is not known. They will be assumed to be symmetric, and the asymmetry treated as a systematic uncertainty. The systematic effect will be the hypothesis that the external neutrons are centered 68.2% of the way from

the equator to either either end of the strings.[10]

Taking into account the z dependence of the backgrounds, the equation to determine the number of NC neutrons becomes

$$N_{\rm NC} = \frac{P_{data} - P_{\alpha} - P_{cable} - P_{K2}}{\epsilon_n} - N_{ext} - N_{D_2O} - N_{NCD} - N_{K5} - N_{atmos}. \qquad (7.10)$$

7.10 Non-Neutron, Non-Alpha Backgrounds

Although the only types of events expected in the neutrino data set are neutron and alpha pulses, one cannot exclude the possibility that non-neutron, non-alpha events ("NNNAs," or "3NAs") made it past the data-cleaning cuts. This is a particular worry when performing an energy analysis since limited information is available about each event. What if an unknown class of events was clustered under the neutron peak and affected the number of neutrons determined by the fit? Of course, it is difficult to place a limit on a type of event about which there is no information available.

Two classes of 3NA events were identified on two strings, N4 and J3. The N4 3NAs were identified by their "bursty" timing characteristics, though the pulses themselves looked reasonable. The J3 3NAs were identified by a large excess of events on J3 over what was expected. In hand-scanning the pulses on that string there were clearly events of a particular unusual pulse shape that comprised the majority of the excess events. Neither string, of course, was used in the final analysis, eliminating the J3 and N4 3NAs from the data set. However, one worries that such events could exist unrecognized on otherwise good strings at low levels.

A 3NA-rich data set can be obtained from the J3 and N4 strings in the neutrino data set with two simple cuts. The N4 events are identified by their timing, and the J3 events can be characterized by their pulse shapes [122]:

- N4: $min(t_{last}, t_{next}) < 0.1$,

[10]Since the z asymmetry of the external neutrons is unknown, one might conservatively assume that the neutron background is centered anywhere from the bottoms to the tops of the strings with uniform probability. Therefore, if choosing the central z randomly, 68.2% of the time it will be between $0.682 * z_{\rm bottom}$ and $0.682 * z_{\rm top}$.

- J3: $log(DWK_{i70} - DWK_{i30}) > 5$,

where t_{last} and t_{next} are the times to the previous and next events on the same string, respectively, in seconds, and DWK_{i70} and DWK_{i30} are variables from the DWK pulse-shape analysis [116] characterizing the 70% and 30% integrated risetimes.

The 3NA pulses can then be characterized by the MC-based pulse fitting. Figure 7.19 shows the $\Delta \log(\chi^2)_{corr}$ distribution for the combined 3NAs compared to that of the ^{24}Na neutrons and ^{4}He alphas. The distribution resembles that of the alphas, though smeared out, with a longer tail extending under the unique neutrons. Note that to determine the shift and scaling parameters for the 3NA strings the ^{3}He array average determined the shift, and the MUX-box average determined the scaling. The values used are shown in Figures 7.11 and 7.13, respectively.

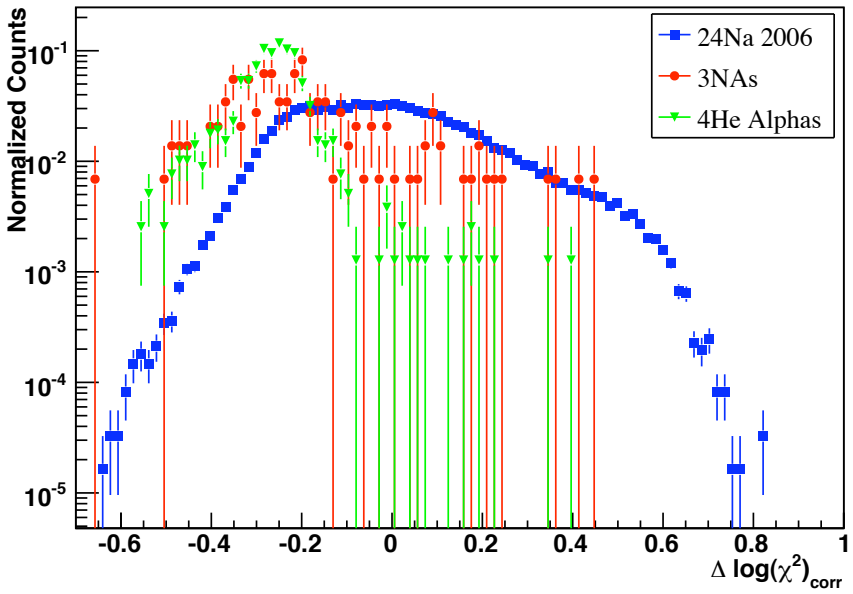

Figure 7.19: The $\Delta \log(\chi^2)_{corr}$ distribution for 3NAs compared to that of ^{24}Na calibration neutrons and ^{4}He-string alphas. The distribution seems to resemble that of the alphas, with a larger tail at high $\Delta \log(\chi^2)_{corr}$.

Figure 7.20 shows the energy distribution of the 3NAs before and after the cut. Both

types of 3NA events cluster at low energies. In the "before" histograms there is, evidently, a small level of neutron contamination in the 3NA data set. It is likely that some portion of the 3NAs that fall under the unique neutrons in Figure 7.19 are, in fact, neutrons. The neutron contamination is estimated to be 8 of the N4 pulses and 13 of the J3 pulses. After accounting for the neutron contamination the cut fractions between 0.4 and 0.82 MeV for N4 and J3 3NAs are 0.99 and 0.90, respectively, for a cut threshold of $\Delta \log(\chi^2)_{\rm corr} > 0.05$.

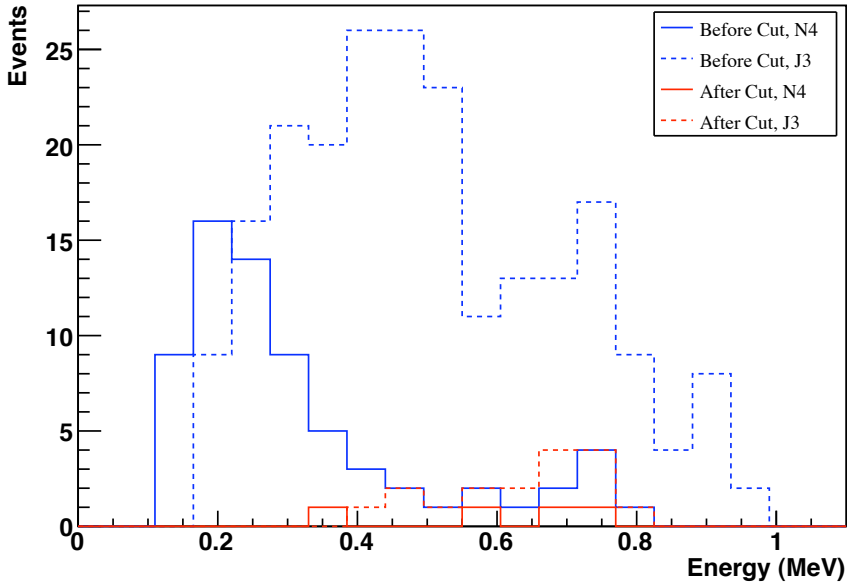

Figure 7.20: The 3NA energy spectra before and after a $\Delta \log(\chi^2)_{corr} > 0.05$ cut. The blue histograms are before the cut, and the red histograms after; The solid histograms are for N4 events, and the dashed histograms for J3 events. There is a small, but significant, neutron contamination.

Several analyses were developed to place limits on the number of 3NAs that might be present in the neutrino data (summarized in [86]). The method for 3NA estimation that was chosen to be implemented in the energy analysis used in the first NCD-phase publication [65] was to produce energy PDFs from data sets of the J3 and N4 3NAs and include them in the energy-spectrum fit. Due to the permissible systematic variations in the shape of the alpha spectrum at low energies the number of 3NAs was highly anti-correlated with the number

of alphas. The fit results suggested that there are 356 ± 192 J3-type 3NAs and 204 ± 170 N4-type 3NAs in the neutrino data. Contamination of the data at that level (560 events out of a total of 7,300) would have been noticed in the extensive checks that had been performed on the data set; the result was only acceptable because it was almost entirely uncorrelated with the resulting number of neutrons. The number of neutrons changed by approximately 3% between including no systematics variations and including all of them (compared with the total uncertainty of approximately 8%) [77].

Unlike with a fit, in a cut based analysis the data cannot be used to constrain the number of 3NA events. The J3 and N4 data can be used to characterize those classes of events, but a separate analysis must be used to limit the number of 3NAs in the data. An energy-spectrum fit is advantageous because the 3NA energy spectrum is significantly different from the neutron and alpha energy spectra. That can be augmented by including $\Delta \log(\chi^2)_{corr}$ in the fit. The 2D PDFs for neutrons, alphas, J3, and N4 3NAs are shown in Figure 7.21. These are fit to the data with the ROOT TFractionFitter class [71]. The fit results are shown in Table 7.8. Only the results for the numbers of 3NA events are revealed to avoid breaking blindness by looking at the numbers of neutron and alpha events. The uncertainties are exceptionally large because the fitting process takes into account the statistical uncertainties of the PDFs. This result is still sufficient for determining an systematic uncertainty due to the potential number of 3NA events if the uncertainties from the fit are ignored and the central value is used as the systematic uncertainty.

Table 7.8: The fit results from the energy-versus-$\Delta \log(\chi^2)_{corr}$ fit, which predict the limits on the number of 3NAs in the neutrino data. The fit returns the fraction of the total data set made up of events in each class, and only the results for the 3NA events are revealed to avoid breaking the blindness restrictions on the data. The numbers of events are based on the total number of events in the neutrino data set. The large uncertainties are a result of the use of ROOT's TFractionFitter class, which takes into account the statistical uncertainties of the PDFs.

Event Class	Fraction	Events
J3 3NAs	0.004 ± 1.49	25
N4 3NAs	0.003 ± 0.32	18

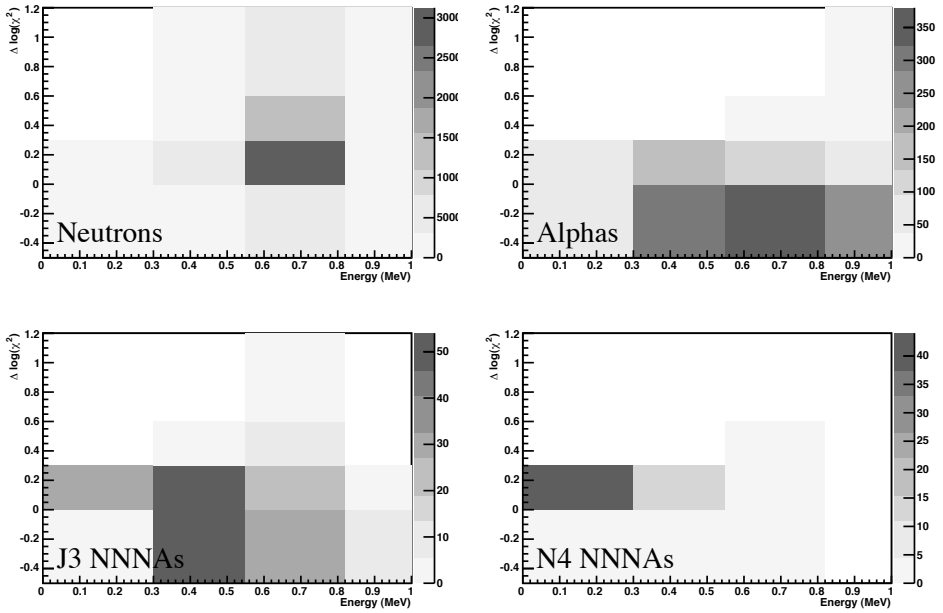

Figure 7.21: $\Delta \log(\chi^2)_{corr}$ vs. energy PDFs for neutrons, alphas, and J3 and N4 3NAs.

Based on the energy-versus-$\Delta \log(\chi^2)_{corr}$ fit, within the shaper-energy range of 0 to 1 MeV, the number of J3-like 3NAs potentially in the data is 69, and the number of N4-like 3NAs potentially in the data is 17. Applying a shaper-energy cut of 0.4 to 0.82 MeV leaves 56.9% of the J3 events and 13.2% of the N4 events. A cut of $\Delta \log(\chi^2)_{corr} > -0.062683$ leaves $(16.8 \pm 0.1)\%$ of the J3 3NAs and $< 17\%$ of the N4 3NAs between 0.4 and 0.82 MeV. Using the central value from the fit there may be 2.4 and < 0.4 J3- and N4-like events in the neutrino data set. These numbers are taken as the uncertainties on the 3NA events passing the $\Delta \log(\chi^2)_{corr}$ cut. The systematic uncertainty on the number of NC neutrons is obtained by dividing the 3NA contaminations by the neutron cut efficiency.

7.11 NC Neutrino Flux Calculation

7.11.1 Cut Optimization

The best $\Delta\log(\chi^2)_{corr}$ cut is the one that minimizes the total uncertainty on the number of NC neutrons. The various uncertainties have different dependences on the cut fraction, and these relative contributions will determine where the minimum uncertainty lies. Choosing the cut threshold based on the actual data set could produce a biased result. Therefore tests with fake data sets, comprised of events randomly drawn from the ^{24}Na and ^{4}He $\Delta\log(\chi^2)_{corr}$ distributions, are used to determine the best cut threshold, as well as perform diagnostics on the performance of the analysis.

The statistics of the fake data set are chosen to match the expected statistics in the full neutrino data set. Approximately 1,200 neutrons are expected, along with 2,400 alphas[11] in the energy region $0.4 < E < 0.82$ MeV. The ^{24}Na and ^{4}He $\Delta\log(\chi^2)_{corr}$ distributions are both smoothed before drawing random events to reduce the statistical variations from bin to bin of the histograms.

A key diagnostic is to verify that the number of neutrons calculated does not vary in any unexpected way (e.g. other than what is expected from statistical variations in the number of events passing the cut). Figure 7.22 shows the number of NC neutrons as a function of cut threshold. There is some variation, but it is largely within the typical systematic uncertainties. The largest variations are due to the fact that the fake alphas are sampled from the ^{4}He data, while the alpha contamination is determined by the alpha fit function.

The sources of uncertainty can be studied as a function of cut threshold. In Figure 7.23 the fractional systematic uncertainties for the fake data test are plotted as a function of cut threshold. Some of the systematic uncertainties prefer a lower threshold, while the alpha-related systematics prefer a higher threshold where fewer alphas contaminate the neutrons. The lowest threshold tested is determined by the fit range of the alpha model. Below $\Delta\log(\chi^2) = -0.16$ the double-exponential model no-longer fits the ^{4}He data, and therefore

[11] Unfortunately there are only 782 ^{4}He-string alpha pulses. Therefore the $\Delta\log(\chi^2)_{corr}$ distribution of the fake-data-set alphas exactly replicates the binned $\Delta\log(\chi^2)_{corr}$ distribution of the ^{4}He-string data (including its statistical variations). Because of the small amount of alpha data available a true statistically-valid test of the alpha distribution cannot be performed.

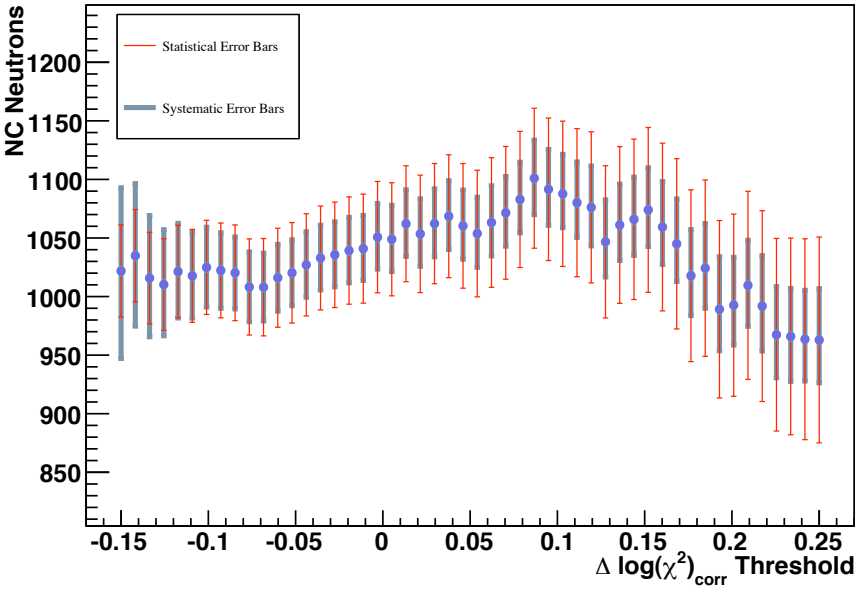

Figure 7.22: The number of NC neutrons as a function of $\Delta \log(\chi^2)_{corr}$ threshold for a fake data test. The largest variations are due to the fake alphas being sampled from the ^{4}He data, while the alpha contamination is determined by the alpha fit function.

the alpha contamination cannot be reliably determined.

The sources of uncertainty are summed together in Figure 7.24. The systematic uncertainties dominate at low $\Delta \log(\chi^2)_{corr}$ thresholds, while the statistical uncertainties dominate at high thresholds. The dominant systematic uncertainties at low thresholds are the ^{4}He shifts and scalings, while the neutron backgrounds dominate at higher thresholds. Of the statistical uncertainties, the uncertainty on P_{data} has the largest effect on $N_{\rm NC}$, while the largest fractional statistical uncertainty is from P_α.

The minimum total uncertainty is determined by averaging the positive and negative total uncertainties and fitting the minimum with a parabola. The minimum uncertainty is found at $\Delta \log(\chi^2)_{corr} = -0.062683$. At this threshold the neutron cut efficiency is $\epsilon_n = 0.5779 \pm 0.0020$.

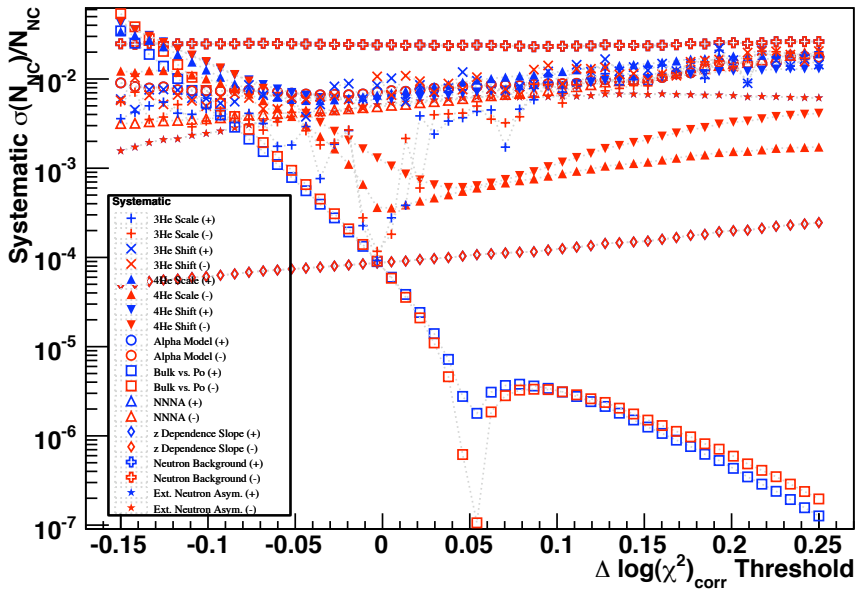

Figure 7.23: The systematic uncertainties on the number of NC neutrons as a function of $\Delta \log(\chi^2)_{corr}$ for the fake data test. The uncertainties (blue for positive, red for negative) are the following: plusses are the ^{3}He scale; $\times$s are the ^{3}He shift; filled upwards triangles are the ^{4}He scale; filled downwards triangles are the ^{4}He shift; hollow circles are the alpha model; hollow squares are the bulk vs. ^{210}Po; hollow upwards triangles are the 3NAs; hollow diamonds are the z-dependence slope; hollow plusses are the neutron backgrounds; and stars are the external neutron asymmetry.

7.11.2 NC Neutrons – Fake Data Test

The number of NC neutrons is first calculated with a fake data test to determine the size of the uncertainties. The final equation for determining the number of NC neutrons detected by the NCD Array is given in Equation 7.10. It includes the z-bias-corrected subtraction of the neutron backgrounds. The neutron cut efficiency and the alpha contamination are determined as described in Sections 7.6 and 7.8, respectively. Based on the tests with fake data sets the best $\Delta \log(\chi^2)_{corr}$ threshold, which will result in the lowest total uncertainty, is $\Delta \log(\chi^2)_{corr} = -0.062683$. The number of NC neutrons in a fake data set with realistic

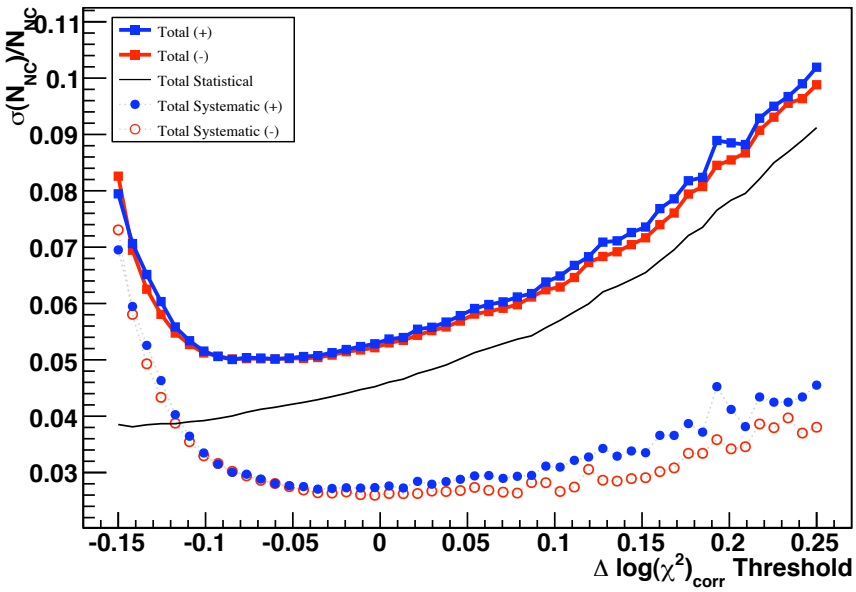

Figure 7.24: The total uncertainties as a function of $\Delta\log(\chi^2)_{corr}$ for the fake data test. All uncertainties are fractional uncertainties on the number of NC neutrons. The minimum total uncertainty (averaging the positive and negative contributions) is at $\Delta\log(\chi^2)_{corr} = -0.062683$.

statistics is thereby determined to be:

$$N_{\mathrm{NC}}^{\mathrm{fake}} = 1009.7 \pm 46.5\ (\mathrm{stat.})\ {}^{+29.3}_{-28.9}\ (\mathrm{syst.}). \tag{7.11}$$

While the central value is pre-determined by how the fake data set was created, the uncertainties are approximately what would be found in an analysis of the full NCD data set. The contributions to the statistical uncertainty are given in Table 7.9. The breakdown of the systematic uncertainties and the total statistical uncertainty are shown in Table 7.10.

The results from the fake data test can be compared to the true number of neutrons in that data set. The fake data set includes 1,198 neutrons. Adding the 185.5 background neutrons to the measured number of NC neutrons gives the total number of neutrons:

Table 7.9: The primary numbers used to produce the number of NC neutrons and their statistical uncertainties for the fake data test.

Parameter	Value	Stat. Uncertainty
P_{data}	748	$\pm$27.3
P_{α}	56.3	$\pm$13.8
ϵ_n	0.5781	$\pm$0.0020

1,195.2. Considering the relevant statistical and systematic uncertainties[12], these numbers are in excellent agreement.

7.11.3 NC Neutrons – One-Third Data Set

The one-third data set is analyzed in exactly the same way as the fake data set, with two exceptions: the estimates of the number of background neutrons and 3NAs are divided by three. The same threshold is used: $\Delta \log(\chi^2)_{corr} = -0.062683$. The number of NC neutrons in a one-third data set determined to be:

$$N_{\rm NC}^{1/3} = 351.8 \pm 25.8 \text{ (stat.) } {}^{+10.6}_{-10.1} \text{ (syst.)}. \tag{7.12}$$

The contributions to the statistical uncertainty are given in Table 7.11. The breakdown of the systematic uncertainties and the total statistical uncertainty are shown in Table 7.12.

To make an estimation of the results from analyzing the full data set, the central value from the analysis of the one-third data set (multiplied by three) can be combined with the uncertainties from the analysis of the fake data set. This projection is not meant to be used for a quantitative measurement of the neutrino flux, but only to illustrate the potential

[12]The uncertainties on the numbers of high-energy alpha events are the dominant contributions to the alpha-contamination uncertainty. There is a systematic uncertainty of approximately nine neutrons due to differences in how the fake data set was created and how it is analyzed; in particular, the neutrons in the fake data set are all symmetric in z while the analysis assumes that some of the background alphas are asymmetric, and the alphas in the fake data set are based directly on the ^{4}He-string data, while the analysis fits that data with the exponential model.

Table 7.10: Breakdown of the uncertainties on the measurement of the number of NC neutrons in the fake data test.

Source	Uncertainty
Systematic	
^{3}HeShift	± 5.53
^{3}HeScaling	$^{+3.57}_{-2.82}$
^{4}HeShift	$^{+8.06}_{-6.89}$
^{4}HeScaling	$^{+6.49}_{-5.08}$
Alpha Model	± 7.25
Bulk vs. Po	$^{+1.23}_{-1.53}$
3NAs	$^{+0.00}_{-4.13}$
z-Dependence Slope	± 0.07
Neutron Backgrounds	± 25.32
External Neutron Asymmetry	± 3.53
Totals	
Statistical	± 46.46
Systematic	$^{+29.30}_{-28.94}$
Combined (Stat. + Syst.)	$^{+54.93}_{-54.74}$

performance of this pulse-shape-based analysis:

$$N_{\mathrm{NC}}^{\mathrm{proj}} = 1055.3 \pm 41.9 \text{ (stat.) } ^{+28.9}_{-28.4} \text{ (syst.)}. \tag{7.13}$$

7.11.4 Comparisons to the Previous Result

The result from the one-third data set and estimated result for the final data set can be compared to the energy-based analysis using the independent systematic and statistical uncertainties. The previous analysis is a joint analysis of the NCD and PMT data, where only NCD data used are the shaper energies. The number of NC neutrons detected by the NCDs above 0.4 MeV is $N_{\mathrm{NC}}^{\mathrm{PRL}} = 983.4^{+57.1}_{-55.1}$ (stat.) $^{+51.7}_{-51.6}$ (syst.) [77].[13] Table 7.13 gives the results of the three analyses with the relevant uncertainty contributions. Comparing the energy-based analysis to the pulse-shape-based analysis of the one-third data set, the

[13]The statistical and systematic uncertainties are separated based on fits performed with and without systematic uncertainties included.

Table 7.11: The primary numbers used to produce the number of NC neutrons and their statistical uncertainties for the one-third data set.

Parameter	Value	Stat. Uncertainty
P_{data}	260	$\pm$16.1
P_{α}	20.6	$\pm$5.1
ϵ_n	0.5781	$\pm$0.0020

results agree within approximately 1.3 σ. When the full NCD data set is analyzed with the pulse-shape-based analysis the uncertainties are reduced, and it is estimated to agree with the energy-based within approximately 1.4 σ.

The primary common systematic uncertainty is due to the neutron backgrounds; it contributes an uncertainty of 25.3 neutrons to the full data set for both this analysis and the energy-fit analysis.[14] This uncertainty is removed by subtracting it in quadrature from the systematic uncertainties.

The dominant contribution to the statistical uncertainty in the pulse-shape-based analysis is from the number of events passing the $\Delta\log(\chi^2)_{corr}$ cut. There are approximately 810 events in the full data set that are not in the one-third data set or that do not pass the $\Delta\log(\chi^2)_{corr}$ cut, but are used in the energy-based analysis. When the full data set is analyzed with the pulse-shape-based analysis there will be approximately 420 events that do not pass the $\Delta\log(\chi^2)_{corr}$ cut. Therefore the uncorrelated portions of the statistical uncertainties due to the events in the neutrino data set is $\sqrt{810} \approx 28.5$ for the one-third data set and $\sqrt{420} \approx 20.5$ for the full data set. The other portions of the statistical uncertainty in this pulse-shape-based analysis are from the alpha contamination and the neutron cut efficiency, which are not shared by the energy-based analysis. This contribution is determined by propagating only the alpha contamination and neutron cut fraction uncertainties to an uncertainty on the number of NC neutrons, and results in an uncertainty of 6.9 NC neutrons.

[14]The number of background neutrons found in [65] is essentially unchanged from the independent estimates of those backgrounds, so the contribution to the uncertainty on the number of neutrons is approximately the uncertainty on the backgrounds.

Table 7.12: Breakdown of the uncertainties on the measurement of the number of NC neutrons in the one-third data set.

Source	Uncertainty
Systematic	
^{3}HeShift	$^{+3.55}_{-3.20}$
^{3}HeScaling	$^{+1.70}_{-0.40}$
^{4}HeShift	$^{+2.90}_{-2.52}$
^{4}HeScaling	$^{+2.36}_{-0.88}$
Alpha Model	± 3.18
Bulk vs. Po	$^{+0.43}_{-0.53}$
3NAs	$^{+0.00}_{-1.38}$
z-Dependence Slope	± 0.02
Neutron Backgrounds	± 8.44
External Neutron Asymmetry	± 1.18
Totals	
Statistical	± 25.77
Systematic	$^{+10.61}_{-10.13}$
Combined (Stat. + Syst.)	$^{+27.87}_{-27.69}$

7.11.5 NC Neutrino Flux

The NC neutrino flux is calculated from the number of NC events detected by the NCDs by comparing with the results of Monte Carlo simulations of the SNO detector and taking into account the various efficiencies of the detection process. The SNOMAN ^{8}B solar-neutrino simulation uses a fixed total flux, ϕ^{MC}, with neutrino energies distributed according to the "Winter-Freedman" ^{8}B spectrum [123]. The neutrino-deuteron NC cross section used is that calculated by Nakamura, *e*t al. [124] ("NSA+"), with radiative corrections as calculated by Kurylov, Ramsey-Musolf, and Vogel [125] ("KMV"). SNOMAN includes the KMV radiative corrections, but the NSA+ calculation also included partial radiative corrections. Those are removed by applying a correction factor, $c_{\mathrm{NSA+}}$, to the simulated event rate. Two further corrections are made to the event rate: c_{MOR} accounts for the fact that the mean orbital radius of the earth around the sun during data-taking is not exactly the year-average in the simulation, and c_d is the ratio of the number of deuterons actually in the spherical portion

Table 7.13: Comparison of $N_{\rm NC}$ from this work and from [65]. Only the relevant uncertainties (i.e. those that are not in common between the analyses) are shown. "(a)−(c)" compares the pulse-shape-based analysis of the one-third data set to the energy-based analysis of the full neutrino data set. "(b)−(c)" compares the estimate of the pulse-shape-based analysis of the full data set to the energy-based analysis of the same data.

	Central	Uncertainties		
Analysis	Value	Statistical	Systematic	Total
(a) One-third	1055.3	±29.3	$^{+6.4}_{-5.6}$	$^{+30.0}_{-29.8}$
(b) Projected	1055.3	±21.6	$^{+14.7}_{-14.0}$	$^{+26.1}_{-25.7}$
(c) Energy fit + PMT data [65]	983.4	N/A	$^{+45.1}_{-45.0}$	$^{+45.1}_{-45.0}$
	Differences			
(a)−(c)	71.9	±29.3	$^{+45.6}_{-45.3}$	$^{+54.2}_{-53.9}$
(b)−(c)	71.9	±21.6	$^{+47.4}_{-47.1}$	$^{+52.1}_{-51.8}$

of the acrylic vessel to the value used in the simulation. $R^c_{\rm MC}$ is the corrected neutron production rate from the simulation, $R^c_{\rm MC} = R_{\rm MC} c_{\rm NSA+} c_{\rm MOR} c_d$

The conversion between the number of NC neutrons and the NC neutrino flux is:

$$\phi^{\rm NCD}_{\rm NC} = \frac{N_{\rm NC}\phi^{\rm MC}}{\epsilon_{acc}\epsilon_{cap}R^c_{\rm MC}T}. \tag{7.14}$$

T is the livetime of the NCD phase. The two relevant efficiencies are the neutron acceptance, ϵ_{acc} and the capture efficiency ϵ_{cap}. The values and uncertainties for the parameters and corrections in Equation 7.14 are given in Table 7.14.

The NC neutrino flux is calculated based on the number of NC neutrons given in Equation 7.12, ($N^{1/2}_{\rm NC}$). Since the one-third data set is being used, the livetime must be divided by three: $T = 385.17/3 = 128.39 \pm 0.004$. The NC neutrino flux is determined to be (in units of 10^6 ν cm^{-2} s^{-1}):

$$\phi^{\rm NCD}_{\rm NC} = 5.93 \pm 0.43 \text{ (stat.)} \, ^{+0.27}_{-0.26} \text{ (syst.)}. \tag{7.15}$$

[15]The livetime is divided by three (and the uncertainty by $\sqrt{3}$) for the analysis of the one-third data set.

Table 7.14: Parameters needed to calculate the NC neutrino flux from the number of NC neutrons detected.

Parameter	Value	Uncertainty	Reference
ϕ^{MC} (10^6 ν cm^{-2} s^{-1})	5.145	N/A	[77]
R^c_{MC} (day^{-1})	12.9633	0.045	[126]
ϵ_{acc}	0.862	0.004	[77]
ϵ_{cap}	0.211	0.007	[121]
T (days)[15]	385.17	0.14	[127]
c_E	0.99662		[^{24}Na 2005]
$c_{\mathrm{NSA+}}$	1/1.024		[128]
c_{MOR}	1.00101		[77]
c_d	1.0112		[128]

Figure 7.25 shows a comparison of the NC flux measurements from the first two phases of SNO [129, 69], the NCD-phase result from [65], this pulse-shape-based NCD analysis, and two SSM predictions. When only the independent uncertainties between the two NCD-phase analyses are considered the results are separated by 1.3 σ. The statistical uncertainties have increased compared to the energy-based analysis, which is understandable since only one-third of the data is being used. The statistical uncertainties are approximately the same. The NCD-phase measurements are largely independent of the salt and D_2O-phase measurements. This analysis agrees with the D_2O- and salt-phase measurements at the 1.1- and 1.4-σ levels, respectively. The SSM flux predictions are from the BPS08 model with the high- (GS) and low-metallicity (AGS) solar abundance inputs [13]. This analysis is in excellent agreement the BPS08(GS) model, and separated by approximately 1.6 σ from the BPS08(AGS) model. Chapter 8 explores the implications of the $\phi^{\mathrm{NCD}}_{\mathrm{NC}}$ result from this analysis in the context of neutrino oscillations and other solar-neutrino experiments.

For the purpose of estimating the potential of the pulse-shape-based analysis, the uncertainties on the NC neutrino flux are calculated based on the projected number of NC neutrons given in Equation 7.13, ($N^{\mathrm{proj}}_{\mathrm{NC}}$):

$$\phi^{\mathrm{NCD}}_{\mathrm{NC}} = 5.93 \pm 0.24 \text{ (stat.)} \ \pm 0.26 \text{ (syst.)}. \tag{7.16}$$

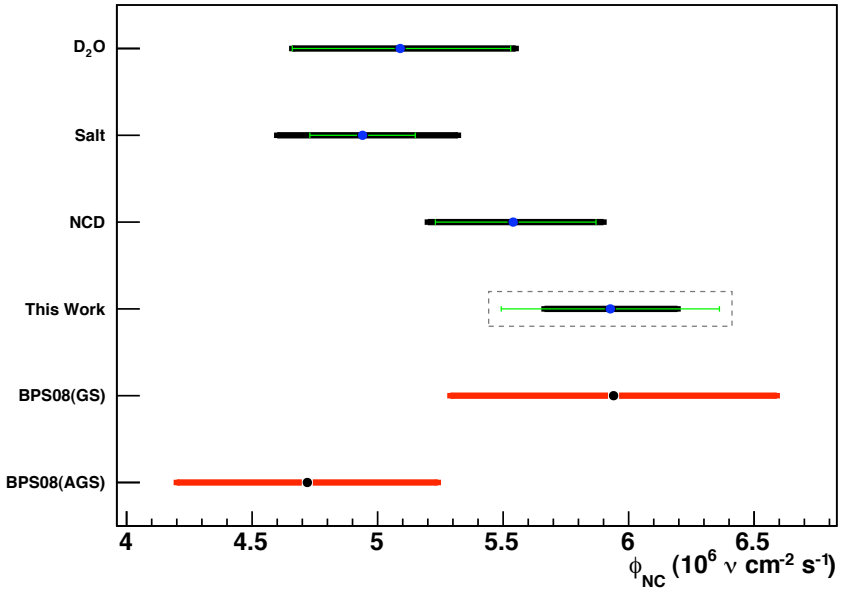

Figure 7.25: ϕ_{NC} comparison, including the results of this analysis on the one-third data set, and the published results from the SNO D_2O [129], salt [69], and NCD [65] phases, and the BPS08 (GS) and (AGS) SSM predictions [13]. The black bars are the systematic uncertainties, and the green lines are the statistical uncertainties.

The central value is the same as in Equation 7.15, but the uncertainties are significantly reduced. These results show that this pulse-shape-based analysis has the potential to greatly improve both the systematic and statistical uncertainties compared to the energy-based analysis. The projected analysis agrees with the D_2O- and salt-phase measurements at the 1.2- and 1.8-σ levels, respectively. It is separated by approximately 2 σ from the BPS08(AGS) SSM model, while still in excellent agreement with the BPS08(GS) model.

Chapter 8

GLOBAL SOLAR-NEUTRINO ANALYSIS

8.1 Introduction

Solar-neutrino experiments have been collecting data for over thirty years, and a plethora of information about the solar-neutrino fluxes exists. Individuals and groups have used models of varying degrees of complexity to combine those results (see, for instance, [70, 65]), sometimes exploring what future experiments might accomplish (e.g. [130]). In the spirit of the latter example, and extending similar work that was done previously [131, 132], we use a set of coupled equations to explore the relationships between the different solar-neutrino measurements and consider the effects of future measurements.

It is also worthwhile to consider the solar luminosity, which is the amount of energy output by the sun every second. The solar luminosity is well measured by observing photons across the electromagnetic spectrum. However, it is also directly related to the production of solar neutrinos through the SSM, assuming that there are no other solar energy sources and given that the sun is in a steady state. As such, it can be used in conjunction with solar-neutrino measurements in two ways: the neutrino measurements themselves can constrain the luminosity, which can then be compared with the photon measurement, or the photon measurement can be used to constrain the neutrino fluxes.

The solar constant is the amount of energy that reaches the top of the earth's atmosphere per second per square meter. The luminosity, $L_\odot$, and the solar constant, $\not{L}_\odot$, are related by the average distance between the earth and the sun, AU:

$$\not{L}_\odot = \frac{L_\odot}{4\pi(AU)^2}. \tag{8.1}$$

The solar constant was originally measured in 1884 by Samuel Pierport Langley [133] by observing the incoming photons at all wavelengths with a bolometer (which he had invented

several years earlier). Modern measurements, typically made with the use of satellites to avoid atmospheric absorption, are incredibly accurate. The primary interest in continued observations of the solar constant is to measure its variations, of which there are several known sources, both periodic and aperiodic. The solar fluctuations can have significant effects on the earth, so understanding them is of great importance.

As a tool to study how the sun is functioning at present all photon-based measurements have one particular feature: the photons reaching the earth were emitted at the surface of the sun, and the energy they carry was released approximately 40,000 years earlier in the stellar core. There is no way to determine what is happening at the core of the sun by looking at the light emitted without waiting a long time. Neutrinos, on the other hand, can provide almost real-time information about what is taking place at the core of the sun since they stream freely outwards after they are emitted. Therefore they could potentially be used to study the solar luminosity on significantly shorter time-scales. They provide the ability to literally predict future solar variations.

According to the SSM the solar constant can be written as a linear combination of the various solar-neutrino fluxes because they constrain the rates of the various reactions in the pp chain and CNO cycle [134]:

$$L_{\odot} = \sum_{i} \alpha_i \phi_i, \tag{8.2}$$

where i indicates the specific neutrino source, ϕ_i are the measured solar-neutrino fluxes, and α_i are the coefficients that specify how the amount of energy liberated by the fusion reactions are related to the neutrino fluxes.

Of course, the detection of solar neutrinos is somewhat more complicated than measuring solar photons. Solar-neutrino experiments operate over longer periods of time than photon-detection experiments to collect enough data, due to the significantly smaller cross-sections for neutrino detection.[1] Furthermore, only some of the solar-neutrino fluxes have been measured, making it more difficult to evaluate the neutrino luminosity. Nevertheless, some reasonable assumptions can be made in Equation 8.2 based on the characteristics of the

[1]Each of SNO's three phases lasted on the order of two years, whereas a photon-based measurement might make individual daily measurements.

measurements that have been performed:

- Set $\phi_{hep} = 0$ since the flux is tiny relative to the other fluxes, and it has not been measured yet [135, 67].
- Simplify the CNO fluxes by setting $\phi_{^{13}\mathrm{N}} = \phi_{^{15}\mathrm{O}}$ and $\alpha_{\mathrm{CNO}} = \frac{1}{2}(\alpha_{^{13}\mathrm{N}} + \alpha_{^{15}\mathrm{O}})$. They also have not yet been measured, independently or collectively.
- Combine ϕ_{pp} with ϕ_{pep}: $\phi_1 \equiv \phi_{pp} + \phi_{pep}$ and $\phi_1 f_{pep} = \phi_{pep}$.

Before substituting ϕ_1 for ϕ_{pp} and ϕ_{pep} Equation 8.2 becomes

$$\mathcal{L}_\odot = \alpha_{pp}\phi_{pp} + \alpha_{pep}\phi_{pep} + \alpha_{^7\mathrm{Be}}\phi_{^7\mathrm{Be}} + \alpha_{\mathrm{CNO}}\phi_{\mathrm{CNO}} + \alpha_{^8\mathrm{B}}\phi_{^8\mathrm{B}}. \tag{8.3}$$

Further simplifying assumptions are used in this analysis to reduce the full oscillation model and the neutrino measurements to a set of eight interrelated equations:

- The neutrino oscillation phenomenology involves three active flavors, and SNO and KamLAND fix the mixing parameters Δm^2_{12} and θ_{12} to the LMA-I solution, where P_{ee} is approximately independent of Δm^2_{12} [70].
- The possibilities of sterile neutrino admixtures, non-standard interactions, and violation of CPT are neglected.
- Spectral distortions of the ^{8}B neutrino flux are negligible at the energies measured by SNO and Super-Kamiokande. The ^{8}B neutrinos are assumed to be subject to matter-dominated oscillations; SNO and Super-Kamiokande measure the flux above at least 5 MeV, while the vacuum-matter transition occurs around 1.8 MeV for ^{8}B neutrinos [130].
- Spectral distortions are also negligible for the pp, pep, and ^{7}Be neutrinos, as they are in the vacuum oscillation region. The vacuum-matter transitions for pp and ^{7}Be neutrinos occur around 3.3 and 2.2 MeV, respectively.[2]

[2]The transition energies for the various categories of solar neutrinos are different because they are produced in different regions of the sun where the density of the sun is different. The matter-dominated oscillation probability and the transition from vacuum oscillations depend on the density where the neutrino is created, and therefore different types of solar neutrinos will transition between vacuum and matter-dominated oscillations at different energies.

- Only solar-neutrino experiments and KamLAND are considered, and resulting constraints on θ_{13} are independent from the results from other experiments.

The experimental observables define eight equations as a function of six floating parameters, including the mixing angles, θ_{12} and $\sin^2\theta_{13}$, and the fluxes, ϕ_1, ,ϕ_7, ϕ_{CNO}, and ϕ_8:

$$P_{ee}^{\mathrm{SNO}} = \epsilon_{\mathrm{LMA}}(\sin^2\theta_{12}\cos^4\theta_{13} + \sin^4\theta_{13}) \tag{8.4a}$$

$$R_{tot}^{\mathrm{SNO}} = \phi_8(\sigma_{8NC}^{D-\mathrm{salt}} + \sigma_{8CC}^{D-\mathrm{salt}} * P_{ee}^{\mathrm{SNO}}) \tag{8.4b}$$

$$\Phi_{ES}^{\mathrm{SK}} = \phi_8(\eta^{-1} + (1-\eta^{-1})P_{ee}^{\mathrm{SNO}}) \tag{8.4c}$$

$$R_{Cl} = (\sigma_1^{Cl}\phi_1 + \sigma_7^{Cl}\phi_7 + \epsilon_{CNO}\sigma_{CNO}^{Cl}\phi_{CNO})P_{ee}^{vac} + \sigma_8^{Cl}\phi_8 P_{ee}^{SNO} \tag{8.4d}$$

$$R_{Ga} = (\sigma_1^{Ga}\phi_1 + \sigma_7^{Ga}\phi_7 + \epsilon_{CNO}\sigma_{CNO}^{Ga}\phi_{CNO})P_{ee}^{vac} + \sigma_8^{Ga}\phi_8 P_{ee}^{SNO} \tag{8.4e}$$

$$R^{\mathrm{Bxno}} = \sigma_7^{\mathrm{Bxno}}\phi_7 P_{ee}^{vac} \tag{8.4f}$$

$$P_{ee}^{\mathrm{KL}} = \left(1 - \sin^2 2\theta_{12}\overline{\sin^2\frac{\Delta m_{21}^2 L}{4E}}\right)\cos^4\theta_{13} + \sin^4\theta_{13} \tag{8.4g}$$

$$\mathcal{L}_\odot = \frac{Q}{2}(0.98004(1-0.09004 f_{pep})\phi_1 + 0.94279\phi_7 + 0.93631\phi_{CNO} + 0.49609\phi_8) \tag{8.4h}$$

The values for the observables are given in Table 8.2 and the floating parameters are given in Table 8.1. The values for the cross sections and other parameters are given in Table 8.3.

All of the cross sections are effective cross sections. In addition to the physics of the particular neutrino interaction they also absorb any detector-related efficiencies. They are calculated such that the flux multiplied by the effective cross section will produce the measured number of events.

Equation 8.4a is the ^{8}B ν_e survival probability as measured by SNO. ϵ_{LMA} is an order-unity parameter that accounts for differences between this approximation and more detailed models, such as those used in [70]. Equation 8.4b is the sum of the CC and NC event rates from SNO, where σ_{8CC}^D and σ_{8NC}^D are the cross sections for the CC and NC interactions with deuterium. Using the sum of the fluxes in this way, rather than the individual rates, removes the need to deal with the correlations between them.

Equation 8.4c is the ^{8}B elastic scattering event rate. Though it has been measured by

several experiments, including SNO [63, 69, 65] and Borexino [136], it is most accurately measured by Super-Kamiokande [137, 67]. η is the ratio of the ES cross section for ν_e to that for ν_μ and ν_τ, above 5 MeV.

Equations 8.4d and 8.4e are the total rates for the chlorine and gallium experiments. The respective chlorine and gallium cross sections are indicated by σ_i^{Cl} and σ_i^{Ga}. In particular, σ_1^{Cl} accounts for the fact that it is only sensitive to the pep contribution to ϕ_1. P_{ee}^{vac} is the vacuum-oscillation survival probability:

$$P_{ee}^{vac} = \left(1 - \frac{1}{2}\sin^2 2\theta_{12}\right)\cos^4\theta_{13} + \sin^4\theta_{13}, \tag{8.5}$$

which is applicable because the transition energy for ^{7}Be is so high (2.2 MeV). The survival probability for CNO neutrinos is slightly lower than P_{ee}^{vac}, and the parameter ϵ_{CNO} is used to account for the difference.

Equation 8.4f is the Borexino event rate due to ^{7}Be neutrinos. As of this writing Borexino has not been able to separate the CNO flux from the ^{210}Bi background [138].

Equation 8.4g is the (anti)neutrino survival probability measured by KamLAND. The $\overline{\sin^2\frac{\Delta m_{21}^2 L}{4E}}$ term averages over the baselines between KamLAND and the nuclear reactors to which it is sensitive, and the antineutrino energy spectrum.

Finally, Equation 8.4h is the luminosity constraint given the assumptions discussed above. For most of the tests in this analysis it is used to constrain the neutrino flux. The one exception is Section 8.2.2, where the solar luminosity is allowed to float and be constrained by the neutrino measurements.

Table 8.1: Initial values for the floating parameters.

Parameter	Initial Value	Reference
θ_{12}	0.6010 ± 0.0273	[66]
$\sin^2\theta_{13}$	$(2 \pm 1) \times 10^{-2}$	[139]
ϕ_1	$(6.055 \pm 0.030) \times 10^{10}$ cm^{-2} s^{-1}	[13]
ϕ_7	$(0.455 \pm 0.027) \times 10^{10}$ cm^{-2} s^{-1}	[13]
ϕ_{CNO}	$(3.26 \pm 0.33) \times 10^{8}$ cm^{-2} s^{-1}	[13]
ϕ_8	$(4.72 \pm 0.52) \times 10^{6}$ cm^{-2} s^{-1}	[13]

Table 8.2: Measured values for the experimental observables.

Parameter	Value	Reference
P_{ee}^{SNO}	0.34 ± 0.039	[69]
R_{tot}^{SNO}	$(2.67 \pm 0.16) \times 10^{-36}$ s^{-1}	[69]
Φ_{ES}	$(2.35 \pm 0.08) \times 10^{6}$ cm^{-2} s^{-1}	[137]
R_{CL}	$(2.56 \pm 0.23) \times 10^{-36}$ s^{-1}	[52]
R_{Ga}	$(6.93 \pm 0.55) \times 10^{-36}$ s^{-1}	[55]
R_{Bxno}	$(1.715 \pm 0.175) \times 10^{-35}$ s^{-1}	[138]
P_{ee}^{KL}	0.578 ± 0.031	[66]
$\mathcal{L}_{\odot}$	$(8.531 \pm 0.034) \times 10^{11}$ MeV cm^{-2} s^{-1}	[11]

With a set of eight equations constraining up to seven floating parameters one could consider simply simultaneously solving them. Since the equations are not polynomials it is easier to create a figure of merit and minimize over the floating parameters. MINUIT [115], implemented in the TFitterMinuit class in ROOT [71], is used to perform the minimization. The Pearson's χ^2 test is used as the figure of merit. For each equation, i, a χ^2 can be calculated:

$$\chi_i^2 = \frac{(A_i^{exp} - A_i^{calc})^2}{\sigma_i^2}, \tag{8.6}$$

where A_i^{exp} are the experimental measurements and A_i^{calc} are the values calculated with the corresponding equations. σ_i are the experimental uncertainties. The total χ^2 is the sum of the χ_i^2 values for all eight equations.

The initial step sizes are chosen based on each parameter's smallest measured uncertainty. Those step sizes are given in Table 8.4.

Prior to the publication of the Borexino results ϕ_7 might have been combined with ϕ_{CNO} in an analysis like this since there was no good way to distinguish between them. Borexino, however, measures ϕ_7 alone, so ϕ_7 and ϕ_{CNO} appear separately in Equations 8.4. One consequence is that, without a measurement of ϕ_{CNO} by Borexino or another experiment there is a significant linear correlation between ϕ_1 and ϕ_{CNO} though the Chlorine and Gallium measurements. This correlation is shown in Figure 8.1, where χ^2 is plotted as a function of ϕ_1 and ϕ_{CNO}. In initial tests it was found that MINUIT would settle on a

Table 8.3: Other parameters that are used in the solar-neutrino calculation.

Parameter	Value	Reference
ϵ_{LMA}	1.10	[132]
ϵ_{CNO}	0.9	[132]
η	6.383	[132]
f_{pep}	0.0023	[132]
$\sigma_{8NC}^{D-\mathrm{salt}}$	2.630×10^{-43} cm^2	[69]
$\sigma_{8CC}^{D-\mathrm{salt}}$	8.000×10^{-43} cm^2	[69]
$\sigma_{8NC}^{D-\mathrm{NCD}}$	8.79×10^{-44} cm^2	Chapter 7
σ_1^{Cl}	3.68×10^{-48} cm^2	[132]
σ_7^{Cl}	2.38×10^{-46} cm^2	[132]
σ_{CNO}^{Cl}	4.95×10^{-48} cm^2	[132]
σ_8^{Cl}	1.1100×10^{-42} cm^2	[132]
σ_1^{Ga}	1.226×10^{-45} cm^2	[132]
σ_7^{Ga}	7.65×10^{-45} cm^2	[132]
σ_{CNO}^{Ga}	0.869×10^{-46} cm^2	[132]
σ_8^{Ga}	2.6731×10^{-42} cm^2	[132]
σ_7^{Bxno}	5.79×10^{-45} cm^2	[138]
$\sigma_{CNO}^{\mathrm{Bxno}}$	6.68×10^{-45} cm^2	[138]
$\sin^2 \frac{\Delta m_{21}^2 L}{4E}$	0.4574	[66]
Q	26.731 MeV	[132]

small local minimum at completely unphysical values of ϕ_{CNO} and $L_\odot$, while significantly increasing the uncertainties of ϕ_1 and ϕ_{CNO}. As a result, except where noted, ϕ_{CNO} is fixed to its SSM value.

8.2 Minimization Studies

The tests performed include:

- The "standard" minimization with θ_{12}, $\sin^2\theta_{13}$, ϕ_1, ϕ_7, and ϕ_8 floating, where the constraint on $\sin^2\theta_{13}$ is of particular interest,
- two-neutrino mixing by fixing θ_{13} to zero,
- neutrino constraints on the solar luminosity by floating $L_\odot$,

Table 8.4: Step sizes for the seven floating parameters used in the analysis. ϕ_{CNO} and $L_{\odot}$ are only floated in the fits where that is explicitly stated. Otherwise they are fixed to the values in Table 8.1.

Parameter	Init. Step Size
θ_{12}	0.03
$\sin^2\theta_{13}$	0.004
ϕ_1	0.06
ϕ_7	0.06
ϕ_{CNO}	0.5
ϕ_8	0.4
$L_{\odot}$	0.3

- considering potential future experimental improvements,

- and implementing the NC neutrino flux determined in Chapter 7.

The fit result values are given in tables, and figures are used where appropriate. The units used throughout this section for θ_{12} are radians, and the units for the fluxes are neutrinos $\mathrm{cm}^{-2}\ \mathrm{s}^{-1}$.

To establish a baseline for what this type of analysis can accomplish the first tests involve floating the parameters in Table 8.1 with the luminosity constraint fixed. The least-well-known floating parameter, θ_{13}, is of particular interest since it has not been experimentally measured.

In the first test there are five floating parameters, and eight equations in the fit, so there are three degrees of freedom. The results are shown in Table 8.5. $\sin^2\theta_{13}$ is 1.2-σ above zero. This is in excellent agreement with the recent hints at a non-zero θ_{13} from at least two independent global analyses of neutrino experiments [139, 140, 141].

Figure 8.2 is the 1-D χ^2 distribution for $\sin^2\theta_{13}$. $\sin^2\theta_{13}$ was fixed at each value along the x-axis and the other four floating parameters were minimized. There is a definite minimum in χ^2 as a function of $\sin^2\theta_{13}$, with a large uncertainty.

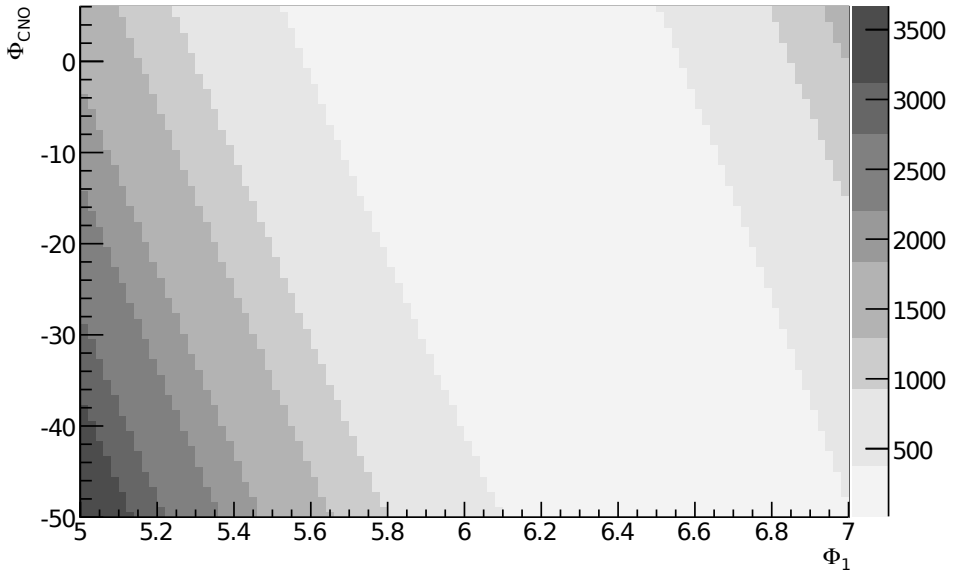

Figure 8.1: A two-dimensional histogram showing the relationship between χ^2, ϕ_1, and ϕ_{CNO}. The two fluxes are linearly correlated, and χ^2 has little preference for any particular pair of flux values.

8.2.1 Two-Neutrino Approximation

The two-neutrino approximation, previously discussed in Chapters 1 and 2, can be tested by setting $\theta_{13} = 0$. The results are shown in Table 8.6. All of the parameters agree with the baseline test within the uncertainties. The most interesting change from the baseline is that the uncertainties on the fluxes decreased without the additional floating parameter.

8.2.2 Neutrino Constraints on the Solar Luminosity

We can compare the solar luminosity derived directly from the neutrino fluxes with the electromagnetic value by allowing $L_\odot$ to float. This procedure makes the "measured" value of $L_\odot$, starting at the value determined by the photon measurements of the luminosity, into a floating parameter. The fluxes, ϕ_1, ϕ_7, ϕ_{CNO}, and ϕ_8, constrain it through the form of Equation 8.4h (with ϕ_{CNO} fixed to its SSM value). The results of the fit with

Table 8.5: The basic global solar-neutrino analysis results. There are eight equations minimized over five floating parameters, and therefore three degrees of freedom.

Parameter	Result
θ_{12}	0.579 ± 0.025
$\sin^2\theta_{13}$	$(2.7 \pm 2.3) \times 10^{-2}$
ϕ_1	$(5.944 \pm 0.064) \times 10^{10}$
ϕ_7	$(0.539 \pm 0.061) \times 10^{10}$
ϕ_8	$(5.33 \pm 0.30) \times 10^{6}$
χ^2	3.33

Table 8.6: The global solar-neutrino analysis results with $\theta_{13} = 0$. There are eight equations minimized over four floating parameters, and therefore four degrees of freedom.

Parameter	Result
θ_{12}	0.583 ± 0.024
ϕ_1	$(5.978 \pm 0.055) \times 10^{10}$
ϕ_7	$(0.503 \pm 0.050) \times 10^{10}$
ϕ_8	$(5.14 \pm 0.23) \times 10^{6}$
χ^2	4.93

$L_\odot$ floating are given in Table 8.7. These can be compared to the fit results in Table 8.5. The value of $\sin^2\theta_{13}$ changed, but remains within the uncertainties of the fit; it now sits at 1.3-σ above zero. The central value of ϕ_1 also changed, and the uncertainty increased by a factor of about 15. This implies that the luminosity measurement was significantly constraining this flux. Since the combination of pp and pep neutrinos makes up the vast majority of the solar neutrinos, it is understandable that this flux is closely related to the solar luminosity. Furthermore, ϕ_1 is not well constrained by neutrino measurements, only having been measured, in combination with other fluxes, by the gallium experiments.

The results of this test show that the neutrino experiments are able to make a 16.5% measurement of the value of $L_\odot$ independent of the electromagnetic measurements. Furthermore, the neutrino-based measurement is in very good agreement with the measurement made with photons ($(8.84 \pm 1.46) \times 10^{11}$ versus $(8.531 \pm 0.034) \times 10^{11}$), even though the

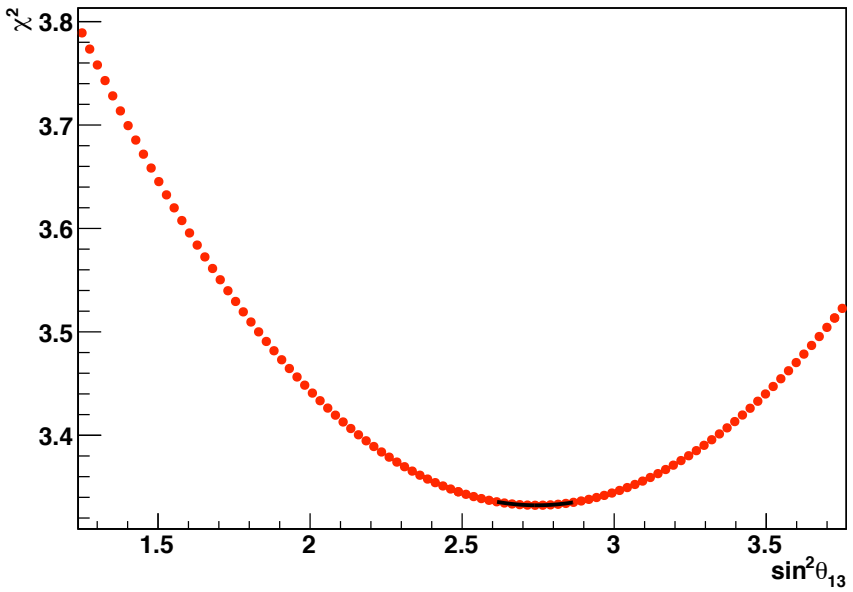

Figure 8.2: χ^2 as a function of $\sin^2\theta_{13}$, where the other four floating parameters are minimized for each value of $\sin^2\theta_{13}$. The minimum value is determined by fitting with a parabola around the minimum. It is found by this method to be $\sin^2\theta_{13} = 2.75 \times 10^{-2}$.

uncertainties are significantly larger. Bahcall and Peña-Garray reported a $> 1\sigma$ discrepancy between the neutrino and electromagnetic measurements [130] that is not confirmed in this analysis.

8.2.3 Potential for Future Results: $P_{ee}^{\rm SNO}$, Φ_{ES}, and $R_{\rm Bxno}$

Three of the experimental results could conceivably be improved in the relatively near future: the value of θ_{12} measured by SNO could be improved when SNO combines the results from the three phases, and Super-Kamiokande and Borexino continue to run and will, presumably, publish new results as they collect additional data. With improvements to their analysis and background discrimination Borexino may also be able to make a measurement of the CNO flux.

Table 8.8 shows what would happen if the uncertainties on $P_{ee}^{\rm SNO}$ and $R_{tot}^{\rm SNO}$ are reduced

Table 8.7: The global solar-neutrino analysis results with $Ł_\odot$ floating. There are eight equations minimized over six floating parameters, and therefore two degrees of freedom.

Parameter	Result
θ_{12}	0.581 ± 0.026
$\sin^2\theta_{13}$	$(3.1 \pm 2.4) \times 10^{-2}$
ϕ_1	$(6.39 \pm 0.96) \times 10^{10}$
ϕ_7	$(0.536 \pm 0.061) \times 10^{10}$
ϕ_8	$(5.33 \pm 0.30) \times 10^{6}$
$Ł_\odot$	$(8.84 \pm 1.46) \times 10^{11}$
χ^2	3.11

by a factor of two. θ_{12} is somewhat smaller, and the uncertainties on θ_{12} and ϕ_8 are both significantly reduced. The measurement of $Ł_\odot$ is improved, with an uncertainty of 13.7%.

Table 8.8: The global solar-neutrino analysis results with $\sigma(P_{ee}^{\rm SNO}) = 0.0165$ and $\sigma(R_{tot}^{\rm SNO}) = 0.037$. There are eight equations minimized over six floating parameters, and therefore two degrees of freedom.

Parameter	Result
θ_{12}	0.576 ± 0.018
$\sin^2\theta_{13}$	$(3.38 \pm 2.18) \times 10^{-2}$
ϕ_1	$(6.39 \pm 0.96) \times 10^{10}$
ϕ_7	$(0.539 \pm 0.061) \times 10^{10}$
ϕ_8	$(5.30 \pm 0.15) \times 10^{6}$
$Ł_\odot$	$(9.12 \pm 1.25) \times 10^{11}$
χ^2	4.22

Super-Kamiokande, still operational in Japan, could potentially improve its ^{8}B ES flux measurement. Currently that flux has also been measured by SNO [65] and Borexino [136], but the most accurate result is still from Super-Kamiokande because of the larger fiducial volume. We can consider what would happen if the combined uncertainties were cut in half, so that $\sigma(\Phi_{ES}^{\rm SK}) = 0.04 \times 10^6$. The results are shown in Table 8.9. There are almost no changes to the central values except for θ_{12}, which changes by less than half of its uncertainty, $\sin^2\theta_{13}$, which decreases by about 20%, and $Ł_\odot$, which increases by about

3%. The measurement of $\sin^2\theta_{13}$ is now at a 1.2-σ significance, and the measurement of $Ł_\odot$ again improves to 13.7%. However, the χ^2 has increased significantly, from 3.11 to 5.65. Figure 8.3 shows why this occurs. There is significant tension between the measured value of Φ_{ES} and the value calculated with Equation 8.4c ($(2.35 \pm 0.04) \times 10^6$ cm^{-2} s^{-1} and 2.19×10^6, respectively). By decreasing the uncertainty in the measurement but not shifting the central value, Equation 8.4c adds significantly to the χ^2 sum.

Table 8.9: The global solar-neutrino analysis results with $\sigma(\Phi_{ES}^{\rm SK}) = 0.04$. There are eight equations minimized over six floating parameters, and therefore two degrees of freedom.

Parameter	Result
θ_{12}	0.590 ± 0.025
$\sin^2\theta_{13}$	$(2.64 \pm 2.32) \times 10^{-2}$
ϕ_1	$(6.39 \pm 0.96) \times 10^{10}$
ϕ_7	$(0.533 \pm 0.061) \times 10^{10}$
ϕ_8	$(5.36 \pm 0.28) \times 10^6$
$Ł_\odot$	$(9.10 \pm 1.25) \times 10^{11}$
χ^2	5.65

The Borexino experiment in Italy is also still in operation, and will likely further improve its measurement of the ^{7}Be solar-neutrino flux. Furthermore, Borexino has the potential to measure the CNO solar-neutrino flux.

The result of reducing the uncertainty on the Borexino neutrino detection rate to 0.09×10^{-35} are shown in Table 8.10. In this case ϕ_7 and $Ł_\odot$ are affected the most significantly. The uncertainties on both parameters are reduced. The solar-neutrino measurement of $Ł_\odot$ in this case is accurate at the 13.3% level. The uncertainty on ϕ_1 is reduced slightly by correlations with ϕ_7, primarily through R_{Ga} and $Ł_\odot$.

A measurement of ϕ_{CNO} by Borexino could break the correlation between ϕ_1 and ϕ_{CNO}. Equation 8.4f acquires an additional term:

$$R^{\rm Bxno} = (\sigma_7^{\rm Bxno}\phi_7 + \epsilon_{CNO}\sigma_{CNO}^{\rm Bxno}\phi_{CNO})P_{ee}^{vac}. \tag{8.7}$$

The best configuration to isolate the CNO flux is with $Ł_\odot$ fixed, using the photon

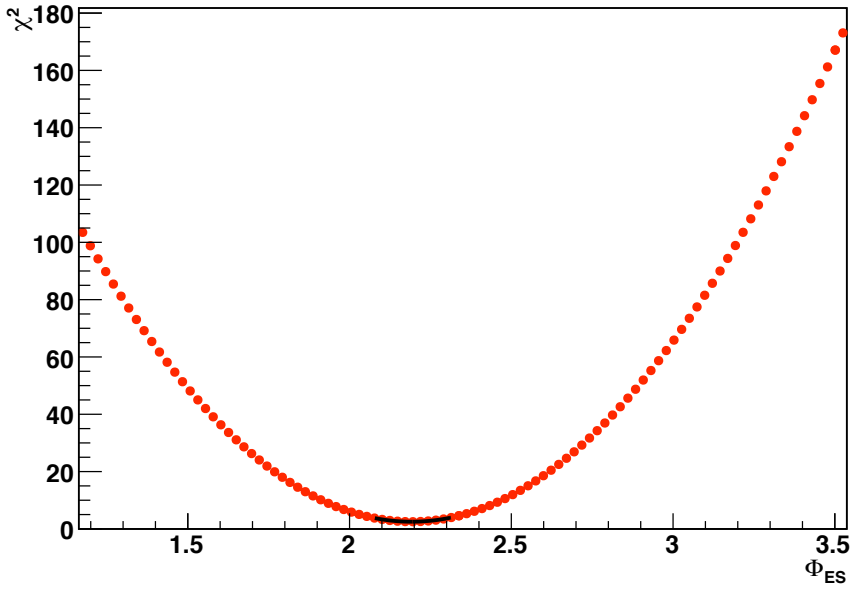

Figure 8.3: χ^2 as a function of Φ_{ES}, with $\sigma(\Phi_{ES}) = 0.04$. The minimum is at $\Phi_{ES} = 2.19$.

measurement of the solar luminosity to help constrain ϕ_{CNO}. However, for immediate comparison with the analyses in Tables 8.7 and 8.10, first $\mathcal{L}_\odot$ is floated and ϕ_{CNO} is fixed. Table 8.12a shows what happens if a 10% CNO measurement at the SSM central value is added to the Borexino rate. The most significant change is to $\mathcal{L}_\odot$, which becomes a 13.7% measurement.

The analysis presented in Table 8.12b includes both the improved measurement of ϕ_7 and the 10% measurement of ϕ_{CNO}. The measurement of $\mathcal{L}_\odot$ is improved to a 13.2% accuracy. The uncertainty on ϕ_7 is not quite as good as without a ϕ_{CNO} measurement, probably due to tension between the different equations that involve both ϕ_7 and ϕ_{CNO}.

With the measurement of ϕ_{CNO}, one can attempt to constrain its value with the other neutrino measurements and the solar luminosity. Tables 8.12c and 8.12d correspond to the same configurations as Tables 8.12a and 8.12b, except that ϕ_{CNO} is allowed to float, and $\mathcal{L}_\odot$ is fixed. The only differences between the two tables are a slight reduction in the uncertainties on ϕ_1 and ϕ_{CNO}. In either case, however, the measurement of ϕ_{CNO} is

Table 8.10: The global solar-neutrino analysis results with $\sigma(R_{\rm Bxno}) = 0.09$. There are eight equations minimized over six floating parameters, and therefore two degrees of freedom.

Parameter	Result
θ_{12}	0.581 ± 0.026
$\sin^2\theta_{13}$	$(3.12 \pm 2.42) \times 10^{-2}$
ϕ_1	$(6.35 \pm 0.91) \times 10^{10}$
ϕ_7	$(0.542 \pm 0.041) \times 10^{10}$
ϕ_8	$(5.33 \pm 0.30) \times 10^{6}$
$Ł_\odot$	$(9.07 \pm 1.21) \times 10^{11}$
χ^2	3.12

sufficient to break the correlation between ϕ_1 and ϕ_{CNO} that is demonstrated in Figure 8.1. The global fit for ϕ_{CNO} is close to the SSM value, though the uncertainties make it consistent with zero, as well.

The final prospective configuration to consider is what happens if all three of these experiments, SNO, Super-Kamiokande, and Borexino, produce improved results. The cases with $Ł_\odot$ floating and ϕ_{CNO} fixed, and with $Ł_\odot$ fixed and ϕ_{CNO} floating are presented in Tables 8.13a and 8.13b. Additionally, the central value of the Φ_{ES} measurement is moved within $\frac{1}{2}$-σ of the value that best agrees with the other parameters and minimizes χ^2: $\Phi_{ES} = 2.17 \pm 0.04$. The most dramatic change in the results is the value of χ^2. The dominant contribution to the χ^2 had been the value of Φ_{ES}. With $Ł_\odot$ floating and ϕ_{CNO} fixed $\sin^2\theta_{13}$ is measured at 1.7-σ, and the smallest uncertainty on $Ł_\odot$ is achieved, 13.0%.

8.2.4 Using the NCD-Only NC Flux

The final configuration to consider is the addition of the NCD NC flux measurement from Chapter 7. That result can be added to this analysis as a separate experiment, provided that the salt-phase results are used for $P_{ee}^{\rm SNO}$ and $R_{tot}^{\rm SNO}$, since the data sets are independent and the uncertainties between the NCD NC flux analysis and the salt-phase analysis are almost entirely uncorrelated. A ninth equation is added to include the NCD NC flux:

$$R_{NC}^{\rm NCD} = \phi_8 \sigma_{8NC}^{D-{\rm NCD}}. \tag{8.8}$$

Table 8.11: Results for four variations of the global solar-neutrino analysis with a 10% measurement of ϕ_{CNO} at the SSM value added to the current ϕ_7 measurement. In the top row, $\mathcal{L}_\odot$ is floating and ϕ_{CNO} is fixed. In the bottom row, $\mathcal{L}_\odot$ is fixed and ϕ_{CNO} is floating. On the left side $R^{\mathrm{Bxno}} = 1.921 \pm 0.176$. On the right side $R^{\mathrm{Bxno}} = 1.921 \pm 0.092$. In all cases there are eight equations minimized over six floating parameters, and therefore two degrees of freedom.

Parameter	Result
θ_{12}	0.581 ± 0.026
$\sin^2\theta_{13}$	$(3.10 \pm 2.41) \times 10^{-2}$
ϕ_1	$(6.35 \pm 0.95) \times 10^{10}$
ϕ_7	$(0.542 \pm 0.063) \times 10^{10}$
ϕ_8	$(5.33 \pm 0.30) \times 10^{6}$
$\mathcal{L}_\odot$	$(9.07 \pm 1.24) \times 10^{11}$
χ^2	3.13

(a)

Parameter	Result
θ_{12}	0.581 ± 0.026
$\sin^2\theta_{13}$	$(3.11 \pm 2.41) \times 10^{-2}$
ϕ_1	$(6.31 \pm 0.90) \times 10^{10}$
ϕ_7	$(0.548 \pm 0.044) \times 10^{10}$
ϕ_8	$(5.34 \pm 0.30) \times 10^{6}$
$\mathcal{L}_\odot$	$(9.03 \pm 1.19) \times 10^{11}$
χ^2	3.15

(b)

Parameter	Result
θ_{12}	0.579 ± 0.026
$\sin^2\theta_{13}$	$(2.80 \pm 2.43) \times 10^{-2}$
ϕ_1	$(5.949 \pm 0.066) \times 10^{10}$
ϕ_7	$(0.547 \pm 0.13) \times 10^{10}$
ϕ_{CNO}	$(5 \pm 12) \times 10^{8}$
ϕ_8	$(5.34 \pm 0.30) \times 10^{6}$
χ^2	3.33

(c)

Parameter	Result
θ_{12}	0.579 ± 0.026
$\sin^2\theta_{13}$	$(2.80 \pm 2.45) \times 10^{-2}$
ϕ_1	$(6.94 \pm 0.051) \times 10^{10}$
ϕ_7	$(0.547 \pm 0.13) \times 10^{10}$
ϕ_{CNO}	$(5 \pm 11) \times 10^{8}$
ϕ_8	$(5.33 \pm 0.30) \times 10^{6}$
χ^2	3.15

(d)

The measured value of R_{NC}^{NCD} and the effective cross section, $\sigma_{8NC}^{D-\mathrm{NCD}}$, are calculated by splitting up Equation 7.14, with $\phi_{\mathrm{NC}}^{\mathrm{NCD}} \equiv R_{NC}^{\mathrm{NCD}}/\sigma_{8NC}^{D-\mathrm{NCD}}$:

$$R_{NC}^{\mathrm{NCD}} = \frac{N_{\mathrm{NC}}}{TN_d}, \tag{8.9}$$

$$\sigma_{8NC}^{D-\mathrm{NCD}} = \frac{\epsilon_{acc}\epsilon_{cap}R_{\mathrm{MC}}^{c}}{\phi^{\mathrm{MC}}N_d}. \tag{8.10}$$

N_d is the number of deuterons in the fiducial volume of SNO, $(6.0321 \pm 0.0012) \times 10^{31}$ [128], which is included only to give sensible units for the cross section.

Table 8.12: The global solar-neutrino analysis results with the improvements in the SNO, Super-Kamiokande, and Borexino measurements: $\sigma(P_{ee}^{\rm SNO}) = 0.0165$, $\sigma(R_{tot}^{\rm SNO}) = 0.037$, $\Phi_{ES} = 2.17 \pm 0.04$, and $R^{\rm Bxno} = 1.921 \pm 0.092$ (including the CNO measurement). In (a) $Ł_\odot$ is floating and ϕ_{CNO} is fixed, and in (b) $Ł_\odot$ is fixed and ϕ_{CNO} is floating. There are eight equations minimized over six floating parameters, and therefore two degrees of freedom.

Parameter	Result
θ_{12}	0.571 ± 0.017
$\sin^2\theta_{13}$	$(3.66 \pm 2.19) \times 10^{-2}$
ϕ_1	$(6.34 \pm 0.89) \times 10^{10}$
ϕ_7	$(0.548 \pm 0.004) \times 10^{10}$
ϕ_8	$(5.30 \pm 0.15) \times 10^{6}$
$Ł_\odot$	$(9.07 \pm 1.18) \times 10^{11}$
χ^2	0.05

(a)

Parameter	Result
θ_{12}	0.570 ± 0.017
$\sin^2\theta_{13}$	$(3.48 \pm 2.15) \times 10^{-2}$
ϕ_1	$(5.93 \pm 0.051) \times 10^{10}$
ϕ_7	$(0.576 \pm 0.13) \times 10^{10}$
ϕ_{CNO}	$(5 \pm 11) \times 10^{8}$
ϕ_8	$(5.30 \pm 0.16) \times 10^{6}$
χ^2	0.18

(b)

The number of neutrons is given in Equation 7.12, and the values for the other parameters are listed in Table 7.14. The values of $R_{NC}^{\rm NCD}$ and $\sigma_{8NC}^{D-{\rm NCD}}$ are determined to be:

$$R_{NC}^{\rm NCD} = (5.26 \pm 0.41) \times 10^{-37}\ {\rm s}^{-1}, \tag{8.11}$$

$$\sigma_{8NC}^{D-{\rm NCD}} = 8.79 \times 10^{-44}\ {\rm cm}^{-2}. \tag{8.12}$$

Two different versions of the analysis including the NCD measurement are performed: Table 8.14a is the basic analysis with the fluxes constrained by $Ł_\odot$, and can be compared to Table 8.5; Table 8.14b uses the neutrino measurements to constrain $Ł_\odot$, and can be compared to Table 8.7.

In the case of Table 8.14a, the new measurement of the NC flux has minor effects. $\sin^2\theta_{13}$ increases, and the uncertainty goes down slightly. It is non-zero at a 1.3-σ level. Additionally, ϕ_8 increases, since the flux measured in Section 7.11.5 is higher than that measured in the previous phases, but the uncertainty also goes up slightly since the measurements are somewhat different.

When $Ł_\odot$ is floating (Table 8.14b), the changes are similar: the central values of $\sin^2\theta_{13}$

and ϕ_8 went up. In addition, the solar luminosity is slightly better constrained by the additional measurement of the ^{8}B flux.

Table 8.13: The global solar-neutrino analysis results with the independent measurement of the NC flux with the SNO NCD Array. In (a) $Ł_\odot$ is fixed, and in (b) $Ł_\odot$ is floating. There are nine equations minimized over five floating parameters in (a) and six floating parameters in (b), and therefore four and three degrees of freedom, respectively.

Parameter	Result
θ_{12}	0.576 ± 0.025
$\sin^2\theta_{13}$	$(3.0 \pm 2.2) \times 10^{-2}$
ϕ_1	$(5.968 \pm 0.063) \times 10^{10}$
ϕ_7	$(0.535 \pm 0.060) \times 10^{10}$
ϕ_8	$(5.55 \pm 0.32) \times 10^6$
χ^2	3.40

(a)

Parameter	Result
θ_{12}	0.571 ± 0.025
$\sin^2\theta_{13}$	$(3.7 \pm 2.4) \times 10^{-2}$
ϕ_1	$(6.32 \pm 0.095) \times 10^{10}$
ϕ_7	$(0.533 \pm 0.060) \times 10^{10}$
ϕ_8	$(5.67 \pm 0.33) \times 10^6$
$Ł_\odot$	$(8.98 \pm 1.26) \times 10^{11}$
χ^2	3.29

(b)

Once the full NCD neutrino data set is analyzed the uncertainties on the number of NC neutrons will be improved, which will improve the measurements of the solar-neutrino parameters. To see the potential effects the uncertainties are estimated with a fake data test and the central value for the number of NC neutrons is extrapolated from the one-third data set; this projected number of neutrons is given in Equation 7.13. The value of R_{NC}^{NCD} ($\sigma_{8NC}^{D-\mathrm{NCD}}$ is the same as above) is:

$$R_{NC}^{\mathrm{NCD}} = (5.26 \pm 0.25) \times 10^{-37}\ \mathrm{s}^{-1}. \tag{8.13}$$

This analysis is intended only to show the improvement in the measurements of the solar-neutirno parameters, and the improvements are significant. As above, Table 8.15a can be compared to Table 8.5 and Table 8.14b can be compared to Table 8.7.

In the case of Table 8.14a, the projected measurement of the NC flux has several effects. The uncertainty on θ_{12} is reduced, while the central value does not move significantly. $\sin^2\theta_{13}$ increases, and the uncertainty goes down slightly. It is now non-zero at a 1.7-σ level. Finally, ϕ_8 increases, since the flux measured in Section 7.11.5 is higher than that

measured in the previous phases, and the uncertainty is reduced.

When $\mathcal{L}_\odot$ is floating (Table 8.14b), the changes are similar: the uncertainties on θ_{12}, $\sin^2\theta_{13}$, and ϕ_8 are smaller, while the central value of θ_{12} went down slightly, and those of $\sin^2\theta_{13}$ and ϕ_8 went up. As is seen above, the solar luminosity is better constrained with the additional measurement of the ^{8}B neutrino flux.

Table 8.14: The global solar-neutrino analysis results with the independent measurement of the NC flux with the SNO NCD Array, where the uncertainties are estimated with a fake data test, and the central value is determined with the one-third data set. In (a) $\mathcal{L}_\odot$ is fixed, and in (b) $\mathcal{L}_\odot$ is floating. There are nine equations minimized over five floating parameters in (a) and six floating parameters in (b), and therefore four and three degrees of freedom, respectively.

Parameter	Result
θ_{12}	0.565 ± 0.021
$\sin^2\theta_{13}$	$(3.64 \pm 2.15) \times 10^{-2}$
ϕ_1	$(5.968 \pm 0.063) \times 10^{10}$
ϕ_7	$(0.535 \pm 0.059) \times 10^{10}$
ϕ_8	$(5.74 \pm 0.24) \times 10^6$
χ^2	4.22

(a)

Parameter	Result
θ_{12}	0.567 ± 0.022
$\sin^2\theta_{13}$	$(3.9 \pm 2.3) \times 10^{-2}$
ϕ_1	$(6.32 \pm 0.095) \times 10^{10}$
ϕ_7	$(0.533 \pm 0.060) \times 10^{10}$
ϕ_8	$(5.74 \pm 0.24) \times 10^6$
$\mathcal{L}_\odot$	$(8.99 \pm 1.23) \times 10^{11}$
χ^2	4.08

(b)

8.3 Summary

As with any idealized or simplified model, this set of eight equations serves as a tool to identify relationships between the oscillation parameters, neutrino fluxes, various experimental measurements, and the solar luminosity. With a variety of modifications it can highlight how the measurements affect the measured oscillation parameters and neutrino fluxes, explore future experimental improvements, and look at the neutrino measurement of the solar luminosity.

Two of the most interesting parameters to study are $\sin^2\theta_{13}$ and ϕ_{CNO}. Neither is well constrained by any individual measurement. The solar-neutrino experiments and the solar luminosity consistently find a value for $\sin^2\theta_{13}$ at greater than 1-σ, though at a value

significantly larger than the limit found with non-solar-neutrino experiments. With the available data it is impossible to attempt to find ϕ_{CNO} because of its correlation with ϕ_1. As has been shown, however, a measurement of ϕ_{CNO} by Borexino would be enough to break that correlation and start to find a value for ϕ_{CNO} in the global analysis.

By floating the luminosity constraint we learn that the photon measurement of the solar luminosity most strongly constrains ϕ_1 since every completion of the pp-chain involves the creation of either a pp or pep neutrino, both of which contribute to this flux. Furthermore, the neutrino experiments themselves make a 16.5% measurement of the solar luminosity. The electromagnetic measurement has 0.4% uncertainties; to establish the steady-state assumption behind the solar model one would like to make a neutrino-based measurement accurate at the 1% level. The improvements explored in this work decrease the uncertainty to approximately 13%.

The future experimental improvements explored in this analysis include P_{ee}^{SNO} and R_{tot}^{SNO}, Φ_{ES}^{SK}, and R_{Bxno}. The SNO measurement holds the most promise for improving the measured values of θ_{12} and ϕ_8. The measured central value of Φ_{ES} seems to have some tension with the other parameters, but improving the accuracy of the measurement does decrease the uncertainties on $\sin^2\theta_{13}$ and $L_{\odot}$. That tension is actually the dominant contribution to χ^2 in this model. An improved measurement of ^{7}Be measurement by Borexino will increase the accuracy of ϕ_1 and ϕ_7. More significantly, if Borexino measures ϕ_{CNO}, then ϕ_{CNO} can be added to the list of floating parameters in this analysis.

Beyond improving the accuracy of existing measurements one could use this simple model to consider the effects of additional measurements. In particular, the LENS experiment [142] has great potential to make a real-time measurement of neutrinos all the way down to the pp flux. That experiment could be added to the model to gain insight about what improvements it would make to our overall understanding of solar neutrinos and the applicable mixing angles.

The analysis of the NCD data presented in Chapter 7 of this thesis produces an improved measurement of the NC flux. Using the analysis of the one-third data set the measurement of θ_{13} improves. When the uncertainties for the full NCD data set are estimated and included in the global analysis it improves the constraints on the ^{8}B neutrino flux as well as θ_{12} and

θ_{13}. When the neutrino fluxes constrain $L_{\odot}$, the new flux measurement also improves the constraint on the solar luminosity.

Chapter 9

CONCLUSIONS

This thesis presents an independent method of measuring the NC ^{8}B solar-neutrino flux using the NCD Array. The NCD Array was added to the SNO detector for the third phase of the experiment. Its purpose is to make a measurement of the NC neutrons that is independent of the PMT array, and thereby break the correlation between the NC and the CC measurements. The first analysis of the NCD-phase data used only the energy information about the NCD pulses. The analysis presented here takes advantage of the full pulse shapes and uses libraries of pulses generated by the NCD Monte Carlo to help differentiate between neutron-capture signal pulses and alpha backgrounds.

The NCD Monte Carlo is a unique, highly-detailed simulation of the NCD system. It includes the physics of ion propagation in the gas and the drift of the primary-ionization electrons to the anode wire, the charge saturation effects that occur near the anode, and the effects of the secondary-ionization ions drifting towards the cathode. After the formation of the pulse on the anode wire the simulation includes the propagation of the pulse along the NCD string and cable, the effects of the preamplifier, and the shaper and MUX data-acquisition systems. The shaper system measures the pulse energy and the MUX system logarithmically amplifies the pulses. The full waveforms are digitized and recorded by a digital oscilloscope.

A variety of measurements of the properties of the NCD system were made in the course of the development and verification of the NCD MC. One of the parameters measured was the average ionization energy, W. In the simulation W determines how many primary-ionization electrons are formed in the gas for a given amount of energy deposited, which primarily affects the size of a pulse. Because the gas gain, M, also affects the size of the pulse, the actual parameter relevant to NCD pulse simulation is M/W. M/W is proportional to the total current produced by the neutron captures in an NCD counter. At the

NCD operating voltage it was found that $M/W = 6.36 \pm 0.33(\text{stat.}) \pm 0.03(\text{syst.})$ eV^{-1}. Furthermore, W itself was determined to be 34.13 ± 12.4 eV with a measurement of the current in the ion-saturation voltage regime.

The ion mobility, μ, is responsible for the shape of the ion tail that accompanies every neutron-capture and alpha pulse. It was measured by fitting the tail of the sharpest neutron-capture pulses. The time constant for the ion tail was determined to be 5.50 ± 0.14 ns, which is equivalent to an ion mobility of $\mu = (1.082 \pm 0.027) \times 10^{-8}$ cm^2 ns^{-1} V^{-1}.

An extensive effort was made to verify the NCD MC. In the course of that effort, tests were performed to verify that the low-level data-cleaning cuts behaved similarly on the MC pulses and on the data. The MC passed this test successfully.

The first goal of any analysis of the NCD data is to determine how many neutron captures took place. This task requires identifying the signal pulses from among the background alpha events. An energy-based analysis is attractive since the energy distribution of neutron-capture pulses is easily differentiated from the energy distribution of the alpha pulses. However, while the neutrons are well understood with extensive calibrations, the only pure sample of alpha events in the neutron-energy region is from the ^{4}He strings. Because there are several alpha emitters involved those events are not necessarily representative of the alpha events on the entire NCD array.

The NCD MC can be used to analyze the full pulse shapes, instead of just the energy distributions. A pulse-fitting algorithm was developed using libraries of neutron-capture and alpha-background pulses. The neutron library used in the MC-based pulse fitting consists of 3,329 pulses, and the alpha background library consists of 2,974 wall alphas and 2,599 wire alphas. Each pulse in a data set is fit with every pulse in both libraries. The goodness-of-fit parameter is the Pearson's χ^2 value between the data-set pulse and the library pulse, with the best fit being the library pulse that produces the lowest value of χ^2. A term is added to the χ^2 to account for the energy difference between the two pulses. The variance used includes both the electronics noise represented by the RMS at the end of the pulse waveform and the digitization noise, which varies with voltage.

The goodness-of-fit parameters for the neutron-library fit and the alpha-library fit are χ^2_n and χ^2_α, respectively. The log of the ratio of the two χ^2s is $\Delta \log(\chi^2) = \log(\chi^2_\alpha/\chi^2_n)$. In

the $\Delta\log(\chi^2)$ parameter space there is a subset of neutron pulses that is almost entirely free of background alphas, and it can be isolated with a simple cut in the one-dimensional space. In such a background-free region the systematic uncertainties due to the alphas are significantly reduced. While the statistical uncertainties are increased by using only part of the data, the total uncertainty is reduced compared with an energy fit using all of the data.

During the development of this pulse-shape analysis it was found that the $\Delta\log(\chi^2)$ distributions varied between the strings. Shift and scaling corrections are used to make the distributions uniform between the strings, resulting in the corrected parameter space, $\Delta\log(\chi^2)_{corr}$. The tail of the alpha distribution is modeled with a double exponential function, which adds to the systematic uncertainties. However, the effects of this uncertainty, and all of the other alpha-related uncertainties, are reduced by having so few events remaining after the $\Delta\log(\chi^2)_{corr}$ cut.

Fake-data tests were used to optimize the $\Delta\log(\chi^2)_{corr}$ cut. Random alpha and neutron-capture events were drawn from the ^{24}Na and ^{4}He data sets so that the number of alpha and neutron-capture events approximated the expected numbers from the full neutrino data set. The optimal cut was found to be $\Delta\log(\chi^2)_{corr} > -0.062683$, where the neutron cut efficiency is approximately 58%. Blindness conditions are still in effect as of this writing, so the full data set has not been analyzed. However, an analysis was performed on a data set consisting of one-third of the full data set. The number of NC neutrons was determined to be 351.8 ± 25.8 (stat.) $^{+10.6}_{-10.1}$ (syst.). This corresponds to a neutrino flux of $\phi_{NC}^{\mathrm{NCD}} = (5.93 \pm 0.43$ (stat.) $^{+0.27}_{-0.26}$ (syst.) $\times 10^6$ ν cm^{-2} s^{-1}. This result is in reasonable agreement with the energy-based analysis of the NCD data and similar uncertainties. It is higher than the NC fluxes measured during the D_2O and salt phases of SNO. Comparing to the SSM predictions, this result agrees well with the BPS08(GS) model. A fake data test is used to estimate the uncertainties that will apply when the full neutrino data set is analyzed. It has been found that the pulse-shape-based analysis of the NCD data will significantly reduce the uncertainties on the NC flux compared to the energy-based analysis.

The implications of the neutrino flux determined by the NCD array are investigated with a model that combines all of the different solar-neutrino measurements and KamLAND with the neutrino-based determination of the solar luminosity. The analysis shows that the neu-

trino experiments can make a measurement of the solar luminosity with a 16% uncertainty. With reasonable experimental improvements in the near future that uncertainty can be reduced to approximately 13%. Furthermore the solar-neutrino measurements and the KamLAND reactor-neutrino measurement, when coupled with the solar luminosity constraints, make a $> 1\sigma$ measurement of $\sin^2\theta_{13}$. Adding the results of the NCD analysis described above improves the measurement of the ^{8}B solar-neutrino flux and the measurements of θ_{12} and θ_{13}.

Almost fifty years of studying solar neutrinos has revolutionized our understanding of neutrinos and confirmed the theoretical models of how the sun generates energy. With more and more data collected with increasingly sophisticated tools we now have the ability to make precision measurements of the solar-neutrino fluxes and the properties of the neutrinos themselves. SNO is in the process of making the best possible measurement of the ^{8}B neutrino flux for the foreseeable future, and the analysis of the NCD data presented in this thesis is contributing to that effort.

BIBLIOGRAPHY

[1] J. N. Bahcall and R. Davis, Jr., *An account of the development of the Solar Neutrino Problem*. Cambridge University Press, 1982, ch. 12, pp. 243–285.

[2] J. N. Bahcall, "Solar neutrinos. I. theoretical," *Phys. Rev. Lett.*, vol. 12, pp. 300–302, 1964.

[3] R. Davis, Jr., "Solar neutrinos. II. experimental," *Phys. Rev. Lett.*, vol. 12, pp. 303–305, 1964.

[4] C. F. von Weizsäcker, *Phys. Z.*, vol. 176, 1937.

[5] ——, *Phys. Z.*, vol. 663, 1938.

[6] H. A. Bethe and C. L. Critchfield, "The formation of deuterium by proton combination," *Phys. Rev.*, vol. 54, p. 248, 1938.

[7] H. A. Bethe, "Energy production in stars," *Phys. Rev.*, vol. 55, p. 436, 1939.

[8] K. Miknaitis, "A search for matter enhanced neutrino oscillations through measurements of day and night solar neutrino fluxes at the Sudbury Neutrino Observatory," Ph.D. dissertation, University of Washington, 2005.

[9] L. C. Stonehill, J. A. Formaggio, and R. G. H. Robertson, "Solar neutrinos from CNO electron capture," *Phys. Rev.*, vol. C69, p. 015801, 2004.

[10] J. N. Bahcall and R. K. Ulrich, "Solar models, neutrino experiments, and helioseismology," *Rev. Mod. Phys.*, vol. 60, p. 297, 1988.

[11] J. N. Bahcall, M. H. Pinsonneault, and G. J. Wasserburg, "Solar models with helium and heavy-element diffusion," *Rev. Mod. Phys.*, vol. 67, no. 781, 1995.

[12] S. Basu and H. M. Antia, "Helioseismology and solar abundances," *Phys. Rept.*, vol. 457, pp. 217–283, 2008.

[13] C. Peña-Garay and A. M. Serenelli, "Solar neutrinos and the solar composition problem," *arXiv:0811.2424 [astro-ph]*, 2008.

[14] W. Pauli, "Letter to the Physical Society of Tubingen," Reproduced in [15], 1930. [Online]. Available: http://cdsweb.cern.ch/record/83282

[15] L. Brown, "The idea of the neutrino," *Phys. Today*, p. 23, September 1978.

[16] J. Chadwick, "Possible existence of a neutron," *Nature*, p. 312, 1932.

[17] E. Fermi, "Trends to a theory of beta radiation," *Nuovo Cim.*, vol. 11, pp. 1–19, 1934.

[18] H. A. Bethe and R. Peierls, "The 'Neutrino'," *Nature*, vol. 133, p. 532, 1934.

[19] C. L. Cowan, Jr., F. Reines, F. B. Harrison, H. W. Kruse, and A. D. McGuire, "Detection of the free neutrino: a confirmation," *Science*, vol. 124, pp. 103–104, 1956.

[20] E. Majorana, "Theory of the symmetry of electrons and positrons," *Nuovo Cim.*, vol. 14, pp. 171–184, 1937.

[21] R. Davis, Jr., "Attempt to detect the antineutrinos from a nuclear reactor by the $Cl^{37}(\overline{\nu}, e^-)A^{37}$ reaction," *Phys. Rev.*, vol. 97, pp. 766–769, 1955.

[22] E. J. Konopinski and M. Langer, "The experimental clarification of the theory of β-decay," *Annual Review of Nuclear Science*, vol. 2, pp. 261–304, 1953.

[23] G. Danby *et al.*, "Observation of high-energy neutrino reactions and the existence of two kinds of neutrinos," *Phys. Rev. Lett.*, vol. 9, pp. 36–44, 1962.

[24] M. L. Perl *et al.*, "Evidence for anomalous lepton production in $e^+ - e^-$ annihilation," *Phys. Rev. Lett.*, vol. 35, pp. 1489–1492, 1975.

[25] K. Kodama *et al.*, "Observation of tau-neutrino interactions," *Phys. Lett.*, vol. B504, pp. 218–224, 2001.

[26] R. Davis, Jr., D. S. Harmer, and K. C. Hoffman, "Search for neutrinos from the sun," *Phys. Rev. Lett.*, vol. 20, pp. 1205–1209, 1968.

[27] M. R. Krishnaswamy *et al.*, "The Kolar Gold Fields neutrino epxeriment I. The interactions of cosmic ray neutrinos," *Proc. Roy. Soc. Lond. A*, vol. 323, pp. 489–509, 1971.

[28] K. Hirata *et al.*, "KAMIOKANDE result on a neutrino burst from the supernova SN1987a," in *Moscow 1987, Proceedings, Cosmic ray*, vol. 9, 1987, pp. 53–56.

[29] J. C. Van Der Velde *et al.*, "Neutrinos from SN1987a in the IMB detector," *Nucl. Instrum. Meth.*, vol. A264, pp. 28–31, 1988.

[30] E. D. Commins and P. H. Bucksbaum, *Weak interactions of leptons and quarks*. Cambridge University Press, 1983.

[31] T.-D. Lee and C. N. Yang, "Parity nonconservation and a two-component theory of the neutrino," *Phys. Rev.*, vol. 105, pp. 1671–1675, 1957.

[32] C.-S. Wu, E. Ambler, R. W. Hayward, D. D. Hoppes, and R. P. Hudson, "Experimental test of parity conservation in beta decay," *Phys. Rev.*, vol. 105, pp. 1413–1414, 1957.

[33] R. L. Garwin, L. M. Lederman, and M. Weinrich, "Observations of the failure of conservation of parity and charge conjugation in meson decays: the magnetic moment of the free muon," *Phys. Rev.*, vol. 105, pp. 1415–1417, 1957.

[34] M. Goldhaber, L. Grodzins, and A. W. Sunyar, "Helicity of neutrinos," *Phys. Rev.*, vol. 109, pp. 1015–1017, 1958.

[35] S. Weinberg, "A model of leptons," *Phys. Rev. Lett.*, vol. 19, p. 1264, 1967.

[36] G. 't Hooft, "Renormalizable Lagrangians for massive Yang-Mills fields," *Nucl. Phys.*, vol. 35, pp. 167–188, 1971.

[37] F. J. Hasert *et al.*, "Observation of neutrino-like interactions without muon or electron in the gargamelle neutrino experiment," *Phys. Lett.*, vol. B46, pp. 138–140, 1973.

[38] G. Arnison *et al.*, "Experimental observation of isolated large transverse energy electrons with associated missing energy at $\sqrt{s} = 540$ GeV," *Phys. Lett.*, vol. 122, pp. 103–116, 1983.

[39] ——, "Experimental observation of lepton pairs of invariant mass around 95 GeV/c^2 at the CERN SPS collider," *Phys. Lett.*, vol. 126, pp. 398–410, 1983.

[40] B. Kayser, F. Gibrat-Debu, and F. Perrier, *The physics of massive neutrinos*, ser. World Scientific Lecture Notes in Physics. World Scientific, 1989, vol. 25.

[41] W. Haxton, "Neutrino oscillations and the solar neutrino problem," *arxiv:nucl-th/0004052*, 2000.

[42] B. Pontecorvo, "Inverse beta processes and nonconservation of lepton charge," *Sov. Phys. JETP*, vol. 7, pp. 172–173, 1958.

[43] Z. Maki, M. Nakagawa, and S. Sakata, "Remarks on the unified model of elementary particles," *Prog. Theor. Phys.*, vol. 28, p. 870, 1962.

[44] S. P. Mikheyev and A. Y. Smirnov, *Sov. J. Nucl. Phys.*, vol. 42, p. 913, 1985.

[45] L. Wolfenstein, "Neutrino oscillations in matter," *Phys. Rev.*, vol. 17, pp. 958–960, 1978.

[46] S. J. Parke, "Nonadiabatic level crossing in resonant neutrino oscillations," *Phys. Rev. Lett.*, vol. 57, p. 1275, 1986.

[47] W. Haxton, "Adiabatic conversion of solar neutrinos," *Phys. Rev. Lett.*, vol. 57, p. 1271, 1986.

[48] E. K. Akhmedov, M. A. Tórtola, and J. W. F. Valle, "A simple analytic three-flavour description of the day-night effect in the solar neutrino flux," *JHEP*, vol. 5, p. 57, 2004.

[49] B. Pontecorvo, "Inverse beta process," Chalk River Laboratory Report PD-205, 1946.

[50] L. W. Alvarez, "A proposed experimental test of the neutrino theory," University of California Radiation Laboratory Report UCRL-328, 1949.

[51] J. N. Bahcall, W. A. Fowler, I. Iben, and R. L. Sears, "Solar neutrino flux," *Astrophys. J.*, vol. 137, pp. 344–346, 1963.

[52] B. T. Cleveland, T. Daily, R. Davis, Jr., J. R. Distel, K. Lande, C. K. Lee, P. S. Wildenhain, and J. Ullman, "Measurement of the solar electron neutrino flux with the Homestake chlorine detector," *Astrophys. J.*, vol. 496, p. 505, 1998.

[53] K. Hirata *et al.*, University of Tokyo ICEPP, Report UT-87-04, 1987.

[54] J. N. Bahcall, "Solar models and solar neutrinos: Current status," *Phys. Scripta*, vol. T121, pp. 46–50, 2005.

[55] C. Cattadori, N. Ferrari, and L. Pandola, "Results from radiochemical experiments with main emphasis on the gallium ones," *Nucl. Phys. Proc. Suppl.*, vol. 143, pp. 3–12, 2005.

[56] Y. Fukuda *et al.*, "Solar neutrino data covering solar cycle 22," *Phys. Rev. Lett.*, vol. 77, pp. 1683–1686, 1996.

[57] K. S. Hirata *et al.*, "Observation of a small atmospheric ν_μ/ν_e ratio in Kamiokande," *Phys. Lett. B*, vol. 280, p. 146, 1992.

[58] D. Casper *et al.*, "Measurement of atmospheric neutrino composition with the IMB-3 detector," *Phys. Rev. Lett.*, vol. 66, p. 2561, 1991.

[59] Y. Fukuda *et al.*, "Study of the atmospheric neutrino flux in the multi-gev energy range," *Phys. Lett.*, vol. B436, pp. 33–41, 1998.

[60] M. H. Ahn *et al.*, "Measurement of neutrino oscillation by the K2K experiment," *Phys. Rev. D*, vol. 74, p. 072003, 2006.

[61] P. Adamson *et al.*, "Study of muon neutrino disappearance using the Fermilab Main Injector neutrino beam," *Phys. Rev. D.*, vol. 77, p. 072002, 2008.

[62] Q. R. Ahmad *et al.*, "Measurement of charged current interactions produced by ^{8}B solar neutrinos at the Sudbury Neutrino Observatory," *Phys. Rev. Lett.*, vol. 87, p. 071301, 2001.

[63] ——, "Direct evidence for neutrino flavor transformation from neutral-current interactions in the Sudbury Neutrino Observatory," *Phys. Rev. Lett.*, vol. 89, p. 011301, 2002.

[64] ——, "Measurement of day and night neutrino energy spectra at sno and constraints on neutrino mixing parameters," *Phys. Rev. Lett.*, vol. 89, p. 011302, 2002.

[65] B. Aharmim *et al.*, "An independent measurement of the total active ^{8}B solar neutrino flux using an array of ^{3}He proportional counters at the Sudbury Neutrino Observatory," *Phys. Rev. Lett.*, vol. 101, p. 111301, 2008.

[66] S. Abe *et al.*, "Precision measurement of neutrino oscillation parameters with KamLAND," *Phys. Rev. Lett.*, vol. 100, p. 221803, 2008.

[67] J. P. Cravens *et al.*, "Solar neutrino measurements in Super-Kamiokande-II," 2008, arXiv:hep-ex/0803.4312.

[68] J. Boger *et al.*, "The Sudbury Neutrino Observatory," *Nucl. Instrum. Meth.*, vol. A449, pp. 172–207, 2000.

[69] B. Aharmim *et al.*, "Electron energy spectra, fluxes, and day-night asymmetries of ^{8}B solar neutrinos from the 391-day salt phase SNO data set," *Phys. Rev. C*, vol. 72, p. 055502, 2005.

[70] G. L. Fogli, E. Lisi, A. Marrone, and A. Palazzo, "Global analysis of three-flavor neutrino masses and mixings," *Prog. Part. Nucl. Phys.*, vol. 57, 2006.

[71] F. Rademakers, M. Goto, P. Canal, and R. Brun, "ROOT status and future developments," 2003 Computing in High Energy and Nuclear Physics, La Jolla, CA, 2003.

[72] W. R. Nelson, H. Hirayama, and D. W. O. Rogers, "The EGS4 code system," SLAC-0265, 1985.

[73] MCNP: A general Monte Carlo N-Particle transport code. [Online]. Available: http://laws.lanl.gov/x5/MCNP/index.html

[74] A. Kling, F. Barao, M. Nakagawa, L. Tavora, and P. Vaz, "Advanced Monte Carlo for radiation physics, particle transport simulation and applications," in *MC2000*, Lisbon, Portugal, October 2000.

[75] D. Casper, "The NUANCE neutrino simulation, and the future," *Nucl. Phys. Proc. Suppl.*, vol. 112, pp. 161–170, 2002.

[76] G. A. Cox, "Data integrity and electronic calibrations for the Neutral Current Detector phase measurement of the ^{8}B solar neutrino flux at the Sudbury Neutrino Observatory," Ph.D. dissertation, Univeristy of Washington, 2008.

[77] B. Jamieson, "SNO NCD phase signal extraction on unblinded data with integration over systematic nuisance parameters by Markov-chain Monte Carlo," SNO Internal Document, 2008.

[78] L. C. Stonehill, "Deployment and background characterization for the Sudbury Neutrino Observatory Neutral Current Detectors," Ph.D. dissertation, University of Washington, 2005.

[79] The NCD Analysis Group, "The NCD unidoc," SNO Internal Document, 2002.

[80] J. F. Amsbaugh *et al.*, "An array of low-background ^{3}He proportional counters for the Sudbury Neutrino Observatory," *Nucl. Instrum. Meth.*, vol. A579, 2007.

[81] T. Bullard and M. Smith, "A technique for separating alpha and neutron events in Neutral Current Detectors," SNO Internal Document.

[82] A. Hime, Private Communication, 2006.

[83] N. Tolich, "NCD data cleaning comparison," SNO Internal Document, 2005. [Online]. Available: http://manhattan.sno.laurentian.ca/sno/ananoteb.nsf/URL/MANN-6JL8NP

[84] H. S. Wan Chan Tseung, "Simulation of NCD alpha background energy PDFs," SNO Internal Document, 2007. [Online]. Available: http://manhattan.sno.laurentian.ca/sno/ananoteb.nsf/URL/MANN-78S64R

[85] B. Beltran, J. Monroe, N. S. Oblath, G. Prior, K. Rielage, R. G. H. Robertson, and H. S. Wan Chan Tseung, "NCD MC readiness report for the first NCD paper," SNO Internal Document, 2008.

[86] K. Rielage *et al.*, "SNO NCD phase analysis unidoc," SNO Internal Document, May 2008.

[87] H. S. Wan Chan Tseung, "Simulation of the Sudbury Neutrino Observatory Neutral Current Detectors," Ph.D. dissertation, Oxford University, 2008.

[88] J. F. Ziegler, "SRIM 2003," Software Package, 2003.

[89] J. F. Ziegler, J. P. Biersack, and U. Littmark, *The Stopping and Range of Ions in Matter*. Pergamon Press, 1985.

[90] A. Hime, "Detector operating parameters & constraints," SNO Internal Document.

[91] H. S. Wan Chan Tseung, "The motion of electrons in NCD gas v2.0," SNO Internal Document, 2007. [Online]. Available: http://manhattan.sno.laurentian.ca/sno/ananoteb.nsf/URL/MANN-6VYDCG

[92] R. Veenhof, "Garfield," Software Package, 2007.

[93] S. McGee, Private Communication, 2007.

[94] H. S. Wan Chan Tseung, "A simulation of space charge effects in NCDs," SNO Internal Document, 2004.

[95] G. F. Knoll, *Radiation Detection and Measurement*, 3rd ed. John Wiley & Sons, Inc., 2000.

[96] D. H. Wilkinson, *Ionization Chambers and Counters*. Cambridge University Press, 1950.

[97] T. Burritt, A. Cox, M. Huang, S. McGee, G. Prior, R. G. H. Robertson, T. van Wechel, and J. Wendland, "NCD ECA unidoc," SNO Internal Document, 2005. [Online]. Available: http://manhattan.sno.laurentian.ca/sno/ananoteb.nsf/URL/MANN-6H97QT

[98] T. Quarles *et al.* The Spice Home Page. [Online]. Available: http://bwrc.eecs.berkeley.edu/Classes/icbook/SPICE/

[99] H. Deng, "Transmission line model and FTD (imppulse) fitter," SNO Internal Document, May 2006. [Online]. Available: http://owl.phy.queensu.ca/~ckrauss/private/Kingston_May_Meeting/Deng_kingston.pdf

[100] J. M. Wouters and A. Hime, "Anode wire constraints for ^{3}He proportional counters in the Sudbury Neutrino Observatory," SNO-STR-95-016, 1995.

[101] H. S. Wan Chan Tseung, "Generation of NCD noise," SNO Internal Document, 2006. [Online]. Available: http://manhattan.sno.laurentian.ca/sno/ananoteb.nsf/URL/MANN-6RTR87

[102] ——, "Electron pulse calculation updates," SNO Internal Document, May 2008.

[103] ——, Private Communication, 2006.

[104] "Average energy required to produce an ion pair," ICRU Report 31, 1979.

[105] G. A. Cox *et al.*, "Sudbury neutrino observatory neutral current detectors signal readout system," *IEEE Trans. Nucl. Sci.*, vol. 51, 2004.

[106] S. McGee, Private Communication, 2006.

[107] X. Yang, S. E. Babayan, and R. F. Hicks, "Measurement of the flourine atom concentration in a carbon tetraflouride and helium atmospheric-pressure plasma," *Plasma Sources Sci. Technol.*, vol. 12, p. 484, 2003.

[108] P. J. Doe, J. V. Germani, A. W. P. Poon, R. G. H. Robertson, T. D. Steiger, and J. F. Wilkerson, "Construction of an array of neutral-current detectors for the Sudbury Neutrino Observatory," SNO-STR-95-023, 1995.

[109] J. Monroe, "Garfield attachment study," SNO Internal Document, 2007.

[110] H. W. Ellis *et al.*, "Transport properties of gaseous ions over a wide energy range," *Atomic Data and Nuclear Data Tables*, vol. 17, p. 177, 1976.

[111] H. Deng, Private Communication, 2008.

[112] N. Tolich, "NCD data cleaning: FREquency analysis kit," SNO Internal Document, 2005. [Online]. Available: http://manhattan.sno.laurentian.ca/sno/ananoteb.nsf/URL/MANN-6J6UNM

[113] W. F. Sheppard, "On the calculation of the most probable values of frequency constants, for data arranged according to equidistant division on a scale," *Proc. London Math. Soc.*, vol. 29, p. 353, 1898.

[114] L. Kristensen and P. Kirkegaard, "Digitization noise in power spectral analysis," *J. Atmos. Oceanic Tech.*, vol. 4, p. 328, 1987.

[115] F. James. MINUIT: Function minimization and error analysis. [Online]. Available: http://wwwasdoc.web.cern.ch/wwwasdoc/minuit/minmain.html

[116] N. Tolich, "DWK description and performance," SNO Internal Document, 2007. [Online]. Available: http://manhattan.sno.laurentian.ca/sno/ananoteb.nsf/URL/MANN-6Y929J

[117] H. Deng, "FTD pulse shape analysis," SNO Internal Document, 2007. [Online]. Available: http://manhattan.sno.laurentian.ca/sno/ananoteb.nsf/URL/MANN-6ZZ2U2

[118] R. Martin, "The Queen's grid fitter: A detailed overview of the analysis scheme," SNO Internal Document, 2007. [Online]. Available: http://manhattan.sno.laurentian.ca/sno/ananoteb.nsf/URL/MANN-6ZXNF5

[119] K. Rielage, "Proposal to remove NCD strings from final NC analysis, version 2.0," SNO Internal Document, 2007.

[120] E. Guillian, "Some correction factors for converting extracted neutron numbers to the solar neutrino flux," SNO Internal Document, April 2008.

[121] N. Jelley, B. Monreal, and R. G. H. Robertson, "Neutron topic committee final report," SNO Internal Document, May 2008.

[122] B. Monreal, Private Communication, 2009.

[123] W. T. Winter *et al.*, "The ^{8}B neutrino spectrum," *Phys. Rev. C*, vol. 73, p. 025503, 2006.

[124] S. Nakamura *et al.*, "Neutrino-deuteron reactions at solar neutrino energies," *Nucl. Phys.*, vol. A707, p. 561, 2002.

[125] A. Kurylov, M. J. Ramsey-Musolf, and P. Vogel, "Radiative corrections in neutrino-deuterium disintegration," *Phys. Rev. C*, vol. 65, p. 055501, 2002.

[126] M. Chen, "Untitled," SNO Internal Document, 2008.

[127] J. Detwiler *et al.*, "Livetime for the full NCD data set," SNO Internal Document, January 2008.

[128] R. G. H. Robertson, "Long D_2O paper: Target properties, v 5," SNO Internal Document, June 2007.

[129] B. Aharmim *et al.*, "Determination of the ν_e and total ^{8}B solar neutrino fluxes with the Sudbury Neutrino Observatory Phase I data set," *Phys. Rev. C*, vol. 75, p. 045502, 2007.

[130] J. N. Bahcall and C. Peña-Garay, "A road map to solar neutirno fluxes, neutrino oscillation parameters, and tests for new physics," *JHEP*, vol. 311, 2003.

[131] K. M. Heeger and R. G. H. Robertson, "Probability of a solution to the Solar Neutrino Problem within the Minimal Standard Model," *Phys. Rev. Lett.*, vol. 77, no. 18, 1996.

[132] R. G. H. Robertson, "Solar neutrinos," arXiv:nucl-ex/0602005v1.

[133] S. P. Langley, *Researches on solar heat and its absorption by the earth's atmosphere*, ser. Professional Papers of the Signal Service, W. B. Hazen, Ed. United States of America, War Department, 1884, vol. XV.

[134] J. N. Bahcall, "The luminosity constrain on solar neutrino fluxes," *Phys. Rev. C*, vol. 65, p. 025801, 2002.

[135] B. Aharmim *et al.*, "A search for neutrinos from the solar hep reaction and the diffuse supernova neutrino background with the Sudbury Neutrino Observatory," *Astrophys. J.*, vol. 653, p. 1545, 2006.

[136] The Borexino Collaboration, "Measurement of the solar 8B neutrino flux with 246 live days of borexino and observation of the MWS vacuum-matter transition," *arXiv:0808.2868*, 2008.

[137] J. Hosaka *et al.*, "Solar neutrino measurements in Super-Kamiokande-I," *Phys. Rev. D.*, vol. 73, p. 112001, 2006.

[138] The Borexino Collaboration, "New results on solar neutrino fluxes from 192 days of Borexino data," *Phys. Rev. Lett.*, vol. 101, p. 091302, 2008.

[139] G. L. Fogli *et al.*, "SNO, KamLAND and neutrino oscillations: theta(13)," *arXiv:0905.3549 [hep-ph]*, 2009.

[140] ——, "Hints of $\theta_{13} > 0$ from global neutrino data analysis," *Phys. Rev. Lett.*, vol. 101, p. 141801, 2008.

[141] M. Maltoni and T. Schwetz, "Three-flavor neutrino oscillation update and comments on possible hints for a non-zero θ_{13}," arXiv:0812.3161v1, 2008.

[142] C. Grieb and R. S. Raghavan, "Probing the temperature profile of energy production in the sun," *Phys. Rev. Lett.*, vol. 98, p. 141102, 2007.

[143] S. McGee, Private Communication, 2005.

[144] J. Detwiler, Private Communication, 2006.

[145] H. S. Wan Chan Tseung, Private Communication, 2008.

[146] N. Oblath, "NCD Monte Carlo pulse scaling and shaper noise," SNO Internal Document, 2007. [Online]. Available: http://manhattan.sno.laurentian.ca/sno/ananoteb.nsf/URL/MANN-7A34RP

[147] A. Cox-Mobrand, Private Communication, 2007.

[148] B. A. Moffat, R. J. Ford, F. A. Duncan, K. Graham, A. L. Hallin, C. A. W. Hearns, J. Maniera, and P. Skensved, "Optical calibration hardware for the Sudbury Neutrino Observatory," *Nucl. Instrum. Meth.*, vol. A554, pp. 255–265, 2005.

[149] L. C. Stonehill, Private Communication, 2006.

[150] N. West *et al.* SNOMAN Companion. [Online]. Available: http://www-pnp.physics.ox.ac.uk/~west/sno/web_snoman/doc/html/companion_frames.html

Appendix A

NCD-ARRAY STRING REFERENCE

This reference chart includes two parts. Table A.1 gives the string number organized by string name. Table A.2 is organized by string number. It gives the SNOMAN string number, the string name, the MUX box, and brief comments.

Table A.1: NCD-string reference chart organized by string name.

Name	Number	Name	Number
I1	36	K5	18
I2	30	K6	11
I3	20	K7	8
I4	29	K8	2
I5	19	L1	34
I6	10	L2	5
I7	3	L3	15
I8	9	L4	24
J1	35	M1	38
J2	32	M2	33
J3	26	M3	27
J4	23	M4	22
J5	16	M5	17
J6	13	M6	12
J7	6	M7	7
J8	4	M8	1
K1	37	N1	39
K2	31	N2	25
K3	28	N3	14
K4	21	N4	0

Table A.2: NCD-string reference chart organized by string number. Strings labeled "bad" were not used in the analysis, with the exception of the 3NA strings, which were used to characterize their respective instrumental events. RCD stands for Resistive Coupler Disconnect, a failure of one component of an NCD string described in detail in [76].

Number	SNOMAN	Name	MUX Box	Comments
0	1	N4	3	Bad; Bursty; 3NA string
1	2	M8	2	Bad; RCD; Low-energy ("Fraser") peak
2	3	K8	1	
3	4	I7	2	^{4}He; Bad
4	5	J8	0	
5	6	L2	1	
6	7	J7	2	
7	8	M7	0	
8	9	K7	3	Bad; Changing gain
9	10	I8	1	
10	11	I6	0	^{4}He
11	12	K6	2	
12	13	M6	1	
13	14	J6	3	
14	15	N3	2	
15	16	L3	0	
16	17	J5	1	
17	18	M5	3	
18	19	K5	0	Bad; Leaking counter
19	20	I5	2	
20	21	I3	3	^{4}He; Bad
21	22	K4	1	

Continued on Next Page . . .

– Continued –

Number	SNOMAN	Name	MUX Box	Comments
22	23	M4	2	
23	24	J4	0	
24	25	L4	3	
25	26	N2	0	
26	27	J3	2	Bad; “Seattle” events; 3NA string
27	28	M3	1	
28	29	K3	3	
29	30	I4	0	
30	31	I2	1	^{4}He
31	32	K2	2	Bad; RCD
32	33	J2	3	
33	34	M2	0	
34	35	L1	2	
35	36	J1	1	
36	37	I1	3	
37	38	K1	0	
38	39	M1	3	
39	40	N1	1	

Appendix B

NCD MC PARAMETERS

Table B.1: NCD MC parameters and uncertainties, where available. For highly-correlated parameters only one was chosen for the investigation of systematics. †: Selected for investigation of systematic effects. ‡: These constants affect the energy scale. The Shaper scaling affects only the shaper values, while the others affect the pulse normalization. Their effects will be highly correlated. §: These constants affect the pulse tails. Their effects will be highly correlated.

Parameter	Value	Range	Reference
Class 1: Measured *ex situ*			
Anode Voltage ‡	1950 V		[80]
Counter Gain Variations	Varies		[93]
Anode Wire Radius	0.0025 cm		[80, 100]
Counter (Inner) Radius	2.5421 cm		[80]
Gas Pressure	2.5 atm		[80]
Mean Ionization Energy ‡	34 eV		[90, 82]
Inverse Propagation Velocity ($\sqrt{LC}$)	0.03876 ns/cm		[100]
String Length	Varies		[143]
Preamplifier Gain	27500 V/A		[97]
Preamplifier Low-Pass RC §	≈3.5 ns		[97]
Preamplifier High-Pass RC §	58 μs		[97]
MUX1 RC †,§	13.3 ns	±0.6	[97]
MUX2 RC §	16.7 ns	±1.8	[97]

Continued on Next Page . . .

– Continued –

Parameter	Value	Range	Reference
Delay Line Time	89 ns		[80]
Cable RC §	3 ns		[97]
NCD LTL Resistance	∼freq.		[100]
NCD LTL Inductance	1.33e-8 H/cm		[144]
NCD LTL Capacitance	7.68e-14 F/cm		[144]
NCD LTL Conductance	0. S/cm/MHz		[144]
Delay Line LTL Resistance	2.75 Ω/cm		[99]
Delay Line LTL Inductance	9.91e-7 H/cm		[99]
Delay Line LTL Capacitance	5.5266e-12 F/cm		[99]
Delay Line LTL Conductance	3e-12 S/cm/MHz		[99]
Direct Pulse Fraction (Preamp) §	0.85		[145]
Cable Delay Times	Varies		
Class 2: Measured *in situ*			
Ion Mobility §	1.082e-8 cm^2 ns^{-1} V^{-1}	±0.027e-8	Section 5.2
Logamp Parameters	Varies	Varies	[97]
Shaper Noise Sigma (Elec.)	1.05		[146]
Shaper Noise Sigma (Phys.)	0.12897105 $1/\sqrt{ADC}$		[146]
Pulse Noise	Varies, ∼freq.		[147]

Continued on Next Page . . .

– Continued –

Parameter	Value	Range	Reference
Class 3: Determined by external simulations or data			
Alpha Straggling	∼E		[84]
Energy Deposition	∼particle, E		[88]
Gas Gain Scaling Constant ‡	1.118 eV/V		[90]
Electron Drift Curve	∼radius		[91]
Electron Drift Resolution	∼radius		[91]
Avalanche Radius	5.79059e-3 cm		[90]
Class 4: Tuned or fit with MC datasets			
Alpha Cocktail †	Varies	Varies	[84]
Mean Po Depth †	0.1 μm		[84]
Mean U & Th Depth †	Varies	Varies	[84]
Electron Drift Curve Scaling †	10%		[84]
Avalanche Width Gradient †	154.321	31	[84]
Avalanche Width Offset †	782.099	120	[84]
Space Charge Scaling Constant	1.5	0.1	[84]
Pulse Scaling †‡	1.054	±0.006	[146]
Shaper Scaling †‡	0.935	±0.006	[146]

Appendix C

PMT CALIBRATION FOR THE NCD PHASE

C.1 Motivation

The timing and gain calibrations of the SNO PMT array are performed using a nearly-isotropic light source that can be moved to different locations within the detector. This calibration was known as the PMT Calibration, or PCA. The light source is a pulsed nitrogen/dye laser system which can operate at six different wavelengths. An 10.9 cm-diameter acrylic diffuser ball, called the laserball, is used to distribute the light nearly-isotropically (to ∼10%). More information on the laser calibration system can be found in [148].

During the previous two phases of SNO the laserball was placed at near center of the detector, so that the light travel-time from the laserball to each PMT was approximately equal. The actual position was offset approximately 21 cm along the y axis, since this was the position, in the $x-y$ plane of the detector, of the portal at the top of the acrylic vessel neck through which the source was deployed. The effect of the offset on the photon timing was taken into account when the calibration was applied to the PMT signals.

During the NCD phase, however, with the laserball at any given location in the detector the NCDs cast shadows on the PMTs. If the previous prescription for PMT calibrations was followed the obstruction by the NCDs would prevent some PMTs from being properly calibrated. The simplest solution is to place the laserball in multiple locations such that all of the PMTs are illuminated sufficiently. This version of the PMT calibration was known as the Multipoint PCA.

C.2 Simulations

Simulations were used to determine the best combination of laserball locations. This included the number of locations necessary and best positions to use. The number of locations

affected the amount of time spent performing the calibration. More runs meant more time calibrating, which reduced the detector livetime. The available laserball locations were confined by the source deployment system to be in the alley-ways between the NCDs along the x or y axes. Furthermore, moving the source too far off-center would mean fewer photons would reach PMTs on the opposite side of the detector.

A simple two-dimensional simulation was used to explore various combinations of laserball locations. It was found that by placing the laserball in the center of the detector and 24 cm offset along the x or y axis $\gtrsim 99\%$ of the PMTs receive sufficient light to be calibrated successfully. An example of simulated shadows is shown in C.1. If only one of those two positions is used, approximately 80% of the PMTs are correctly calibrated. This particular combination of positions ((0,0,0) cm and ($\pm$24,0,0) or (0,$\pm$24,0) cm) was used throughout the NCD phase for the PMT timing and gain calibrations.

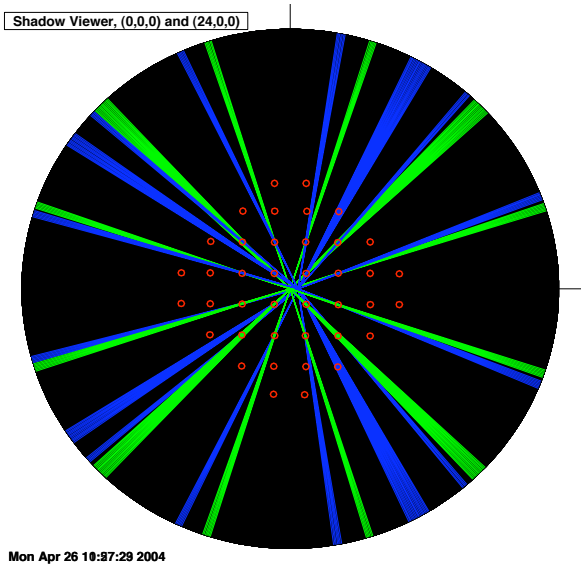

Figure C.1: Simulation of shadows from the ideal laserball positions, (0,0,0) cm and (24,0,0) cm. All NCD positions are indicated, but only shadows from the central 16 NCDs are shown.

C.3 Implementation

Any given Multipoint PCA consisted of at least one run at each laserball location. Combining multiple runs at a single laserball location was as simple as combining the data from the runs together. Combining multiple locations was more complicated because the timing of the photons from the different locations to the PMTs changes.

The most-straightforward way to combine the Multipoint PCA runs is to adjust the PMT signal times so that it appears as if the laserball is at a single location. For simplicity, the timing of timing of the PMT signals is adjusted by Δt such that the laserball appears to be in the center of the detector:

$$\begin{aligned} \Delta t &= t_{\mathrm{c}} - t_{\mathrm{oc}}, \\ t_{\mathrm{c}} &= \tfrac{r_{\mathrm{AV}}}{c_{\mathrm{hw}}} + \tfrac{r_{\mathrm{PMT}} - r_{\mathrm{AV}}}{c_{\mathrm{lw}}}, \\ t_{\mathrm{oc}} &= \tfrac{d_{\mathrm{hw}}}{c_{\mathrm{hw}}} + \tfrac{d_{\mathrm{lw}}}{c_{\mathrm{lw}}}, \end{aligned} \tag{C.1}$$

where r_{AV} and r_{PMT} are the acrylic vessel and PMT array radii, d_{hw} and d_{lw} are the distances the light travels in the heavy- and light-water regions from the off-center laserball location to a PMT, and c_{hw} and c_{lw} are the speeds of light in heavy and light water, respectively. Figure C.2 shows the effect of the PMT timing change for a laserball offset 75 cm from the center of the detector x axis. Each point represents a simulated PMT hit plotted as a function of its time-of-arrival at the PMT and the azimuthal angle of the PMT in detector coordinates. The dark band is the prompt peak, and the spread at later times is due in part to reflections. The curved distribution of the prompt peak in Figure C.2a is due to the light arriving earlier at PMTs closer to the laserball, and later at PMTs farther from the laserball. After the PMT signal times are adjusted, in Figure C.2b the prompt-peak distribution shows that the photons are coming from a source equidistant in the $x - y$ plane from all PMTs. The ∼1.5-ns spread in the prompt peak is the inherent PMT jitter due to the different paths electrons take in traveling from the PMT cathode to the dynode stack. This effect limits the accuracy of the PMT timing. The accuracy of the manipulator system is approximately 2 cm, so the effect on the timing correction is negligible ($2\,\mathrm{cm}/25\,\mathrm{cm\,ns^{-1}} \ll 1.5\,\mathrm{ns}$). The timing fix, combined with the determination of the preferred laserball locations, allowed the

PCA to be accurately conducted during the NCD phase.

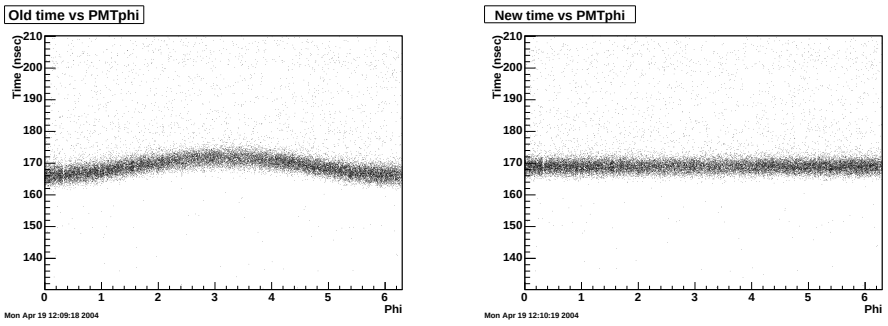

(a) Before (b) After

Figure C.2: SNOMAN simulation of a PCA run with the laserball offset along the x axis by 75 cm. (a) is before the timing fix, and (b) is after. Each point is a PMT hit plotted as a function of the hit time and the azimuthal angle in detector coordinates. The broad band is the PMT prompt peak.

Appendix D

NCD GAS DENSITY CALCULATION

The temperature during NCD gas fill was approximately 75°F, or 297 K [149]. The gas pressure was filled to 2.5 atm. The gas pressure is then determined with the Ideal Gas Law for both the ^{3}He and ^{4}He gas mixtures:

$$\begin{aligned} P_0 &= 2.5 \text{ atm} \\ T_0 &= 297 \text{ K} \\ m_3 &= 3.02 \text{ g/mole} * 0.85 + 88.00 \text{ g/mole} * 0.15 = 15.77 \text{ g/mole} \\ m_4 &= 4.00 \text{ g/mole} * 0.85 + 88.00 \text{ g/mole} * 0.15 = 16.60 \text{ g/mole} \end{aligned}$$

$$\rho_3 = \frac{P_0}{kT_0}\frac{1}{N_A}m_3 = 1.62 \times 10^{-3} \ \frac{\text{g}}{\text{cm}^3} \tag{D.1}$$

$$\rho_4 = \frac{P_0}{kT_0}\frac{1}{N_A}m_4 = 1.70 \times 10^{-3} \ \frac{\text{g}}{\text{cm}^3}, \tag{D.2}$$

where k is Boltzmann's constant, and N_A is Avagadro's constant. The uncertainties on the densities are estimated to be approximately ± 0.01 g/cm^3.

For good measure we also calculate the pressure of the NCD gas in the SNO detector. The pressure after gas fill was 2.5 atm. Due to temperature differences, however, the pressure would decrease. The temperature in SNO is $T_{\text{SNO}} = 283.15$K:

$$P_{\text{SNO}} = P_0\frac{T_{\text{SNO}}}{T_0} = 2.38 \text{ atm} \tag{D.3}$$

Appendix E

SNOMAN CODE MODIFICATIONS FOR PULSE LIBRARIES

The modified versions of SNOMAN used to produce the neutron, wall alpha, and wire alpha pulse libraries are based on SNOMAN 5_0292. This Appendix includes a section for every modified source file, and a final section that lists the command files used to produce the three libraries. All of SNOMAN, including these modifications, is written in FORTRAN77.

E.1 dir_ncd_usr.for

As a diagnostic for tracks that hit an NCD endcap the error messages in this subroutine were expanded. Lines 70-73 were replaced by:

```
      write(iqprnt,*) 'ERROR: not in counter gas or nickel.
     +    Do not use dir_ncd_usr. Sinking vertex.',
     +       iq(lmcvxc+kmcvx_idm), ige_reg_typ
      write(iqlog,*) 'ERROR: not in counter gas or nickel.
     +    Do not use dir_ncd_usr. Sinking vertex.',
     +       iq(lmcvxc+kmcvx_idm), ige_reg_typ
```

E.2 mc_ncd_logamp.for

This routine is responsible for logarithmically amplifying the NCD pulse, passing it through the "MUX2" low-pass filter, and adding noise if requested. Noise is specifically turned off at run time (see Section E.12), so that portion of the simulation is not run. Since we want the NHP to output delogged pulses, this routine is used to invert the process of logarithmic amplification. Lines 133-136 are replaced by:

```
      do ibin = 1, pulse_width_bins
         rq(lmcns + kmcns_current + ibin - 1) =
     +        (10.**((before_scope_signal(ibin) - logamp_c)
     +               / logamp_a) - 1) * logamp_b
      enddo
```

E.3 mc_ncd_scope.for

The standard version of this routine adds the time and voltage offsets, and simulates digitization by rounding each bin value to an integer. It usually acts on logged pulses. As is

mentioned in Section E.2 the pulses in the modified simulation have been delogged. The voltage offset is zero for an ideal, delogged pulse, so line 68 is replaced by:

```
scope_offset = 0.
```

To avoid simulating digitization, line 82 is replaced by:

```
+        recorded_pulse(ibin)
```

E.4 mcg_set_direction.for

For NCD events the initial direction of a track is set by the two angles, θ and ϕ. The portion of this routine that sets the direction according to what is specified at run time by the user was modified to instead take the angles from the `thetadir` and `phidir` arrays. Two extra include files were necessary:

```
INCLUDE 'shl_com.inc'
INCLUDE 'ncd_data.inc'
```

The angles are selected on lines 636 and 637:

```
THETA =  thetadir(nev)
PHI = phidir(nev)
```

E.5 mcg_set_energy.for

The particle energy for neutron captures is fixed at 573 keV and 191 keV for the proton and triton, respectively. Therefore the modifications to this routine were only used to produce the alpha library. Two additional files were included at line 88:

```
INCLUDE 'shl_com.inc'
INCLUDE 'ncd_data.inc'
```

The setting of the energy on line 145 of the original routine was replaced by:

```
RQ(LMCTKC+KMCTK_ENE) = alphaen(NEV)
```

E.6 mcg_set_position.for

Setting the initial position for a track involves determining the radius and the z position. One additional file was included at line 75:

```
INCLUDE 'shl_com.inc'
```

For wall alphas the radius is the inner surface of the NCD counter, which is specified at run time in the command file (see Section E.12). Similarly for wire alphas, the radius is the outer radius of the anode wire. Therefore, the modification for setting the radius was only made to produce the neutron library. The choice of radius, made on lines 627-638, was replaced by:

```
R = RPOS(NEV)
```

The modification for choosing the z position was common to the neutron and alpha code. Lines 646-684 in the original routine were replaced by:

```
RQ(LMCVXC+KMCVX_PSZ) = ZPOS(NEV)
```

E.7 ncd_data.inc

The arrays needed to store the grid points for both the neutron and alpha simulations were added to the general NCD MC include file. They were put in a new common block, `/GRID/`.

The arrays were defined by adding the following below line 54:

```
      integer max_grid_pts
      parameter ( max_grid_pts = 100000)
      real zpos(max_grid_pts),
     +     rpos(max_grid_pts),
     +     alphaen(max_grid_pts),
     +     thetadir(max_grid_pts),
     +     phidir(max_grid_pts)
```

The /GRID/ common block definition was added at line 437:

```
      common /GRID/ zpos, rpos, alphaen, thetadir, phidir
```

E.8 nhp_exe.for

The code to output pulses through the NHP processor into an HBOOK file required extensive changes. The size of the PAWC memory bank was increased via the `user_define_memory_size.for` routine (see Section E.11. However, the bank size is ultimately limited by the integer variable that specifies that size. This was not large enough for the required pulse library sizes, so this routine was modified to periodically dump the histograms in memory to disk and clear the memory. One variable needed to be declared, around line 87:

```
      integer           icycle
```

By default the NHP processor would stop outputting pulses after it reached 10,000 pulses. Lines 129-133 were replaced with the following to output the pulses in memory to disk instead:

```
 if ( inhp_enr .ge. 1000 ) then
   write(iqprnt,90003)
   call hcdir('//NHP_HISTS', ' ')
   call hrout(0, icycle, ' ')
   call hdelet(0)
   inhp_enr = 0
 endif
```

Extensive changes were needed to output smooth delogged pulses instead of logged pulses that had been "digitized." The pulses stored in the MCNS bank were used instead of those in the NEMS bank. In the NEMS bank the pulse is stored as an integer array, while it is stored as a floating-point array in the MCNS bank. Furthermore, the NEMS pulse array compressed into a smaller byte-packed array, with 4 bytes per 32-bit integer word. The step of uncompressing the pulse is not necessary when using the MCNS bank. The histogram naming scheme was modified so that each histogram was named "h[number]," where [number] is replaced by the Monte Carlo event number. This change made it simple to match the histogram in the NHP file to the event in the standard MCEvent and QEvent data structures. All of this was accomplished by replacing lines 241-285 with:

```
 if (icons(ldtnhp+ktnhp_bnk_nr).eq.3.or.
+     icons(ldtnhp+ktnhp_bnk_nr).eq.0) then
    bankname = 'MCNS'
    banktype = 3
    numbins_offset = kmcns_num_bins
    binwidth_offset = kmcns_bin_width
    data_offset = kmcns_current
    bank_nr = 1
    lmcns = lq(lmc - KMC_MCNS)
    banklink = lmcns
    do while ( banklink.ne.0 .and. bank_nr.le.99 )
       hist_id = iq(lmc + kmc_evn)
       hist_nbins= iq(banklink+numbins_offset)
       hist_width= rq(banklink+binwidth_offset)
       hist_min  = 0       ! rq(lmcnc+KMCNC_BIN_LO) too low precision?
       hist_max  = hist_min+hist_nbins*hist_width
       write(hist_number,90005) iq(banklink+KMCNS_STRING_NO)
       hist_title = bankname//hist_number
       call hbook1(hist_id,hist_title,
+           hist_nbins,hist_min,hist_max,0.)
       do hist_bin = data_offset, data_offset+hist_nbins-1
          call hfill(hist_id,
+              hist_min+(real(hist_bin-
+              data_offset)-0.5)*hist_width,
+              0.,rq(banklink+hist_bin))
       enddo
```

```
         bank_nr    = bank_nr    + 1
         inhp_nnems = inhp_nnems + 1
         banklink = lq(banklink)
      enddo
   endif
```

The final code modification simply replaced the too-many-histograms error message defined on line 295 with a notice that 1000 histograms had been saved to disk:

```
90003 format(' NHP_EXE: 1000 histograms saved to disk.')
```

E.9 pta_segments.for

Two modifications were made to this subroutine. The first simply added print statements to warn when an ionization track extended into an endcap region. These lines were added after line 433:

```
      if (ec.eq.1) then
         write(iqprnt,*)"Track went into endcap", sqrt(
     +        (rq(lmcnt+kmcnt_start_psx)-rq(lmcnh+kmcnh_str_psx))**2 +
     +        (rq(lmcnt+kmcnt_start_psy)-rq(lmcnh+kmcnh_str_psy))**2),
     +        rq(lmcnt+kmcnt_start_psz), rq(lmcnt+kmcnt_theta),
     +        rq(lmcnt+kmcnt_phi), rq(lmcnt+kmcnt_tot_energy_dep)
         write(iqlog,*)"Track went into endcap", sqrt(
     +        (rq(lmcnt+kmcnt_start_psx)-rq(lmcnh+kmcnh_str_psx))**2 +
     +        (rq(lmcnt+kmcnt_start_psy)-rq(lmcnh+kmcnh_str_psy))**2),
     +        rq(lmcnt+kmcnt_start_psz), rq(lmcnt+kmcnt_theta),
     +        rq(lmcnt+kmcnt_phi), rq(lmcnt+kmcnt_tot_energy_dep)
      endif
```

The second modification reduced the low-energy cutoff point from 2.5 MeV to 1.4 MeV, the chosen threshold for the pulse-fitting analysis. Warning messages were also added to point out tracks that deposited more than 1.4 MeV in the gas. The following code replaced line 437:

```
      if (rq(lmcnt+kmcnt_tot_energy_dep).gt.1.4) then
         write(iqprnt,*)"Track exceeded energy deposition limit",
     +        rq(lmcnt+kmcnt_tot_energy_dep),init_energy,
     +        rq(lmcnt+kmcnt_start_psz), rq(lmcnt+kmcnt_theta),
     +        rq(lmcnt+kmcnt_phi)
         write(iqlog,*)"Track exceeded energy deposition limit",
     +        rq(lmcnt+kmcnt_tot_energy_dep),init_energy,
     +        rq(lmcnt+kmcnt_start_psz), rq(lmcnt+kmcnt_theta),
     +        rq(lmcnt+kmcnt_phi)
```

E.10 qnext.for

This routine is responsible for the main event processing loop for both Monte Carlo generation and data processing. Prior to looping over the events to be generated for each pulse library the grid points in the neutron and alpha phase spaces needed to be read in from text files. The routine needed access to the arrays to store the grid points, so `ncd_data.inc` was included on line 71:

```
include 'ncd_data.inc'
```

A variable was also defined to iterate the loop over the grid points, defined on line 78:

```
integer i
```

For neutrons the grid points were loaded in from the file `input_neutrons.txt` before line 80 as follows:

```
open(unit=41,file='input_neutrons.txt')
do i=1,ijobne
  read(41,*) zpos(i),rpos(i),thetadir(i),phidir(i)
enddo
close(41)
```

The routine was modified slightly-differently for alphas. The input file is `input_alphas.txt` and the energy array is loaded instead of the radial-position array.

```
open(unit=41,file='input_alphas.txt')
do i=1,ijobne
  read(41,*) zpos(i),alphaen(i),thetadir(i),phidir(i)
enddo
close(41)
```

For wire alphas the arrays are the same but the input file is `input_wirealphas.txt`.

E.11 user_define_memory_size.for

Outputting thousands of pulses through the NHP processor required extending the PAWC memory block. The unmodified subroutine is a dummy. The following was added:

```
integer       MAX_PAWC
parameter    (MAX_PAWC = 500000000 )

real          pawc_array
common /pawc/ pawc_array(MAX_PAWC)

ishl_pawc_size = MAX_PAWC
```

E.12 Command Files

Command files are used to input commands into SNOMAN at run time. Those commands set switches and parameters, and determine how SNOMAN will operate. Separate command files were used to produce the neutron, wall-alpha, and wire-alpha libraries. A single command file has been reprinted here with extensive comments to explain the settings. As written it will produce a neutron library. Optional lines are also included in comments to produce wall- and wire-alpha libraries. The comment character is an asterisk at the beginning of a line. All of the commands are explained in more detail in the SNOMAN Companion [150].

```
*****   Job control
define event_loop
  call MCO
  call NHP
  call NCL(1)
  call NCL(2)
  call NCL(3)
  call QIO(2)
  quit_event
end_def

$seed_file             'rseed.dat        '
$pegs_file             'pegs4_10.dat     '

*****   Ouput files
*** The QIO files will contain the MCTree and QTree data structures.
*** The NHP file will contain the pulses.
file qio 1 libs/lib_neutrons_50290a_sparse2.root
file nhp 1 libs/nhp_neutrons_50290a_sparse2.ntp

*****   MC Control
*** Enable the NCD geometry, and set the date during the NCD phase.
@geom_ncd.cmd
$initial_date 20050104 0

*** Set the number of events in the event list
*** This should be changed to 4200 for the wall-alpha library, and 3500 for
*** the wire-alpha library.
$num_events            3350

$killvx                0
$killvx_neutron        2
```

```
*** Set the parameters that determine how the NCD simulation proceeds.
$enable_hadrons         $on
$ncd_signal_simulation  $on
$space_charge           $on
$ncd_pulse_reflection   $on
$ncd_electronics        $on
$ncd_noise              $off
$gain_fluctuation       $off
$ion_scatter            $off
$electron_tracks        $off

*****   MC Generation
$mc_num_seed_vx 1
*** Give the interaction type.  The alpha command is below.
$mc_interaction_type   $3he$$n_pt$$any_channel
* $mc_interaction_type   $start$$alpha
*** It is necessary that the position be set with $pos_ncd.
*** For neutrons only the string number (first parameter after $pos_ncd)
*** matters out of the parameters given here.
*** The wall-alpha and wire-alpha commands are given below.  For alphas the
*** string and radius (first two parameters after $pos_ncd) are used.
$mc_position           $pos_ncd 40. 1. 1. -450.
* $mc_position           $pos_ncd 40. 2.542 1. -450.
* $mc_position           $pos_ncd 40. 0.0025 1. -450.
*** Since both theta and phi are grid parameters, these values aren't used.
$mc_direction          $dir_ncd_usr 45. 0.
*** The time setting is not used.
$mc_time               $tim_fixed      100.

***** Changes to pulse-generation parameters
*** This line should be uncommented for wall alphas.  It cuts events that
*** deposit more than 1.4 MeV in the NCD gas.
*$low_energy_pulses $on

***** NHP output
*** The first line sets the modified SNOMAN to output histograms
*** from the MCNS bank.  The second line increases the size
*** of the HBOOK record length so that the NHP output file can hold
*** all of the histograms in a single library.
$nhp_bank_output 3
$hbk_lrecl 8191

***** QIO output: no data-cleaning words stored
set bank TQIO 3 word 19 to 0
```

```
*****  MC DAQ error recovery
$mcdaq_ztell           $off

***** Titles files
*** These files must be manually loaded; they are not currently in the SNO
*** database.
titles nhp_data.dat
titles nqxx.dat

@run_snodb
```

VITA

Noah S. Oblath grew up in a number of places along the west coast of the United States, though primarily in Bellingham, WA, and Santa Rosa, CA. He started college at Cornell University in 1998 and was selected for the Cornell Presidential Research Scholars program. Through the CPRS program Noah participated in research all four years he was at Cornell. During his freshman and sophomore years he worked with Professor David Cassell on the CLEO experiment. During his junior and senior years he worked with Professor Eberhard Bodenschatz on a table-top experiment studying plate tectonics with a wax model.

Noah applied for a summer internship with the US Department of Energy's Energy Research Undergraduate Laboratory Fellowship in 1999 and was assigned to work for Dr. Kevin Lesko at Lawrence Berkeley National Laboratory that summer. He, along with fellow undergraduate Ykaterina Opachich, started working on the Sudbury Neutrino Observatory, shortly before it turned on for its first phase. He and Ms. Opachich studied non-physics background events. Noah participated in the ERULF program again for the summer of 2000, working with the same research group and studied the neutron detection characteristics during ^{252}Cf calibrations in the first phase of SNO. During the summer of 2001 he worked with the SNO group for the third time, placing a limit on the number of antineutrinos detected by SNO in its first phase.

After graduating from Cornell in 2002, Noah started graduate school at the University of Washington later that year. He spent two quarters teaching undergraduate introductory physics laboratory sections and then joined the Electroweak Interactions group at CENPA. He worked for Professor Hamish Robertson on a variety of projects for the third phase of SNO. These included adapting the PMT Calibration to account for the NCD proportional counters, building and commissioning a ^{3}He detection system, leading the group working on the NCD Monte Carlo, and using the simulation to fit real data. He earned his M.S. degree in Physics in 2004, and his Ph.D. in 2009. In 2009 he began work on the KATRIN

experiment with Professor Joe Formaggio at MIT.

In his free time Noah enjoys cycling, reading, and tinkering with computers. During graduate school he has participated in the Seafair Milk Carton Derby, including designing, building, and captaining a boat each year from 2004 to 2008. He also volunteered weekly at the Pacific Science Center as a "Science Interpreter."